Study of the Role of Superstructural Phases and Interfacial Properties on the Growth of InN Films

A Thesis

Submitted for the Degree of

Doctor of Philosophy

In faculty of Science

By

Jithesh Kuyyalil

Chemistry and Physics of Materials Unit

JAWAHARLAL NEHRU CENTRE FOR ADVANCED SCIENTIFIC RESEARCH

(A Deemed University)

BANGALORE, INDIA

February 2012

Dedicated to

My mother Sugatha Kumari

February 8, 2012

DECLARATION

I hereby declare that the matter embodied in the thesis entitled **"Study of the Role of Superstructural Phases and Interfacial Properties on the Growth of InN Films"** is an authentic record of research work carried out by me at the Chemistry and Physics of Materials Unit, Jawaharlal Nehru Centre for Advanced Scientific Research, Bangalore, India under the supervision of Prof. S. M. Shivaprasad and that it has not been submitted elsewhere for the award of any degree or diploma.

In keeping with the general practice in reporting scientific observations, due acknowledgment has been made whenever the work described is based on the findings of other investigators.

……………………………….
Jithesh Kuyyalil

JAWAHARLAL NEHRU CENTRE FOR ADVACNED SCIENTIFIC RESEARCH

Jakkur, Bangalore 560064, India

Prof. S. M. Shivaprasad
PHONE: +91 80 22082947
E-MAIL: smsprasad@jncasr.ac.in

February 8, 2012

Certificate

I hereby certify that the matter embodied in this thesis entitled **"Study of the Role of Superstructural Phases and Interfacial Properties on the Growth of InN Films"** has been carried out by Mr. Jithesh Kuyyalil at the Chemistry and Physics of Materials Unit, Jawaharlal Nehru Centre for Advanced Scientific Research, Bangalore, India under my supervision and that it has not been submitted elsewhere for the award of any degree or diploma.

………………………………

Prof. S. M. Shivaprasad

Acknowledgements

Preface

The realization of the exotic properties promised by the fact that group III nitrides form continuous alloys requires the best quality material be synthesized in the entire range and their fundamental properties be established. For example, due to the low dissociation energy of InN, its band gap and effective mass are yet to be established. We perform several experiments in forming InN films and probe using several complementary characterization tools to zero in on these fundamental attributes. On the other hand, Si surfaces are known to exhibit scientifically fascinating reconstructions hosting rich structural and electronic properties. We study the initial stages of growth of group III elements on high and low index Si surfaces to form several ordered 2D reconstructions. These super structural templates where the unit cell dimensions are integrally matched enable us to grow good quality InN and GaN at considerably low temperatures. The thesis is systematically organized into chapters as follows.

Chapter I: Presents the challenges encountered in the group III nitride research and the scope of study of metal induced reconstructions on Si surfaces that forms the motivation for the present work. **Chapter II:** Presents literature review of reported work that becomes the basis for the present studies. **Chapter III:** The main experimental and computation techniques used in the work are described.

Chapter IV: Presents the results of the submonolayer studies of Ga and Al adsorption on Si(111) and Si(55 12) surfaces carried out in Ultra High Vacuum using Auger Electron Spectroscopy and Low Energy Electron Diffraction. We show that at low temperatures Ga grows in the Stranski-Krastanov growth mode and at high temperatures it changes to Volmer-Weber mode. Al adsorption on both high and low index Si surfaces shows a deviation from layer by layer growth above 2ML. We present a comparative study of experimental and simulated uptake curve to understand evolution of island height and size above the wetting layer. Comprehensive 2D phase diagrams arrived at by carrying out several adsorption/desorption studies are presented for both the systems.

Chapter V: Describes a comparative study of submonolayer adsorption/desorption of In on Si(111) and Si(55 12) surfaces. In shows anomalous growth mode on both surfaces, exhibiting layering and clustering of In islands which is also observed during residual thermal desorption studies. We try to understand this peculiar behavior in the light of literature on quantum size effects, step-edge diffusion barrier on adatom

islands and strain relaxation in the overlayer. On the high index surface we observe the formation of In nano-wires and chains. *Ab initio* DFT study of the structure of Si(111)-2√3-In is also presented.

Chapter VI: Presents a study of the structural and optoelectronic properties of MBE grown InN using several complementary characterization tools. The effect of several suggested reasons in the literature such as oxynitrides, In inclusions, quantum size effects etc., on the observed band gap of InN is studied. We present a study of the effect of conduction band non-parabolicity on the effective mass of InN. Also, the surface electron accumulation in InN (0001) surface is studied using XPS valence band analysis.

Chapter VII: We use the phase diagrams of group III metal induced reconstructions presented in Chapters IV and V as guidance to obtain reconstructed Si surfaces of different unit cell dimensions and study the influence of these interfaces on the structural and electronic properties of over-grown GaN and InN films. We show that √3x√3 reconstruction for GaN and 1x1 phase for InN respectively, form a better lattice matched template to grow good quality GaN and InN films at a much lower temperature than usually employed. We discuss these improvements in terms of lattice matching epitaxy of the unit cell of the reconstructions with that of film.

Chapter VIII: Summarizes the work done and presents the main conclusions drawn out this work. A future outlook is also presented.

Contents

Publications

1. Govind, **Jithesh Kuyyalil**, Mahesh Kumar, S.M. Shivaprasad, *"Formation of In-Induced superstructural phases on Si(111)7x7 reconstructed surface"*, J. Nanosci. Nanotech. 9 (2009) 5417

2. **Jithesh Kuyyalil,** Govind, U.V. Waghmare, S.M. Shivaprasad, *"Experimental deduction of In/Si(111) 2D phase diagram and ab-initio DFT modeling of 2√3 phase",* Appl. Surf. Sci. 8 (2009) 120

3. **Jithesh Kuyyalil**, Govind, Mahesh Kumar, S.M. Shivaprasad, *"Clustering and layering of In adatoms on low and high index silicon surfaces: A comparative study"*, Surf. Sci. 604 (2010) 1972

4. Praveen Kumar, **Jithesh Kuyyalil** and S.M. Shivaprasad, *"Ga induced superstructures as templates for lattice matched epitaxial growth of GaN on Si(111) substrate",* Appl. Phys. Lett. 97 (2011) 221913

5. **Jithesh Kuyyalil**, Malleswararao Tangi, S.M. Shivaprasad, *"Dependence of crystal orientation and band gap on substrate temperature of molecular beam epitaxy grown InN on bare $Al_2O_3(0001)$"*, J. Appl. Phys. 109 (2011) 093513

6. Praveen Kumar, **Jithesh Kuyyalil**, Mahesh Kumar, S.M. Shivaprasad, *"Superstructural 2D-phase diagram for Ga on Si(111)-7x7 system"*, Thin. Solid. Films (Accepted)

7. **Jithesh Kuyyalil**, Malleswararao Tangi, S.M. Shivaprasad, *"Discounting the role of In inclusions and oxides on the band gap of InN",* Europhys. Lett. (under revision)

List of manuscripts under preparation

1. **Jithesh Kuyyalil**, Malleswararao Tangi and S.M. Shivaprasad, *"Lattice matching epitaxy of In induced phases on Si for improved quality InN"*

2. **Jithesh Kuyyalil**, Malleswararao Tangi and S.M. Shivaprasad, *"InN: Effective mass and surface electron accumulation"*

3. **Jithesh Kuyyalil**, Praveen Kumar Mahesh Kumar, S.M. Shivaprasad, *"Growth mode of Al on Si(111)-7X7 Surface"*

4. **Jithesh Kuyyalil**, Praveen Kumar Mahesh Kumar, S.M. Shivaprasad, *"A 2D phase diagram for Al induced superstructural phases on Si(111) surface"*

5. **Jithesh Kuyyalil**, Praveen Kumar Mahesh Kumar, S.M. Shivaprasad, *"Initial stages adsorption and formation of 1D nanowires of Al on Si(55 12) surface"*

Acronyms

1D/2D/3D	One-Dimensional/Two-Dimensional/Three-Dimensional
AES	Auger Electron Spectroscopy
AFM	Atomic Force Microscopy
ARUPS	Angle Resolved Ultraviolet Photoelectron Spectroscopy
BE	Binding Energy
CL	Core level
CL	Cathodoluminescence
CVD	Chemical Vapor Deposition
DAS	Dimer Adatom Stacking Fault (Model)
DD	Double Domain
DFT	Density Functional Theory
DME	Domain Matching Epitaxy
DOS	Density Of State
EELS	Electron Energy Loss Spectroscopy
ELOG	Epitaxial Lateral Overlayer Growth
ESCA	Electron Spectroscopy for Chemical Analysis
FESEM	Field Emission Scanning Electron Microscopy
FM	Frank van-der Merwe (growth mode)
FWHM	Full Width at Half Maximum
HBT	Hetero-junction Bipolar Transistor
HREELS	High Resolution Electron Energy Loss Spectroscopy
HRXRD	High Resolution X-ray Diffraction
HT	High Temperature
HVPE	Hydride Vapor Phase Epitaxy
IMFP	Inelastic Mean Free Path
LD	Laser Diode
LED	Light Emitting Diode
LEED	Low Energy Electron Diffraction
LME	Lattice Matching Epitaxy

LT	Low Temperature
PA-MBE	Plasma Assisted-Molecular Beam Epitaxy
MIGS	Metal Induced Gap State
ML	Monolayer
MOCVD	Metal Organic Vapor Phase Epitaxy
MOSFET	Metal Oxide Semiconductor Field Effect Transistor
PES	Photoelectron Spectroscopy
PVD	Physical Vapor Deposition
PL	Photoluminescence
RHEED	Reflection High Energy Electron Diffraction
RMS	Root Mean Square
RT	Room Temperature
RTD	Residual Thermal Desorption
SAG	Selective Area Growth
SEM	Scanning Electron Microscopy
SK	Stranski-Krastanov (growth mode)
SPE	Solid Phase Epitaxy
SSQ	Sum of Squares of Errors
STM	Scanning Tunneling Microscopy
SXPS	Synchrotron X-ray Photoelectron Spectroscopy
TDS	Thermal Desorption Spectroscopy
TEM	Transmission Electron Microscopy
UHV	Ultra High Vacuum
VW	Volmer- Weber (growth mode)
XPS	X-ray Photoelectron Spectroscopy
XPD	X-ray Photoelectron Diffraction
XRD	X-ray Diffraction

Chapter I

Introduction and motivation

This chapter introduces InN as an important material among group III nitrides by detailing its fundamental properties that determine its promising applications. Challenges in InN research such as growth issues and ambiguity concerning basic material parameters are discussed. Possibility of incorporating III-nitrides, InN in particular, into Si industry is evaluated by considering Si reconstructions as growth templates. The chapter concludes by presenting the scope and organization of the thesis.

1.1   Introduction

Semiconductors have revolutionised many aspects of life over the past 50 years. Techniques which have led to low cost, high density processing of silicon have resulted in silicon integrated circuits becoming ubiquitous within modern society. The astonishing progress which has been achieved in the processing of silicon is encompassed by Moore's law.[1] In 1965, only 5 years after the first planar integrated circuit was produced, Gordon Moore noted that the density of transistors being fabricated on silicon integrated circuits was doubling approximately every 2 years. Remarkably this trend has continued to the present day and the latest generation of microprocessors now pack more than half a billion transistors onto a square centimetre.

While the ability of semiconductors to rapidly process information may be the most visible application, semiconductors are used in applications as wide reaching as solid state lighting, power distribution, photovoltaics, lasers and high speed communication. When considering which semiconductor is preferred for a given application, a number of material properties must be considered. High frequency devices rely on high peak carrier drift velocities along with compatibility with high k dielectrics. For light emitting applications, the size and nature of the electronic band gap must be considered, while high power operation requires the material to be relatively insensitive to moderate changes in temperature. With

many different material properties influencing the choice of semiconductor for a given application, there is constant effort towards realising novel materials.

1.2   Group III-nitrides

An area of much recent interest has been the III-nitride semiconductors: AlN, GaN, InN and their alloys. One of the fascinating points is the fact that they form continuous alloys as shown in Fig. 1.1 which promises potential applications in white light emitting diodes, full spectrum solar cells etc.. The first report of III-nitride synthesis was in 1938 by Juza *et al.* who synthesized GaN and InN crystallites.[2] GaN was formed by flowing ammonia over
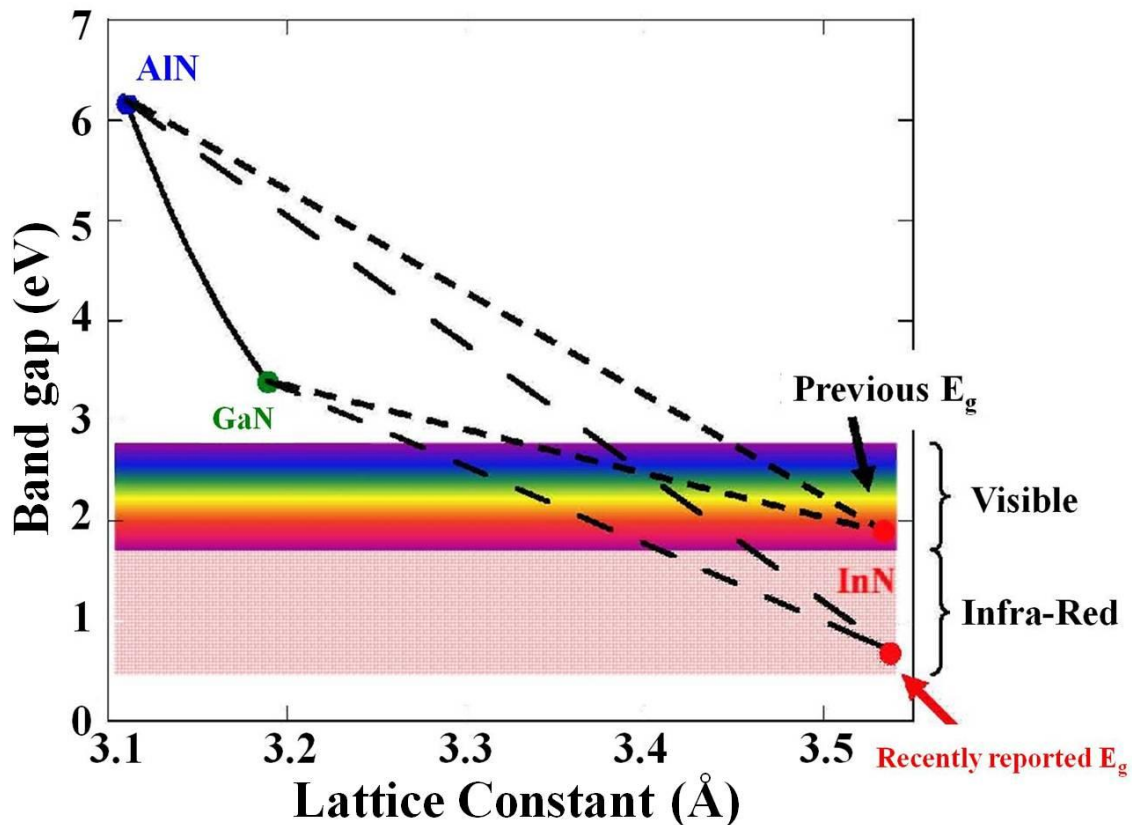
Fig. 1.1: *Band gap versus lattice parameter for various III-nitrides.*

hot gallium, and InN from $InF_6(NH_4)_3$ reduction. The purpose of this initial study was to measure lattice parameters of the materials and there was little interest in their optical properties at that stage. It was 30 years later, when Maruska *et* al. first grew GaN layers by vapour phase deposition on sapphire substrates, that interest in the nitrides increased.[3] Following this report, blue LEDs based on GaN:Zn/n-GaN structures were produced by

Pankove *et al.* on vapour phase grown GaN. These structures relied on hot carrier injection from avalanche breakdown to generate holes. Despite subsequent advances in growth, p-type GaN proved elusive and it was not until 1989 when Amano *et al.* succeeded in reliably producing p-type GaN by Mg doping.[4] Research carried out at Nichia Chemical Industries by Nakamura *et al.* utilised Mg doping to form p-n junctions, and at the time, fabricated the brightest blue LEDs made from any material system.[5] Blue and green LEDs were then commercialised by Nichia Chemical Industries and others. Akasaki *et al.* and Nakamura *et al.* subsequently produced the first laser diodes based on the material system.[6,7] Progress has continued at a remarkable rate, with a number of research groups studying the III-nitrides ballooning. Recent efforts have focused on improving the efficiency of nitride based LEDs and laser diodes and extending the range of wavelengths over which they operate. Added effort has also been applied to HEMTs based on nitride heterojunctions.[8] The unique properties of group III-nitride compound semiconductors, i.e. AlN, GaN, InN and their alloys, have inspired many advanced device designs/structures, integrating electrical, optical, and magnetic functionalities. A key challenge in the realization of such true multifunctional devices lies in the integration of InN and indium rich group III-nitride heterostructures ($x >$ 0.2) in existing $Ga_{1-x}Al_xN$ device structures.[9,10]

1.3   InN as a potential member of III-nitrides

The development in blue/UV light emitting diodes (LEDs) and laser diodes (LDs), and also high-frequency transistors operating at high powers and temperatures, has proved the benefits of the nitride materials system.[9,11-14] Indium nitride (InN) is an important III-nitride semiconductor with many potential applications. The use of InN and its alloys with GaN and AlN makes it possible to extend the emission of nitride-based LEDs from ultraviolet to near infrared region.[15] For example, along with GaN, the InN ternary alloy, InGaN, has found application in a variety of heterostructures based optoelectronic devices, such as LEDs and lasers.[16-18] The InGaN quantum wells are indispensable for light emitting devices because incorporation of small concentrations of In in the active GaN layer increases luminescence efficiency considerably. InN was predicted to have lowest effective mass for electrons in all the III–nitride semiconductors,[13] which leads to high mobility and high saturation velocity. The theoretical maximum mobility calculated in InN and GaN at 300 K are about 4400 and 1000 cm^2/Vs, respectively, while at 77 K the limits are beyond 30,000 and 6000 cm^2/Vs, respectively.[19] The electron transport in wurtzite InN was studied using an ensemble Monte
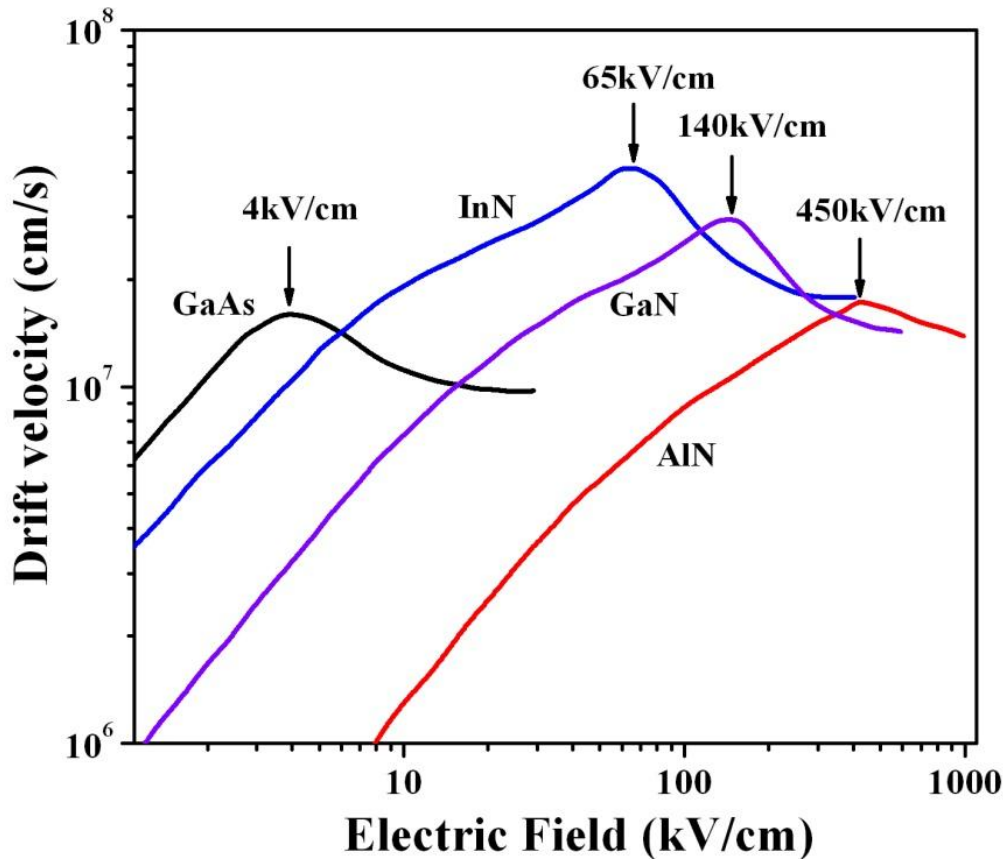
Fig. 1.2: *Velocity-field characteristics of wurtzite GaN, InN, AlN and zincblende GaAs.*

Carlo method.[20-22] It was found that InN exhibits an extremely high peak drift velocity at room temperature. The saturation velocity is much larger than that of gallium arsenide (GaAs) and gallium nitride (GaN). Fig. 1.2 shows the velocity–field characteristics associated with wurtzite GaN, InN, AlN, and zincblende GaAs. The critical field at which the peak drift velocity was achieved for each velocity–field characteristic is clearly marked. It can be seen that each of these III–V semiconductors achieves a peak in its velocity–field characteristic. InN achieves the highest steady-state peak drift velocity: 4.2×10^7 cm/s, which contrasts with the case of GaN, 2.9×10^7 cm/s, AlN, 1.7×10^7 cm/s, and of GaAs, 1.6×10^7 cm/s. It was concluded[21] that the transport characteristics of InN are superior to those of GaN and GaAs, over a wide range of temperature from 150 to 500 K and a doping concentration up to 10^{19} cm^{-3}. The transport characteristics were shown to be relatively insensitive to variations in temperature and doping concentration, unlike GaAs. This suggests that there may be distinct advantages offered by using InN in high frequency centimetre and millimetre wave devices. The transient electron transport, which is expected to be the dominant transport mechanism in submicron-scale devices, was also studied in InN.[22] It is found that InN exhibits the highest

peak overshoot velocity and that this velocity overshoot lasts over the longest distance when compared with GaN and AlN. It was predicted that InN-based field-effect transistors (FET) have an extremely high speed with a cut-off frequency of over 1 THz for 0.1 mm gates. Thus, InN is a highly potential material for the fabrication of high-speed high-performance heterojunction FETs. These potential properties of InN promise several applications.

1.4   Applications of InN

The unique properties of group III-nitride compound semiconductors, e.g. AlN, GaN, InN and their alloys have inspired many advanced device designs/structures, integrating electrical, optical, and magnetic functionalities. Ultimately, the usefulness of indium nitride and group III-Nitride alloys depends on the determination of the band gap. A higher band gap is preferred for microwave transistor devices, a smaller band gap is preferable for a full solar spectrum cell based on InGaN applications.

1.4.1   Optical applications

Electronic lightning technology becomes important with the invention of first light emitting diode LEDs in 1962.[23] Following the achievement of LED technology, light amplification by stimulated emission (LASER) was demonstrated in a semiconductor by 4 groups.[24,25] Development of semiconductors allowed the production of bright light emitters that are used in optical fibre networks, data storage (Compact-Disc Technology), and document printing (Laser printers). But LEDs based on GaAs operate only in the red to yellow portion of the spectrum. SiC has been used for the fabrication of blue LEDs. However SiC or II-VI based LEDs were not emitting with enough intensity due to their indirect band gap. The first blue LEDs based on the III-V nitrides were made commercially available by Nichia in early 1994. Much research has been done on III nitrides comprising the Al-Ga-In-N alloys that show great promise for meeting the next generation optical applications.

1.4.1.1 LED applications

InN is important as a component of group III-Nitrides $(Ga_{1-y-x}Al_y In_x)N$ enabling the fabrication of high-efficient light emitting diodes in a wide spectral region, depending on the composition. As shown in Fig. 1.1, $(Ga_{1-y-x}Al_y In_x)N$ alloys system span a wide range of band gap energies from 0.6 eV to 6.2 eV which correspond to wavelengths ranging from near infrared to deep ultraviolet. In addition, the band gap of the Group III-N system is direct, leading to high quantum efficiency and faster switching speeds. Nakamura and his colleagues

demonstrated the first blue/green light emitting diode based on InGaN. The structure consisted of a 3 nm layer $In_{0.2}Ga_{0.8}N$ sandwiched between p-type AlGaN and n-type GaN, all grown on sapphire substrate.[26] Achieving a red light emitting diode based on InGaN structures depends on indium rich InGaN heterostructures. White LEDs have been developed recently by coating GaN LED with yellow phosphorus which produces light that appears white.[27] However, this structure is not as efficient as the commercial fluorescent light sources. Combining red light emitting diodes with blue/green ones having the same power and brightness can produce full colour displays and efficient white lamps. Researchers at IBM demonstrated an InN nanowire LED, which emits infrared light.[28] The nanowires emit infrared light, which makes them ideal for optical communications between devices on microchips that would speed up computers drastically. If the mechanism in InN nanowires can be tuned to emit red, green and blue light, all nanowire LED could be manufactured on the same substrate. That could make LEDs even cheaper and lead to the devices with improved performance.

1.4.1.2 Laser applications

Fabrication of high quality LEDs enables the fabrication of semiconductor lasers that operate at light wavelengths from ultraviolet to green. The advantage of blue GaN/InGaN lasers with shorter wavelength (405 nm) than a red laser (605 nm) allows five times more storage capacity (25 GB) over traditional DVDs. Blue-ray disc technology was recently adopted by world leading in consumer electronics (including Apple, Dell, HP, JVC, LG, Mitsubishi, Samsung, Sharp, Philips, Pioneer and Sony Corp.) which enable recording and rewriting.[29] The impressive accomplishments taking place and opening a variety of potential markets such as blue-ray are only the beginning of the application of this technology. The performance issues that are related to the crystal growth itself limit further development. It is possible to mix the Al, Ga, and In in appropriate ratios to make ternary and quaternary alloys such as $(Ga_{1-y-x}Al_y In_x)$ N. It is therefore possible, in principle, to make semiconductor lasers that emit light from the deep ultraviolet with a photon energy of 6 eV, to the infrared with photon energy of 1 eV. However, only a much narrower range of operation from the near ultraviolet (3.5 eV) to the green (2.4 eV) has been demonstrated. InN one dimensional (1D) nanostructures, such as nanowires, nanorods, nanotubes and nanobelts are currently the most attractive structures due to the easier growth in single crystal forms without defects, and lasing in the crystals could be expected.[30] Hu *et al.* reported the investigation of infrared

lasing in high quality single crystalline InN nanobelts grown by MOCVD.[30] This can be considered a "major advance" in the nanophotonics field and will impact imaging in chemistry, biology, and optical communications.

1.4.2   InN based THz applications

The terahertz region of the electromagnetic spectrum (300 GHz to 30 THz), correspond to the sub-millimetre wavelength range between 1 mm and 10 μm. There are many applications, which require operation in the terahertz region. There are two major component technologies for terahertz applications: sensor and sources (emitter, generators etc.). However, the main challenge in terahertz applications is the lack of suitable terahertz sources and detectors. One potential way to extend terahertz detection beyond the 3.2 THz is to utilize the properties of InN and indium-rich InGaN alloys and heterostructures. These may lead to more advanced THz detector and emitter devices, operating at temperatures higher than 77K and having higher sensitivity.[31,32] Furthermore, the ferromagnetic behavior of transition metal doped indium rich InGaN may enable unique enhancements of the absorption rates and hence the photo response under an applied magnetic field. Studies on InN show it to be a good material for optically excited THz emission.[31,33] Monte Carlo simulations of InN, GaN and AlN showed that high frequency power generation in a constant electric field occurs for the whole sub millimetre range (0.25THz-4THz) around the liquid nitrogen temperature.[34] The possibility of THz radiation generated from InN films was observed by Ascazubi *et al.*.[33] From this study they concluded that if the carrier concentration of InN films can be reduced by an order of magnitude, InN will surpass InAs as the most efficient semiconductor THz emitter.[33] Chern *et al.* also concluded that power generated from InN films will improve with low carrier concentration.[31] However, the inferior material quality of InN obtainable now is presently delaying final conclusions about THz generation and sensing in InN films.

1.5   InN – Research challenges

Though InN offers several potential applications resulting from its properties, InN research faces several fundamental challenges. Two main fundamental problems related to obtaining good quality InN material are:

- InN has low dissociation temperature compared to other group III nitrides which mainly results from low In-N bond energy (1.99eV).[35]

- There is high vapour pressure of N over InN compared to other nitrides as described in Fig. 1 of Ref[36].

    For epitaxial growth it is necessary to keep substrate temperature as high as possible so as to enable high adatom mobility to form flat films. But, at high temperature InN dissociates putting a constraint on the available growth temperature. The high vapour pressure

$$[11\underline{2}0]_{\text{III-N}} \parallel [11\underline{2}0]_{\text{sap}} \qquad [10\underline{1}0]_{\text{III-N}} \parallel [11\underline{2}0]_{\text{sap}}$$
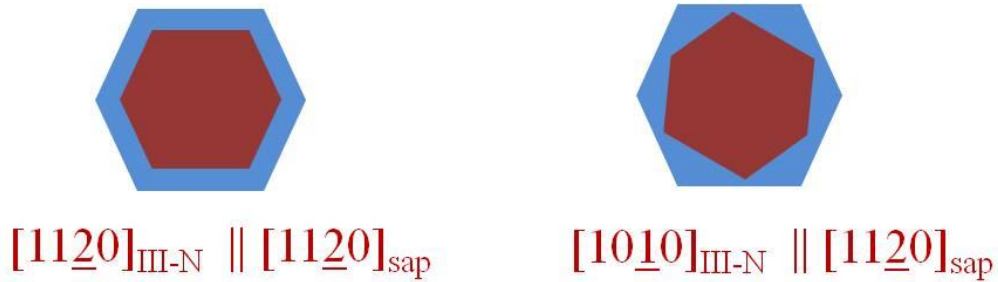
Fig. 1.3: *Two possible epitaxial orientation of InN with sapphire (0001) surface*

of nitrogen over InN creates problem in obtaining stoichiometric InN. As the single crystalline materials of these nitrides are not available they are usually grown on foreign substrates. One of the most widely used substrate is sapphire because of reasons like it is inexpensive and easily available, stability, and feasibility of *in-situ* and *ex-situ* cleaning.[15] Sapphire also has similar crystal structure to that of wurtzite group III nitrides and also offers the possibility of nitridation of its surface to form a thin AlN layer. The main parameter which govern heteroepitaxial growth is the lattice mismatch defined as[37],

$$\frac{a_{III-N} - a_{Sapphire}}{a_{Sapphire}}$$

$$(1.1)$$

where a is the lattice parameter and subscripts represent the substrate and nitride. There are two possible epitaxial orientations for the III-nitrides grown on sapphire (0001) surface, which are shown in Fig. 1.3.[38] Table 1.1 below shows the lattice mismatch values in the two orientations for different nitrides with sapphire substrate. The magnitude of lattice mismatches of InN

Epitaxial Relation / Material	$[11\bar{2}0]_{\text{III-N}} \parallel [11\bar{2}0]_{\text{sap}}$	$[10\bar{1}0]_{\text{III-N}} \parallel [11\bar{2}0]_{\text{sap}}$
GaN	-33.0%	+16.0%
InN	-25.4%	+29.2%
AlN	-34.6%	+13.3%

Table 1.1: *Table showing the lattice mismatch of III-nitrides with two possible epitaxial orientations on sapphire(0001) surface*

in the two epitaxial directions with sapphire is very close compared to other nitrides viz. AlN and GaN. Thus, there is an equal probability for InN to grow in both the epitaxial directions tending to make it polycrystalline. These growth related problems make it difficult to obtain good quality InN with good optoelectronic properties, which has resulted in the reported InN properties being growth condition dependent. Literature shows a range of values for basic properties, like band gap for InN.

1.5.1   InN – its controversial band gap

Until recently, the interest in indium nitride has been restricted to its role as a binary endpoint of InGaN alloys. However, over the last many years a fascinating debate has taken place over the true band gap energy of intrinsic InN. Historically the band gap of InN has been accepted to be 1.9 eV. This value was determined in 1986 by Tansley and Foley after studying absorption spectra from radio frequency (RF) sputtered InN films.[39] A band gap near 2 eV was confirmed by other groups also using sputtering techniques for the film growth.[40,41] As the thin film techniques of MOCVD and MBE have increased in sophistication, the growth of epitaxial InN films became feasible. In 2001 Davydov *et al.* reported the observation of both a strong absorption onset and bright photoluminescence (PL) located below 1 eV for InN films grown by MBE.[42] This was quickly followed by other reports from Wu *et al.* and Matsuoka *et al.* who confirmed that MBE and MOCVD grown InN was showing evidence for a band gap near 0.7 eV.[43,44] The prospect of a band gap near 0.7 eV generated much interest as it raised the possibility that the nitrides could be used to make optical devices which operated from the UV to the infrared (IR), somewhat of a holy

grail for optoelectronic applications. Publications concerning the material increased sharply after the initial publication by Davydov *et al.*.[42] Many other MBE and MOCVD groups confirmed the presence of the 0.7 eV feature as debate continued over the merits of PL and absorption in determining the band gap in the InN case.

GaN and AlN are both known to exhibit PL and absorption features which arise from deep traps within the band gap.[45] In some cases these effects can dominate optical measurements, so the occurrence of a similar effect seemed very plausible within InN. Metallic indium clusters were detected within some InN films and Shubina *et al.* showed that the luminescence from InN films was greatly enhanced in regions around these clusters.[46] This raised the possibility that the 0.7 eV emission could be a result of Mie resonances. Specht *et al.* used valence electron energy loss spectroscopy (VEELS) to show that InN could exhibit an apparent gap near 1.7 eV, although questions have since been raised about the effects that electron damage induced by VEELS could have on the samples.[47] Butcher *et al.* have shown that the stoichiometry of InN films can sometimes be far from unity. They have suggested that the wide variety of results could possibly be explained as In_xN_y alloys with varying composition.[45,48] Davydov *et al.* and Wu *et al.* have argued that the higher absorption features observed can be explained in terms of the Burstein-Moss effect.[49,50] The Burstein-Moss effect describes the shift in the absorption edge of a degenerately doped material as the Fermi energy moves higher into the conduction band. This can lead to an absorption edge and PL peak of very different energy. The effect was shown to describe the behaviour of some MBE grown films very effectively using a two band Kane model.[49]

Indium oxide is an indirect gap material with a band gap near 3.75 eV.[51] The role of oxygen contamination within InN films has thus been a contentious issue. InN films are known to suffer from considerable oxidation at the surface but the effect of this layer on measured electrical and optical properties remains unclear. It has often been argued that the inherently higher oxygen contamination in case of sputtered films can be used to explain the higher observed band gap, as InN-In_2O_3 alloys would exhibit a wider absorption edge than InN.[50,52,53] Indeed, polycrystalline films were shown to exhibit a strong correlation between oxygen content and absorption onset by Yoshimoto *et al.*.[52] Additionally, Bhuiyan *et al.* used different growth techniques to produce films of variable oxygen content and absorption edges that again appeared to correlate with oxygen composition.[53] However, as noted by Monemar *et al.*, the measured oxygen content in these films appears to be inadequate to account for a shift from 0.7 eV to 1.9 V assuming common levels of band gap bowing. It is also noted by

Monemar *et al.* that other reports show that In_2O_3 appears to segregate within the InN lattice and not alloy. In this case the additional absorption feature should occur near 3.75 eV and not 1.9 eV.

Debate over the true band gap of InN continues. To an extent, the number of different explanations proposed has served to confuse the topic as much as the light shed light by it. What is clear from the literature is that the only reliable optical feature that is reproduced in laboratories around the world is the 0.7 eV feature. It is this value that most of the InN community now seem to place more weight behind, but the matter is by no means settled. The observation of exitonic peaks in PL would be a big step towards resolving the matter but to achieve this would require growth of non-degenerate InN layers.

1.5.2   Other challenges in InN research

Different predicted properties of InN have attracted much attention for application in high efficiency solar cells and high speed-electronic devices. One of the key problems in the realization of InN based device application has been proposed to be related to the unusual phenomena of strong electron accumulation on as-grown InN surfaces.[54] This surface electron accumulation layer causes problems in p-doping in InN as it will cause an n-type surface inversion layer which will prevent direct electrical contact to the bulk InN.[55] Recent studies predict universality of the accumulation layer for polar surfaces.[56,57] Surface charge accumulation has not been studied in great detail and the origin has not been well understood as yet. Another important observation concerning the band gap of InN is conduction band non-parabolicity.[49] There are reports which show that effective mass of InN varies with carrier concentration. In narrow band gap semiconductors because of conduction band valence band interaction, the conduction band edge can get perturbed resulting in a non-parabolic character. When the conduction band is non-parabolic effective mass becomes carrier concentration dependent. The confirmation of these effects requires the assignment of a proper band gap for InN.

1.6   Incorporation of nitrides into Si industry

One of major challenge in III-nitride research is to incorporate the nitrides into the well established Si industry to make it inexpensive and integrate it with Si electronics. In the case of InN research in this direction has been nominal. Researchers have tried use of different buffer layers like AlN and GaN so as to reduce the lattice mismatch with the

underlying Si.[58-60] Another possibility which has not yet been looked into is the use of Si reconstructions which may provide a lattice matched template for InN growth. Silicon surfaces, especially low index surfaces, have been frequent centres of interest and studied extensively for various applications in semiconductor technology because of their scientific and technological utility.[61-63] Surfaces in general, especially semiconducting surfaces have dangling bonds on the surface which result in surface reconstructions.[64,65] One of the well established reconstructions of Si is the 7x7 reconstruction which is explained by the famous DAS model.[66] Moreover the native reconstruction of these surfaces can be altered by adsorption of foreign atoms.[64,65] The sources of the metals for the III-nitrides in conventional MBE system are Al, Ga and In. Literature shows the different possible reconstruction for these adsorbates on Si(111) surface. It has been shown that the formation of these adsorbate induced reconstructions depends on the kinetics of adsorption process. Thus, a careful and systematic study is necessary to elucidate the different kinetic pathways for the formation of all the possible reconstructions. Also the application of these structurally and electronically rich reconstructions as a template for good quality InN growth has not yet been explored.

Another major interest in recent times has been the formation of ordered nanostructures on surfaces. Si(111)-7x7 reconstruction is endowed with faulted and unfaulted halves which provide different adsorption sites for the adsorbates.[66] Thus, by kinetically controlling adsorption of these metal atoms (Al, Ga and In) there is the possibility of formation of self assembled nanostructures which has great potential in future device miniaturization. With advent of probes like STM there has been a great deal of interest in studying high index surface of Si, for example Si(5 5 12) surface.[67-69] This high index surface has well defined trenches which can be manipulated for the formation of self assembled nanochains of metal atoms.[70,71] Studies on initial stage adsorption of Al and In on Si(5 5 12) surface has not been reported in literature.

1.7   Scope and organization of the thesis

The prospect of InN having a band gap near 0.7 eV has caused much excitement as people have envisioned devices based on the $In_xGa_{1-x}N$ system spanning the entire visible spectrum and much of the infrared. Such a material system would hold a great deal of promise for applications in solar cells and optoelectronics. Regardless of the band gap, InN remains a promising material for applications in high electron mobility transistors, and dilute magnetic semiconductor applications. HEMTs offer a particularly achievable near term

application; the device structure is simple and it was one of the first devices realised in GaN technology.

Despite the prospect of applying InN in these ways, the material research is still in its infancy in terms of our understanding of processing and preparing the material in appropriate thin film forms. For example, band gap and effective mass are yet to be established for InN. In the present work, we perform several experiments in forming InN films and probe the system carefully by using several complementary characterization tools to zero in on these fundamental attributes. On the other hand, Si surfaces are known to exhibit scientifically fascinating reconstructions hosting rich structural and electronic properties. We study the initial stages of growth of group III elements on high and low index Si surfaces to form several ordered 2D reconstructions. Some of these superstructural templates where the unit cell dimensions are integrally matched enable us to grow good quality InN and GaN at considerably low temperatures. The thesis is systematically organized into chapters as follows.

Chapter I: Presents the introduction to the challenges encountered in group III nitride research and the scope of study of metal induced reconstructions on Si surfaces, as motivation for the present work.

Chapter II: Presents literature review of reported work that forms the basis for the present studies.

Chapter III: Main experimental and computation techniques used for the work are described.

Chapter IV: Presents the results of the submonolayer studies of Ga and Al adsorption on Si(111) and Si(5 5 12) surfaces carried out in Ultra High Vacuum using Auger Electron Spectroscopy and Low Energy Electron Diffraction. We show that at low temperatures Ga grows in the Stranski-Krastanov growth mode and at high temperatures it changes to Volmer-Weber mode. Al adsorption on both high and low index Si surfaces shows a deviation from layer by layer growth above 2ML. We present a comparative study of experimental and simulated uptake curve to understand evolution of island height and size above the wetting layer. Comprehensive 2D phase diagrams arrived at by carrying out several adsorption/desorption studies are presented for both the systems.

Chapter V: Describes a comparative study of submonolayer adsorption/desorption of In on Si(111) and Si(5 5 12) surfaces. In shows anomalous growth mode on both surfaces, exhibiting layering and clustering of In islands which is also observed during residual thermal desorption studies. We try to understand this peculiar behavior in the light of literature on quantum size effects, step-edge diffusion barrier on adatom islands and strain relaxation in the overlayer. On the high index surface we observe the formation of In nano wire and chains. Ab initio DFT study of the structure of Si(111)-2√3-In is also presented.

Chapter VI: Presents a study of the structural and optoelectronic properties of MBE grown InN using several complementary characterization tools. The effect of several suggested reasons in the literature such as oxynitrides, In inclusions, quantum size effects etc., on the observed band gap of InN is probed. We present a study of the effect of conduction band non-parabolicity on the effective mass of InN. Also, the surface electron accumulation in InN (0001) surface is studied using XPS valence band analysis.

Chapter VII: We use the phase diagrams of group III metal induced reconstructions presented in Chapters IV and V as guidance to obtain reconstructed Si surfaces of different unit cell dimensions and study the influence of these interfaces on the structural and electronic properties of over-grown GaN and InN films. We show that √3x√3 reconstruction for GaN and 1x1 phase for InN respectively, form a better lattice matched template to grow good quality GaN and InN films at a much lower temperature than usually employed. We discuss these improvements in terms of "Lattice Matching Epitaxy" of the unit cell of the reconstructions with that of the film.

Chapter VIII: Summarizes the work done and presents the main conclusions drawn out this work. A future outlook is also presented.

References

[1] G. E. Moore, Electronics Magazine **38**, 114 (1965).

[2] R. Juza and H. Hahn, Anorg. Allgem. Chem. **234**, 282 (1938).

[3] H. P. Maruska and J. J. Tietjen, Appl. Phys. Lett. **15**, 327 (1969).

[4] H. Amano, I. Akasaki, T. Kozowa, H. Hiramatsu, N. Sawak, K. Ikeda, and Y. Ishii, J. Luminescence **121**, 40 (1988).

[5] S. Nakamura, M. Senoh, N. Iwasa, and S. Nagahama, Japan. J. Appl. Phys. **34**, L797 (1995).

[6] I. Akasaki and H. Amano, GaN, Academic, New York **1**, (1998).

[7] S. Nakamura, M. Senoh, S. ichi Nagahama, N. Iwasa, T. Yamada, T. Matsushita, H. Kiyoku, and Y. Sygimoto, Appl. Phys. Lett. **68**, 2105 (1996).

[8] A. J. Sierakowskia and L. F. Eastman, J. Appl. Phys. **86**, 3398 (1999).

[9] S. C. Jain, M. Willander, J. Narayan, and R. V. Overstraeten, J. Appl. Phys. **87**, 965 (2000).

[10] J. I. Pankove, GaN and Related Materials, **2**, (1997).

[11] S. Strite and H. Morkoc, J. Vac. Sci. Technol. B **10**, 1237 (1992).

[12] S. J. Pearton, J. C. Zolper, R. J. Shul, and F. Ren, Ibid **86**, 1 (1999).

[13] S. N. Mohammad and H. Morkoc, Prog. Quantum Electron. **20**, 361 (1996).

[14] O. Ambacher, J. Phys. D **31**, 2653 (1998).

[15] A. G. Bhuiyan, A. Hashimoto, and A. Yamamoto, J. Appl. Phys. **94**, 2779 (2003).

[16] I. Akasaki, H. Amano, N. Koide, M. Kotaki, and K. Manabe, Physica B **185**, 428 (1993).

[17] S. Nakamura, M. Senoh, and T. Mukai, Japan. J. Appl. Phys. **Part 2 32**, L8 (1993).

[18] S. Nakamura, M. Senoh, S. Nagahama, N. Iwasa, T. Yamada, T. Matsushita, H. Kiyoku, and Y. Sugimoto, Japan. J. Appl. Phys. **Part 2 35**, L74 (1996).

[19] V. W. L. Chin, T. L. Tansley, and T. Osotchan, J. Appl. Phys. **75**, 7365 (1994).

[20] S. K. O'Leary, B. E. Foutz, M. S. Shur, U. V. Bhapkar, and L. F. Eastman, J. Appl. Phys. **83**, 826 (1998).

[21] E. Bellotti, B. K. Doshi, K. F. Brennan, J. D. Albrecht, and P. P. Ruden, J. Appl. Phys. **85**, 916 (1999).

[22] B. E. Foutz, S. K. O'Leary, M. S. Shur, and L. F. Eastman, J. Appl. Phys. **85**, 7727 (1999).

[23] J. Black, H. Lowckwood, and S. Mayburg, J. Appl. Phys. **34**, 178 (1963).

[24] R. D. Dupuis, IEEE Quant. Electr. **QE-23**, 651 (1987).

[25] M. G. Craford, IEEE Circuit Devices **8**, 25 (1992).

[26] S. Nakamura and G. Fasol, The Blue Laser Diode, Springer, Berlin (1997).

[27] D. B. Nicol, Ph. D Thesis, Georgia Institute Of Technology (2006).

[28] K. Bullis, Technology Review Published By MIT **August 01**, (2007).

[29] Www.blue-ray.com (n.d.).

[30] M. S. Hu, G. M. Hsu, K. H. Chen, C. J. Yu, H. C. Hsu, L. C. Chen, J. S. Hwang, L. S. Hong, and Y. F. Chen, Appl. Phys. Lett. **90**, 123109 (2007).

[31] J. S. Speck, with G.Koblmuller, Appl. Phys. Lett. **89**, 141115-3 (2006).

[32] V. Gruzinskis, P. Shiktorov, E. Starikov, L. Reggiani, L. Varani, and J. C. Vaissière, Semicond. Sci. Technol. **19**, S173 (2004).

[33] R. Ascazubi, I. Wilke, K. Denniston, H. Lu, and W. J. Schaff, Appl. Phys. Lett. **84**, 4810 (2004).

[34] E. Starikov, P. Shiktorov, V. Gruzinskis, L. Reggiani, L. Varani, J. C. Vaissiere, and J. H. Zhao, Physica B **314**, 171 (2002).

[35] H. P. Lei, P. Ruterana, G. Nouet, X. Y. Jiang, and J. Chen, Appl. Phys. Lett. **90**, 111901 (2007).

[36] O. Ambacher, M. S. Brandt, R. Dimitrov, T. Metzger, M. Stutzmann, R. A. Fischer, A. Miehr, A. Bergmaier, and G. Dollinger, J. Vac. Sci. Technol. B **14(6)**, 3532 (1996).

[37] M. Ohring, The Materials Science Of Thin Films, Boston, Academic Press (1992).

[38] Y. Nanishi, Y. Saito, and T. Yamaguchi, Japan. J. Appl. Phys. **42**, 2549 (2003).

[39] L. T. Tansley and C. P. Foley, J. Appl. Phys. **59**, 3241 (1986).

[40] K. L. Westra, R. P. W. Lawson, and M. J. Brett, J. Vac. Sci. Technol. A **6**, 1730 (1988).

[41] K. Kubota, Y. Kobayashi, and K. Fujimoto, J. Appl. Phys. **66**, 2984 (1989).

[42] J. Graul, with O.Semchinova, Phys. Status. Solidi B **229**, R1 (2001).

[43] J. Wu, W. Walukiewicz, K. M. Yu, J. W. Ager III, E. E. Haller, H. Lu, W. Schaff, Y. Saito, and Y. Nanishi, Appl. Phys. Lett. **80**, 3967 (2002).

[44] T. Matsuoka, H. Okamoto, M. Nakao, H. Harima, and E. Kurimoto, Appl. Phys. Lett. **81**, 1246 (2002).

[45] K. S. A. Butcher and T. L.Tansley, Superlattices Microstruct. **38**, 1 (2005).

[46] T. V. Shubina, S. V. Ivanov, V. N. Jmerik, D. D. Solnyshkov, V. A. Vekshin, P. S. Kop'ev, A. Vasson, J. Leymarie, A. Kavokin, H. Amano, K. Shimono, A. Kasic, and B. Monemar, Phys. Rev. Lett. **92**, 117407-1 (2004).

[47] P. Specht, J. C. Ho, X. Xu, R. Armitage, E. R.Weber, R. Erni, and C. Kisielowski, Solid State Comm. **135**, 340 (2005).

[48] K. Scott, A. Butcher, M. Wintrebert-Fouquet, P. P.-T.Chen, K. E. Prince, H. Timmers, S. K. Shresthta, T. V. Shubina, S. V. Ivanov, R. Wuhrer, M. R. Phillips, and B. Monemar, Phys. Status. Solidi C **2**, 2263 (2005).

[49] J. Wu, W. Walukiezicz, W. Shan, K. M. Yu, J. W. Ager III, E. E. Haller, H. Lu, and W. J. Schaff, Phys. Rev. B **66**, 201403 (2002).

[50] V. Yu. Davydov, A. A. Klochikhin, V. V. Emtsev, D. A. Kurdyukov, S. Ivanov V., V. V. Vekshin, F. Bechstedt, J. Furthmuller, J. Aderhold, J. Gral, A. V. Mudryi, H. Harima, A. Hashimoto, A. Yamamoto, and E. E. Haller, Phys. Status. Solidi B **234**, 787 (2002).

[51] I. Hamberg and C. G. Granqvist, J. Appl. Phys. **60**, R123 (1986).

[52] M. Yoshimoto, H. Yamamoto, W. Huang, H. Harima, J. Saraie, A. Chayahara, and Y. Horino, Appl. Phys. Lett. **83**, 3480 (2003).

[53] A. Ghani Bhuiyan, K. Sugita, K. Kasashima, A. Hashimoto, A. Yamamoto, and V. Yu. Davydov, Appl. Phys. Lett. **83**, 4788 (2003).

[54] I. Mahboob, T. D. Veal, and C. F. McConville, Phys. Rev. Lett. **92**, 036804-1 (2004).

[55] R. E. Jones, K. M. Yu, S. X. Li, W. Walukiewicz, J. W. Ager, E. E. Haller, H. Lu, and W. J. Schaff, Phys. Rev. Lett. **96**, 125505 (2006).

[56] D. Segev and C. G. Vand de Walle, Europhys. Lett. **76**, 305 (2006).

[57] David Segev and Chris G Van De Walle, Surface Science **601**, 0-3 (2007).

[58] Y. -H. Wang and W. -L. Chen, Physica E **41**, 848 (2009).

[59] C. C. Huang, R. W. Chuang, S. J. Chang, J. C. Lin, Y. C. Cheng, and W. J. Lin, J. Electron. Mater. **37**, 1054 (2008).

[60] K. R. Wang, L. W. Tu, S. J. Lin, Y. L. Chen, Z. W. Jiang, M. Chen, C. L. Hsiao, K. H. Cheng, J. W. Yeh, and S. K. Chen, Phys. Status. Solidi B **243**, 1461 (2006).

[61] A. Hryciw, Y.C. Jun, and M.L. Brongersma, Nat. Mater. **9**, 3 (2010).

[62] T. Schmidt, S. Gangopadhyay, J.I. Flege, T. Clausen, A. Locatelli, S. Heun, and J. Falta, New J. Phys. **7**, 193 (2005).

[63] H.F.O. Schmidt and T.J. Watson, IBM J. Res. Dev. **43**, 351 (1999).

[64] H. N. Waltenburg and J. Yates Jr., Chem. Rev. **95**, 1589 (1995).

[65] J. P. LaFemina, Surf. Sci. Rep. **16**, 133 (1992).

[66] K. Takayanagi, Y. Tanishiro, S Takahashi, and M. Takahashi, Surf. Sci. **164**, 367 (1985).

[67] T. Suzuki, H. Minoda, Y. Tanishiro, and K. Yagi, Surf. Sci. 335 (1996).

[68] T. Suzuki, H. Minoda, Y. Tanishiro, K. Yagi, T. Sueyashi, T. Sato, and M. Iwatsuki, Surf. Sci. **357**, 522 (1996).

[69] A. A. Baski and L. J. Whitman, Phys. Rev. Lett. **74**, 153 (1995).

[70] A. A. Baski, K. M. Jones, and K. M. Saoud, Ultramicroscopy **83**, 23 (2001).

[71] J. W. Dickinsonm, J. C. Moore, and A. A. Baski, Surf. Sci. **561**, 193 (2004).

Chapter II

Overview of Literature

In this chapter, the literature background for the work presented in this thesis is provided. Firstly the historic development of InN research, regarding its growth, structure and properties are described. Then, the established structures of the Si(111)-7x7 and Si(5 5 12)-2x1 surfaces are elucidated and previously reported literature on metal adsorption on these reconstructed surfaces is presented.

2.1   Growth and properties of InN

2.1.1   InN: Historical overview

Research on InN was initiated in 1938 when synthesized powder samples were analyzed by X-ray diffraction in order to determine the crystallographic properties of this material.[1] Juza and Hahn obtained InN from decomposition of $InF_6(NH4)_3$ at 600^oC.[1] Juza and Hahn reported the crystal structure of InN to be wurtzite having lattice parameters a= 3.5377 Å, c= 5.7037 Å which are in excellent agreement with the present reported values. Research onto InN was sporadic between 1938 and 1990.

In the 1970's, McChesney *et al.* reported the disassociation pressure of InN as extremely high and stated that the formation of InN may require interaction of indium metal with atomic or other excited nitrogen species at high temperature high pressures.[2] They showed that the phase relation of InN results in a P-T^{-1} relation as depicted Fig. 2.1 according to

$$\Delta H_F = -\frac{1}{2} R \frac{d \ln P_{N2}}{d(1/T)} \qquad (1.1)$$

in which the dissociation pressure rises very steeply towards higher nitrogen pressure. Another report by Trainor and Rose in 1974 argued that partial pressure of atomic nitrogen, rather than diatomic nitrogen, is a more fundamental parameter describing thermal equilibrium.[3] The thermal stability studies of InN indicated that InN samples decomposed in

a few minutes leaving an indium residue in N_2 (at standard pressure) at 500°C during the annealing process. However, if the InN samples were heated to 500°C in nitrogen pressure (10^{-3} torr) InN would not decompose. The stability of InN films can be achieved by thermal
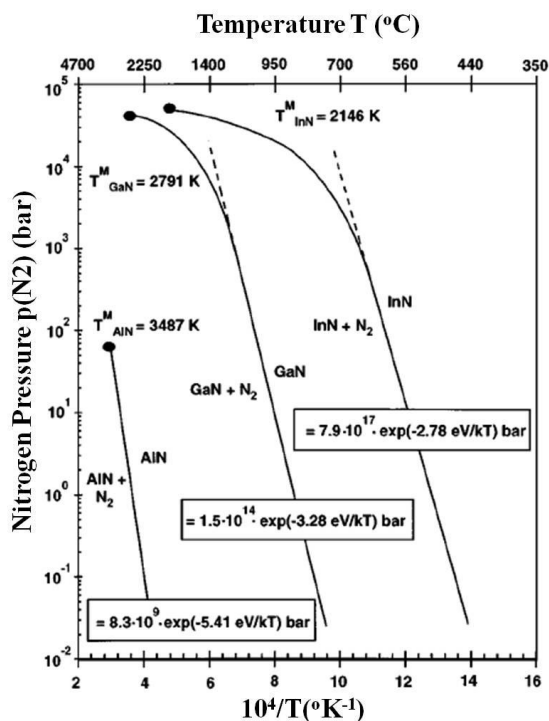
Fig. 2.1: *Phase relations of InN shown by the decomposition curve separating InN and In+N2 phase fields.*[4]

dissociation of N_2. Trainor and Rose found the fundamental band edge for InN films to be 1.7 eV and their absorption study suggested that InN is a direct band gap semiconductor, due to the similarity in the shape of fundamental absorption edge to that of GaN. InN samples grown on sapphire by reactive evaporation had a Hall effect mobility of 20 cm^2/Vs and carrier concentration in the 10^{20} cm^{-3} range as measured by hall effect experiments. Trainor and Rose also suggested that higher quality films could be achieved by growing the films at higher temperatures (~600°C) and lower growth rates. Hovel and Cuomo produced polycrystalline InN films grown on sapphire and silicon substrates with some reasonably good electrical properties (Hall mobility μ=250 ± 50 cm^2/Vs, and n-type carrier concentration 5.8x10^{18} cm^{-3}) by reactive radio frequency (RF) sputtering.[5] The InN films appeared dark red and possessed a resistivity in the range of 10 Ωcm. Marasina *et al.* utilized chemical vapor deposition to produce InN epitaxial layers with an electron concentration of 2x10^{20}-8x10^{21}cm^{-3} and a mobility of 50-30 cm^2/Vs.[6] They reported that the disassociation of InN rapidly occurred at 600°C, and there was no deposition of InN layers above 670°C.

In the 1980's the properties of InN films grown via metallic Indium in a nitrogen environment were mainly studied by Tansley and Folley, who reported an electron mobility as high as 5000 cm^2/Vs and a low background carrier concentration in the InN film ($5x10^{16}cm^{-3}$) . Those results were early indicators of the potential of InN for high mobility FET devices. However, the optical absorption data of InN samples prepared by reactive RF sputtering indicate an optical absorption edge at 1.89 eV. Recently epitaxial single-phase InN films have been grown on (0001) sapphire in the temperature range of 400-600°C by microwave-excited metal organic vapor phase epitaxy (MOVPE) using $(CH_3)_3$In and pure atomic nitrogen or excited nitrogen species supplied by microwave discharge of N_2.[7] It was shown that (0002) InN layers could be grown on (0001) sapphire at temperatures around 500°C.

More recent publications, mostly describing molecular beam epitaxy (MBE) InN layers, indicate a lower energy band gap, initially reported at around 1.1 eV[8] (Mg-doped InN samples), but later at progressively lower values of 0.9 eV[9] and then 0.8-0.7 eV[10,11]. Recently, a band gap value of 0.65eV[12] has been proposed. These studies include growth by MOVPE and MBE on different substrates and underlying layers over a wide range of growth conditions. The highest mobility and lowest background concentration are 2000 cm^2/Vs and $3.6x10^{17}cm^{-3}$ for ~1.2 μm InN layers grown by MBE.[13,14] The first growth of InN at high pressures was made by Dietz et al. in a High Pressure Chemical Vapor Deposition (HPCVD) system developed at Georgia State University.[15]

2.1.2   Structural properties

It is essential to know and characterize the crystal structure of the InN in order to improve the quality and performance of the InN based device structures. X-ray diffraction (XRD) is a versatile non-destructive technique, which reveals detailed information about the chemical composition and crystallographic structure of any natural and manufactured materials. The crystal and microstructure of InN films, which may include dislocation, grain boundaries etc., are typically investigated by X-ray diffraction and transmission electron microscopy (TEM) while, Rutherford back scattering spectrometry (RBS) measurements are used to assess film stoichiometry, Low energy electron diffraction (LEED) is a technique used to analyze the crystal structure of the surface.
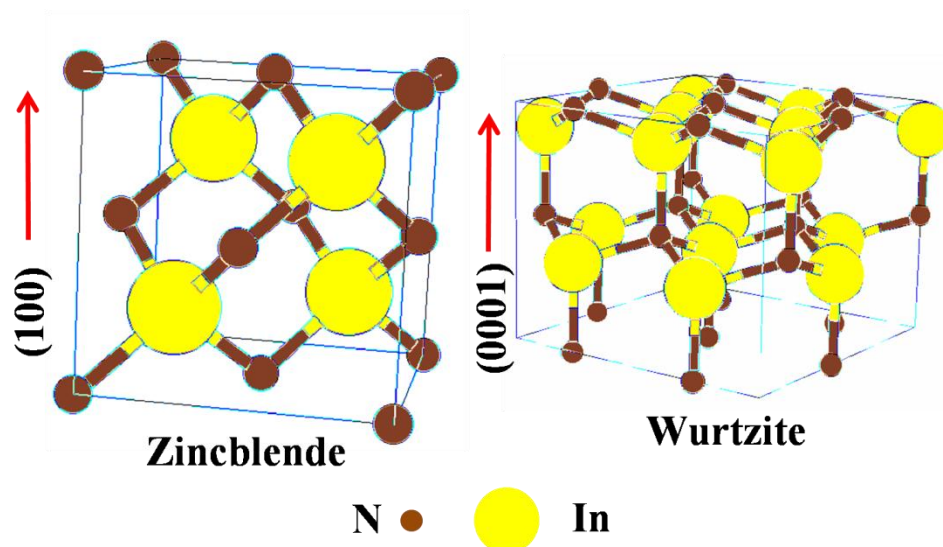
Fig. 2.2: *Crystal structures of InN.*

By using all of the structural characterization techniques mentioned above, it has been shown in the literature that the crystal structure of indium nitride epitaxial layers is similar to that of GaN films prepared under similar conditions. InN can crystallize in three different structures, wurtzite, zincblende and rock salt, similar to that of other nitrides. Thermodynamically, the stable crystal structure is the hexagonal wurtzite structure. However, InN can also be obtained in the cubic zincblende structures when grown on (001) crystal planes of cubic substrates like silicon and GaAs. The wurzite structure has a hexagonal unit cell and thus two lattice constants c and a. It contains of six atoms of each type. The zincblende structure has a cubic unit cell, containing four indium atoms and four nitrogen atoms. The main difference between the cubic and the hexagonal structure is that they have a different stacking sequence of the closest packed diatomic planes. In both cubic and hexagonal crystal structures, each indium atom is coordinated by four nitrogen atoms and each nitrogen atom is coordinated by four indium atoms as shown in the Fig. 2.2.[16]

The lattice constant values of InN may be influenced by the growth conditions, impurity concentrations, and the film stoichiometry. Juza and Hahn[1] first reported the crystal structure of InN to be wurtzite having lattice parameters a = 3.53 Å, and c = 5.69 Å. These values are quite close to a = 3.5480 Å, c = 5.7600 Å reported by Tansley & Foley[17], and a = 3.544 Å, c =5.718 Å reported by Osamura *et al.*[18]

2.1.3   Band gap

The material properties of InN change dramatically with the growth techniques employed and thus the understanding of this novel semiconductor still remains very poor. During the last decade there have been several conflicting reports on the band gap of InN; values have varied between 0.6 and 2 eV in different papers.[11,19] Bagayoko and Franklin presented an overview of two groups of experiments that provided different values of the band gap of w-InN.[20] Experiments in the first set, mostly before 2000, reported band gap values of 1.9–2.0 eV, while the ones in the second set found band gap values of 0.7–1.0 eV, depending on the free carrier concentrations. Samples studied by in the second set, mostly grown by molecular beam epitaxy, were believed to be of much higher quality than those of first set that mostly investigated polycrystalline films. Inushima $et\ al.$[8] determined that the band gap of InN grown on sapphire by MBE was between 0.89 and 1.46 eV at respective electron concentrations of 5×10^{19} cm^{-3} and 2×10^{20} cm^{-3}. Kadir $et\ al.$ studied samples of InN grown by metal-organic vapor phase epitaxy (MOVPE), and they reported that the band gap E_g for the InN samples is ~ 0.7 eV.[21] Recently, the Hydride Vapor Phase Epitaxy (HVPE) growth technique has received attention because it is a useful method for growing thick layers of group III-Nitrides.[22-24] Cathodoluminescence (CL) spectrum measurements of single crystalline (0002) InN grown by HVPE exhibit a strong peak at 0.75 eV.[25] In conclusion, InN films grown by Molecular Beam Epitaxy (MBE)[9,26], HVPE and MOVPE[27] revealed that the band gap energy of InN is about 0.7 eV.

Until recently, the band gap energy of ≈0.7 eV was considered as the fundamental narrow band gap due to measurements by infrared photoluminescence (PL) and optical absorption of InN grown by MBE, MOCVD, and HVPE. However, the growth of high quality InN layers and related indium rich III-N alloys remains difficult due to InN stoichiometric instabilities, limited carrier concentration and low dissociation temperatures, leading to inconsistent and process dependent material properties.[28] Nevertheless, Butcher et $al.$[29] have shown that In:N stoichiometry affects the apparent band gap of the InN film very strongly, and evaluation of stoichiometry variations in InN films (MBE grown and Remote Plasma Assisted Chemical vapor deposition (RPECVD)) suggests that these films should not to be treated as homogenous materials. For instance, the electron carrier concentration dependence of the optical absorption edge for epitaxial material does not follow the Moss-Burstein effect[30,31] for InN samples grown by different techniques. Fig. 2.3 shows the apparent change in the band gap of InN materials grown by different techniques. The solid

curve shown in Fig. 2.3 is proposed by Schaff *et al.* to describe the differences in the measured band gap with an alternate model.[32] It is clearly shown in Fig. 2.3 that the Moss-Burstein model cannot explain those data points below carrier concentration of 10^{19} cm^{-3}, which have high optical absorption edge values above 1.5 eV.
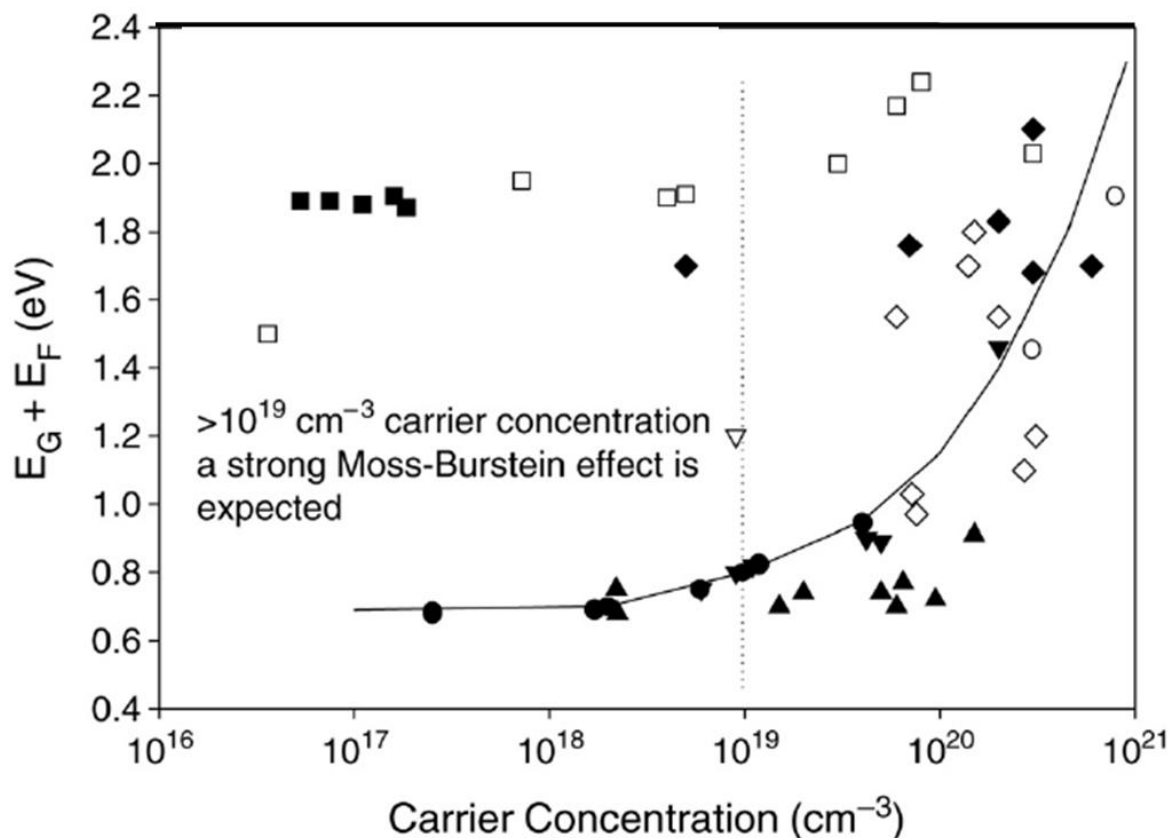
Fig. 2.3: *Different reported band gap values for InN in literature.   Continuous curve represents the theoretical prediction for Moss-Burstein shift.*

2.1.4   Heteroepitaxial growth on lattice mismatched substrates

As single crystals of InN are not available several other substrates have been tried for InN growth. Sapphire is the most extensively used substrate material for the epitaxial growth of InN and other III-nitrides.[33] Large area good quality crystals of sapphire are easily available at relatively low cost. They are transparent and stable at high temperatures. High quality epitaxial InN film can be grown easily on sapphire substrates by the popular growth methods, MOVPE and MBE. The
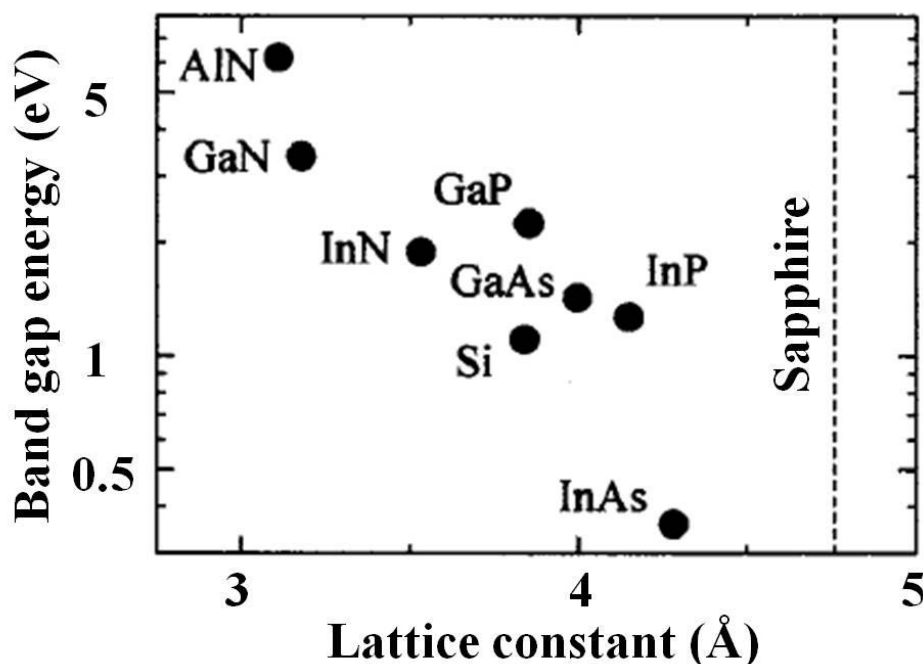
Fig. 2.4: *Band gap versus lattice constant for different substrates used to grow InN.*

band gap and lattice constant in the hexagonal atomic space-plane of InN and the materials which are widely used as a substrate or underlying layer for the epitaxial growth of InN are shown in the Fig. 2.4. The InN has a large lattice mismatch of 25% with sapphire compared with the other substrates. The large lattice mismatch and thermal expansion coefficient difference can result in an extremely high density of structural defects. However, researchers have revealed that the substrate surface pre-treatment and insertion in of an intermediate buffer layer between the substrate and epilayer can significantly improve the film quality. Nitridation of the sapphire substrate surface significantly improves the crystalline quality of InN as a result of the formation of AlN.[34-36] The marked improvement of InN film quality by the formation of an AlN layer is due to the fact that AlN has the same lattice structure as InN, and the lattice mismatch is reduced from 25% for InN/α-Al$_2$O$_3$ to 13% for InN/AlN.[34] The quality of the InN film is strongly influenced by the nitridation condition, temperature and time. In addition to the substrate surface treatment, it was found that incorporation of a buffer layer of AlN, GaN or InN greatly improves the structural and electrical properties of the InN films grown on sapphire substrate.

Si is a suitable semiconductor substrate material for InN having smaller lattice mismatch compared with the insulating sapphire substrate; 8% for InN(0001)/ Si(111) and 25% for InN(0001)/α-Al2O3(0001). In the early days of InN growth, Si was widely used as a

substrate but the film quality was very poor. Yamamoto *et al.* attempted the MOVPE growth of InN on Si substrate for the first time in 1994.[34,37] The MOVPE growth of InN directly on Si substrate was unsuccessful because of the formation of an amorphous SiN_x layer on the substrate surface, as a result of the unintentional nitridation of the substrate surface during the growth. The Si substrate surface nitrides during the growth even at a low growth temperatures (≈400 °C), which forms SiN_x on the substrate surface and cause poor effect on the grown InN film. On the other hand, growth at a temperature lower than 400°C was found to be polycrystalline due to reduced migration of the deposited materials on Si and/or reduced decomposition rate of the raw materials. Later, a GaAs intermediate layer on Si substrate was used to avoid the surface nitridation and the InN film was successfully grown on Si substrate using a GaAs(111) intermediate layer.[38,39] Recently, Yodo *et al.* have reported the growth of InN film on Si substrate by ECR MBE.[40,41] They claimed to have obtained InN layer on Si (111) and Si (001), which exhibited strong band edge PL emission at ≈0.7eV at room temperature. They demonstrated by XRD analysis that the InN film exhibited the dominant hexagonal WZ structure along with a low-intensity ZB.

The highest mobility and lowest carrier concentration (2050 cm^2/Vs and 3.49×10^{17} cm^{-3}) in the MBE InN film reported recently was grown on HVPE grown bulk GaN template by Lu *et al.*.[42] They also reported that using a comparatively thicker AlN layer can significantly improve the structural and electrical properties of the InN film.[43] It is believed that an AlN film of better quality can be obtained by growing a thicker film, which can serve as a better foundation for later InN growth. On the other hand, one of the best mobilities in the MOVPE InN, reported by Yamaguchi *et al.* was grown on a GaN layer.[44] They reported that use of GaN for the underlying layer of the InN film was found to lead to structural improvement of the epitaxial InN film. Recently, Xu *et al.* have investigated the rf-MBE growth of InN on GaN templates.[45] They reported that high quality InN films can be grown on a MBE grown N-polarity GaN template. An InN film grown with N polarity on GaN showed a Hall mobility of 800 cm^2/Vs at room temperature with a background carrier concentration of 2.13×10^{19} cm^{-3}.[45] Some other groups also have studied the epitaxial growth of InN on GaN.[46-50] Two-dimensional growth of InN on GaN has been observed by using MBE in spite of about 10% lattice mismatch.[48,49] In the MOVPE growth of InN, Adachi *et al.* however found that InN grown on GaN/sapphire in a reduced pressure and at a temperature above 550 °C has a much higher metallic–In content compared with that nitrided sapphire and other substrates.[47] Surface polarity of GaN and InN are seemed to be responsible for the

In drop formation. If high quality InN film can be grown on GaN or AlN, it will be significant in device applications. For the realization of InN based electronic devices, the use of high-temperature deposited GaN (high-quality GaN)is essential, and only GaN has the required high quality among nitride semiconductors for device fabrication.

2.1.5 Electronic properties

The values of carrier concentration and carrier mobility of the first polycrystalline InN films grown by radio frequency sputtering of metallic indium in a nitrogen atmosphere were reported to be in the high 10^{18} cm^{-3} range and 250 cm^{2}V^{-1}s^{-1} respectively.[5] Later, Lakin *et al.* reported carrier concentrations of samples prepared by similar methods in the order of high 10^{19} cm^{-3} and carrier mobilities around 100 cm^{2}V^{-1}s^{-1}.[51,52] But Tansley and Foley, who characterized most of the fundamental properties of InN, have reported carrier concentrations in the range of 10^{16} cm^{-3} and carrier mobilities as high as 3980 cm^{2}V^{-1}s^{-1}.[53] No one has reported a lower value for carrier concentration or a higher mobility. However, Butcher *et al.* implemented the same technique and tried to reproduce the result but could not.[54] Instead, they reported carrier concentrations around 3×10^{19} cm^{-3} and mobilities less than 100 cm^{2}V^{-1}s^{-1}, which are in close agreement with the values reported for polycrystalline samples.

Tansley and Foley have also reported that the band gap of InN is around 1.9 eV which was universally accepted until around 2002.[17] But from optical absorption, photoluminescence (PL) and photomodulated reflection (PR) measurements performed on MBE grown InN with low electron concentrations, it has been shown that the energy gap of InN is 0.67 ± 0.05 eV.[9,55,56] For these MBE grown samples, the lowest value of carrier concentration reported was 3×10^{17} cm^{-3} and the highest value of carrier mobility was 2200cm^{2}V^{-1}s^{-1}.[57] However, this interpretation of optical absorption and photoluminescence data for the band gap of InN has been questioned by Shubina *et al.* who claimed that the band gap of InN is much wider than this newly accepted value.[58] According to their report, the lower absorption edge is due to Mie scattering by metallic indium clusters, and the PL peak at 0.7 eV in InN originates from optical transitions involving interface states between the indium clusters and the indium nitride matrix. Carrier concentrations in N-polar indium nitride layers grown by HPCVD have been studied by HREELS and room temperature infrared (IR) reflection measurements in the range of 200-8000 cm^{-1}.

2.1.6   Surface electron accumulation

Surface electron accumulation is observed to be an intrinsic property of the InN epitaxial layer. Recently, this surface electron accumulation phenomenon on InN layers has attracted much attention because the high density of electrons on the surface has great technological importance such as formation of Ohmic contacts. However, the main cause of electron accumulation on the InN surface and how it is related to the surface atomic configuration are still not clear. We can find several explanations for surface electron accumulation on semiconductor surfaces reported in the literature. Electron accumulation layers at the semiconductor surfaces have been observed through techniques that include high resolution electron energy loss spectroscopy[59], angle-resolved photoemission spectroscopy[60] and electron tunneling spectroscopy.[61] Surface electron accumulation is not only observed in InN layers but also observed in both InAs and InSb.[62] The main reason for surface electron accumulation on InAs layer is the donor like intrinsic surface states whose energy spectrum is determined by the surface reconstructions.[63] Yamaguchi *et al.* have reported that electron accumulation on InAs/GaAs depends on the layer thickness and is induced by the quantum size effect.[64] They also have suggested that the dislocations due to lattice mismatch at the InAs/GaAs interface may also be responsible for surface electron accumulation.

The phenomenon of surface electron accumulation on InN layers was first observed by Mahboob *et al.* by using (HREELS).[65] According to their report, an intrinsic surface electron accumulation layer is found to exist and is explained in terms of a particularly low Γ-point conduction band minimum in wurtzite InN. The electron accumulation is a consequence of ionized donor type surface states pinning the surface Fermi level above the conduction band minimum. Piper *et al.*[66] have calculated energy positions of Γ-point, conduction band minimum and valence band maximum of AlN, GaN and InN with respect to the branch point energy and concluded that the conduction band minimum lies far below the branch point energy and is the cause of electron accumulation in InN layers. D. Segev and C. G. Van De Walle have reported that the cause of electron accumulation on polar InN is In-In bonds leading to occupied surface states above the conduction band minimum.[67] In recent results from angle resolved photoelectron spectroscopy of InN, it has been reported that the electrons in the accumulation layers reside in discrete quantum well states, defined perpendicular to the film surface.[68] By using electron tunneling spectroscopy, Veal *et al.* also have reported the native electron accumulation layer at the surface of *n*-type InN.[61]

2.2   Metal adsorption studies on reconstructed Si surfaces

2.2.1   Si (111) 7×7: Structure

The best cleavage face of silicon is the Si (111) plane due to its minimized energy. The (111) planes of Si can be thought of as a double layer, which are attached to each other by one bond per atom, perpendicular to the layers. Within the double layer a mesh of the remaining tetrahedral bonds (three per atom) connect the atoms in 3-fold symmetric coordination. The ideal bulk terminated Si (111) would be the surface with one dangling bond per surface atom. However, this surface can be observed only under special surface treatments like impurity stabilization, high temperature or laser annealing. Annealing the (7×7) surface of Si (111) also results in the phase transition from 7×7 to 1×1.[69-71] In contrast with the Si (100) surface, since there is only one bond per surface adatom, the surface has the tendency for reconstructions having comparatively long range order.

The discovery of the Si(111)-7×7 reconstructed surface is a milestone in surface crystallography of semiconductors. Since the reconstruction was first observed through low energy electron diffraction (LEED) in 1959[72], a large number of models have been proposed to explain the available experimental data. The currently accepted model for the Si(111)-7×7 surface is the dimer-adatom-stacking fault (DAS) model, which was proposed in 1985 by Takayanagi *et al.*[73,74] after a detailed analysis of transmission electron diffraction data. Binnig, Rohrer, Gerber, and Weibel reported its real-space scanning tunneling microscopy (STM) images in 1983[75], the first STM micrographs of a semiconductor surface ever made. These STM studies established the presence of 12 adatoms and large holes at the corners of the diamond shaped (7×7) unit cells, strongly favoring the DAS model with adatoms and corner vacancies. More supporting evidences for DAS structure were provided in the medium-energy ion scattering[76] and grazing x-ray diffraction studies[77] as well as other experimental and theoretical investigations.[78-80]

The DAS model proposed by Takayanagi *et al.*[73,74] is schematically presented in top and side views in Fig. 2.5, which shows a unit cell (a rhombohedra-like dimensions of 46.56 Å for the long diagonal and 26.88 Å for the short diagonal) covering a surface area equivalent to 49 atoms of the (111) plane. There are two triangular subunits, which are rendered inequivalent by a stacking fault (present in the second atomic layer) in one half of the 7×7 unit cell.[81] The first layer of the cell contains 12 adatoms so that each one of them saturates three atoms of the second layer. Nevertheless six of the second layer atoms remain

unsaturated, which are called rest atoms. At the third atomic layer, there are 9 dimers along the edge of the (7×7) structure. One atom is missing at the corner of unit cell (*i.e.* one missing atom per unit cell), which leaves a place for fourth layer atom, creating the corner hole. The most important structural effect of the reconstruction is a severe reduction in the number of surface dangling bonds in the (7×7) unit cell from 49 to 19, where 12 are from the adatoms, 6 from the rest atoms, and one from the corner hole.
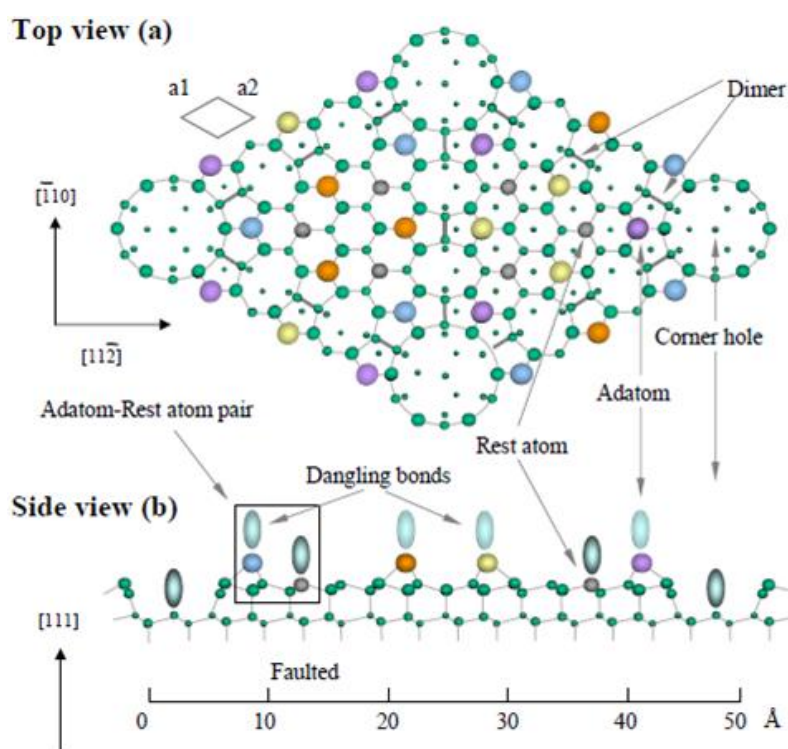
Fig. 2.5: *Top and side view of DAS model for Si(111)-7x7 reconstruction.*

2.2.2   Thin film nucleation and growth

The individual atomic processes responsible for adsorption and crystal growth on surfaces are illustrated in Fig. 2.6.[82] The primary mechanism in the growth of thin films as well as surface nanostructures from adsorbed species is the transport of these species on a flat terrace (see Fig. 2.6), involving random hopping processes at the substrate atomic lattice. Atoms or molecules are deposited from the vapour phase. On adsorption, they diffuse on terraces to meet other adatoms, resulting in nucleation of aggregates or attachment to already existing islands. This surface diffusion is thermally activated; that is, diffusion barriers need to be surmounted when moving from one stable (or metastable) adsorption configuration to

another. As is typical for such processes, the diffusivity D — the mean square distance travelled by an adsorbate per unit time — obeys an Arrhenius law; this holds for atoms as well as rigid organic molecules. If we now consider a growth experiment where atoms or molecules are deposited on a surface at a constant deposition rate F, then the ratio D/F determines the average distance that an adsorbed species has to travel to meet another adsorbate, either for nucleation of a new aggregate or attachment to an already formed island. The ratio of deposition to diffusion rate D/F is thus the key parameter characterizing growth kinetics.[83] If deposition is slower than diffusion (large values of D/F), growth occurs close to equilibrium conditions; that is, the adsorbed species have enough time to explore the potential energy surface so that the system reaches a minimum energy configuration. If deposition is fast relative to diffusion (small D/F), then the pattern of growth is essentially determined by kinetics; individual processes, notably those leading to metastable structures, are increasingly important.   Metallic islands are controlled by growth kinetics at small D/F values. Semiconductor nanostructures are usually grown at intermediate D/F and their morphology is determined by the complex interplay between kinetics and thermodynamics. Strain effects are particularly important and can be used to achieve mesoscopic ordering.
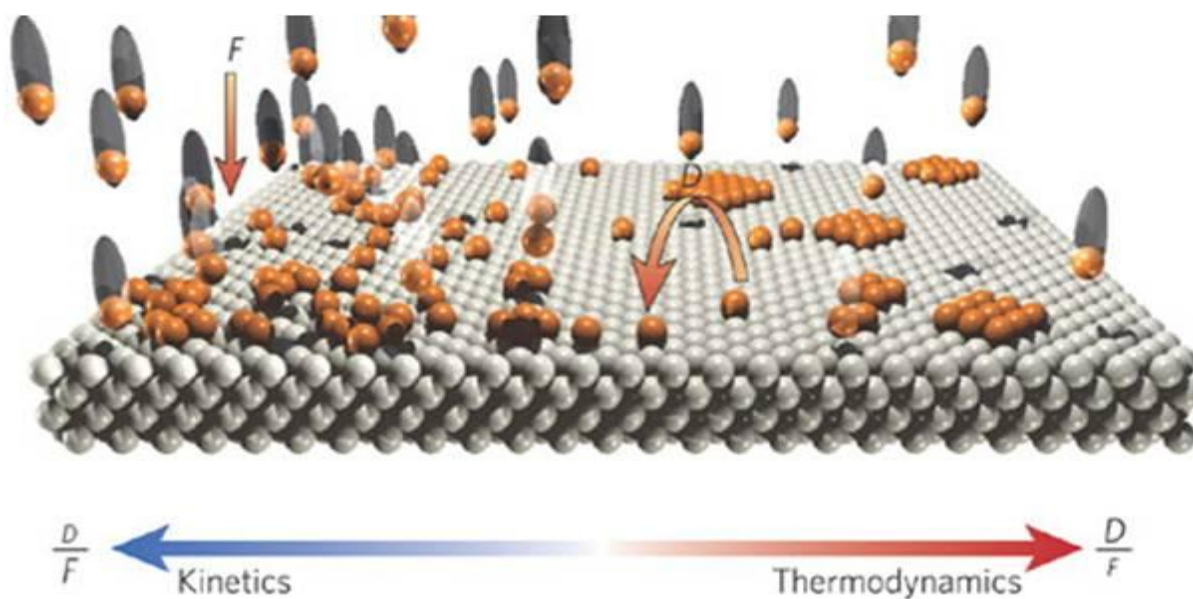
Fig. 2.6: *Thin film nucleation and growth – different processes involved*[83]

2.2.3   In/Si(111)-7x7

In on Si represents an interesting overlayer system which allows us to study the interfacial bonding between simple metal and an elemental semiconductor in variety of

different interfaces. The present interest in the interfaces between group III-V and group IV semiconductors supply additional motivation for fundamental studies of initial interaction of group III materials on group IV substrates. Moreover, indium is of relevance as a dopant for coevaporative doping during Si molecular beam epitaxy and it appears that the dopant overlayer plays a critical role in governing the dopant concentration in the growing film.[84,85] It is therefore important to possess detailed knowledge on the structure and energetics of thin In overlayers on Si surfaces.[86]

Indium is known to induce a number of ordered surface phases on Si(111)-7x7 substrate surfaces up to coverages of 1-2 monolayers (ML).[87-91] Beyond those coverages the growth of epitaxial In islands has been reported.[90,92] In the first low energy electron diffraction (LEED) study of the In-Si system of Lander and Morrison[87] eight two dimensional structures have been observed. Although not all of the LEED patterns could be identified as individual phases in later work, the phase diagrams as proposed by Kawaji, Baba and Kinbara[89] and Kelly *et al.*[90] suggest the following sequence of structures for In/Si(111)-7x7 as a function of In coverage and temperature: (7x7)→(1x1)→($\sqrt{3}$x$\sqrt{3}$)R30^o→($\sqrt{31}$x$\sqrt{31}$)→(4x1)→(1x1)R30^o. The last structure is incommensurate with respect to the substrate and similar to that of an unreconstructed, 30° rotated In(111) surface. This structure is presumably associated with the flat, hexagonal In islands which have been observed in the coverage regime 1-2ML by scanning tunneling microscopy (STM).[91]

The In-Si surface phase which has attracted most scientific attention so far is the ($\sqrt{3}$x$\sqrt{3}$)R30^o reconstruction with a nominal In coverage $\Theta_{In}\approx0.3$ML. This surface has been studied experimentally by k-resolved direct and inverse UV photoelectron spectroscopy (ARUPS and IPES)[93-95], STM, electron energy loss spectroscopy (EELS)[96] and theoretically by first principles pseudopotential total energy and electronic structure calculations.[97] The atomic and electronic structure of the $\sqrt{3}$-In surface is therefore rather well understood. Much less is known, however, about the other ordered In-Si structures. Of particular interest, for example is the (4x1) –In surface: it is formed at $\Theta_{In}\approx0.6$-1ML at elevated temperature and is presumably the basic interfacial layer for subsequent Stranski-Krastanov growth. The In-Si(4x1) surface also acts as an intermediate layer over which surface electromigration of In islands has been observed with high mobility.[98,99] The atomic structure of the 4x1 surface has been investigated by STM,[88] impact collision ion scattering spectroscopy[100], and Auger

electron diffraction[101] but no generally accepted structure model has emerged as yet. There is very little information available on the electronic nature of this surface. The pseudomorphic $(1x1)R30^o$ layer which is observed for $\Theta_{In}>1ML$, is also interesting since it marks the transition from layer growth to three dimensional islanding and the onset of metallicity in In overlayers. Depending on the particular coverage the coexistence of different ordered structures has often been observed[91] and transitions between them as a function of temperature, or even time, have been reported in the literature.[87-90]

As mentioned above, there are a few reports concerning the construction of phase diagram for In/Si(111)-7x7 systems in the literature. One of the well accepted phase diagrams is from the studies of Hirayama et al. who studied the system in wide temperature and coverage regimes using RHEED.[102] The phase diagram is observed by adsorbing In onto Si at different temperatures. This phase diagram shows superstructural phases in the coverage range of 0-1ML and a temperature range of 300 to 600^oC. 7x7 reconstruction is shown to extend from 300 to 600^oC in the coverage range of 0-0.2ML and in the coverage range 0.2-0.45ML it extends up to 600^oC. 7x7 reconstruction changes into 1x1 at around 0.5ML of In adsorption in the temperature range of 300 to 400^oC which in turn converts into 4x1 phase at higher coverages. The 4x1 phase occupies a temperature range of 300 to 450^oC and a coverage range of 0.55 to 0.85ML. This phase is manifested as a 3D (three domain phase) as it has three equivalent orientation on silicon surfaces and superimposition of their diffraction patterns should result in three fold symmetric pattern which is observed in the coverage range of 0.55 to 0.75ML . For higher coverages they are able to observe a single domain 4x1 phase. They have observed the √3x√3 phase in a narrow coverage range of 0.25 to 0.45ML and a temperature range of 450 to 600^oC. √31x√31 phase occupies a temperature and coverage range of respectively 450 to 550^oC and 0.5 to 0.8ML. There have been no reports in the literature of the observation of √31x√31 phase using LEED and it has been only reported using RHEED.[89] Above 0.9ML for all temperature studied 1x1 pattern has been observed in RHEED. The phase diagram proposed by Kawaji et al. does not include the behavior of In/Si(111) for temperatures $<300^oC$ including room temperature. Other phase diagram reported in the literature has been mainly limited to a narrow temperature and coverage range.[103] It has been reported in the literature that the evolution of superstructural phases on the surface depends on the kinetics and hence one has to also look in to the desorption behavior of In on the surface.[83] We observe that a phase diagram which is

constructed on the basis of combined adsorption and desorption studies of In on the Si(111)-7x7 surface is lacking in the literature.

Literature shows studies focused to understand the different reconstructions observed. $\sqrt{3}x\sqrt{3}$ reconstruction is one of the well studied systems in the case of group III metals on Si surfaces because of the low coverage and its structural simplicity makes it computationally less expensive and experimental observation unambiguous.[104,105] This reconstructions forms the most understood phase among all other phases of In/S(111)-7x7 system and has well accepted structure and electronic properties.[106-109] The structure of $\sqrt{3}x\sqrt{3}$ phase consists of In atoms adsorbed on the T_4 (four fold site) sites of bulk truncated Si(111) with each In atom satisfying three Si dangling bonds thereby chemically passivating the surface. The first STM observation of Si(111)-4x1 phase has been carried out by Nogami *et al.* who showed that its structure consists of row of In atoms running along 'x4' direction.[91] Recently, because of the immense interest in the formation of self assembled nanostructures on the surface, 4x1 phase has got overwhelming interest in the literature.[110] The model proposed by Bunk *et al.* shows that the structure indeed is a self assembly of nanochains of In atoms which also involves the reconstruction of the underlying Si atoms.[111] This phase was a subject to the study of several fascinating 1D physics like Peierl's distortion. There are only two structural models for $\sqrt{31}x\sqrt{31}$ phase one from Gai *et al.*[112] and other proposed by Saranin *et al.*[113]. Theoretical calculations needed to verify the energetics of these phases are still lacking in the literature. Another recent interest has been focused on the study of formation of magic clusters of In and Al on Si(111) surface and researchers were able to form ordered assembly of nanoclusters of these atoms.

There have been fewer studies in the literature concerning growth mode of In/Si(111)-7x7 system as most of the study were concerned about the structure and electronic properties of the different phases observed. Öfner *et al.* and Sun et al. showed a 2ML SK growth mode at room temperature (RT) for the system.[114] Though desorption studies of Sun *et al.* showed a peculiar layering of In islands just before desorption, it does not give any detailed understanding regarding such peculiar observation.[115] Finney *et al.* observed a uniform growth of In islands up to 1ML and reported that 1-2ML marks formation of In islands on the surface.[116] We observe lack of systematic studies concerning initial stages of adsorption and behaviour of the system under residual thermal desorption.

2.2.4   Ga/Si(111)-7x7

Adsorption of gallium atoms on silicon surfaces has been studied extensively in recent decades for its importance in the heteroepitaxy of III–V semiconductors and a special behavior given by the distinct nature of atomic bonding in semiconductor substrates and metallic layers. Various attempts to use these specific heterostructures as a platform for the self-assembled growth of nanostructures have been made and recently also to fabricate Ga metallic nanostructures by the selective growth on semiconductor surfaces patterned by nano-lithographic methods (e.g. e-beam lithography, SPM local oxidation).[117,118] Hence, the understanding of the behavior of Ga on Si surfaces at different temperatures and a wide range of coverages is a very important issue.

Gallium superstructures on the Si(111)-(7×7) surface (coverages up to 1 ML) have been studied mostly by methods like low energy electron diffraction (LEED)[92,119-125], x-ray standing-wave technique (XWS)[122,126,127], scanning tunneling microscopy (STM)[128-147] electron energy loss spectroscopy (EELS)[146,147], photoelectron diffraction (XPD)[148,149], reflection high energy electron diffraction (RHEED)[150-152], density functional theory (DFT)[153,154], low energy electron microscopy (LEEM)[155,156], auger electron spectroscopy (AES)[119,157] and other techniques.[158,159] It has been observed that the gallium structure on the Si(111)-(7x7) surface strongly depends on gallium coverage and deposition and/or annealing temperature. The deposition of a small amount of gallium corresponding to coverages of 0.24–0.28 ML (1 ML ~7.83 × 10^{14} atoms cm^{-2} for the Si(111) unreconstructed surface) at room or enhanced (up to 350°C) temperature leads to the formation of magic clusters.[145,150] For coverage of 1⁄3 ML of Ga with deposition (annealing, respectively) temperature of 550°C, the ($\sqrt{3}\times\sqrt{3}$) R30∘ surface reconstruction was found. Gallium atoms (sp^3 hybridization) occupy half of the fourfold coordinated T_4 sites and completely terminate all the silicon surface dangling bonds.[160] Further increase of Ga coverage up to 1 ML at elevated temperature leads to the formation of an incommensurate structure with an approximate periodicity of 2.4 nm.[122,123] Within a coverage range of 0.7–1 ML three different incommensurate structures (6.3×6.3), (11×11) and ($6.3\sqrt{3}\times6.3\sqrt{3}$) R30° were observed by STM after annealing the Ga layers at 550°C. According to STM studies by Hanada et al.[161] and by Zegenhagen et al.[109,122], the ($\sqrt{3}x\sqrt{3}$)-R30° structure is composed of a periodic arrangement of Ga atoms adsorbed at T_4 sites of the bulk extrapolated (111) surface and the Ga coverage is 1/3 monolayer (ML).[150] The 6.3x6.3 incommensurate structure appears on

Si(111) surfaces with Ga coverage of more than 1/3 ML.[150] In these structures Ga atoms occupy the substitutional positions in the top half of the Si(111) double plane[122,129], forming a Ga–Si bilayer ($sp^3 \rightarrow sp^2$ re-hybridization of gallium atoms takes place). Depending on the type of deposition and annealing, new structures and features can be obtained. For instance, based on the STM measurements[162] and theoretical calculations[163] it was found that during the additional deposition of 1/6 Ga ML on the ($\sqrt{3} \times \sqrt{3}$) R30° at elevated temperatures Ga superstructure triangular clusters (with two to five atoms on their side) and incommensurate islands were formed. After forming the ($\sqrt{3}$x$\sqrt{3}$) R30° structure, Lai *et al.*[140,162] further deposited 1/6ML of Ga on the surface and carried out annealing. STM images from the surfaces showed that novel structures such as magic clusters, small island, and large triangular and trapezoidal islands formed on the surface, at annealing temperatures of 200°C, 350°C and 450°C, respectively. These structures are probably transient ones appearing during formation of the incommensurate 6.3x6.3 structure. They commented that if the annealing was carried out at high temperatures above 350°C, such a variety of structures could not be observed. This implies that STM observations during transitions from one surface structure to another provide us fruitful findings. Most results reported so far have been obtained from static STM observations after surface reaction completion. If such dynamic observations as watching surface reactions progress are attempted, much more valuable results can be expected to be acquired.

2.2.5   Al/Si(111)-7x7

Aluminium is widely used in the fabrication of Si-based semiconductor devices as a gate metal and a p-type dopant for lightly doped base profiles and heavily doped junction termination systems. Al/n-Si(111) Schottky contact is very important because of the controlled variation of Schottky barrier height upon post deposition heat treatment. Al is also an important material for construction of integrated circuitry owing its low diffusivity, low contact resistivity and simple fabrication process. Al/Si(111) system is also interesting since several different ordered two dimensional (2D) phases can be formed depending on the coverage of aluminium atoms and substrate temperature during deposition. This system has been studied with a variety of techniques such as angle resolved photoemission spectroscopy[164-167] and scanning tunneling spectroscopy.[107] However the detailed formation conditions of 2D phases and precise atomic geometries of these structures are unknown, except for that of the $\sqrt{3}$x$\sqrt{3}$ structure.[168]

In 1964 Lander and Morrison[169] first evaporated Al on the Si(111)-7x7 surface and found five different phases as examined with LEED.[170] α-Si(111)-7x7-Al at 0.5ML; α-Si(111)-√3x√3-Al at 0.33ML on heated Si; and γ-Si(111)-7x7-Al at 0.5ML on heated Si. They also measured the first order-disorder transition between the α-√3 and the disordered '1x1' phase. This pioneering work is the starting point of the exploration of this complex system. There are a few phase diagrams in the literature for Al/Si(111)-7x7 system.[168,170-172] α-7x7 phase appears as soon as 0.1ML of Al has been evaporated on cold Si(111)-7x7 substrate and is detectable up to 0.8-1.0ML with background intensity increasing with coverage.[170] It is distinguished from the clean 7x7 phase by its different spot intensities. In 1993 Yoshimura et al.[173,174] proposed a model based on STM where three Al atoms are resting on each half of every unit cell of the Si(7x7) reconstruction. The coverage for this model is 0.1ML. Uemura et al.[175] proposed another model in 1996 where Al atoms sit on the rest atom, adatom and dimer sites of DAS structure explaining the coverages up to 0.7ML. Gröger et al. showed that for a coverage of 0.1ML the phase is stable up to a coverage of 1128K.[170]

The Si(111)-√3x√3R30°- Al is the most investigated structure of the Al/Si(111) system. In fact it is so well know today that it is being used for the evaluation of measuring methods.[176] Lander and Morrison observed two such structures.[169] The α-Si(111)-√3x√3-Al and β- α-Si(111)-√3x√3-Al. α-√3 structure was observed after evaporation of 0.33ML on a sample kept at a temperature of >773K; evaporation on a cold sample with subsequent heat treatment to >773K; or heating one of the next phases high enough to desorb Al. The β-√3 structure is produced by continuous evaporation on the α-√3 structure and was supposed to have a different I-E spectra and heat treatment effects. At >773K it should covert irreversibly into γ7x7 phase was never reported. From theoretical studies[177-179], photoemission spectroscopy[95,164,167], electron diffraction and spectroscopy[180,181], and STM and STS experiments[107,182,183] it was concluded that the Al atoms of the √3 structure saturate all the dangling bonds of the Si substrate and reside in the fourfold top T_4 position rather than in the threefold hollow H_3 sites.[166,184-186]

The diffraction spots of the Si(111)-√7x√7R19.1°-Al structure lie on the same positions as certain spots of the 7x7 superstructure.[170] This suggests that the phase that Lander and Morrison[169] identified as α-Si(111)-7x7-Al at 0.5ML could actually have been the √7 phase, the discovery of which Hansson et al. claimed in 1981.[166] They proposed a model

based on photoelectron spectroscopy which was refined in 1989 by Hamers based on STM observations.[107]   However, the √7 structure has not yet been elucidated completely. This phase is observed in the coverage range of 0.4-0.6ML by evaporating 0.5ML Al on the Si(7x7) phase creating α7x7 phase and subsequently heating to 900K for a few seconds. If an α7x7structure at a coverage of 0.5-0.8ML is heated, the superstructure diffraction spots disappear at a temperature of 670K. At 800K new spots appear and the γ-phase is formed, first described by Lander and Morrison[169] who found it to have a 7x7 symmetry and therefore named it γ-Si(111)-7-Al or γ-7x7. Its true structure and periodicity are still controversial. Zotov et al.[187,188] found an 8x8 symmetry in their LEED pattern, Yoshimura's STM pictures[189] showed a 9x9 superstructure and Gröger et al. showed a periodicity of 10x10.[170]

There are hardly any studies concerning the growth mode of Al on Si(111)-7x7 surface. Zotov *et al.*[188] reported layer by layer growth mode for RT adsorption of Al on Si(111)-7x7 surface and at higher temperatures the growth mode changes to Stranski-Krastanov mode. However, there is no mention of the changes in the LEED pattern at room temperature with adsorption of Al. It has been reported that with deposition of Al on the Si(111) surface, fractional order spots of 7x7 persist up to a coverage of 2ML above which it converts to 1x1 pattern.[170]   Thus, there is necessity of a systematic adsorption/desorption studies of Al on Si(111)-7x7 surface to elucidate its growth mode and understand the thermal stability of these overlayers.

2.2.6   Si(5 5 12)-2x1: structure

The Si (5 5 12)-2×1 surface was discovered first by Suzuki *et al.*[190,191] during their Reflection Electron Microscopy (REM) and STM studies, but, the first reported model of this surface, was proposed by Baski *et al.*[192]. Since then, a number of models have been proposed by various researchers. The Si (5 5 12) surface is oriented 30.5° away from (0 0 1) towards (1 1 1), or approximately midway between these two low-index planes. This surface forms a single-domain reconstruction consisting of row- like structures. These structures are oriented

Fig. 2.7: *Bulk truncated Si viewed from (100). The composition of Si(5 5 12) surface is indicated.*

along the [$\underline{1}$ 1 0] direction and have an inter-row periodicity of 5.35 nm and presents the largest unit cell observed with size 7.7 Å × 53.5 Å. As 0.77 nm along [$\underline{1}$ 1 0] is twice of 0.38 nm, the unit length of bulk terminated surface along [$\underline{1}$ 1 0], and 5.35 nm is the unit length perpendicular to [$\underline{1}$ 1 0] of bulk terminated surface, so the reconstruction is known to be Si (5 5 12)-2×1. This reconstructed surface model consists of two kinds of (3 3 7) and one (2 2 5) unit cells. However, as other high index Si surfaces, such as (3 3 7-*31.2^o*), (2 2 5-*29.5^o*) and (7 7 17-*30.2^o*), exist close to Si (5 5 12) within 1° difference (shown in Fig. 2.7), one unit cell of Si (5 5 12) can also be closely matched with combination of these surfaces:

$$(5\ 5\ 12) = (7\ 7\ 17) + (3\ 3\ 7)$$

$$(5\ 5\ 12) = (2\ 2\ 5) + (3\ 3\ 7) + (3\ 3\ 7)$$

$$(5\ 5\ 12) = (1\ 1\ 3) + (3\ 3\ 7) + 2.\,(3\ 3\ 7)$$

$$(5\ 5\ 12) = (113) + 3.(337)$$

$$(5\ 5\ 12) = (1\ 1\ 3) + (1\ 1\ 3) + (1\ 1\ 2) + 2.(3\ 3\ 7)$$

$$(5\ 5\ 12) = 2x(1\ 1\ 3) + (5\ 5\ 11) + (3\ 3\ 7)$$

$$(5\ 5\ 12) = (1\ 1\ 3) + (2\ 2\ 5) + (5\ 5\ 11)$$

On the reconstructed Si (5 5 12), various atomic structures have been suggested using STM images and theoretical calculations by various researchers.[193,194]

The real time STM image of the Si (5 5 12)-2×1 surface as observed by Baski is shown in Fig. 2.8(a).[192] STM image of the clean (5 5 12) surface shows the well-ordered, periodic
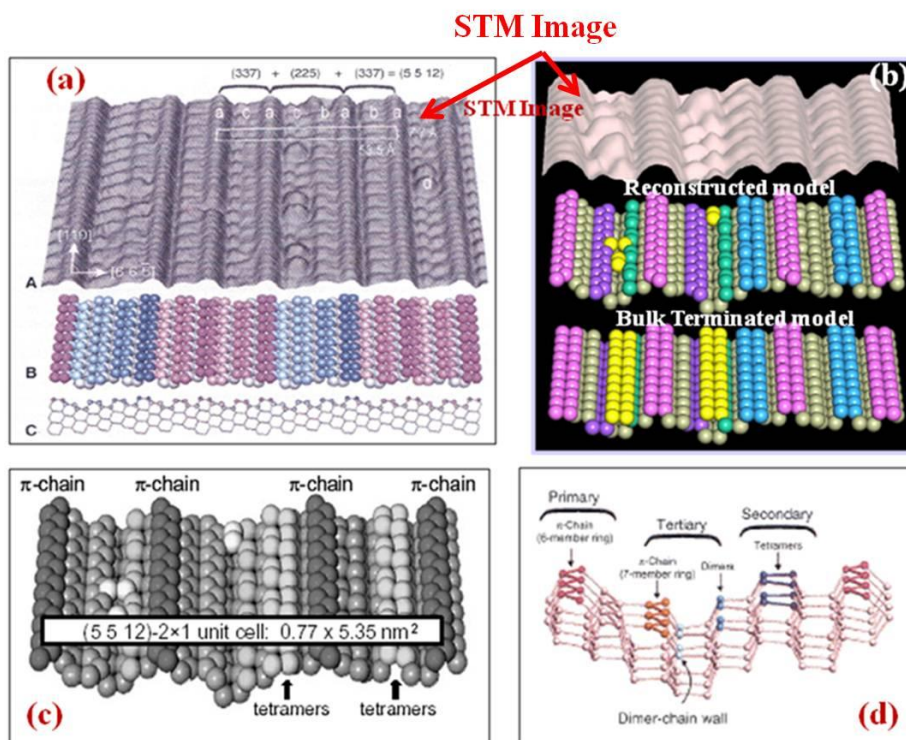
Fig. 2.8: *(a) & (b) Si(5 5 12)-2x1 reconstructed surface, (c) Proposed model of 2x1 reconstructed Si(5 5 12)-2x1 surface and (d) The model of (225) plane observed in the Si(5 5 12)-2x1 surface showing the primary, secondary and tertiary rows along with the π bonded chains[192].*

arrangements of row structures oriented along the [$\underline{1}$ 1 0] direction. As mentioned earlier and also indicated in Fig. 2.8 each unit cell of the bulk-terminated (5 5 12) surface is equivalent to two unit cells of (3 3 7) plus one unit cell of (2 2 5). The atomic-scale topography of the filled electronic states on the Si(5 5 12) surface is dominated by three types of row structures having very specific locations with respect to each other, as illustrated in Fig. 2.8. The most prominent rows on the surface are the primary rows. These rows define the (2 2 5) and (3 3 7) subunits and consist of oblong maxima with a bulk-like a_o period along [$\underline{1}$ 1 0] direction ($a_o =$ 0.38 nm). Within each unit of (2 2 5) there are two internal rows: secondary and tertiary as shown. The block-like secondary rows always occur to the right (*i.e.* towards [6 6 $\underline{5}$] of the typically zigzag-shaped tertiary rows. In contrast, each unit of (3 3 7) has only one internal row, which is a secondary row if the (3 3 7) unit is to the right of a (2 2 5) unit, and a tertiary row if it is to the left. In addition to the row structures, protrusions are occasionally observed exclusively on top of the tertiary rows. The secondary and tertiary rows both have a $2a_o$ period along [$\underline{1}$ 1 0] direction; hence, the (5 5 12) surface has a 2×1 reconstruction with a unit cell of 7.7 Å × 53.5 Å.

Thus, Baski has proposed a model consisting of simple structural units: π-bonded chains, dimers, and tetramers. Within this unit cell the original, bulk-terminated 68 surface atoms are locally rearranged to halve the number of dangling bonds per 2×1 unit cell from 48 to 24. As dimers on Si (001)2×1 are found in both flat and buckled configuration, this model assumes that both occur on the (5 5 12) surface as well. Additionally, the dimer chain wall in the center of the tertiary row induces a weak $2a_o$ periodicity in the adjacent π-bonded chain to the left. The left half of the (225) subunit is a (111) plane segment, which reconstructs to form the two types of π-bonded chains: π_6 and π_7. The π_7 chains are like those that occur on the metastable Si (111)-2×1 reconstruction.[195,196] The π_6 chains have not been previously observed, but they appear to be stable in first-principles electronic-structure calculations of the relaxed surface. The right half of the subunit is a stepped (001) plane segment, which forms dimers and tetramers like those found on (001) surface. The correlation between these atomic structures and the observed rows is as follows: row I= π_6 chain; row II=tetramers; and row III= π_7 chain + dimer row. When this proposed model is used in conjunction with first-principles, electronic-structure calculations to obtain simulated STM images, the agreement between theory and experiment is excellent.

Due to the recent discovery (1995) and complicated structural models, of the Si (5 5 12) surface there are only a few growth studies on this surface. Studies of adsorption of noble metals and few other metals on this surface have been reported, which led to the various theoretical works for the determination of the proper structural models and the formation of 1D nanostructures. The pioneering work by Baski et al.[193] reported the nano-scale faceting of the high index surface of Si (112) faceting to the (337) and (111), and suggested the possibility of the growth of 1-D nanostructures on the corrugated surface. The orientational phase diagram proposed by Song et al.[197,198] for stepped Si (113) led to the coexistence of Si (5 5 12) and Si (113) facets at the temperature of 1180K. As discussed above, Baski et al.[192] observed the first real time STM image of the surface and proposed a model for the reconstructed surface. Some modifications in the model were also proposed[193,194] due to the modified energy minimization studies. The first study of the Ga adsorption on Si (337) resulted in the faceting of this surface to (5 5 12) unit.[144] They also observed the large terraces of Si (5 5 12) planes separated by multiple height steps or single unit cell wide 7×7 or 5×5 reconstructed Si(111) planes.

1.2.7   In and Al adsorption on Si(5 5 12)-2x1

There have been no previous reports of In or Al adsorption on Si(5 5 12)-2x1 surface. We discuss here the previous reports of other metal adsorption on Si(5 5 12) surfaces. The STM studies of the adsorption of Ag on Si (5 5 12) surface shows the growth of Ag along the row like structures forming the 1D structures of large aspect ratio.[199-201] The photoemission studies combined with RHEED and STM provided a phase diagram of Ag/Si (5 5 12) surface. The phase diagram shows the gradual fading of the clean pattern with RT adsorption of Ag. Annealing the adsorbed surface to 500°C resulted in the diffuse 3× periodicity. While the coverage of 0.3 ML at 400°C give back the 1× spots of the clean surface and the STM images showed the presence of long and ordered mono-atomic chains of Ag atoms. The increase in the annealing temperature resulted in the formation of 3× chains and resulted in the nano faceting of the surface. the STM and STS studies performed by Jones *et al.*[202] has also showed the formation of 1D nanowires arrays of Ag on this surface. The Au adsorption studies resulted in the formation of faceting of the large unit cell to the nearby planes in the vicinity of the (5 5 12) orientation. The first reported study of Au adsorption on Si (5 5 12) surface by High Resolution Reflection Electron Microscopy (HR-REM) reported the observation of strongly anisotropic 1D structures along the rows of the Si (5 5 12) morphology.

The RHEED studies showed the changes at 715°C from (5 5 12) to two fold (337), (5 5 11) and (225) facets as the coverage of Au is increased to 2.2 ML while the deposition of Au at 780°C and its annealing at same temperature for long time shows the coexistence of (113) and (337) facets on the surface.[203] The STM studies performed by Baski *et al.* resulted in the complete phase diagram of the Au/Si(5 5 12) system.[201,204] The electronic structure of these phases were studied by Ahn *et al.* by ARPES, Valence Band PES and LEED.[205-207] PES and LEED studies had showed the strong correlation of the Au atomic chains with the Au/Si (557) system which also presents a good template for the anisotropic nanowires growth.[208] The quasi one dimensional nature of the Au atomic chains was confirmed by Lee *et al.* by their LEED and synchrotron studies.[194] Kumar et al. and Paliwal et al. have studied the Sb/Si(5 5 12) interface extensively.[209-212]   They have formed several 1D nanostructures on this surface and have formed 2D phase diagram for the system. The growth of Cu on Si (5 5 12) surface resulted in two main growth phases: at lower temperature ''nanowires'' grown along the underlying Si tetramer rows and at higher temperature (113)2×2 facets.[208] Cu behaves in a similar manner to Au and Ag at low temperatures, and mostly like Au at higher

temperatures. The similarities between Cu and Au are due to their higher desorption temperatures (800–1000°C), as opposed to Ag which desorbs at only 650°C. In addition, oxygen etching of Au-induced saw tooth has been shown to produce similar trapezoidal islands to those seen for etched Cu-induced saw tooth. The one difference is that Au does not desorb from the surface as Cu does, presumably due to its higher desorption temperature. The atomic structure of the Cu-induced 113 and 111 saw tooth appear to be very stable, because higher depositions of Cu (2 ML) do not lead to any different surface morphologies.[208] Formation of Ga 1D nanostructures have been studied by Praveen et al. and they have formed a phase 2D diagram for the system.[213] The adsorption of Bi on Si (5 5 12) surface also resulted in the 1D row structure formation at a higher temperature of 450°C. The study reported the formation of (337) facets with the adsorption of Bi. The Bi adsorption studies demonstrate the coexistence of dimers/adatoms and tetramers in the same row.

References

[1] R. Juza and H. Hahn, Anorg. Allgem. Chem. **234**, 282 (1938).

[2] J. MacChesney, P. M. Bridenbaugh, and P. B. O'Connor, Mater. Res. Bull. **5**, 783 (1970).

[3] K. Rose J. W Trainor, J. Electron. Mater. **3**, 821 (1974).

[4] O. Ambacher, M. S. Brandt, R. Dimitrov, T. Metzger, M. Stutzmann, R. A. Fischer, A. Miehr, A. Bergmaier, and G. Dollinger, J. Vac. Sci. Technol. B **14(6)**, 3532 (1996).

[5] H. J. Hovel and J. J. Cuomo, Appl. Phys. Lett. **20**, 71 (1972).

[6] L. A. Marasina, I. G. Pichugin, and M. Tlaczala, Krist. Tech. **12**, 541 (1977).

[7] A. Wakahara, T. Tsuchiya, and A. Yoshida, J. Cryst. Growth **99**, 385 (1990).

[8] T. Inushima, V. V. Mamutin, V. A. Vekshin, S. V. Ivanov, T. Sakon, M. Motokawa, and S. Ohoya, J. Cryst. Growth **227**, 481 (2001).

[9] V. Y. Davydov, A. A. Klochikhin, V. V. Emtsev, D. A. Kurdyukov, S. V. Ivanov, V. A. Vekshin, F. Bechstedt, J. Furthmuller, J. Aderhold, J. Graul, A. V. Mudryi, H. Harima, A. Hashimoto, A. Yamamoto, and E. E. Haller, Phys. Status. Solidi B **234**, 787 (2002).

[10] J. Wu, W. Walukiezicz, W. Shan, K. M. Yu, J. W. Ager III, E. E. Haller, H. Lu, and W. J. Schaff, Phys. Rev. B **66**, 201403 (2002).

[11] Y. Nanishi, Y. Saito, and T. Yamaguchi, J. Appl. Phys. **42**, 2549 (2003).

[12] M. Higashiwaki and T. Matsui, J. Cryst. Growth **269**, 162 (2004).

[13] A. A. Klochikhin, V. Y. Davydov, V. V. Emtsev, A. V. Sakharov, V. Kapitonov A., B. A. Andreev, H. Lu, and W. J. Schaff, Phys. Rev. B **71**, 195207 (2005).

[14] H. Lu, W. J. Schaff, and L. F. Eastman, Mater. Res. Soc. Symp. Proc. **9**, 693 (2002).

[15] N. Dietz, M. Strassburg, and V. Woods, J. Vac. Sci. Technol. A **23**, 1221 (2005).

[16] Z. G. Qian, W. Z. Shen, H. Ogawa, and Q. X. Guo, J. Phys.: Condens. Matter **16**, R381 (2004).

[17] T. L. Tansley and C. P. Foley, J. Appl. Phys. **59**, 3241 (1986).

[18] K. Osamura, S. Naka, and Y. Murakami, J. Appl. Phys. **46**, 3432 (1975).

[19] K. S. A. Butcher and T. L. Tansley, Superlattices Microstruct. **38**, 1 (2005).

[20] D. Bagayako and L. Franklin, J. Appl. Phys. **97**, 123708 (2005).

[21] A. Kadir, T. Ganguli, M. R. Gokhele, A. P. Shah, S. S. Chandvankar, B. Arora M., and A. Bhattacharya, J. Cryst. Growth **298**, 403 (2007).

[22] A. Nikolaev, I. Nikitina, A. Zubrilov, M. Mynbaeva, Y. Melnik, and V. Dimitriev, Mater. Res. Soc. Symp. Proc. **595**, W6.5 (2000).

[23] H. Lee and J. J. S. Harris, J. Cryst. Growth **169**, 689 (1996).

[24] A.Koukitu, J. Cryst. Growth **281**, 62 (2005).

[25] A.Koukitu, J. Cryst. Growth **300**, 57 (2007).

[26] J. Wu, W. Walukiewicz, K. M. Yu, J. W. Ager III, E. E. Haller, H. Lu, W. Schaff, Y. Saito, and Y. Nanishi, Appl. Phys. Lett. **80**, 3967 (2002).

[27] A. Yamamoto, H. Miwa, Y. Shibata, and A. Hashimoto, Thin Solid Films **491**, 74 (2006).

[28] N. Dietz, III-Nitrides Semiconductor Materials, Edited By Z. C. Feng, Imperial College Press 203 (2006).

[29] K. Scott, A. Butcher, M. Wintrebert-Fouquet, P. P.-T.Chen, K. E. Prince, H. Timmers, S. K. Shresthta, T. V. Shubina, S. V. Ivanov, R. Wuhrer, M. R. Phillips, and B. Monemar, Phys. Status. Solidi C **2**, 2263 (2005).

[30] M. Alevli, G. Durkaya, W. Fenwick, A. Weerasekara, V. Woods, I. T. Ferguson, A. G. U. Perera, and N. Dietz, Appl. Phys. Lett. **89**, 112119 (2006).

[31] K. S. A. Butcher, A. J. Fernandes, P. P. T. Chen, M. W. Fouquet, H. Timmers, S. K. Shrestha, H. Hirshy, R. M. Perks, and B. Usher, J. Appl. Phys. **101**, 123702 (2007).

[32] W. J. Schaff, with H. Lu, J. Cryst. Growth **269**, 119 (2004).

[33] A. G. Bhuiyan, A. Hashimoto, and A. Yamamoto, J. Appl. Phys. **94**, 2779 (2003).

[34] A. Yamamoto, M. Tsujino, M. Ohkubo, and A. Hashimoto, J. Cryst. Growth **137**, 415 (1994).

[35] Y. C. Pan, W. H. Lee, C. K. Shu, H. C. Lin, C. I. Chiang, H. Chang, D. S. Lin, M. C. Lee, and W. K. Chen, Japan. J. Appl. Phys. **38**, 645 (1999).

[36] T. Tsuchiya, H. Yamano, O. Miki, A. Wakahara, and A. Yoshida, Japan. J. Appl. Phys. **38**, 1884 (1999).

[37] A. Yamamoto, M. Tsujino, M. Ohkubo, and A. Hashimoto, Sol. Energy Mater. Sol. Cells **35**, 53 (1994).

[38] A. Yamamoto, Y. Yamauchi, T. Ogawa, M. Ohkubo, and A. Hashimoto, Inst. Phys. Conf. Ser. **142**, 879 (1996).

[39] A. Yamamoto, Y. Yamauchi, M. Ohkubo, A. Hashimoto, and T. Saitoh, Solid-State Electron. **41**, 149 (1997).

[40] T. Yodo, H. Ando, D. Nosei, and Y. Harada, Phys. Status. Solidi B **228**, 21 (2001).

[41] T. Yodo, H. Yona, H. Ando, D. Nosei, and Y. Harada, Appl. Phys. Lett. **80**, 968 (2002).

[42] H. Lu, W. J. Schaff, L. F. Eastman, J. Wu, W. Walukiewicz, K. M. Yu, J. W. Auger III, E. E. Haller, and O. Ambacher, Abstract Of the 44th Electronic Material Conference, Santa Barbara, CA (2002).

[43] H. Lu, W. J. Schaff, J. Hwang, H. Wu, G. Koley, and L. Eastman, Appl. Phys. Lett. **79**, 1489 (2001).

[44] S. Yamaguchi, M. Kariya, S. Nitta, T. Takeuchi, C. Wetzel, H. Amano, and I. Akasaki, J. Appl. Phys. **85**, 7682 (1999).

[45] K. Xu, W. Terashima, T. Hata, N. Hashimoto, Y. Ishitani, and A. Yoshikawa, Phys. Status. Solidi C **0**, 377 (2002).

[46] S. Keller, I. Ben-yaacov, S. P. Denvers, and U. K. Mishra, Proceedings Of the International Workshop On Nitride Semiconductors (IWN' 2000) Nagoya, Japan, IPAP Conference Series **1**, (2000).

[47] M. Adachi, A. Seki, A. Hashimoto, and A. Yamamoto, Proceedings Of the International Workshop On Nitride Semiconductors (IWN' 2000) Nagoya, Japan, September, IPAP Conference Series **1**, 347 (2000).

[48] S. Y. Tong, Appl. Phys. Lett. **81**, 3960 (2002).

[49] C. Norenberg, M. G. Martin, R. A. Oliver, M. R. Castell, and G. A. D. Briggs, J. Phys. D **35**, 615 (2002).

[50] C. Norenberg, R. A. Oliver, M. G. Martin, L. Allers, M. R. Castell, and G. A. D. Briggs, Phys. Status. Solidi A **194**, 536 (2002).

[51] V. A. Tyagi, V. A. Eustignev, A. M. Krasiko, A. F. Andreeva, and V. Y. Malatidio, Sov. Phys. Semicond. **11**, (1977).

[52] K. L. Westra, R. P. W. Lawson, and M. J. Brett, J. Vac. Sci. Technol. A **6**, 1730 (1988).

[53] T. L. Tansley and C. P. Foley, Semi-Insulating III-V Compounds Edited By D. C. Look and J. S. Blakemore (1984).

[54] K. S. A. Butcher, M. Winterhert-Fouquet, P. P. T. Chen, T. L. Tansley, and S. Srikeaw, Mat. Res. Soc. Symp. Proc. **693**, (2001).

[55] Y. Nanishi, Y. Saito, and T. Yamaguchi, Japan. J. Appl. Phys. **42**, 2549 (2003).

[56] J. Wu, W. Walukiewicz, K. M. Yu, J. W. Ager III, E. E. Haller, H. Lu, W. Schaff J., Y. Saito, and Y. Nanishi, Appl. Phys. Lett. **80**, 3967 (2002).

[57] C. H. Swartz, R. P. Tompkins, N. C. Giles, T. H. Myers, H. Lu, W. J. Schaff, and L.F. Eastman, J. Cryst. Growth **269**, 29 (2004).

[58] T. V. Shubina, S. V. Ivanov, V. N. Jmerik, D. D. Solnyshkov, V. A. Vekshin, P. S. Kop'ev, A. Vasson, J. Leymarie, A. Kavokin, H. Amano, K. Shimono, A. Kasic, and B. Monemar, Phys. Rev. Lett. **92**, 117407-1 (2004).

[59] T. D. Veal and C.F. McConville, Phys. Rev. B **64**, 085311 (2001).

[60] L. O. Olsson, C. B. M. Andersson, M. C. Hakansson, J. Kanski, L. Ilver, and U.O. Karlsson, Phys. Rev. Lett. **76**, 3626 (1996).

[61] T. D. Veal, L. F. J. Piper, M. R. Phillips, M. H. Zareie, H. Lu, W.J. Schaff, and C.F. McConville, Phys. Status. Solidi A **204**, 536 (2007).

[62] V. Y. Aristov, V. M. Zhilin, C. Grupp, A. Taleb-Ibrahimi, H. J. Kim, P. S. Mangat, P. Soukiassian, and G. Le Lay, Appl. Surf. Sci. **166**, 263 (2000).

[63] M. Noguchi, K. Hirakawa, and T. Ikoma, Phys. Rev. Lett. **66**, 2243 (1991).

[64] H. Yamaguchi, J.L. Sudijono, B.A. Joyce, T.S. Jones, C. Gatzke, and R.A. Stradling, Phys. Rev. B **58**, R4219 (1998).

[65] I. Mahboob, T. D. Veal, and C. F. McConville, Phys. Rev. Lett. **92**, 036804-1 (2004).

[66] L. F. J. Piper, T. D. Veal, C. F. McConville, H. Lu, and W. J. Schaff, Appl. Phys. Lett. **88**, 252109 (2006).

[67] D. Segev and C. G. Vand de Walle, Europhys. Lett. **76**, 305 (2006).

[68] L. Colakerol, T. D. Veal, H. K. Jeong, L. Plucinski, A. DeMasi, T. Learmonth, P.A. Glans, S. C. Wang, Y. F. Zhang, L. F. J. Piper, P. H. Jefferson, A. Fedorov, T. C. Chen, T. D. Moustakas, C. F. McConville, and K. E. Smith, Phys. Rev. Lett. **97**, 237601 (2006).

[69] D. E. Eastman, F. J. Himpsel, and J. F. Vanderveen, Solid State Comm. **35**, 345 (1980).

[70] Y. J. Chabal, J. E. Rowe, and S. B. Christman, J. Vac. Sci. Technol. **20**, 763 (1982).

[71] F. J. Himpsel, Physica B **117-118**, 767 (1983).

[72] R. E. Schlier and H. E. Farnsworth, J. Chem. Phys. **30**, 917 (1959).

[73] K. Takayanagi, Y. Tanishiro, S Takahashi, and M. Takahashi, Surf. Sci. **164**, 367 (1985).

[74] K. Takayanagi, Y. Tanishiro, M. Takahashi, and S. Takahashi, J. Vac. Sci. Technol. A **3**, 1502 (1985).

[75] G. Binnig, H. Rohere, C. Gerber, and E. Weibel, Phys. Rev. Lett. **50**, 120 (1983).

[76] R. M. Tromp and E. J. van Loenen, Surf. Sci. **155**, 441 (1985).

[77] I. K. Robinson, W. K. Waskiewica, P. H. Fuoss, J. B. Stark, and P. A. Bennett, Phys. Rev. B **33**, 7013 (1986).

[78] T. Komeda, R. Hasunuma, H. Mukaida, and H. Tokumoto, Surf. Sci.. **386**, 149 (1997).

[79] K. Takahashi, C. Nara, T. Yamagishi, and T. Onzawa, Appl. Surf. Sci. **151**, 299 (1999).

[80] W. Shimada and H. Tochihara, Surf. Sci. **526**, 219 (2003).

[81] J. A. Jensen, C. Yan, and A. C. Kummel, Science **267**, 493 (1995).

[82] J. A. Venables, G. D. T. Spiller, and M. Hanbucken, Rep. Prog. Phys. **47**, 399 (1984).

[83] Johannes V Barth, Giovanni Costantini, and Klaus Kern, Nature **437**, 671-9 (2005).

[84] J. Knall, J.-E. Sundgren, J. E. Greene, A. Rockett, and S. A. Barnett, Appl. Phys. Lett. **45**, 689 (1984).

[85] J. Knall, S. A. Barnett, J.-E. Sundgren, and J. E. Greene, Surf. Sci. **209**, 314 (1989).

[86] H. Ofner, S. L. Surnev, Y. Shapira, and F. P. Netzer, Phys. Rev. B **48**, 10940 (1993).

[87] J. Morrison, J. Appl. Phys. **36**, 1706 (1965).

[88] A. Kinbara, Surf. Sci. **85**, 29 (1979).

[89] M. Kawaji, S. Baba, and A. Kinbara, Appl. Phys. Lett. **34**, 748 (1979).

[90] M. K. Kelly, G. Margaritondo, J. A. Anderson, D. J. Frankel, and G. J. Lapeyre, J. Vac. Sci. Technol. A **4**, 1396 (1986).

[91] J. Nogami, Sang-il Park, and C. F. Quate, Phys. Rev. B **36**, 6221 (1987).

[92] D. Bolmont, P. Chen, C. A. Sebenne, and F. Proix, Surf. Sci. **137**, 280 (1984).

[93] G. V. Hansson, J. M. Nicholls, P. Martensson, and R. I. G. Uhrberg, Surf. Sci. **168**, 105 (1986).

[94] T. Kinoshita, H. Ohta, Y. Enta, Y. Yaegashi, S. Suzuki, and S. Kono, J. Phys. Soc. Jpn. **56**, 4015 (1987).

[95] J. E. Northrup, Phys. Rev. B **35**, 4137 (1987).

[96] H. Hirayama, S. Baba, and A. Kinbara, Jpn. J. Appl. Phys. **25**, L452 (1986).

[97] J. M. Nicholls, P. Martensson, G. V. Hansson, and J. Northrup E., Phys. Rev. B **32**, 1333 (1985).

[98] J. M. Zhou, S. Baba, and A. Kinbara, Thin Solid Films **98**, 109 (1982).

[99] K. Anno, N. Nakamura, and S. Kono, Surf. Sci. **260**, 53 (1992).

[100] D. M. Cornelison, C. S. Chang, and I. S. T. Tsong, J. Vac. Sci. Technol. A **8**, 3443 (1990).

[101] N. Nakamura, K. Anno, and S. Kono, Surf. Sci. **256**, 129 (1991).

[102] H. Hirayama, S. Baba, and A. Kinbara, Appl. Surf. Sci. **33/34**, 193 (1988).

[103] T. Aiyama and S. Ino, Surf. Sci. **82**, L585 (1979).

[104] M. S. Finney, C. Norris, and P. B. Howes, Surf. Sci. **277**, 330 (1992).

[105] M. S. Finney, C. Norris, P. B. Howes, R. G. van Silfhout, G. F. Clark, and J. M. C. Thornton, Surf. Sci. **291**, 99 (1993).

[106] K. Nishikata, K. Murakami, M. Yoshimura, and A. Kawazu, Surf. Sci. **269-270**, 995 (1992).

[107] R. J. Hamers, Phys. Rev. B **40**, 1657 (1989).

[108] M. Chester and T. Gustafsson, Surf. Sci. **264**, 33 (1992).

[109] J. Zegenhagen, J. R. Patel, P. Freeland, D. M. Chen, J. A. Golovchenko, P. Bedrossian, and J. E. Northrup, Phys. Rev. B **39**, 1298 (1989).

[110] S. Riikonen, A. Ayuelab, and D. Sánchez-Portalc, Surf. Sci. **600**, 3821 (2005).

[111] O. Bunk, G. Falkenberg, J. H. Zeysing, L. Lottermoser, R. L. Johnson, M. Nielsen, F. Berg-Rasmussen, J. Baker, and R. Feidenhans'l, Phys. Rev. B **59**, 12228 (1999).

[112] Z. Gai, R. G. Zhao, Y. He, H. Ji, C. Hu, and W. S. Yang, Phys. Rev. B **53**, 1539 (1996).

[113] A. A. Saranin, A. V. Zotov, A. N. Tovpik, M. A. Cherevik, E. N. Chukurov, V. G. Lifshits, M. Katayama, and K. Oura, Surf. Sci. **340**, 36 (2000).

[114] H. Ofner, S. L. Surnev, Y. Shapira, and F. P. Netzer, Phys. Rev. B **48**, 10940 (1993).

[115] Manhui Sun, Chuan Hu, R.G. Zhao, and Hang Ji, Thin Solid Films **489**, 111 (2005).

[116] M. S. Finney, C. Norris, P. B. Howes, and E. Vileg, Surf. Sci. **277**, 330 (1992).

[117] V. Destefanis, J. M. Hartmann, M. Hopstaken, V. Delaye, and D. Bensahel, Semicond. Sci. Technol. **23**, 105018 (2008).

[118] T. Yasuda, S. Yamasaki, and S. Gwo, Appl. Phys. Lett. **77**, 3917 (2000).

[119] B. Bourguignon, K.L. Carleton, and S.R. Leone, Surf. Sci. **204**, 455 (1988).

[120] J. Cechal, M. Kolibal, P. Kostelnik, and T. Sikola, J. Phys.: Condens. Matter **19**, 016011 (2007).

[121] M.Z. Allmang and L.C. Feldman, Surf. Sci. **191**, L749 (1987).

[122] J. Zegenhagen, M. S. Hybertsen, P. E. Freeland, and J. R. Patel, Phys. Rev. B **38**, 7885 (1988).

[123] T. M. Jung, R. Kaplan, and S. M. Prokes, Surf. Sci. **289**, L577 (1993).

[124] Th. Schmidt, J. I. Flege, M. Speckmann, T. Clausen, S. Gangopadhyay, A. Locatelli, T. O. Mentes, S. Heun, F. Z. Guo, P. Sutter, and J. Falta, Phys. Status. Solidi A **206**, 1717 (2009).

[125] T. M. Jung, S. M. Prokes, and R. Kaplan, J. Vac. Sci. Technol. **12**, 1838 (1994).

[126] T. Thundat, S.M. Mohapatra, B.N. Dev, W.M. Gibson, and T.P. Das, J. Vac. Sci. Technol. A **6**, 681 (1988).

[127] J.R. Patel, J. Zegenhagen, P.E. Freeland, M.S. Hybertsen, J.A. Golovchenko, and D.M. Chen, J. Vac. Sci. Technol. B **7**, 894 (1989).

[128] T. Yamanaka, N. Shimomura, and S. Ino, Surf. Sci. **356**, 39 (1996).

[129] D. M. Chen, J. A. Golovchenko, P. Bedrossian, and K. Mortensen, Phys. Rev. Lett. **61**, 2867 (1988).

[130] M. Y. Lai and Y. L. Wang, Phys. Rev. B **61**, 1764 (1999).

[131] H. Norenberg and C. M. Goringe, Appl. Surf. Sci. **117/118**, 660 (1997).

[132] K. Fujita, Y. Kusumi, and M. Ichikawa, Appl. Phys. Lett. **68**, 770 (1996).

[133] S. Gangopadhyay, T. Schmdit, and J. Falta, Surf. Sci. **552**, 63 (2004).

[134] H. Hibino and T. Ogino, Phys. Rev. B **54**, 5763 (1996).

[135] Y. L. Wang, A. A. Saranin, A. V. Zotov, M. Y. Lai, and H. H. Chang, Inter. Rev. Phys. Chem. **27**, 317 (2008).

[136] T. Ichikawa, T. Onodera, and A. Mizouchi, Jpn. J. Appl. Phys. **41**, 2176 (2002).

[137] Q.H. Wang and M.C. Hersam, Small **4**, 915 (2008).

[138] H. Sakama, A. Kawazu, T. Sueyoshi, T. Sato, and M. Iwatsuki, Phys. Rev. B **54**, 8756 (1996).

[139] H. Nakahara, H. Suzuki, S. Miyata, and A. Ichimiya, Appl. Surf. Sci. **212-213**, 334 (2003).

[140] M. Y. Lai and Y. L. Wang, Phys. Rev. B **64**, 241404 (2001).

[141] K. Fujita, Y. Kusumi, and M. Ichikawa, Phys. Rev. By **58**, 1126 (1998).

[142] K. Fujita, Y. Kusumi, and M. Ichikawa, Surf. Sci. **357-358**, 490 (1996).

[143] K. Irokawa, Y. Nagura, H. Kobayashi, S. Hara, H. I. Fujishiro, H. Miki, A. Kawazu, and K. Watanable, Surf. Sci. **603**, 1197 (2009).

[144] A. A. Baski and L. J. Whitman, J. Vac. Sci. Technol. B **14**, 992 (1996).

[145] Jin-Feng Jia, Xi Liu, Jun-Zhong Wang, Jian-Long Li, X. S. Wang, Qi-Kun Xue, Zhi Qiang Li, Zhenyu Zhang, and S. B. Zhang, Phys. Rev. B **66**, 165412 (2002).

[146] M. Scrocco, Phys. Rev. B **36**, 9732 (1987).

[147] J.E. Rowe, G. Margaritondo, and S.B. Christman, Phys. Rev. B **15**, 2195 (1977).

[148] H.H. Chang, M.Y. Lai, J.H. Wei, C.M. Wei, and Y.L. Wang, Phys. Rev. Lett. **92**, 066103 (2004).

[149] A. Ohtake, Phys. Rev. B **73**, 033301 (2006).

[150] M. Y. Lai and Y. L. Wang, Phys. Rev. B **61**, 12608 (2000).

[151] M. Otsuka and T. Ichikawa, Japan. J. Appl. Phys. **24**, 1103 (1985).

[152] H. Suzuki, H. Nakahara, S. Miyata, and A. Ichimiya, Surf. Sci. **493**, 166 (2001).

[153] Y. J. Ko, K. J. Chang, and J. Y. Yi, Phys. Rev. By **60**, 1777 (1999).

[154] A. A. Baski, S. C. Erwin, and L. J. Whitman, Surf. Sci. **423**, L265 (1999).

[155] H. Hibino, H. Kageshima, and M. Uwaha, Surf. Sci. **602**, 2421 (2008).

[156] M. Speckmann, Th. Schmidt, J. I. Flege, P. Sutter, and J. Falta, J. Phys.: Condens. Matter **21**, 314020 (2009).

[157] K. Higashiyama, S. Kono, and T. Sgawa, Surf. Sci. **175**, L794 (1986).

[158] S. Andreu, F. Arnaud, D. Avitaya, and J. C. Pfister, Surf. Sci. **238**, 53 (1990).

[159] M. Kolibal, T. Cechal, E. Brandejsova, J. Cechal, and T. Sikola, Nanotechnology **19**, 475606 (2008).

[160] A. Kawazu and H. Sakama, Phys. Rev. B **37**, 2704 (1988).

[161] T. Hanada, H. Daimon, S. Nagano, S. Ino, S. Suga, and Y. Murata, Phys. Rev. B **55**, 16420 (1997).

[162] M. Y. Lai and Y. L. Wang, Phys. Rev. B **60**, 1764 (1999).

[163] S. F. Tsay, M. H. Tsai, M. Y. Lai, and Y. L.Wang, Phys. Rev. B **61**, 2699 (2000).

[164] T. Kinoshita, S. Kono, and T. Sagawa, Phys. Rev. B **32**, 2714 (1985).

[165] T. Kinoshita, S. Kono, and T. Sagawa, Solid State Comm. **56**, 681 (1985).

[166] G. V. Hansson, R. Z. Bachrach, R. S. Bauer, and P. Chiaradia, Phys. Rev. Lett. **46**, 1033 (1981).

[167] R. I. G. Uhrberg, G. V. Hansson, J. M. Nicholls, P. E. S. Persson, and S. A. Flodstrom, Phys. Rev. B **31**, 3805 (1985).

[168] V. G. Lifshits, A. V. Zotov, and A. A. Saranin, Surface Phases On Silicon; Preparation, Structure and Properties. John Wiley: Chichester (1994).

[169] J. J. Lander and J. Morrison, Surf. Sci. **2**, 553 (1964).

[170] R. M. Groger and M. R Barczewski, Surf. Interf. Anal. **32**, 154 (2001).

[171] K. Nishikata, K. Murakami, M. Yoshimura, and A. Kawazu, Surf. Sci. **269/270**, 995 (1992).

[172] T. Michely, M. C. Reuter, and R. M. Tromp, Phys. Rev. B **53**, 4105 (1996).

[173] M. Yoshimura, K. Takaoka, T. Yao, T. Sato, T. Sueyoshi, and M. Iwatsuki, Phys. Rev. B **47**, 13930 (1993).

[174] M. Yoshimura, K. Takaoka, T. Yao, T. Sueyoshi, T. Sato, and M. Iwatsuki, J. Vac. Sci. Technol. B **12**, 2434 (1994).

[175] A. Uemura, A. Ohkita, H. Inaba, S. Hasegawa, and H. Nakashima, Surf. Sci. **357/358**, 825 (1996).

[176] S. Sumitani, T. Abukawa, R. Kosugi, S. Suzuki, S. Sato, and S. J. Kono, Electron Spectrosc. Relat. Phenom. **101-103**, 245 (1999).

[177] Jr. Chelikowsky, Phys. Rev. B **16**, 3618 (1977).

[178] Hi. Zhang and M. Schluter, Phys. Rev. B **18**, 1923 (1978).

[179] H. Tsuge, M. Arai, and T. Fujiwara, Jpn. J. Appl. Phys. **30**, L1583 (1991).

[180] T. Aizawa, T. Tsuno, H. Daimon, and S. Ino, Phys. Rev. B **36**, 9107 (1987).

[181] S. T. Li, S. Hasegawa, S. Nakamura, and H. Nakashima, Jpn. J. Appl. Phys. **30**, L1671 (1991).

[182] R. J. Hamers, J. Vac. Sci. Technol. B **6**, 1462 (1988).

[183] R. J. Hamers and J. E. Demuth, Phys. Rev. Lett. **60**, 2527 (1988).

[184] M. Yoshimura, Takaoka K., Tao T., T. Sato, T. Sueyoshi, and M. Iwatsuki, Phys. Rev. B **47**, 13930 (1993).

[185] J. E. Northrup, Phys. Rev. Lett. **53**, 683 (1984).

[186] H. Huang, S. Y. Tong, J. Quinn, and S. Jona, Phys. Rev. B **41**, 3276 (1990).

[187] E. A. Khramtsova, A. V. Zotov, A. A. Saranin, V. S. Ryzhkov, A. Chub, and V. Lifshits, Appl. Surf. Sci. **82/83**, 576 (1994).

[188] A. V. Zotov, E. A. Khramtsova, S. V. Ryzhkov, A. A. Saranin, A. B. Chub, and V. G. Lifshits, Surf. Sci. **316**, L1034 (1994).

[189] M. Yoshimura, Takaoka K., Tao T., T. Sato, T. Sueyoshi, and M. Iwatsuki, J. Vac. Sci. Technol. B **12**, 2434 (1994).

[190] T. Suzuki, H. Minoda, Y. Tanishiro, K. Yagi, T. Sueyashi, T. Sato, and M. Iwatsuki, Surf. Sci. **357**, 522 (1996).

[191] T. Suzuki, H. Minoda, Y. Tanishiro, and K. Yagi, Surf. Sci. 335 (1996).

[192] A. A. Baski, S. C. Erwin, and L. J. Whitman, Science **269**, 1556 (1995).

[193] A. A. Baski and L. J. Whitman, Phys. Rev. Lett. **74**, 153 (1995).

[194] S. S. Lee, N. D. Kim, C. G. Hwang, H. J. Song, and J. W. Chung, Phys. Rev. B **66**, 115317 (2002).

[195] H. Kim, G. Duvjir, O. Dugerjav, H. Li, and J. M. Seo, Phys. Rev. B **81**, 245422 (2010).

[196] J. Wei, X. S. Wang, J. L. Goldberg, N. C. Bartelt, and E. D. Williams, Phys. Rev. B **68**, 3885 (1992).

[197] S. Song, M. Yoon, and S. G. J. Mochrie, Surf. Sci. **348**, 153 (1995).

[198] S. G. J. Mochrie, Phys. Rev. B **51**, 153 (1995).

[199] S. R. Blankenship, H. H. Song, A. A. Baski, and J. A. Carlisle, J. Vac. Sci. Technol. A **17**, 1615 (1999).

[200] H. H. Song, K. M. Jones, and A. A. Baski, J. Vac. Sci. Technol. A **17**, 1696 (1999).

[201] A. A. Baski, K. M. Jones, and K. M. Saoud, Ultramicroscopy **83**, 23 (2001).

[202] K. M. Jones, H. H. Song, and A. A. Baski, Cluster Sci. **10**, 573 (1999).

[203] Y. Peng, H. Minoda, Y. Tanishiro, and K. Tagi, Surf. Sci. **493**, 508 (2001).

[204] J. W. Dickinsonm, J. C. Moore, and A. A. Baski, Surf. Sci. **561**, 193 (2004).

[205] J. R. Ahn, Y. J. Kim, H. S. Lee, C. C. Hwang, B. S. Kim, and H. W. Yeom, Phys. Rev. B **66**, 153403 (2002).

[206] J. R. Ahn, W. H. Choi, Y. K. Kim, H. S. Lee, and H. W. Yeom, Phys. Rev. B **68**, 165314 (2004).

[207] J. R. Ahn and H. W. Yeom, Phys. Rev. B **69**, 233311 (2004).

[208] P. H. Woodworth, J. C. Moore, and A. A. Baski, J. Vac. Sci. Technol. A **21**, 1332 (2003).

[209] M. Kumar, Govind, V. K. Paliwal, A. G. Vedeshwar, and S. M. Shivaprasad, J. Nanosci. Nanotechnol. **7**, 1841 (2007).

[210] M. Kumar, V. Govind, K. Paliwal, A. G. Vedeshwar, and S. Shivaprasad M., Surf. Sci. **2745**, 600 (2006).

[211] M. Kumar, V.K. Paliwal, Govind, and S.M. Shivaprasad, Mater. Res. Soc. Symp. Proc. (2006).

[212] M. Kumar, V. K. Paliwal, A. G. Joshi, and S. M. Shivaprasad, Surf. Sci. **596**, 206 (2005).

[213] P. Kumar, M. Kumar, B. R. Mehta, and S. M. Shivaprasad, Surf. Sci. **605**, 1426 (2011).

Chapter III

Experimental and theoretical methods

This chapter gives an introduction to various experimental methods used in this study and provides technical details of the apparatus used for both synthesis and characterization. Also the theoretical methods used in the study are described.

3.1   Introduction

Broadly classifying, the thesis consists of two parts i) formation of metal induced reconstructions on Si surfaces and ii) the growth of InN and GaN on various single crystal surfaces and reconstructed templates. The first part involves careful adsorption studies of submonolayer quantities of metals on semiconductor surfaces which require atomically clean surfaces and its maintenance of atomic cleanliness for the experimental duration. Thus, all these experiments have been performed in Ultra High Vacuum (UHV) with a base pressure $<5x10^{-11}$torr.[1] For performing metal deposition studies, the metal source was in the form of a tiny homemade Tantalum Knudsen cell and the surface morphological, structural and electronic evolution of these ultra thin films is monitored using Auger Electron Spectroscopy (AES) and Low Energy Electron Diffraction (LEED). To model the surface structure of one of the reconstructions, we have performed *ab-inito* Density Functional theory based geometry relaxation calculations. For InN thin film growth, Molecular Beam Epitaxy system with effusion cells for metal and Radio Frequency plasma for N_2* sources are used. Grown InN samples are characterized *ex-situ* using several complementary characterization tools described below.

The experimental setup used for the present work for surface science experiments is shown in Fig. 3.3 which is a Ultra High Vacuum (UHV) system (Varian Inc., USA) comprising of AES, LEED and EELS. A schematic of the system is also shown in Fig. 3.3. The material to be deposited is put in the tiny Knudsen cell and the flux rate is controlled by using passing appropriate current with precise control in the submonolayer regime.   The sample was cleaned chemically *ex-situ*[2,3], before inserting in the vacuum chamber. Sample

was mounted into the manipulator with homemade Ta sample holder. After inserting into the vacuum chamber, the sample is degassed at $600^{o}C$ by direct resistive heating for 12 hours followed by repeated flashing up to $1000^{o}C$-$1200^{o}C$ for 5sec and cooling to RT at a very slow rate of $2^{o}C$/sec. The sample temperature is monitored by a W-Re (5%, 25%) thermocouple mounted behind the sample and also confirmed by an optical pyrometer. The atomic cleanliness of a sample was ascertained by the absence of carbon and other contamination on the surface by AES and observation of the characteristic sharp LEED. For surface science experiments the tantalum-Knudsen cell was degassed thoroughly before using it for evaporation and the flux rate was controlled by regulating the current to the cell, and measured in terms of coverage by measuring the metal to Si peak intensity ratio by AES.
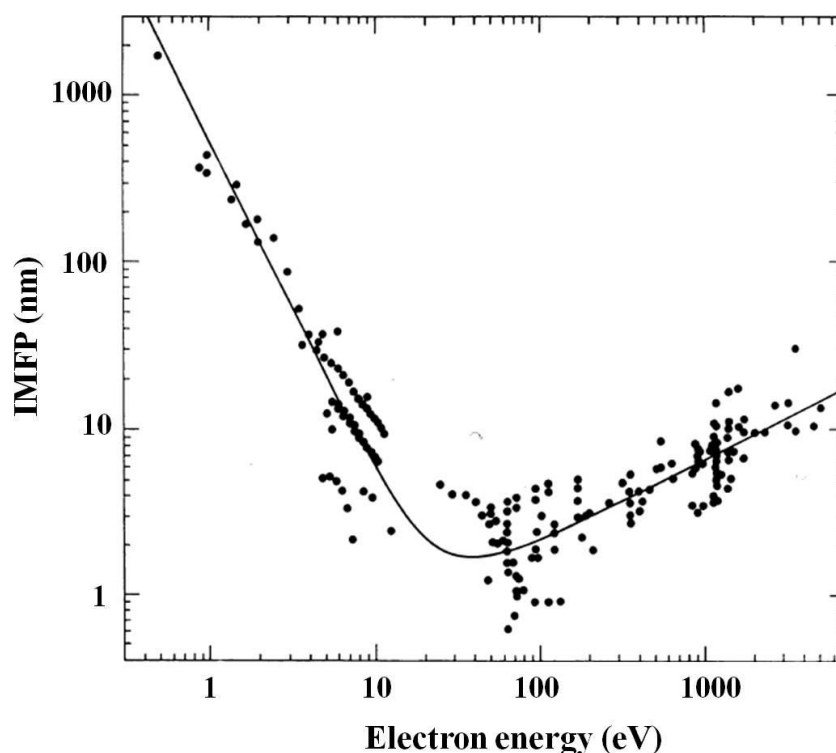
Fig. 3.1: *The inelastic mean free path curve of electron versus electron energy. The dots are experimental values.*

3.2   Surface Sensitive Probes

The scattering of electrons, ions, atoms and photons from surfaces make them interesting both as probe and response particles. One of the main reasons for using electrons in surface science is the inelastic mean free path of electrons in matter. [4,5] The inelastic mean free path of the electrons in this regime is plotted in the Fig. 3.1.[6] The curve shows an

empirical curve of the mean free path independent of the material and the points are measured data from many elemental solids. The data points scatter more or less around the calculation for all elements and is therefore universal curve. The reason for this universality is that the inelastic scattering of electrons in this energy range is mostly involving excitations of conduction electrons, which have more or less the same density in all elements. At lower energies other scattering mechanisms will be important, like scattering with phonons. Inelastic mean free path curve has a broad (log-log scale) minimum around a kinetic energy of about 70 eV *i.e.* it is less than 10Å. This means that if we observe an electron with this kinetic energy, which has left the solid without suffering an inelastic scattering event it must originate from the first few layers. We know that the electron has not been scattered in-elastically from the energy loss associated with a scattering from the valence electrons, which is rather large. Therefore, it is relatively easy to distinguish between in-elastically scattered and non-scattered electrons.
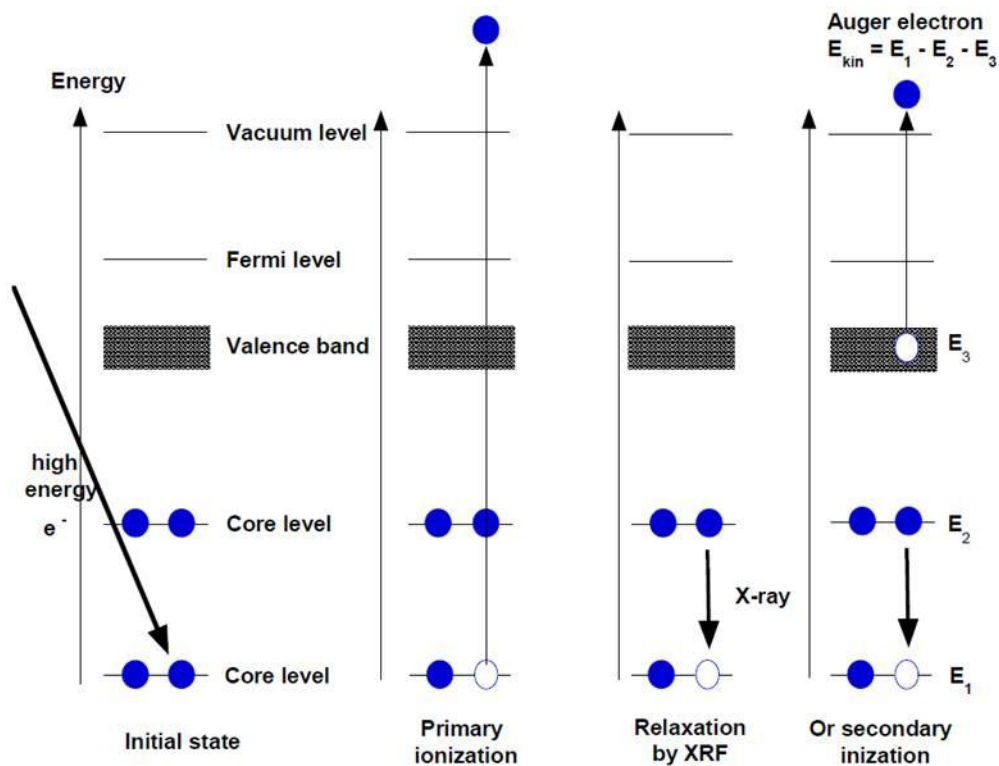
Fig. 3.2: *Auger electron emission*

3.2.1   Auger electron spectroscopy

Auger electrons were first identified in nuclear physics by Pierre Auger[7], a French physicist, in 1925 and the application of Auger electrons in surface chemical analysis was first suggested by Lander[8] in 1953. Auger Electron Spectroscopy (AES) is one of the most commonly used surface sensitive techniques for monitoring of surface cleanliness and determining surface composition.[4,6,9,10] The sensitivity of AES is ~ 0.1% of a monolayer for all elements except for hydrogen and helium, since AES is a three electron process.

In any Auger process, the atom is ionized by removal of an electron from the core level by an impinging high energy electron beam. The atom may decay to a lower energy state by emission of x-rays, or alternatively by ejecting an electron called an Auger electron, which leaves the atom in a doubly ionized state. The energy difference between these two states is given to the ejected Auger electron which will have a kinetic energy characteristic of the parent atom.[11] When the Auger transitions occur within the few Angstroms of the surface, the Auger electron may be ejected without loss of energy giving rise to peaks in the secondary electron energy distribution. The energy and shape of these Auger features can be used to identify the composition of the solid surfaces. AES is based upon the measurement of kinetic energies of the emitted electrons.
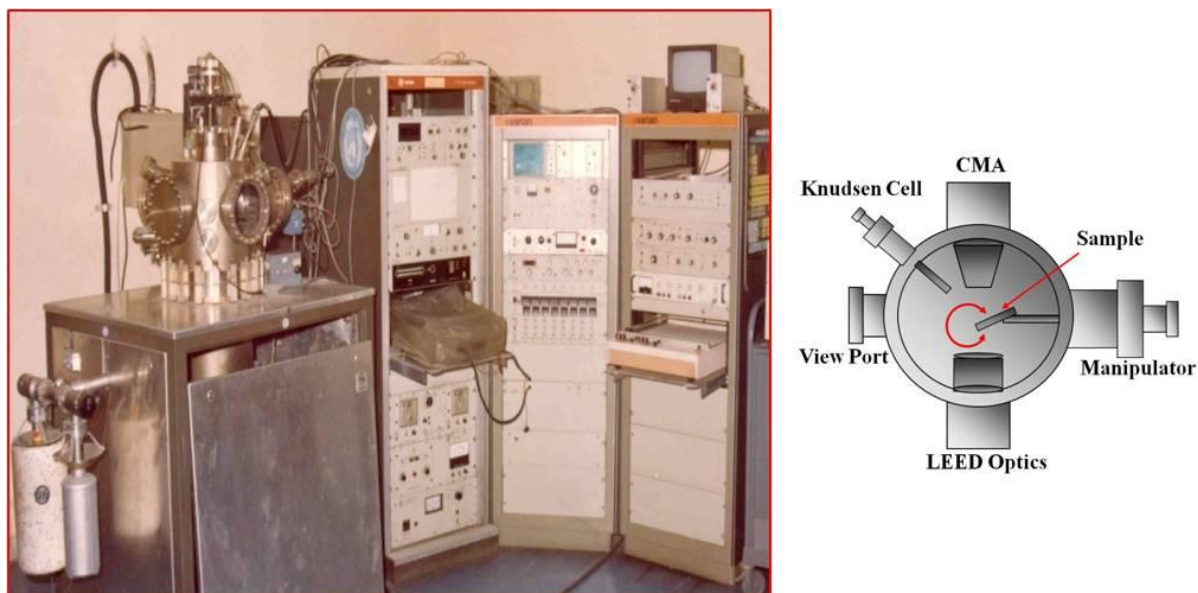
Fig. 3.3: *UHV system used in this study for carrying out AES and LEED. A schematic of the in-situ deposition and analysis system is also shown on the right side.*

Fig. 3.2 demonstrates the complete Auger process along with another possibility of the release of some energy in the form of x-rays. In Fig. 3.2, a high energy beam of electrons knocks out a core level electron from the atom with an energy state having energy E_1. The vacancy created by this is filled by the transfer of an electron from the higher energy level having energy E_2 with the release of an Auger electron from the energy level having energy E_3. The kinetic energy of the Auger electron is given by

$$E_{kin} = E_1 - E_2 - E_3 \qquad\qquad (3.1)$$

A correction for the work function has to be added to the kinetic energy formula if the emitted Auger electron is from the valence band of a solid. The kinetic energy of the Auger electron is independent of the mechanism of initial core hole formation and is characteristic of the material. Each element in a sample being studied will give rise to a characteristic spectrum of peaks at various kinetic energies shown in Fig. 3.4.[11]
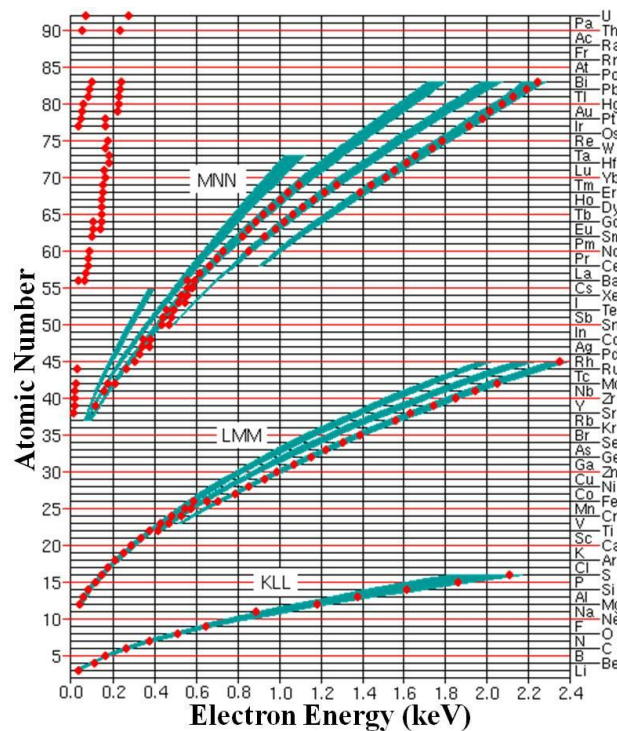
Fig. 3.4: *Auger transitions and energies for different elements.*[11]

Fig. 3.3 shows the UHV system (VT112, Varian Inc.) used for metal deposition, AES and LEED in this study, consists of electron source, sample, electron energy analyzer (CMA and electron detector), and data processing electronics. The Auger spectrum is taken in the derivative mode using a lock-in amplifier in order to reduce the contribution of the in-elastically scattered electrons. By modulating the
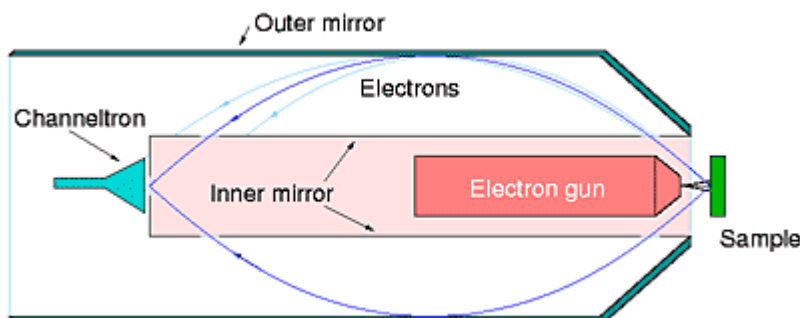
Fig. 3.5: *A schematic of cylindrical Mirror Analyzer*

voltage on the analyzer and amplifying the signal, one can measure the derivative of the signal to suppress the background of the secondary electrons. Standard Auger electron spectra have been published for all the elements of the periodic table.[11] This way, the surface composition (quantitative Auger analysis) and cleanliness (presence of the oxygen and carbon peaks) can be determined. Because of the small Auger signals AES is usually carried out in the derivative mode to suppress the large background of true secondary electrons.

A schematic of the single pass Cylindrical Mirror (CMA) analyzer that is used to measure the energies of the electrons emitted or scattered from a surface is shown in Fig. 3.5.[5] CMA analyzer with intrinsic energy band-pass characteristics is used to measure the number of electrons in a desirable energy window. This is achieved by passing the electrons through a dispersing (electric or magnetic) field in which the deflection is a function of the electron energy. For AES, a single pass CMA is preferred because of its high transmission at moderate energy resolution. The CMA is used in the constant relative resolution (CRR) mode, in which the peak-to-peak intensity of Auger signal remains high (high luminosity implying high electron counts due to large acceptance solid angle) for all energies, but the energy resolution decreases with increase in energy. This relative resolution can only be specified with respect to a particular kinetic energy, and hence is expressed in terms of percentage resolution (0.18% in our case). For angular dependence measurements, CMA is not suitable because it collects over 360° angle. The electron current amplified by the channeltron and a pre-amplifier is detected by a phase sensitive lock-in-amplifier.

We have used AES to identify the growth modes of metals on Si surfaces. The use of AES to identify the growth mode in various adsorbate/substrate systems is well established.[12-14] Fig. 3.6 shows the three possible growth modes in heteroepitaxy.[15] As
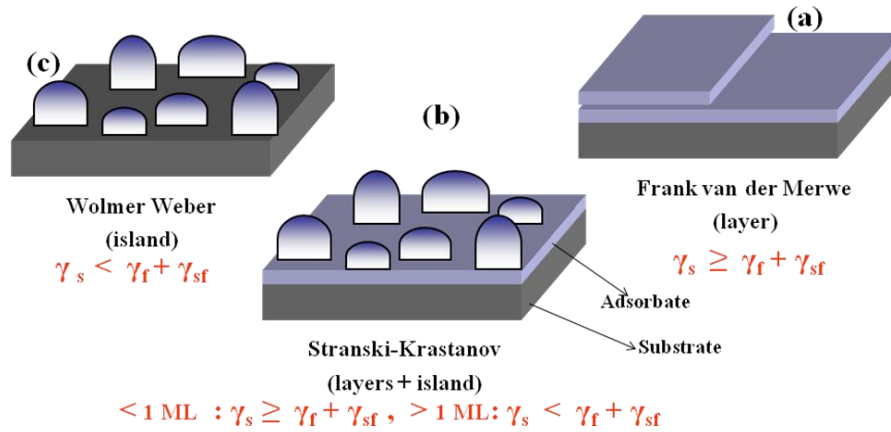
Fig. 3.6: *Schematic of different possible growth modes*

shown in Fig. 3.6 (a) Frank-van der Merwe (FM) mode (or layer by layer mode) refers to the successive addition of 2-D layers to the substrate crystal. The second mode called Volmer-Weber (VW) mode (island mode), as shown in Fig. 3.6(c), will occur when the added material can minimize its free energy by forming an island structure. A third mode called Stranski-Krastanov (SK or layer plus island mode) as shown in Fig. 3.6(b) will happen when the substrate-overlayer bond is stronger than the adatom-adatom bond for the first few layers and then form islands on top. In this process, growth starts with a strained 2-D wetting layer, but islands form after the first few monolayers. The driving force for the subsequent island formation is the incorporation of dislocations within the islands to relieve stress.
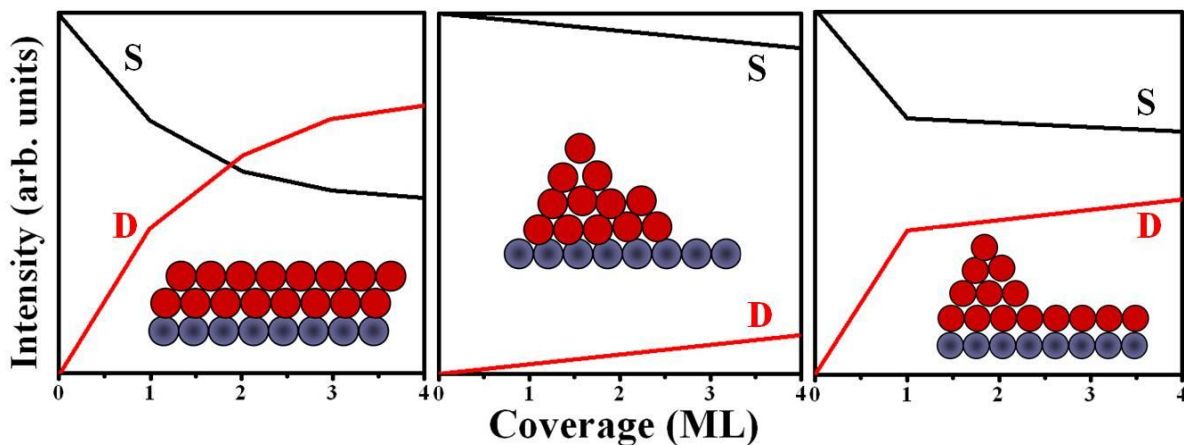
Fig. 3.7: *Schematic of uptake curves for a) layer by layer growth b) island growth and c) layer plus island growth. S and D respectively denote the Auger intensities for substrate and deposit. Insets show ball model for the surface morphology in the three cases.*

All these three growth modes can be identified by the 'uptake curves' obtained during adsorption. Uptake curve is a plot of intensity of Auger signal of the overlayer and substrate

plotted versus deposition time. For a better signal to noise ratio usually the ratio of Auger intensities of overlayer to that of substrate is plotted versus deposition time. The uptake curves in Fig. 3.7(a) of the substrate and overlayer signals with linear segments show the layered growth. The Auger intensity from the overlayer increases linearly with deposition of the first layer. With the onset of formation of the second layer as the signal from the first layer gets attenuated by the second layer, there will be a change in slope of the uptake which can be used for calibration of the coverage. The island growth is shown in Fig. 3.7(b), which leads to a very slow growth of the signal from the deposit because in the case of island formation signal from atom buried inside the island gets attenuated. The SK mode as shown in Fig. 3.7(c) is characterized by a linear increase up to 1ML or sometimes few monolayers followed by a sharp break point, after which the Auger amplitude increases only slowly as islands are formed on the surface. The gradient after the breakpoint depends on the island density and shape. The simultaneous layer growth mode has also been identified, under certain circumstances. Both layer and SK growth mode can approach this behaviour. Several other possibilities have been described by Argile *et al.*[14], where the behaviour depends on the deposition temperature and flux rate of incident beam.

Taking into account various factors governing the Auger electron emission, the intensities of the Auger emission from the adsorbate and the substrate for a fractional coverage of the adsorbate are given by following expressions[4,5]:

$$I_B = I_B^\infty \left\{ 1 - \phi_A + \phi_A \exp\left[\frac{-a_A}{\lambda_A(E_B)\cos\theta} \right] \right\} \tag{3.2}$$

$$I_A = \phi_A I_A^\infty \left[\frac{1 + r_B(E_A)}{1 + r_A(E_A)} \right] \left\{ 1 - \exp\left[\frac{-a_A}{\lambda_A(E_A)\cos(\theta)} \right] \right\} \tag{3.3}$$

where A and B subscripts respectively represent substrate and overlayer.

For the case of substrate covered by a full monolayer,

$$I_B = I_B^\infty \left\{ \exp\left[\frac{-d_A}{\lambda_A(E_B)\cos\theta} \right] \right\} \tag{3.4}$$

$$I_A = I_A^\infty \left[\frac{1 + r_B(E_A)}{1 + r_A(E_A)} \right] \left\{ 1 - \exp\left[\frac{-d_A}{\lambda_A(E_A)\cos(\theta)} \right] \right\} \tag{3.5}$$

Here the different parameters are:

I = *Intensity of Auger signal*

I^{∞} = *Intensity from a semi-infinite film*

φ = *coverage*

a = *monolayer thickness of overlayer*

λ = *Inelastic mean free path*

r = *Back scattering factor*

θ = *Analyzer acceptor angle*

d = *Thickness of thee overlayer*

For calculating inelastic mean free path we have used Tanuma-Powell TP2 formula and for backscattering factor we have used formulae from Ref[4,16,17]. We have used the above expressions to calculate ratio of Auger intensities from the substrate and the overlayer so as to compare it with the experimental observation.

3.2.2   Low Energy Electron Diffraction

The hypothesis that the electron behaves like a wave was first proposed by de-Broglie in his doctoral dissertation work, where he associated the wavelength with the momentum of the particle and the Planck's constant. The first experimental evidence that particles really have an associated wavelength was given by Clinton J. Davidson and Lester H. Germer in 1927 in the famous Davidson-Germer experiment of electron diffraction. They were able to determine the electron wavelength, and demonstrated the wave particle duality in an electron diffraction experiment. According to their result, electrons get diffracted from a crystal, the same way that x-ray diffraction occurred in Bragg's experiments. Later such electron diffraction experiments began to be commonly used to see the crystal structure on surfaces and epitaxial films.[18] Along with the chemical composition of the surface, the structure of the surface layers, i.e., the arrangement of atoms in these layers must also be determined. Because of the advantages of using electrons in surface investigations, elastic electron diffraction naturally suggests itself as a possible tool. Two different geometries have been used to see the crystal structure which are glancing-incidence reflection high energy electron diffraction (RHEED) and the near normal incidence reflection of electrons called low energy electron diffraction (LEED). Between the two methods of electron diffraction, LEED is a true surface sensitive technique due to its low incident electron energy around 100 eV, with

penetration depth of the order of 1nm before being scattered. The electron energy in RHEED experiments is 5-100 keV, but are surface sensitive due to the geometry of operation and will be discussed later.

Determination of surface structure by LEED can be done quantitatively or qualitatively.[19,20] In quantitative analysis, intensities of various diffracted beams are recorded and plotted as a function of the incident energy of the electron. The plot of I-V curve can be used to get the information about the atomic spacing by comparing it with theoretical (multiple-scattering) curves.[21] In qualitative analysis, the diffraction pattern is recorded and the analysis of spot positions yield the information about size, symmetry and rotational alignment of the adsorbate or surface unit cell with respect to the substrate unit cell. The angular spacing between the beams gives the information about atomic spacing. The intensity of the background indicates the amount of surface disorder, i.e., bright spots and a dark background reveal that the surface is well ordered. In our experiments, we use the qualitative analysis method to study different metal induced reconstructions on Si surfaces. The basic principle underlying the low energy electron diffraction is Bragg's law. Electrons follow the wave-particle duality. From De-Broglie relation, the wavelength of the electron having momentum P is given by $\lambda = h / P$ where momentum $P = mv = (2mE_k)^{1/2} = (2meV)^{1/2}$, h = Planck's constant, m = mass of an electron, e = charge of an electron, V = accelerating voltage. If the incident energy of the electron is in the range of 20-200 eV, then the wavelength varies from 2.7 to 0.87 Å, matching with the lattice spacing which is one of the necessary conditions for diffraction effects associated with atomic structure to be observed.
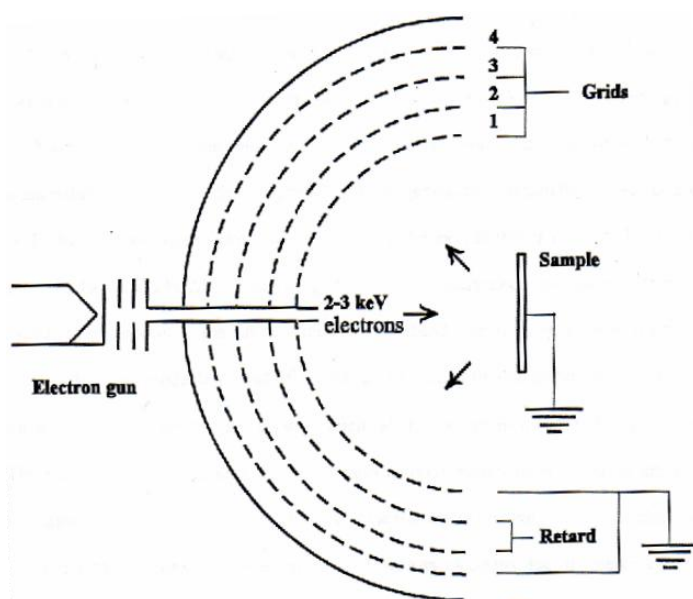
Fig. 3.8: *A schematic of instrumentation for LEED*

A schematic diagram of the LEED apparatus is given in the Fig. 3.8.[22] The system, which is a high pass electron energy filter, consists of an electron gun (which produces the primary electron beam), the sample (mounted perpendicular to the electron gun), four hemispherical grids of high transparency, and a fluorescent screen which is maintained at a 6 keV positive potential. The beam of electrons produced from the cathode is focused electrostatically (approximate electron beam size, ~1 mm^2) and allowed to impinge on the surface of the sample. The focused beam of electrons scatters from the surface in various directions. Grid 1, closest to the sample is grounded in order to provide a field free path for diffracted electrons from sample to the first grid. The second and third grids are biased with a few volts of positive potential relative to the gun filament, which allows the rejection of the inelastically scattered electrons. The fourth grid is also grounded and shields the retarding grids from the fluorescent screen potential. The high potential of the phosphor screen causes visible fluorescence when struck by the electrons. Thus, elastically scattered electrons, after passage through the retarding field, are post-accelerated by a large positive potential and impinge on the spherical fluorescent screen where the diffraction pattern is displayed. The spots of the diffraction pattern are photographed by a digital camera through a window behind the fluorescent screen and image analyzed to find position and intensity of the diffracted spots.

3.2.3   Electron Energy Loss Spectroscopy

The inelastic scattering of electrons from the surfaces of solids is useful in studying their electronic structure. During inelastic scattering, the primary electron beam loses energy in various processes due to various interactions. Fig. 3.9 shows the EELS process and the typical EELS spectra. The Electron Energy Loss Spectroscopy technique measures energy loss of the beam of electrons that interact with the specimen. It measures energy transfer between the electrons in the incident beam and atomic electrons. Information regarding the local environment of the atomic electrons and nearest neighbour atoms can be obtained. In Electron Energy Loss Spectroscopy, electrons which experience inelastic interaction with the sample are analyzed. The entire beam of electrons do not interact with the specimen in-elastically, the EELS spectrum thus, contains information about both elastically and in-elastically scattered electrons.[23] All features, except zero-loss peak, result from the inelastic scattering of the incident electron beam. Inelastic scattering refers to the electrons that are scattered by the inner or outer shell atomic electrons, caused by Coulomb repulsion.

Primarily the in-elastically scattered electrons carry information about the nature of the atoms, their electronic structure and bonding effects with the surrounding atoms. Different energies are involved in inner and outer-shell scattering; therefore, these losses occupy different parts of the EELS spectrum.
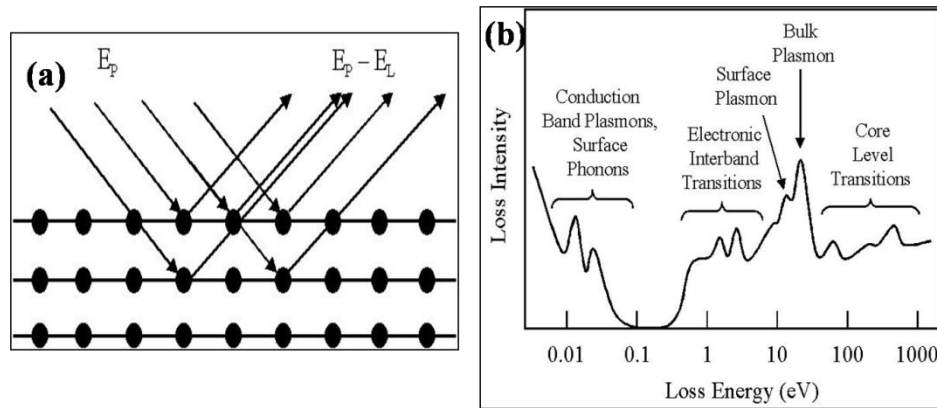
Fig. 3.9: *Left panel shows the incident electron getting reflected from a surface losing it energy. Right panel shows a schematic of loss spectra.*

Zero - loss peak is the most intense feature in the spectrum and contains elastically scattered electrons that experience very small energy losses. Therefore, these electrons have approximately the same energy as the electron beam. Low-Loss spectrum appears adjacent to the zero-loss peak and is much less intense. It contains electrons that interacted with the weakly bound outer shell electrons of the sample resulting in low energy losses (up to ~50eV). Surface and bulk mode plasmon oscillations are produced dominating low-loss spectrum. High-Loss part of the spectrum contains electrons that interacted in-elastically with tightly bound inner shell (core) electrons and it appears above 50eV. The energy needed for the atom ionization process is transferred from the electron beam to the particular shell electron. The amount of energy lost by the electron beam is the same energy, which is required for the atom ionization and is called ionization energy. Therefore, the ionization process is a characteristic of an atom and particular shell ionization. Ionization cross-section and the basic core-loss profile are determined by the generalized oscillator strength which is defined as the probability of a transition of a bound electron from its ground state to a particular state in continuum.

Phonons: On its way through the solid and at the surface the electrons can be scattered in-elastically by absorbing or creating phonons. The phonon energies are small, usually less than 100 meV. The phonon losses one observes in an EELS spectrum can be

used to map the dispersion of the surface phonons or to learn about the adsorbates by measuring their vibrational frequencies.

Interband transitions: Another loss mechanism is the creation of electron-hole pairs. In a metal, electron-hole pairs can be created with infinitely small energies by lifting an electron from an energy level just below the Fermi energy to a level just above. Electron-hole creation does thus contribute to the dielectric function at all energies. For a semiconductor the situation is different *i.e.* there is a minimum energy for electron-hole pair creation, the energy of the fundamental gap. In semiconductors, a structure in the dielectric function can be found which corresponds to excitations over the gap. At slightly lower energy, the excitons are found. For both, metals and semiconductors so-called critical points in the band structure give rise to strong features in the dielectric function. A critical point is, for example, a situation where the occupied bands and unoccupied bands are parallel in a larger region of k-space. Then the optical transitions from the region all have the same energy and contribute strongly to 'ε'.

Bulk and surface plasmon: A plasmon is a quantized oscillation in the density of an electron gas. Such oscillations can be excited by shooting a charged particle or a photon. The coulomb field of the charged particle or the electromagnetic field of the photons causes a redistribution of charge in the electron gas, which launches plasma oscillations. The energy of a plasmon is related to the density of a free electron gas, n by[24,25]

$$E = \hbar\omega = \hbar \ (ne^2/m\varepsilon_o)^{1/2} \tag{3.6}$$

where e is the electronic charge, ε_o is the permittivity of free space and $\hbar$ is reduced Planck's constant. The energy of the surface plasmon is given by,

$$E_s = E_b/\sqrt{2} \tag{3.7}$$

where E_b is the energy of bulk plasmon. The excitation of plasmons and surface plasmons is the major reason for the inelastic scattering of the electrons in the low energy regime of EELS. When considering the universal curve we can see that the mean free path is long for lower energies because it is not possible to excite the plasmons. Above the edge for plasmon creation the mean free path drops drastically. At high energies it goes up again because the cross section for the plasmon creation diminishes.

3.2.4 X-ray Photoelectron Spectroscopy

X-ray photoelectron spectroscopy (XPS),[26,27] also known as Electron Spectroscopy for Chemical Analysis (ESCA), has been widely used to investigate the chemical composition and oxidation state at the sample surface, after it was introduced in the mid

1960s by K. Siegbahn and his research group at the University of Uppsala, Sweden. XPS is able to detect most of the elements except hydrogen and helium, because of their low sensitivities.[28] Principle of the technique is based on the photoelectric effect outlined by Einstein in 1905. For the x-ray sources employed in surface chemical analysis, one normally uses Al or Mg as an anode material since most of the core levels are in the 0-1000eV range. The most intense lines are called $K_{\alpha 1}$ and $K_{\alpha 2}$, but often the doublet is viewed as one line and called $K_{\alpha 12}$. It has energy of 1253.6 eV and 1486.6 eV, for Al and Mg, respectively. Typically a hemispherical analyzer is provided for the collection of the photoelectrons in XPS though double pass CMAs are also employed for the purpose. A hemispherical analyzer, which acts as a band-pass filter, is often used for applications where higher resolution is needed. It consists of two con-centric hemispheres held at different potentials. The electrons enter and leave through slits. Electrons with the right kinetic energy, the so-called pass energy E_p can pass the analyzer. An electrostatic lens-system can be placed in front of the hemispheres in order to focus the electrons into the analyzer and to change the angular acceptance.
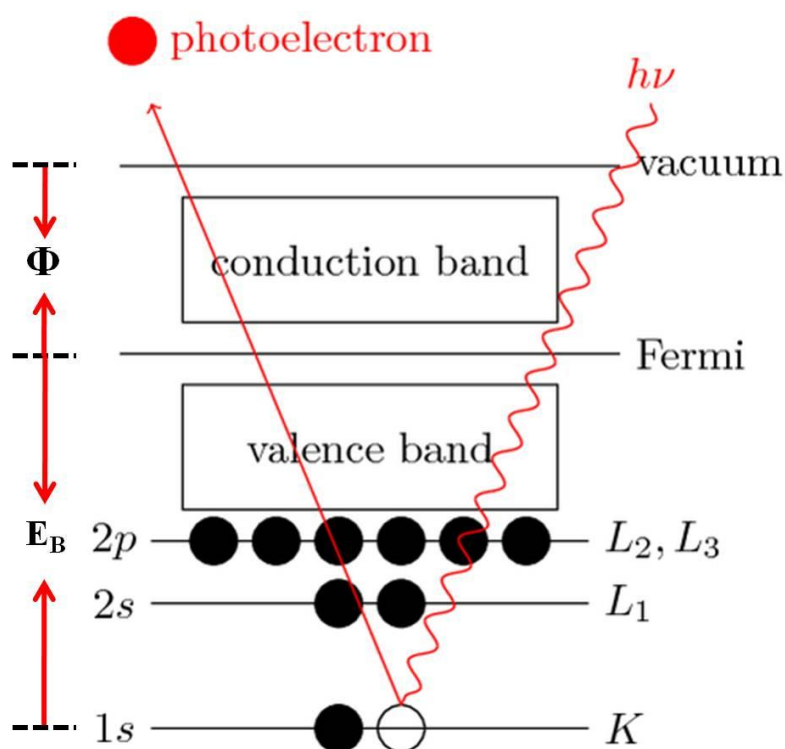
Fig. 3.10: *X-ray photoelectron emission*

Photoemission principle states that if an atom absorbs a photon, an electron from the core shell of the atom will be ejected out from the atom, provided that the photon energy is

greater than the sum of that electron binding energy (E_B) and the work function (Φ) between Fermi level (E_F) and Vacuum level (E_V) as shown in Fig. 3.10.[4,22,29] The Fermi level (E_F) is defined to be at zero binding energy position. Hence, the resultant kinetic energy, E_K, possessed by the photoelectron will be given by applying the principle of the energy conservation:

$$E_K = h\nu - E_B - \Phi. \qquad (3.8)$$

Although it is the kinetic energies of the outgoing photoelectrons that are measured experimentally, spectra are usually displayed on a binding energy scale to allow easy elemental identification.   This is achieved by changing into binding energy,

$$E_B = h\nu - E_K - \Phi. \qquad (3.9)$$

Here, if $h\nu$ and Φ are known, the measured E_K would allow us to obtain the E_B. Since each element has unique set of core levels, kinetic energies, this can be used to identify elements, each element giving its characteristic peak in the XPS spectrum.[30]

An X-ray photoelectron spectrum of a solid-state sample always contains a background, which is formed by inelastically scattered photoelectrons. To estimate the peak shape and the stoichiometry from an experimental spectrum, first the background should be subtracted. Subtraction or removal of the background from XPS peaks is essential in determining the accurate peak position (binding energy, or B.E.) and the peak area, with the later being important for further quantification purpose. There are currently three background subtraction methods available.[31,32] (1) Linear background is a simple subtraction method based on the assumption that the background corresponds to a straight line connecting the start and end points of the peak. (2) Shirley background assumes that intensity of the background is proportional to the peak area on the lower B.E. side of the peak.[33] According to Shirley the subtraction of the background shape depends on the assumptions of a constant energy spectrum of scattered photoelectrons and a constant scattering probability in the peak region.[34] The shape has been shown to have a significant error in the case of a metallic sample[35], but otherwise, it gives realistic results. Relative ease in use makes this background type widely used. When the high B.E. end of the peak has a higher intensity value than the low B.E. end, the Shirley background typically gives a curved S shape as shown in Fig. 3.11. When both ends of the peak have
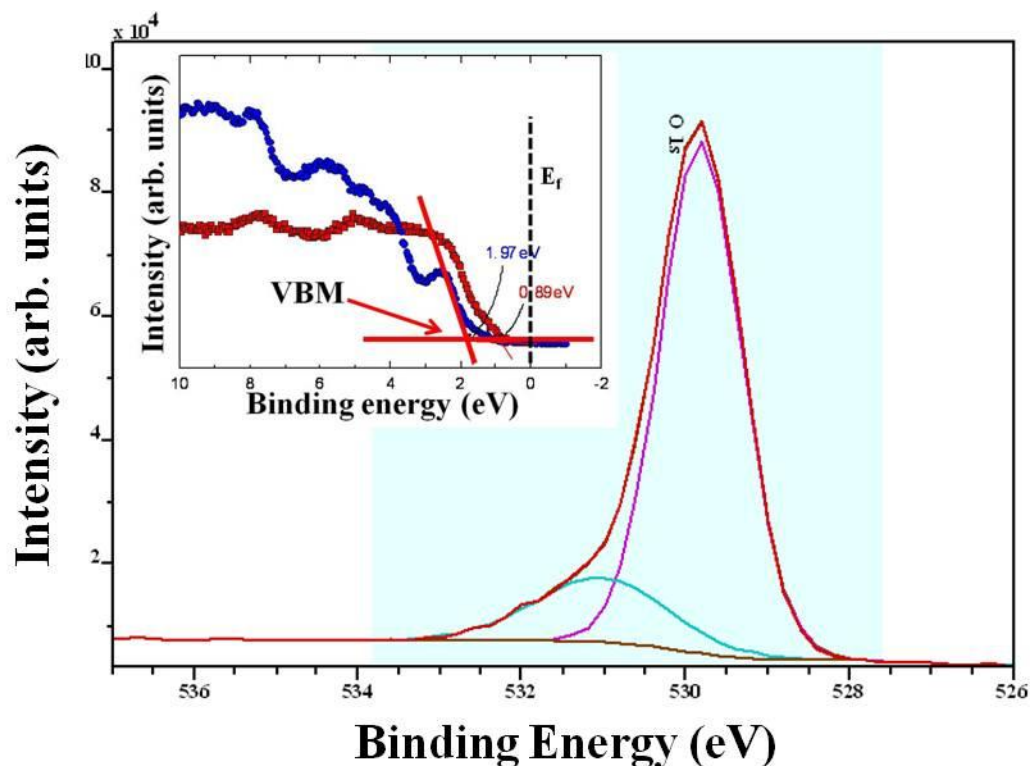
Fig. 3.11: *XPS core level oxygen 1s spectra showing Shirley background and peak deconvolution. Inset shows a schematic of valence band spectra showing valence band maximum (VBM).*

similar intensity values, the Shirley background behaves like a linear background. (3) The Tougaard option is a complex background which is calculated from empirical energy loss functions. It works well on pure clean metals with wide energy range but is not very useful where only a small scan range has been acquired. Throughout our study, we use Shirley-type background subtraction.[36]

In some cases, XPS peaks may consist of a number of overlapping peaks, often of different peak shapes and intensities. In this situation, peak fitting/deconvolution is required to separate overlapping peaks in a spectrum as shown in Fig. 3.11.[37] Our XPS spectral deconvolution is achieved using the standard software with a curve-fitting mathematical process based on a Voight profile which is implemented in Fityk and Xpspeak open source packages. The shapes of the peak (height, width, Gaussian/Lorentzian function, etc.) are automatically varied until the best fit to the observed spectrum is achieved. Constraints like peak position and FWHM etc., have to be fixed so that the results of the fitting process remain physically realistic. Another potential use of XPS is valence band measurements,[38] where we can identify the position of the Fermi level with respect to valence band maximum (VBM) and some surface and interface states as shown in the inset to Fig. 3.11.

In the present study, we have used XPS to characterize InN samples by measuring percentage composition, stoichiometry, presence of external impurities, oxidation states, formation of oxides and presence of metallic In. XPS measurements are carried out using Omicron SPHERA analyzer with non monochromatic X-rays viz. MgK_α ($h\nu = 1256.6 eV$) and AlK_α ($h\nu = 1486.6 eV$).

3.2.5 Scanning Tunneling Microscopy (STM)

STM is a powerful and unique tool for the determination of the structural and electronic properties of surfaces. The first STM was built by Gerd Binning and Heinrich Rohrer in IBM Research Laboratory in 1982.[39] Since then STM and its variants have been used to investigate real space atomic structures and processes on surfaces. The basic physical phenomenon at the origin of this technique is the quantum mechanical tunneling between a sharp metallic tip and a conducting surface through vacuum. Real space information is particularly important for the study of non-periodic and localized features such as vacancies, interstitials, impurity sites, steps, dislocations and domain boundaries. In STM, a small bias voltage is applied between a sharp metallic tip and a conducting substrate, typically between a few millivolts (mV) to a few volts (V).[40-47] After applying a bias voltage, quantum mechanical tunneling of electrons occurs from the occupied states of the tip to the unoccupied states of the surface or vice versa, for opposite bias, when the separation between the tip and sample is extremely small (0.5 to 1.0 nm). The operating tunneling current of STM generally varies from a few pico-Amperes (pA) to a few nano-Amperes (nA). The tunneling current I, is given by[48-50]

$$I \propto \exp(-2kd) \tag{3.10}$$

where $k = \dfrac{\sqrt{2m(\Phi - E)}}{\hbar}$

Here Φ is the work function, m, mass of electron and E, the energy of electron. Thus, tunneling current depends exponentially on the tip sample separation which allows topography of the surface to be acquired by rastering the tip over the surface. STM image, more than geometric, is electronic in nature.[51] As the process of tunneling involves movement of electrons from occupied states of tip to the unoccupied states of the surface or vice-versa, one can map both filled and empty states of the surface.

3.3   Molecular Beam Epitaxy growth and thin film characterization

3.3.1   Molecular Beam Epitaxy

The term MBE was first used in 1970 by Alfred Y. Cho at Bell Telephone Laboratories[52] after extensive work on epitaxial films by Davey and Pankey[53], Shelton and Cho[54], and Arthur[55]. MBE growth is characterized by the interaction of a single or multiple molecular or atomic beams at the surface of a heated crystalline substrate, in an ultra-high vacuum chamber ($\sim 10^{-11}$ torr). At this pressure the mean free path of the ambient gas particle is approximately 40 km; and thus provides a clean environment for deposition and film formation. The low background pressure also provides the best available purity, because the arrival rates of contaminants are significant orders of magnitude less than typical chemical vapour deposition conditions. Unlike other deposition techniques, MBE growth provides impurity-free, quality films with abrupt layers.[56] Fig. 3.12 is a schematic of a typical MBE system.[57] The chamber is cryogenically cooled with liquid nitrogen (LN_2), which prevents degassing and spurious atoms from bouncing off the chamber walls, therefore acting as a cryopump during growth.

As shown in the schematic in Fig. 3.12, the group III-metal sources and dopant materials are introduced through effusion cells, where a solid material is placed in a crucible, typically made of pyrolytic boron nitride (PBN) and heated until the material sublimates or evaporates. The temperature of the effusion
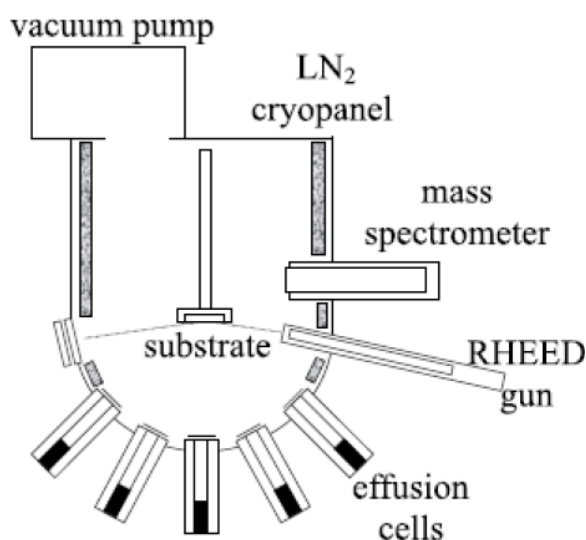
Fig. 3.12: *A schematic of Molecular Beam Epitaxy system*

cells is controlled by proportional-integral-derivative (PID) control parameters, where the flux intensity can be maintained to better than 1%. The group-V source can be delivered by

different methods. Our system uses a nitrogen RF plasma source, where purified N_2 is converted into a more active atomic and molecular species. Shutters placed in front of the III-V sources permit direct control of the epitaxial growth surface at a monolayer level by changing the incoming beam with the opening and closing of the shutter.

In this work, Plasma Assistant Molecular Beam Epitaxy (PAMBE) system (SVTA Assoc. Inc., USA) is used in the growth process which is shown in Fig. 3.13. The system is configured for 3″ wafers, with growth uniformity of <1% over the diameter of 2.8″. It consists of a preparation chamber and a UHV growth chamber, each of which is connected to a turbo-molecular pump and a diaphragm pump. The preparation chamber has a water-cooled sample heating/degassing facility up to $700^{\mathrm{o}}C$ and also a cathodoluminescence facility. Besides, the growth chamber is also connected to a titanium getter pump (TGP), a sputter ion pump (IP) and cryo pump to achieve UHV of the order of $\sim 3\times10^{-11}$ torr and maintaining high quality ambient. Normally, the pressure in pre-chamber can reach 1×10^{-10} torr while the pressure in growth chamber can reach 3×10^{-11} torr. The system has seven Knudsen cells (K-cells) [Ga, In, Al, Mg, Sb, Bi and Si], a nitrogen plasma source and one Ammonia gas injector, with each of them having its own mechanical shutter to control the on/off state of the beam flux. The operation of the MBE system can be carried out through the touch-panel control board as well as computer automation.

Fig. 3.13: *SVTA MBE system used in the present study for the growth of InN and GaN films*

In the growth chamber, the substrate is placed in a special holder, which faces the molecular K-cells. There is a circular filament heater behind the holder, so that the substrate temperature (T_S) can be fixed at an optimum value for the epitaxial growth. The T_S is measured by a thermocouple located at the centre of the substrate heater. In addition, the growth chamber also incorporates a RHEED, Ellipsometry, QCTM, Mass spectrometer, while preparation chamber has Cathodoluminescence for *in-situ* film quality monitoring. The system also has an optical pyrometer cum reflectivity measurement and atomic absorption systems which are used to determine species flux rates and for calibrating the temperature measurements.

3.3.2   Reflection high energy electron diffraction (RHEED)

RHEED is a very powerful tool for *in-situ* growth monitoring and is commonly used for MBE. When applied fully, RHEED can yield growth rate, surface structure and strain relaxation information. The technique utilises a grazing angle high energy electron beam (~10 keV) in which the wavelength of the electrons is comparable to typical atomic spacings
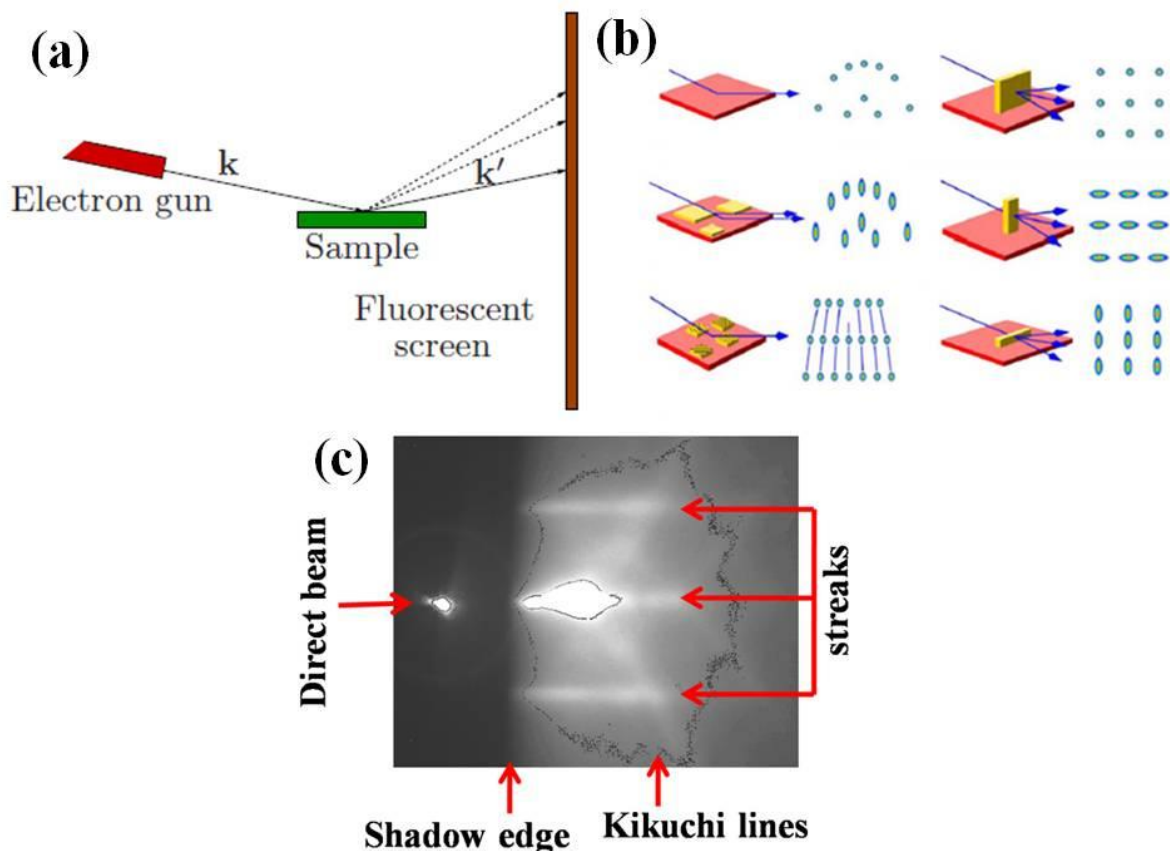
Fig. 3.14: *(a) RHEED geometry, (b) Schematics of surface morphology and corresponding RHEED pattern and (c) A RHEED pattern showing characteristics features.*

0.1-1 nm. The electrons reflected from different atomic planes within the first several nanometres of the film and interfere constructively and destructively to form a diffraction pattern on a phosphor screen. From this diffraction pattern (or RHEED pattern) one can infer properties about the growing crystal. There has been much research into understanding how different features within RHEED patterns relate to film properties; a very thorough review is given by Braun.[58] Typical nitride RHEED patterns are dominated by a combination of reciprocal lattice streaks and Kikuchi lines as shown in Fig. 3.14. The shadow edge signifies where the beam is blocked by the film/substrate, and the separation of this and the direct beam represent the angle of incidence of the beam impinging on the film. Depending on the surface features the emerging RHEED pattern depicts different features as shown in the figure.[59] Typical spot sizes for the electron beam are ~100μm. As the name suggests, the spacing of the reciprocal lattice streaks is inversely proportional to the spacing of the atomic planes taking part in diffraction. Whether the streaks appear continuous or broken can be used to assess the roughness of the growth front. Streaky reciprocal lattice features indicate that the film is smooth on a nm scale and the patterns are due solely to refection/diffraction. If however, the reciprocal lattice features appear spotty then it indicates there is roughness on the nm scale. In this case some electrons are transmitted through surface features and cause interference pattern (spotty reciprocal lattice features). In this thesis RHEED is primarily used to determine the crystalline nature of the film surface, e.g. poly or single crystal and atomically flat or rough. We have used SVTA RHEED gun with SVTA video RHEED capture and analysis system. The electron gun was typically operated at 9kV and 1.5 A.

3.3.3   Atomic Force Microscopy (AFM)

Atomic force microscopy is a technique for deriving atomic-resolution information about the surface morphology and surface roughness.[60] In this technique, an atomically sharp tip mounted at the end of a cantilever is scanned across the surface of the sample. When the tip moves up and down over its topography, the displacement caused by the atomic forces of the features on the surface can be measured to create an image. The AFM measures the van der Waals force between the tip and the surface; this may be either the short-range repulsive force (in contact-mode) or the longer-range attractive force (in non-contact mode). There are three scanning modes associated with AFM, namely; contact mode, non-contact mode, and tapping mode. Contact mode is the scanning mode in which the tip is in contact with the surface and the image is obtained by repulsive forces between tip and the sample. In tapping mode, the image is obtained by the tip, which just taps the surface for small periods of time.

In non-contact mode, the tip oscillates above the surface, and the image is obtained from the attractive forces between the tip and the sample. The tip is scanned over a surface with feedback mechanisms that enable the piezo-electric scanners to maintain the tip at a constant force (to obtain height information) or height above the sample surface (to obtain force information). As the tip scans the surface of the sample, the focused laser beam is deflected off the attached cantilever into a position sensitive dual photodiode system. Feedback from the dual photodiode system and the control software enables the tip to maintain either a constant force or constant height above the sample. The surface morphology including rms surface roughness of the InN and GaN layers in this thesis was analyzed using a Dimension 3100 SPM (Veeco, USA) in both contact and non-contact modes.

3.3.4   Field Emission Scanning Electron Microscope (FESEM)

A Field Emission Scanning Electron Microscope (FESEM, FEI) was used to observe the topography and morphology of the InN surface with high resolution. The image is formed in FESEM by scanning an electron beam across a sample and collecting the secondary electron signal from the beam-sample interaction, which is used to control the intensity of the spot on a cathode ray tube which is scanning in synchronization with the beam on the sample.[61] The picture obtained is a plane view from above the sample and looking down on it with highly magnified vision. Tilting of the sample is also possible to obtain a cross-sectional view. Because the probe used for imaging is an electron beam, some interesting contrast mechanisms (and signals) can be produced. The appearance of the image is usually as though the sample was "illuminated" by the detector being used to form the image, up to the point of "shadows" and the like. Dark spots are surface contamination.

3.3.5   X- ray diffraction

X-ray diffraction is a powerful, non-contact method used in order to understand the crystalline phases in bulk materials, thin films and powder samples.[62,63] Additionally, X–ray diffraction can determine the strain state, grain size, epitaxy, phase composition, preferred orientation, and defect structure of individual phases. The principle of this technique involves X-ray waves interacting with atomic planes in materials that will exhibit the phenomenon of diffraction. X-rays scattered off the sample will do so at an equal angle. X-rays scattering off of neighbouring parallel planes of atoms will interfere destructively at a certain angle of

incidence. At other angles, these waves will interfere constructively and result in a large output signal at those angles. These constructive interferences occur when the Bragg condition is met for these X-rays, given by the famous expression:[24,25,62]

$$n\lambda = 2d\sin\theta \qquad (3.11)$$

where n is an integer, λ is the wavelength of the X-ray source, d is the lattice spacing, and θ is the Bragg angle. The reflected diffraction pattern from the epilayer determines the a- spacing and c-spacing lattice constants of a material according to Bragg's law. The line width of a
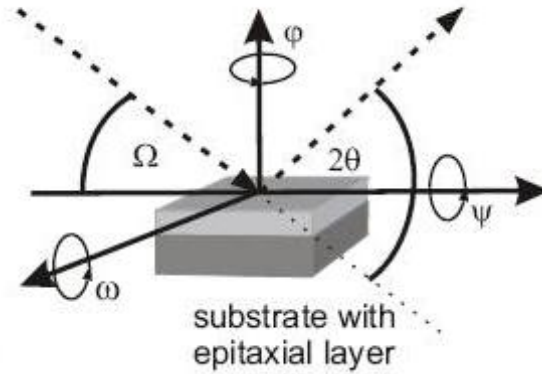
Fig. 3.15: *Defines different angles in XRD measurements*[64].

rocking curve measurement (ω scans) i.e., the full width at half maximum (FWHM), determines the crystalline quality. Different angles are defined in Fig. 3.15. Crystalline quality of thee InN samples have been analyzed using both powder diffraction as well as high resolution XRD. We have used Bruker D8 diffractometer using Cu K_α X-rays for XRD measurements.

3.3.6   Infrared reflection spectroscopy

IR reflectance spectroscopy results are analyzed by introducing an IR dielectric function in order to obtain plasmon properties. The IR dielectric function can be written as (neglecting the phonon contribution)[65],

$$\varepsilon(\omega) = \varepsilon_\infty(1 - \frac{\omega^2}{\omega(\omega + i\gamma)}) \qquad (3.12)$$

where γ is the electron damping due to the scattering from randomly distributed stationary impurities, ω_p is the plasmon frequency and ε_∞ is the dielectric response in the high-energy limit for the film.

Reflectivity of semi-infinite medium can be written as[66],

$$R = \frac{(n-1)^2 + k^2}{(n+1)^2 + k^2} \tag{3.13}$$

Here n is the real part of the refractive index and k is the extinction coefficient. The relation between n and k is given by the complex dielectric function,

$$\varepsilon(\omega) = (n - k)^2 \tag{3.14}$$

where γ is the electron damping constant. It can be seen that using eq.(3.12) and (3.14) we can write,

$$n = n(\omega, \gamma, \omega_p)$$
$$k = k(\omega, \gamma, \omega_p) \tag{3.15}$$

From eq.(3.13) and (3.15) it follows that,

$$R = R(\omega, \gamma, \omega_p) \tag{3.16}$$

Thus, it follows that by fitting eq.(3.16) to the experimental data of one can extract the value of plasma frequency. We have used Reffit open source package to fit the experimentally observed reflectivity spectra to the theoretical model[67]. Infrared reflection measurements were carried out using Perkin Elmer System (Lamda 900) and Bruker IFS 66v/S. The best-fit parameters for the InN film films were obtained using the nonlinear Levenberg-Marquart fitting algorithm which is implemented in Reffit open source package[67].

3.3.7 Transmission spectroscopy

The band gap of InN films grown in this study has been measured through transmission spectroscopy.[68] A Tauc plot[69] is a convenient way of displaying the optical absorption spectrum of a material pioneered by J. Tauc, who proved that momentum is not conserved even in a direct optical transition.[70] Typically, a Tauc plot shows the quantity hv (the energy of the light) on the abscissa and the quantity $(\alpha h v)^r$ on the ordinate, where α is the absorption coefficient of the material.[71] The value of the exponent r denotes the nature of the transition; for example, r = ½ for indirect transitions. The resulting plot has a distinct linear regime which denotes the onset of absorption. Thus, extrapolating this linear region to the abscissa yields the energy of the optical band gap of the material. However, if the material in

question does not have a single phase, it will likely not have a single distinct absorption onset, which corresponds to a more gradually-sloping curve in the Tauc plot.   Room temperature transmission measurements were performed with a Perkin Elmer system with near-infrared-visible-UV spectrometer (Lamda 900) scanning spectral range between 200 nm and 2500 nm. Emission from a mercury lamp source was used to provide the spectral range for the measurements.

3.3.8   Photoluminescence

Photoluminescence (PL) refers to the emission of the light resulting from optical stimulation.[72]   In the PL technique, a suitable laser or filtered light from mercury lamp that has
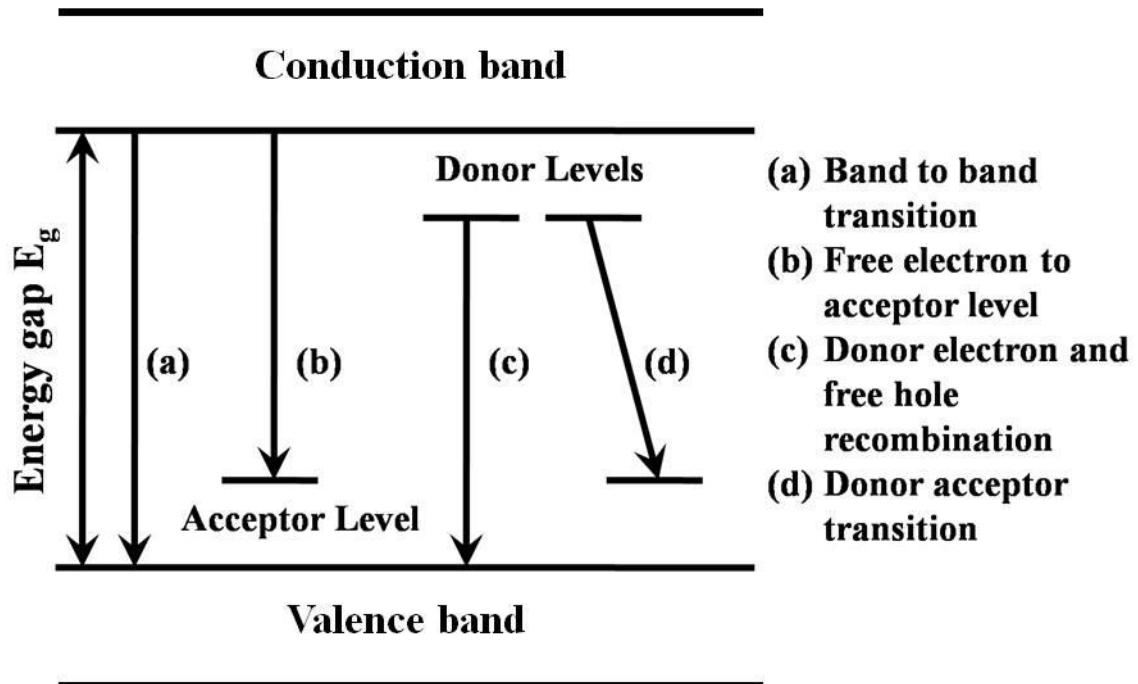
Fig. 3.16: *Different possible transitions during photoluminescence.*

a photon energy output higher than the band gap of the semiconductor is incident on the surface of the sample, which will generate electron hole pairs. Those electron hole pairs will recombine, often through a radiative transition back to the ground state of the atom. Some of the observed recombination pathways are presented in Fig. 3.16. Information about the band structure, donor and acceptor levels, defect types, impurities, crystalline quality, and defect densities in the material system can be extracted by measuring the wavelength of the emitted

photon. We have used Bruker PL system with mercury lamp as the source of light and the required excitation wavelength is generated using optical grating.[73]

3.3.9   Hall Effect – Van-der –Pauv Method

Hall effect measurement is the most widely used method to determine carrier concentrations in semiconductors.[74]   A common geometry used for measurements of the sheet resistance and Hall voltage of a sample, and that used in this work, is the van der Pauw geometry, shown schematically in Fig. 3.17. [75,76]
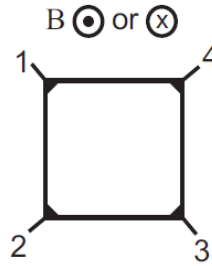
Fig. 3.17: *Preferred geometry for Van der Pauw measurements.*

If a current is passed between contacts 1 and 2, I_{12}, and a voltage measured across contacts 3 and 4, V_{34}, the resistance[77]

$$R_{12,34} = \frac{V_{34}}{I_{12}} \qquad (3.17)$$

Van der Pauw[75,76] showed that, for flat continuous lamina of arbitrary shape, the sheet resistance R_s satisfies

$$\exp(-\pi R_{12,34}/R_s) + \exp(-\pi R_{23,41}/R_s) = 1 \qquad (3.18)$$

allowing the sheet resistance to be determined from simple electrical measurements. From the reciprocity theorem, $R_{12,34} = R_{34,12} = R_{21,43} = R_{43,21}$, and so these quantities can be averaged to yield a much more accurate determination of the sheet resistance, cancelling out any offset voltages. In a similar way, the reciprocity theorem can be used to yield accurate values of the Hall voltage.[77,78] A current can be applied between a set of contacts on opposite corners, for example I_{13}, in the presence of either a positive or negative magnetic field, and a Hall voltage is measured between the other two corners, for example $V_{24}^{\pm}$, where $\pm$ denotes the polarity of the magnetic field. The average Hall voltage is then given from

$$V_H = \frac{V_{13}^+ - V_{13}^- + V_{24}^+ - V_{24}^- + V_{31}^+ - V_{31}^- + V_{42}^+ - V_{42}^-}{8} \qquad (3.19)$$

Using each set of currents and voltages, for the Hall voltage and sheet resistance measurements, it is therefore possible to obtain an accurate value for the sheet density and mobility of the sample.

Hall effect measurements reported in this work were performed using an Ecopia HMS-3000 Hall effect measurement system. Indium contacts are made to the samples in the van der Pauw geometry discussed above. The system includes a 0.58 T permanent magnet, and the polarity of the field is changed by rotating the magnet through 180°. The system can pass a current up to 20 mA. Current-voltage (*I-V*) measurements can also be taken between each set of contacts, and Hall effect measurements were only made if a linear *I-V* curve was obtained, indicating Ohmic contacts had been formed to the material. During measurements, the sample sits in a container that can be filled with liquid nitrogen for performing measurements at 77 K if required.

3.4 Density Functional Theory

In this method, the electron density, which is a functional of the many-body wave-function

$$n(r) = \langle \psi(r) | \psi(r) \rangle \qquad (3.20)$$

is treated as the central variable, rather than the many-body wavefunction itself. Hohenberg and Kohn[79] showed that, for *N* interacting electrons in an external potential, V_{ext}, the external potential, and hence the Hamiltonian and the eigenstate energy is a unique functional of the electron density

$$E[n] = F[n] + \int dr n(r) V_{ext}(r) \qquad (3.21)$$

where *F*[*n*] is a universal functional valid for any number of particles and any external potential. The ground state energy is obtained by minimizing the functional, corresponding to the ground state electron density, $E_0[n_0]$.

Kohn and Sham[80] (KS) separated the functional *F*[*n*] into three parts to account for the kinetic energy of a non-interacting electron gas, and the Hartree (Coulomb) and exchange-correlation (XC) effects of the electron-electron interaction. They showed that the ground state energy could be obtained by solving *N* one-electron Schrödinger-like equations, self-consistently with the charge density. The Hamiltonian of the one-electron equations is of the form of Schrödinger equations but with the potential replaced by an effective KS potential

including Hartree and XC parts. Therefore, while the individual solutions do not include inter-particle interactions (one-electron approximation), the KS particles do interact indirectly via the density dependence of the Hartree and XC parts of the potential within a mean-field approximation.

The theory discussed above is exact. However, the functional for XC is not known for all but a few simple situations (such as a homogeneous free-electron gas). A common approximation, the local density approximation (LDA), is therefore to approximate this functional by the energy of an electron in a uniform electron gas of the same density. Another approach, the generalized gradient approximation (GGA), also includes the gradient of the density in the calculation. In the present study, we have used Quantum Espresso[81] open source package which implements DFT by expanding wave function using plane waves and the code uses pseudopotentials.

References

[1] A. Roath, Vacuum Technology, Elsevier Sci. Phublisher B. V. Sara Burgerhartstraat, Netherland (1982).

[2] Y. Enta, S. Suzuki, S. Kono, and T. Sakamoto, Phys. Rev. B **39**, 56 (1989).

[3] G.S. Higashi, Y.J. Chabal, G.W. Trucks, and K. Raghavachari, Appl. Phys. Lett. **56**, 656 (1990).

[4] D. Briggs and M. P. Seah, Practical Surface Analysis By Auger and X-ray Photoelectron Spectroscopy, 2nd Edition, John Wiley and Songs, Ltd, Chichester, UK (1990).

[5] D Briggs and J. T. Grant, Surface Analysis By Auger and X-ray Photoelectron Spectroscopy, Comwell Press, Trowbridge, UK (2003).

[6] A. Zangwill, Physics at Surfaces, Cambridge University Press, Cambridge (1990).

[7] P. Auger, J. Phys. Radium **6**, 205 (1925).

[8] J. J. Lander, Phys. Rev. **91**, 1382 (1953).

[9] G. Ertl and J. Kuppers, Verlag Chemie, GmbH, Weinbeim (1974).

[10] I. F. Ferguson, Auger Micro Probe Analysis, IOP Publishing, New York (1989).

[11] P. W. Palmberg, Handbook Of Auger Electron Spectroscopy, Physical Electronics Industries (1972).

[12] F. C. Frank and J. H.V. Merwe, Proc. Roy. Soc. London A **198**, 205 (1949).

[13] J. W. Evans, P. A. Thiel, and M. C. Bartelt, Surf. Sci. **61**, 1 (2006).

[14] C. Argile and G. E. Rhead, Surface Science Reports **10**, 277-356 (1989).

[15] R. J. Nicholas, E. Bunge, H. Meyer, and H. Baumgartl, Surf. Sci. **335**, 110 (1995).

[16] S. Tanuma, C. J. Powell, and D. R. Penn, Surf. Interf. Anal. **21**, 165 (1993).

[17] S. Tougaard, Copyright (c) 2000-2002 Quases-Tougaard Inc. (n.d.).

[18] J. B. Pendry, Low Energy Electron Diffraction, Academic Press, London (1974).

[19] M. A. V. Hove, W. H. Weinberg, and C. M. Chan, Low-energy Electron Diffraction: Experiment, theory and Surface Structure Determination, Springer-Verlag, (1986).

[20] M. A. Van Hove, W. H. Weinberg, and C. M. Chan, Low Energy Electron Diffraction, Springer-Verlag, Berlin (1986).

[21] P. M. Marcus and F. Jona, Determination Of Surface Structure By LEED, Plenum Press, New York and London (1984).

[22] D. P. Woodruff and T. A. Delchar, Modern Techniques Of Surface Science, 2nd Edition Cambridge University Press, Cambridge (1990).

[23] R. Brydson, Electron Energy Loss Spectroscopy, Bios In association With the Royal Microscopical Society **48**, (2001).

[24] Charles Kittel, Introduction To Solid State Physics, 7th Ed., Wiley (1996).

[25] N. W. Ashcroft and N. D. Mermin, Solid State Physics, Saunders (1976).

[26] S. Hufner, Photoelectron Spectroscopy: Principles and Applications, 3rd Edition Springer Verlag, Berlin, (2003).

[27] M. Prutton, Introduction To Surface Physics, Oxford Science Publications, Clarendon Press (1994).

[28] K. Siegbahn, Philos. T . Roy. Soc. A **268**, 33 (1970).

[29] H. Luth, Surface and Interface Of Solid Materials, 3rd Edn, Springer Verlag, Berlin (1996).

[30] C. D. Wagner, W. M. Riggs, L. E. Davis, J. F. Moulder, and G. E. Muilenberg, Handbook Of X-Ray Photoelectron Spectroscopy, PerkinElmer Corp., Eden Prairie, MN, (1979).

[31] J. F. Watts and J. Wolstenholme, An Introduction To Surface analysis By XPS and AES, J. Wiley (2003).

[32] B.L.Maschhoff, J. Vac. Sci. Technol. A (1988).

[33] S.A. Richardson, with J.E.Castle and I.Abu-Talib, Mater. Res. Soc. Symp. Proc. **48**, 471 (1985).

[34] D.A. Shirley, Phys. Rev. B **5**, 4709 (1972).

[35] S. Tougaard and B. Jorgensen, Surf. Sci. **143**, 482 (1984).

[36] S. Tougaard, J. Vac. Sci. Technol. A **8**, 2197 (1990).

[37] R. O. Ansell, T. Dickinson, A. F. Povey, and P. M. A.Sherwood, J. Electroanal. Chem. **98**, 79 (1979).

[38] C. S. Fadley, J. Electron. Spectroscopy Rel. Phenom. **178-179**, 2 (2010).

[39] G. Binnig and H. Rohrer, Helv. Phys. Acta. **55**, 726 (1982).

[40] G. Binnig and H. Rohrer, Surf. Sci. **152/153**, 17 (1985).

[41] R.J. Hamers, R.M. Tromp, and J.E. Demuth, Phys. Rev. Lett. **56**, 1972 (1986).

[42] D.M. Eigler and E.K. Schweizer, Nature **344**, 524 (1990).

[43] M. Froment, C.P. Lutz, and D.M. Eigler, Science **262**, 218 (1993).

[44] L.J. Whitman, J.A. Stroscio, R.A. Dragoset, and R.J. Celotta, Science **251**, 1206 (1991).

[45] M. Pratzer, H.J. Elmers, M. Bode, O. Pietzsch, A. Kubetzka, and R. Wiesendanger, Phys. Rev. Lett. **87**, 127201 (2001).

[46] O. Pietzsch, A. Kubetzka, M. Bode, and R. Wiesendanger, Science **292**, 2053 (2001).

[47] A. Wachowiak, J. Wiebe, M. Bode, O. Pietzsch, A. Kubetzka, M. Morgenstern, and R. Wiesendanger, Sciencei **298**, 577 (2002).

[48] R. Wiesendanger, Scanning Probe Microscopy and Spectroscopy: Methods and applications, Cambridge University Press, New York (1994).

[49] R. Wiesendanger and H.-J. Güntherodt, Scanning Tunneling Microscopy III: Theory Of STM and Related Scanning Probe Methods, Springer-Verlag, New York (1996).

[50] H.-J. Güntherodt and R. Wiesendanger, Scanning Tunneling Microscopy I: General Principles and applications To Clean and adsorbate-covered Surfaces, Springer-Verlag, New York (1992).

[51] R.H. Fowler and L. Nordheim, Proc. Roy. Soc. London A **119**, 173 (1928).

[52] A.Y. Cho, M.B. Panish, and I. Hayashi, 3rd Int. Symp. On Gallium Arsenide and Related Compounds, The Institute Of Physics, Conference Series **9**, 18 (1970).

[53] J.E. Davey and T. Pankey, J. Appl. Phys.. **39**, 1941 (1968).

[54] H. Shelton and A.Y. Cho, Appl. Phys. Lett.p **37**, 3544 (1966).

[55] J.R. Arthur Jr, J. Appl. Phys. **39**, 4032 (1968).

[56] A. Cho, Molecular Beam Epitaxy, American Institute Of Physics (1994).

[57] F. Rinaldi, Basics Of Molecular Beam Epitaxy (MBE), Http://www-opto.e-technik.uni-ulm.de/forschung/jahresbericht/2002/ar2002_fr.pdf (n.d.).

[58] W. Braun, Applied RHEED. Springer, New York (1999).

[59] A. Ichimiya and P. I. Cohen, Reflection High Energy Electron Diffraction, Cambridge University Press (2004).

[60] Franz J. Giessibl, Rev. Mod. Phys. **75**, 949 (2003).

[61] G. I. Goldstein, D. E. Newbury, P. Echlin, D. C. Joy, C. Fiori, and E Lifshin, Scanning Electron Microscopy and X-ray Microanalysis. New York: Plenum Press. (1981).

[62] S. L. Chang, X-ray Multiple-wave Diffraction: Theory and application, Springer-Verlag Berlin Heidelbergy (2004).

[63] A. Authier, Dynamical theory Of X-ray Diffraction, Oxford University Press Inc. New York (2002).

[64] High Resolution X-ray Diffraction, Www2009.ph.tum.de, HRXRD Userguide (2009).

[65] M. Born and E. Wolf, Principles Of Optics, Pergamon Press (1968).

[66] C. Wetzel, E. E. Haller, H. Amano, and I. Akasaki, Applied Physics Letters **68**, 2547 (1996).

[67] A. Kuzmenko, Http://optics.unige.ch/alexey/reffit.html (n.d.).

[68] O. Stenzel, The Physics Of Thin Film Optical Spectra: An Introduction 214 (2005).

[69] J. Tauc, Mater. Res. Bull. **3**, 37 (1968).

[70] J. Tauc, R. Grigorovici, and A. Vancu, Phys. Status. Solidi **15**, 627 (1966).

[71] D. B. Buchholz, J. Liu, T. J. Marks, M. Zhang, and R. P. H. Chang, ACS App. Mater. Int. **1**, 2147 (2009).

[72] S. Perkowitz, Optical Characterization Of Semiconductors: Infrared, Raman, and Photoluminescence Spectroscopy (Techniques Of Physics), Academic Press (1993).

[73] B. Monemar, Mater. Sci. Eng. B **59**, 122 (1999).

[74] E. Hall, American J. Math. **2**, 287 (1879).

[75] L. J. Van der Pauw, Philips Res. Rep. **13**, 1 (1958).

[76] L. J. Van der Pauw, Philips Tech. Rev. **20**, 220 (1958).

[77] S. M. Sze, Semiconductor Devices: Physics and Technology. New York: Wiley 53 (2001).

[78] H. A. Lorentz, Amsterdammer Akademie Der Wetenschappen **4**, 176 (1896).

[79] P. Hohenberg and W. Kohn, Phys. Rev. **136**, B864 (1964).

[80] W. Kohn and L. J. Sham, Phys. Rev. **140**, A1133 (1965).

[81] Espresso, Quantum, Http://www.quantum-espresso.org/ (n.d.).

Chapter IV

Initial stages of growth of Al and Ga on Si(111)-7x7 and Si(5 5 12)-2x1 surfaces

In this chapter, results of the systematic adsorption/desorption studies of Al and Ga on low index Si(111)-7x7 surface and high index Si(5 5 12)-2x1 surface are described. We carry out experiments *in-situ* in UHV and follow the surface compositional and structural evolution using AES and LEED as surface sensitive chemical and structural probes. Growth modes of the systems are analyzed and their thermal stability is evaluated. Comprehensive coverage versus temperature phase diagrams showing the superstructural phases for Al/Si(111) and Ga/Si(111) are presented.

4.1. Adsorption/desorption of Al on Si(111)-7x7 surface

4.1.1 Introduction

Recently there is overwhelming interest in the study of group III elemental adsorption on Si surfaces especially Si(111)7x7 reconstructions which shows the formation of ordered assembly of metal nanostructures such as 1D nanowires, which are not only promising for miniaturization of devices but also to a host of interesting 1D physics. Al/Si(111)-7x7 system, had been first analyzed by Lander and Morrison who observed several super-structural phases using LEED.[1] Later the studies have been mainly focused on the structure of the different phases, though a full understanding has been achieved only for the √3x√3 reconstruction. With the advent of advanced structural probes like STM, these systems have been revisited and the main force has been to understand the structural properties of the different phases observed.[2-8] We find that the studies concerning the initial stages of growth of Al on Si surfaces have been lacking in the literature and a few studies which aim at understanding the initial stages of growth of Al on Si(111)7x7 surfaces show ambiguity concerning the growth mode.[9] Thus, the present study aims at carrying out a systematic adsorption study of Al on Si(111)7x7 surface in Ultra

High Vacuum using *in-situ* AES and LEED to understand the interface structural and morphological evolution. We study the growth mode of Al on Si(111)7x7 surface using experimental uptake curve and compare it with theoretical simulation. We also look at the residual thermal desorption behavior of adsorbed Al adlayer to understand the kinetics of the Al adatoms on the surface.

4.1.2   Room temperature adsorption

Fig. 4.1 shows the uptake curve for Al/Si(111)7x7 systems with the substrate kept at Room Temperature (RT). The graph shows the plot of Auger intensity ratio of Al LVV (68eV)
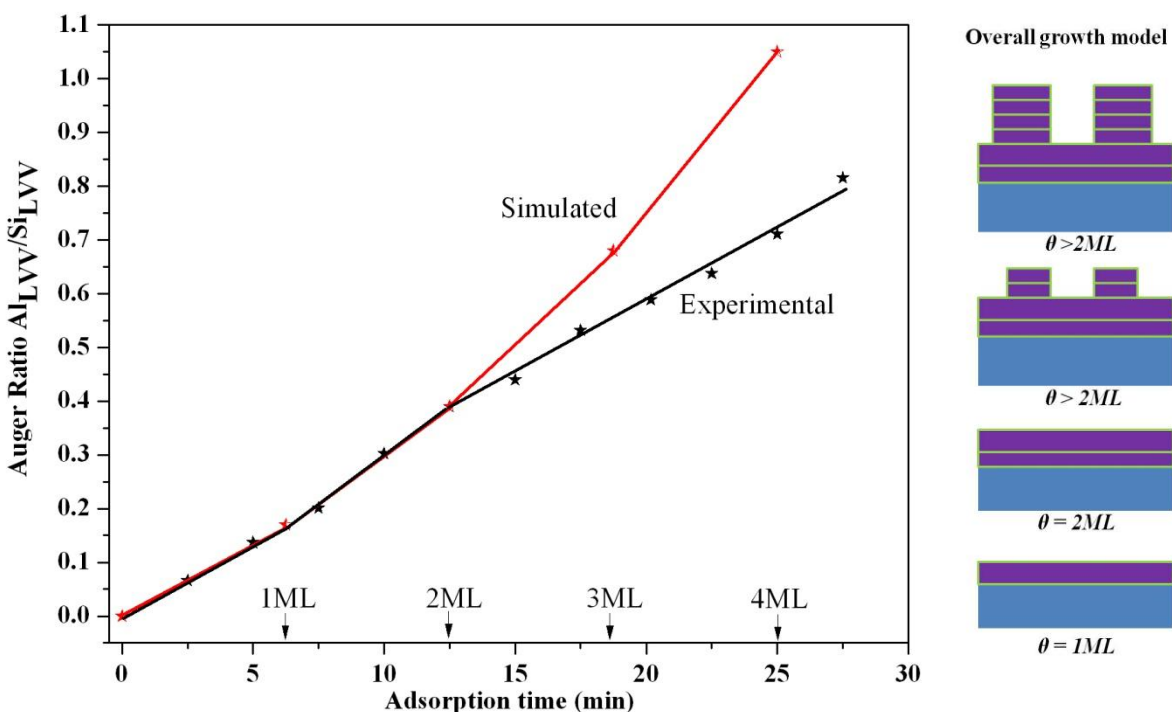
Fig. 4.1: *Room temperature uptake curve for Al/Si(111) system. Auger intensity ratio of Al LVV (68eV) and Si LVV (92eV) is plotted versus deposition time. A schematic of the growth mode for RT adsorption is shown on the right side.*

signal to Si LVV (92eV) peak versus deposition time. We observe that initially Auger intensity increases linearly with deposition of Al on the surface, showing the formation of uniform layer of Al on the surface. We observe a deviation of this linear behavior above ~6 min of adsorption.

Above this point the slope of the uptake is larger than that of the first segment of the uptake curve. Following the well accepted analysis of Auger uptake curve,[10,11] this change in slope corresponds to the formation of 1ML of Al on the surface. Above this break point the uptake curve shows (Fig. 4.1) a linear segment with higher slope showing the formation of second uniform monolayer on the surface. The curve shows another break around ~12min of adsorption, which shows the completion of second monolayer on the surface, and as per the calibration of coverage given by the first break, it corresponds to 2 flat layers of Al on the surface. Above 2ML, we see another break in the curve shown in Fig. 4.1 and the intensity ratio monotonically increases with further adsorption of Al on the surface without any break points. We note that the slope of this part of uptake curve (>2ML) is less than the previous segment of the uptake curve. This shows that above 2ML there is a deviation from layer by layer growth and there is the formation of islands on the surface. The adsorption process is accompanied by the observation of surface symmetry using LEED. As the Al atoms are adsorbed on the surface, the intensity of the fractional spots of 7x7 LEED pattern shown in Fig. 4.2(a) diminishes and we observe the α7x7 pattern shown in Fig. 4.2(b). 7x7 pattern is observed up to a coverage of 0.1ML and above which α7x7 pattern is evident. It has been reported in the literature that α7x7 persist up to about 1ML or about 2ML of adsorption of Al on the Si(111) surface.[7] There is an ambiguity concerning the coverage at which α7x7 converts to 1x1 pattern shown in Fig. 4.2(g). We observe that the α7x7 phase persists above 2ML of adsorption of Al, which is not to be expected if Al grows as a layer by layer above 2ML. Thus as seen by the uptake curve, there is a deviation of layer by layer growth above 2ML of adsorption of Al on the surface. To understand the surface evolution above 2ML we carry out uptake simulation for Al/Si(111) system.

4.1.3   Uptake simulation

Taking into account various factors governing the Auger electron emission, the intensities of the Auger emission from the adsorbate and the substrate for a fractional coverage of the adsorbate is given by the following expressions[12,13],

$$I_B = I_B^\infty \left\{ 1 - \phi_A + \phi_A \exp\left[\frac{-a_A}{\lambda_A(E_B)\cos\theta} \right] \right\}$$

(4.1)

$$I_A = \phi_A I_A^{\infty} \left[\frac{1 + r_B(E_A)}{1 + r_A(E_A)} \right] \left\{ 1 - \exp\left[\frac{-a_A}{\lambda_A(E_A)\cos(\theta)} \right] \right\} \tag{4.2}$$

where A and B subscripts respectively represent substrate and overlayer, and the parameters are:

I = Intensity of Auger signal

I^{∞} = Intensity from a semi-infinite film

φ = coverage

a = monolayer thickness of overlayer

λ = Inelastic mean free path

r = Back scattering factor

θ = Analyzer acceptor angle

For calculating inelastic mean free path we have used Tanuma-Powel TP2 formula and for backscattering factor we have used formulae from Ref[14,15]. We have calculated the Auger intensity ratios of Al LVV (68eV) and Si LVV (92eV) signals from the above expressions at the completion of different coverages like, 1ML, 2ML, etc., which is plotted in Fig. 4.1 along with the experimental uptake curve.[16] It can be seen that up to 2ML there is a good agreement between the calculated and the theoretical curve, whereas above 2ML the experimental curve deviates from that of the simulated curve. This means that above 2ML, there is a deviation from that of perfect layer by layer growth mode. Since above 2ML Al starts clustering, we try to understand further by simulating the island morphology above 2ML by calculating the island height and area covered by islands above 2ML.

For the case of substrate covered by a full monolayer the intensities of Auger emission from the adsorbate and the substrate can be written as:

$$I_B = I_B^{\infty} \left\{ \exp\left[\frac{-d_A}{\lambda_A(E_B)\cos\theta} \right] \right\} \tag{4.3}$$

$$I_A = I_A^{\infty} \left[\frac{1 + r_B(E_A)}{1 + r_A(E_A)} \right] \left\{ 1 - \exp\left[\frac{-d_A}{\lambda_A(E_A)\cos(\theta)} \right] \right\} \tag{4.4}$$

where, the parameters are described above.

For given island height and the total area carried by island, we can write the Auger intensity ratio as:

$$\frac{I_A}{I_B} = f(h, \phi) \quad \rightarrow \quad \theta_o = h\phi \tag{4.5}$$

Thus, by knowing the ratio of the intensities of the Auger emission from the experiment and the coverage from the auger uptake curve, we can calculate the island height and the total area covered by the islands using equations (4.1) to (4.2). Fig. 4.1 shows the results of the calculations where the island height above 2ML and the total area covered by the island above 2ML are plotted versus coverage above two flat layers of Al adatoms. We observe that both the area covered by islands as well as the height of the islands increases above 2ML as the coverage increases. It is clear that, though the uptake curve do not get saturated at 2ML there is a large fraction of uncovered area above 2ML at higher coverages. This corroborates with the observation of LEED pattern which shows the reflection from the α7x7 surface even at higher coverages.

The results of the room temperature adsorption of Al on Si(111)7x7 surface can be summarized by the schematic analysis of the surface morphology shown in Fig. 4.1. When we adsorb Al on the surface, the first two layers grows in the layer by layer growth mode resulting in two flat layers of Al on the surface. When the coverage is increased above 2ML the Al adatoms starts clustering to from Al islands on the surface. With increase in coverage above 2ML, Al islands starts growing in its size as well as height. Thus, the growth of Al islands on the Si(111) surface follows 2ML – Stranski – Krastanov growth mode where the formation of islands takes place above two flat layers of Al.

4.1.4   Residual thermal desorption

Fig. 4.3 shows the results of residual thermal desorption of Al on the Si(111)7x7 surface. In residual thermal desorption a certain coverage of Al on the surface is annealed at different temperatures for fixed intervals of time and after each stage of annealing the residual Al present on the surface in analyzed using AES and LEED. Fig. 4.3 shows desorption curves for Al

adsorbed at room temperature, having different initial coverages on the surface. The graph shows the ratio of Auger intensities of Al LVV (68eV) to the Si LVV (92eV) peak plotted versus annealing temperature.   Curve 4.3 (a) shows the desorption curve for an initial coverage of about
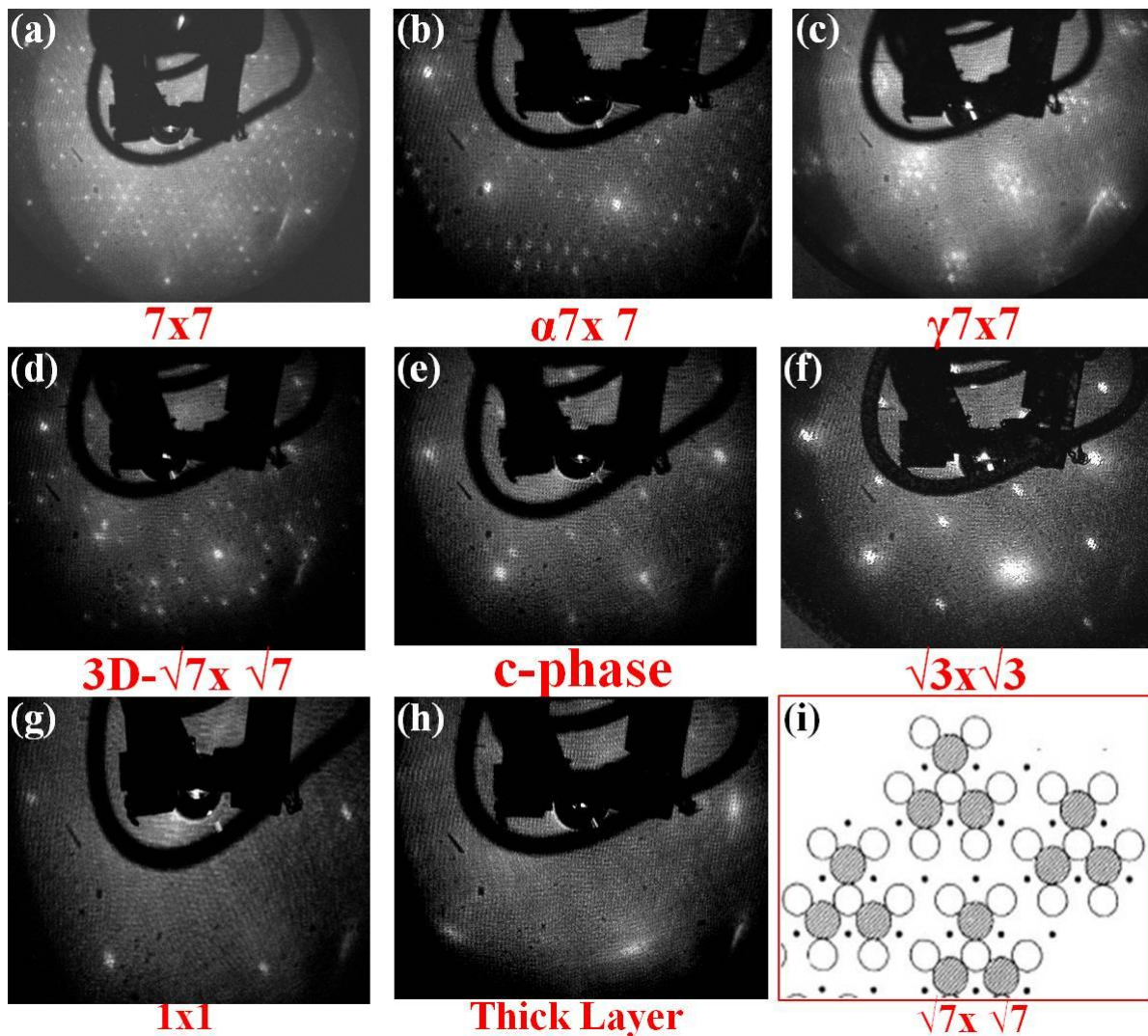
Fig.4.2: *LEED patterns of different superstructural phases observed during adsorption/desorption studies. Structural model for √7x√7 pattern from literature is also shown*[17].

4ML of Al on the surface and the LEED shows 1x1 pattern suggesting the pseudomorphic adsorption of Al adatoms on the surface . For a mild annealing up to 100°C the ratio shows a flat regime, with no appreciable variation of Auger intensity ratio, indicating that the surface

morphology remains essentially the same with the increase of temperature. As seen in the uptake curve, at room temperature the initial surface morphology consists of 2ML of flat islands with large Al islands on top of it. As the diffusion of large clusters are necessary here for agglomeration of Al adatoms, which requires high substrate temperature, the surface morphology remains same without appreciable change in the temperature range <100°C. With increase in temperature beyond this flat region of the desorption curve (>100°C), the intensity ratio monotonically decreases, showing agglomeration of Al on the surface which reduces the Auger intensity from the Al islands and increases the Auger signal from the substrate thereby reducing the Auger intensity ratio. This is also evident from the LEED observation which shows a 1x1+1x1shown in Fig. 4.5(a) pattern where the second reflection comes from the agglomerated Al adatoms showing the formation of islands on the surface. For temperatures higher than 600°C the desorption curve is quite flat showing very less slope compared to the previous region of the desorption curve showing strong bonding of the adsorbate to the surface. This regime also shows desorption of Al from the surface. In this region we observe several superstructural phases that show strong bonding to the substrate and thus desorbs hierarchically with increase in temperature. The different reconstructions observed in the regime from 500°C to ~ 800°C are γ7x7, c-phase, √7x√7 and √3x√3 phase which are shown in Fig. 4.2(c), (e), (d) and (f) respectively. Only √3x√3 is well understood in terms of its structure which was previously described in Chapter 2. A structural model for √7x√7 is shown in Fig. 4.2(i) where Al adatoms are shown to occupy three T_4 sites forming trimers.[17]   Above 800°C Al desorbs completely from the surface showing clean Si(111)7x7 pattern (Fig. 4.2(a)).

Desorption curve (b) shown in Fig. 4.3 correspond to about ~ 2ML of Al adsorbed at room temperature on the Si(111)-7x7 surface. Here the initial surface morphology prior to desorption consists of two flat layers of Al on the surface. When the temperature is increased the Auger intensity ratio monotonically decreases up to a temperature of 350°C showing the agglomeration of Al adatoms. At this temperature (350°C) the intensity ratio corresponds to a coverage of about 0.75ML, which remains the same up to temperature of about 600°C. Thus, it is clear that the initially adsorbed 2ML of Al adatoms agglomerate above 0.75ML of Al adlayer. This is also well corroborated with the higher substrate temperature adsorption studies, to be

discussed later, which shows a saturation of uptake above 0.75ML for adsorption at high temperatures. In this region the LEED pattern shows a α7x7 pattern. Above 600°C the
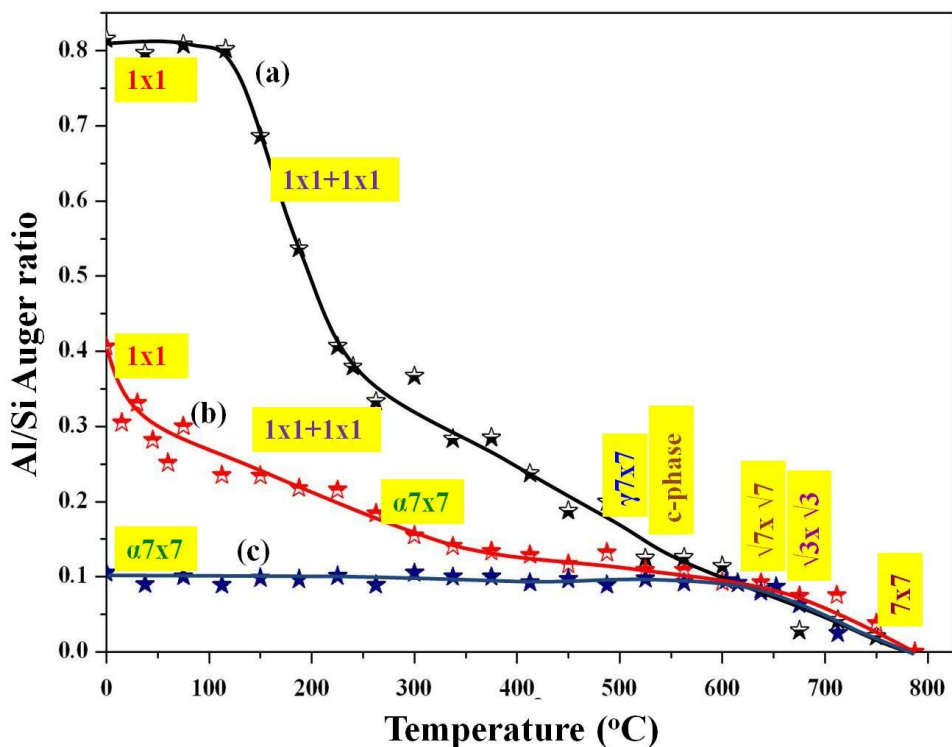
Fig. 4.3: *Residual thermal desorption curve for room temperature adsorbed Al for different initial coverages. Auger intensity ratio of Al LVV (68eV) and Si LVV (92eV) is plotted versus annealing temperature.*

desorption curve (b) shown in Fig. 4.3 matches with curve (a) shown in Fig. 4.3 (a) and manifests different superstructural phases discussed above.

Desorption curve (c) shown in Fig. 4.3 corresponds to that of 0.5ML of RT adsorbed Al on the surface. The surface morphology in this case consists of partially covered 2D layer of Al on the Si(111) surface, before the onset desorption process. Intensity ratio shows a flat region up to a temperature of about 600°C. We observe that surface morphology remains essentially the same in this temperature range showing no appreciable variation in the Auger intensity ratio, as the adsorbate being strongly bonded to the surface does not undergo any agglomeration. As in the previous case the region beyond 600°C is common for all the cases where the surface

undergoes several structural changes causing different reconstructions and the intensity ratio gradually reduces owing to the desorption of Al from the surface.

4.1.5   High temperature adsorption

Fig. 4.4 shows the results of adsorption studies carried out at different substrate temperatures. For comparison, the RT uptake curve is also shown in the figure. The graph shows the plot of ratio of Auger intensities of Al LVV (68eV) to Si LVV (92eV) versus deposition time. Curve (b) in Fig. 4.4 shows the uptake curve for a substrate temperature of
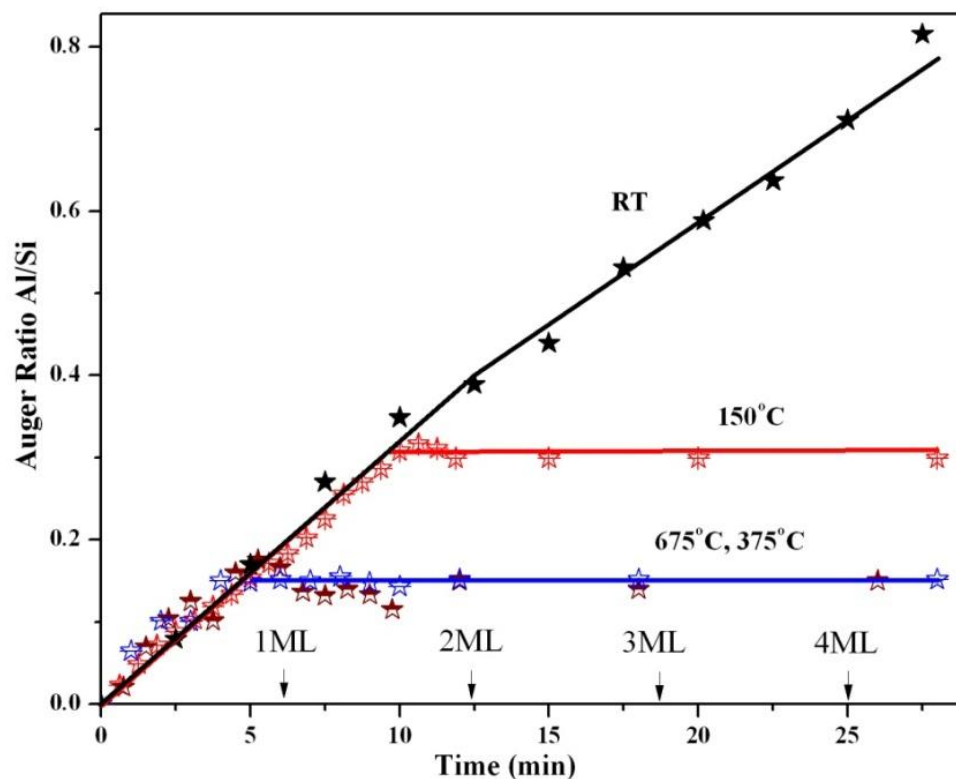
Fig. 4.4: *Uptake curve of Al/Si(111) system for different substrate temperatures. Auger intensity ratio of Al LVV (68eV) and Si LVV (92eV) is plotted versus deposition time.*

150°C. This uptake curve shows a linear rise in the intensity ratio up to about 9min of adsorption. The break point which is prominent in the case of RT adsorption is very weak in this case. The curve saturates at an intensity ratio of about 0.3 which corresponds to about ~1.5ML and further adsorption of Al beyond 9min, does not bring any change in the uptake curve. It can

be understood that at this temperature the first layer grows as a uniform flat layer and above this layer only about 0.5ML Al is grown as 2D layer. Before the completion of the second monolayer, islands form on the surface resulting in a saturated region of the uptake curve. Thus at 150°C Al follows SK growth mode and there is formation of islands above partially covered second monolayer. We have followed the structural changes on the surface at different stages of adsorption process using LEED. We observe that up to about 0.1ML of Al adsorption the fractional spots of 7x7 spots show reduction in intensity and beyond 0.1ML, α7x7 pattern is observed. The formation of islands above 1ML is well corroborated with the LEED observation which show 1x1+1x1 pattern shown in Fig. 4.5(a), where the second 1x1 reflection comes from the relaxed Al islands.
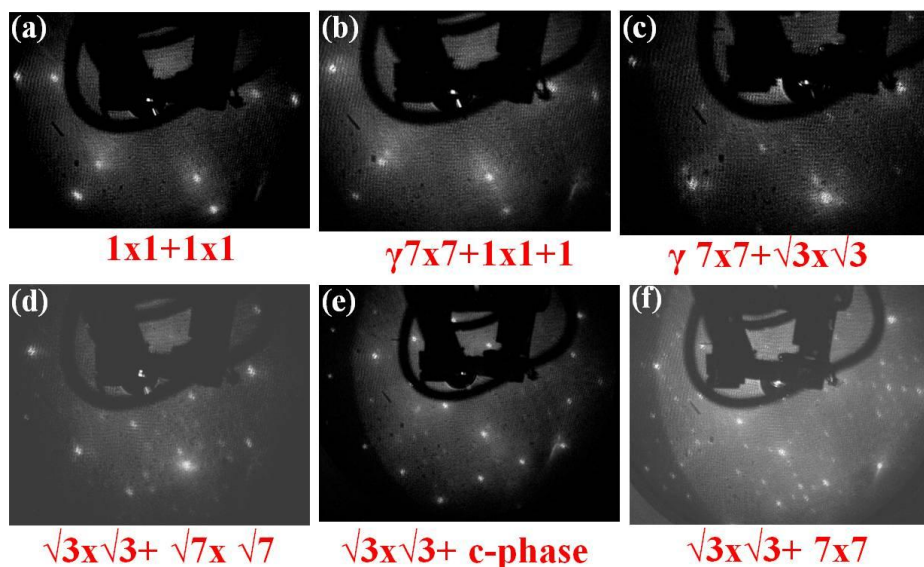
Fig.4.5: *LEED pattern of different mixed superstructural phases observed during adsorption/desorption studies.*

In Fig. 4.4 curve (c) shows the uptake curve for high temperature adsorption carried out at a temperature of 375°C. In this case, the uptake curve shows a linear rise up to a ratio of 0.17 which corresponds to a coverage of 0.75ML on the surface. Beyond this coverage the intensity ratio remains the same with further adsorption of Al on the surface. As the desorption of Al from the surface is negligible at this temperature the flat region can be attributed to the formation of islands on the surface. Thus, we observe that at this temperature the formation islands takes

place even at very less coverages compared to the adsorption at substrate temperature of 150°C. The growth mode here consists of islands on top of 0.75ML of Al. At this temperature as seen in the previous case of adsorption, at about 0.1ML of adsorption 7x7 pattern converts into α7x7 pattern. At about 0.17ML we observe 1x1+1x1 which is in accordance with the Auger uptake curve at this temperature (375°C) which shows island formation on the surface.

Fig. 4.4(d) shows the adsorption uptake curve corresponding to a considerably higher substrate temperature of about 675°C. Here the uptake curve is similar to that of adsorption carried out at substrate temperature of 375°C. However, there is a prominent difference in the surface structure observed on the surface at this adsorption temperature. Uptake shown in Fig. 4.4(d) shows a linear rise up to a coverage of 0.75ML followed by a flat portion showing no appreciable change in the intensity ratio. Thus, there is 2D growth of Al on the surface up to a coverage of 0.75ML. Saturation in the uptake curve in this case cannot be fully ascribed to the formation of islands on the surface as at this temperature Al desorption also starts from the surface as is evident from the desorption curve discussed previously. Moreover, we do not observe 1x1+1x1 diffraction pattern in the saturated region of the uptake which would have present if island growth takes place. In the flat region we observe γ7x7 pattern LEED which is shown in Fig. 4.2(c). Thus, this flat portion of the uptake curve can be attributed to the lesser sticking coefficient of Al on 1ML Al the surface at this higher substrate temperature (675°C). In the region 0-0.75ML at this temperature, LEED shows progressive appearance of 7x7-√3x√3-√7x√7-c-pahse and γ7x7 shown in Fig. 4.2(a), (f), (d), (e) and (c) respectively. Though the overall trend of the uptake curve remains the same, but the surface structure is markedly different for the case of 675°C when compared to 375°C owing to the difference in kinetics of growth of the adatoms at these temperatures.

4.1.6   Phase diagram

The consolidation of the results of the different adsorption desorption process employed in the study is shown in Fig. 4.6 as a 2D phase diagram, which shows the coverage and temperature of occurrence of different phases observed in the case of Al/Si(111) system. In constructing the phase diagram we have considered the results of adsorption/desorption studies performed for various coverages and temperatures. In the phase diagram y-axis represents the

temperature range of occurrence and x-axis the ratio of Auger intensities of Al LVV (68eV) to Si LVV (92eV) peak. As discussed previously, we observe several superstructural phases viz. 7x7, $\sqrt{3}x\sqrt{3}$, $\sqrt{7}x\sqrt{7}$,c-phase, γ7x7, α7x7 and 1x1+1x1 shown in Fig. 4.2. In phase diagram, 7x7 phase shown in Fig. 4.2(a) extends up to a coverage range of 0-0.1ML for different temperatures. α7x7 phase shown in Fig. 4.2(b) is observed for a broad coverage range of 0.1 to 1.75ML and
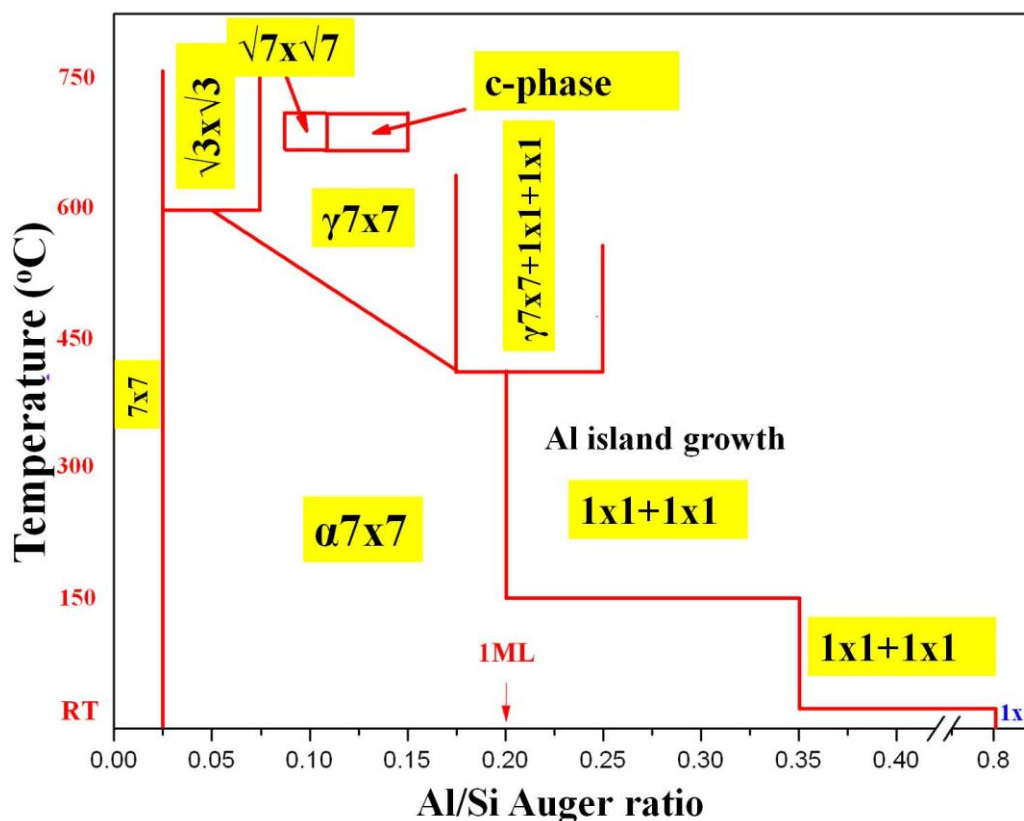
Fig. 4.6: *Phase diagram of Al/Si(111) system. Y-axis represents the temperature and x-axis is Auger intensity ratio of Al LVV (68eV) and Si LVV (92eV) signals.*

temperature range of RT-600°C. In the temperature range of RT-150°C the phase occupies a coverage range of 0.1 to 1.75ML and for higher temperatures (>150°C), the phase is observed only up to 1ML of Al on the surface. One of the interesting phases that has caught attention of researchers is the γ7x7 shown in Fig. 4.2(c), whose structure and periodicity is still ambiguous in the literature.[9] We have carried out several analysis using intensity line scan of LEED images from different adsorption/desorption experiments and for different energies to find the

periodicity to be eight for this phase. Fig. 4.7 shows a representative line scan of the LEED image this phase. We have calculated the separation between the bulk related spots and that between the fractional order spots. Averaged value over several LEED images show that the separation between the fraction order spots is $1/8^{th}$ of that of separation between bulk spots giving a periodicity of 8 for $\gamma 7 \times 7$ phase.

The structural and electronic properties of the $\sqrt{3}\times\sqrt{3}$ shown in Fig. 4.2(f) has been well established in the literature for group III adsorbates on Si(111)-7x7 surface. We have observed the phase in the case of adsorption at high temperature as well as during desorption studies where the phase appears just prior to the complete desorption of Al from the surface. The phase is observed in a temperature range of 600°C to 700°C and for at a coverage of ~0.33ML of Al. The $\sqrt{7}\times\sqrt{7}$ phase shown in Fig. 4.2(d) is only observed in a very narrow temperature and coverage range. We have observed 3D-$\sqrt{7}\times\sqrt{7}$ (3 domain) phase where reflections from different domains on the surface superimpose to give the LEED pattern. The phase appears at a temperature of ~650°C and coverage of 0.5ML of Al. Another interesting phase that we have observed is the complex c-phase shown in Fig. 4.2(e). The phase has only been reported for the case of adsorption on vacuum cleaved Si(111)-2x1 surface and there are no previous report of observation of the phase on Si(111)-7x7 surface. With systematic and careful studies we are able to observe the phase in the case of Al adsorption on Si(111)-7x7 surface. As seen in the phase diagram, the phase only appears in a very narrow range of coverage and temperature. The growth of Al islands on the surface is seen by LEED as 1x1+1x1 pattern where the second 1x1
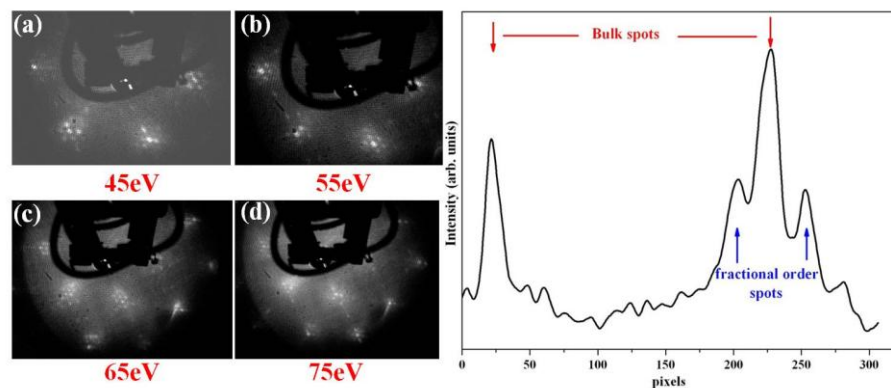
Fig. 4.7: *LEED pattern for γ7x7 phase taken at different e⁻ beam energy. The right panel shows the intensity line scan of the LEED spots.*

reflections comes from the relaxed Al islands. At low substrate temperatures ($<150^{o}$C) island growth is observed above 1.75ML and for higher substrate temperatures the phase appears at a much lower coverage of ~1ML, as higher substrate temperature results in diffusion of adatoms resulting in agglomeration and island formation. For a thick amorphous layer deposition, the LEED shows a characteristic ring pattern shown in Fig. 4.2(h) corresponding to an amorphous surface. The region between transition from one phase to another is marked by the observation of different mixed phases comprising of reflections from pure phases. We have observed 1x1+1x1, γ7x7+1x1+1x1, γ7x7+$\sqrt{3}$x$\sqrt{3}$, $\sqrt{3}$x$\sqrt{3}$+ $\sqrt{7}$x$\sqrt{7}$x, $\sqrt{3}$x$\sqrt{3}$+c-phase and 7x7+$\sqrt{3}$x$\sqrt{3}$ whose LEED pattern are shown in Fig. 4.5 and consolidated in the 2D phase diagram in Fig. 4.6.

4.2   Adsorption/desorption of Al on Si(5 5 12)-2x1 surface

4.2.1. Introduction

Si(5 5 12) surface forms an high index surface which is endowed with several trenches and grooves and thus can serve as a template to grow ordered assembly of nanowires of metal adsorbates. The main characteristic of the (5 5 12) surface is its faceted nature which are of two kinds (337) and (225) units as described earlier. These facets can be converted into one another by adsorption of metal atoms as has been shown previously for several metal adatoms. Several research groups including ours have previously shown the formation metal 1D nanowires and nanochains on this high index surface. However, there have been no reports in the literature for the adsorption of Al on Si(5 5 12) substrate. Thus a systematic investigation of Al adsorption on (5 5 12) surface is lacking in the literature.

We perform careful adsorption/desorption studies of Al on Si(5 5 12)-2x1 surface in-situ in UHV using AES and LEED as chemical and structural probes. We compare the behaviour of the Al adatoms on this surface that with of Al/Si(111) system.

4.2.2   Room temperature adsorption

Fig. 4.8 shows the uptake curve for Al adsorption at Room Temperature (RT) on Si (5 5 12)-2x1 surface. The graph is a plot of the variation of the ratio of Al LVV (68eV) peak to the Si LVV (92eV) peak as function of deposition time in minutes. The graph shows a linear rise in the intensity ratio up to about 6min of adsorption of Al on the surface which manifests the formation of an uniform layer of Al on the surface. The different stages of adsorption process are

accompanied by the observation of LEED pattern to follow the changes in the surface structure with Al adsorption on the surface as shown in Fig. 4.9. The Si(5 5 12)-2x1 reconstruction is composed of two kinds of (337) unit and one kind of (225) unit. As Al atoms are adsorbed on the surface the intensity of the fractional order spots of Al decreases. At about 0.3ML of adsorption we observe a different facet on the surface as seen in the LEED pattern shown in Fig. 4.9(b). The intensity line scan along the [665̲] direction shows that the structure consists of
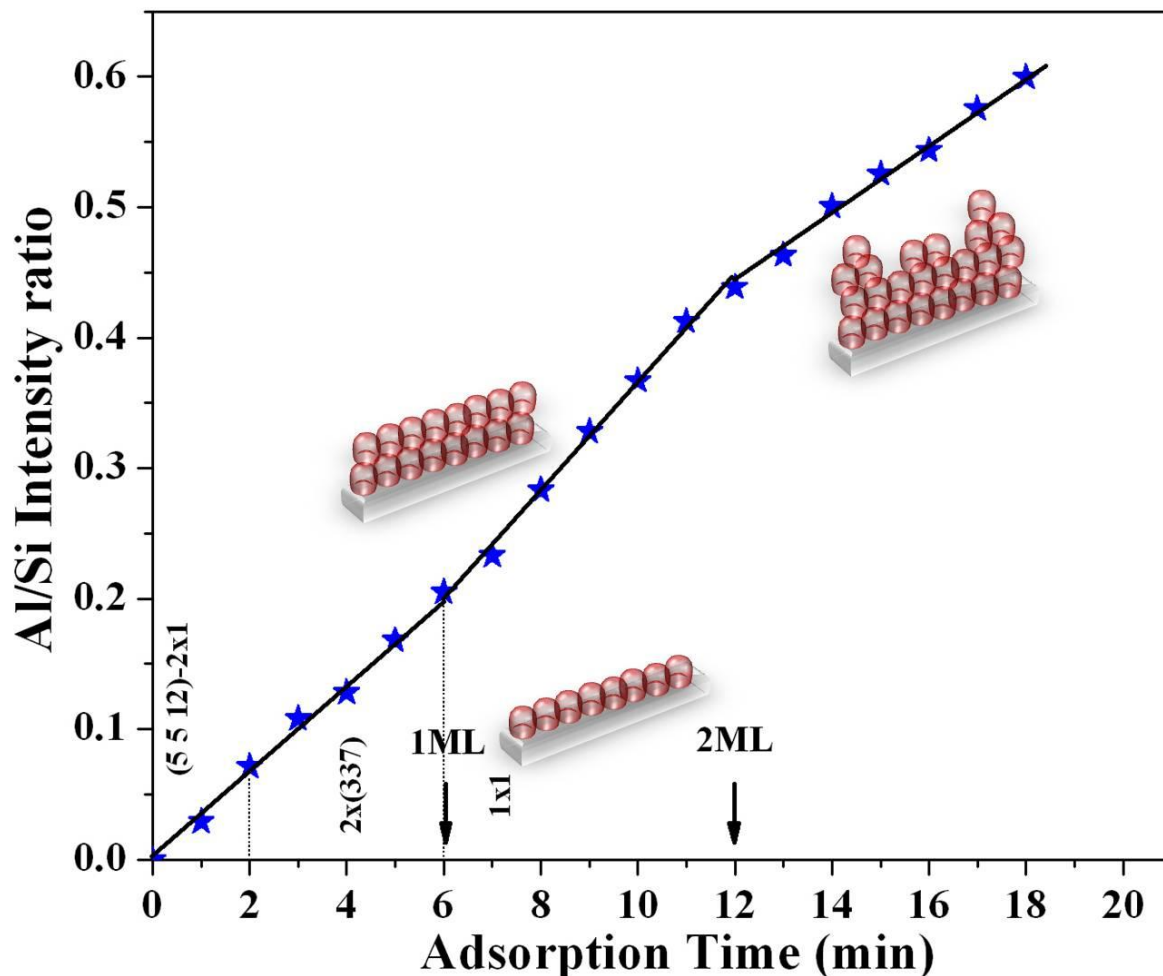
Fig. 4.8: *Room temperature uptake curve for Al/Si(5 5 12)-2x1 system. Ratio of Auger signals of Al LVV (68eV) and Si LVV (92eV) signals are plotted are versus deposition time.*

2×337 facets as seen in Fig. 4.9(b) similar to the earlier reports for Au and other metals on Si (5 5 12) surface which demonstrate them to be made up of quasi 1D metal nanochain structures.

The interchain separation of these facets determined by measuring the separation between the LEED spots along the [66$\underline{5}$] direction is 3.2 nm. The absence of the weak streak along the ($\underline{1}$10) direction indicates that the periodicity along this direction remains to be that of bulk structure. Thus, it can be seen that there is a conversion of Si(5 5 12)-2x1 facet from D(337)+(225)+T(337) (D-Dimer and T-Tetramer) in to a single facet 2x(337) unit. It has been previously shown that this structure consists of self assembly of metal nanochains on the surface. With our careful adsorption studies we are able to show the formation of self assembled nanochains of Al on this high index Si surface. With increased coverage of Al, we observe a weakening of the LEED fractional spot intensity, and at around 6min of adsorption of Al, we observe 1x1 pattern as shown in Fig. 4.9(c).
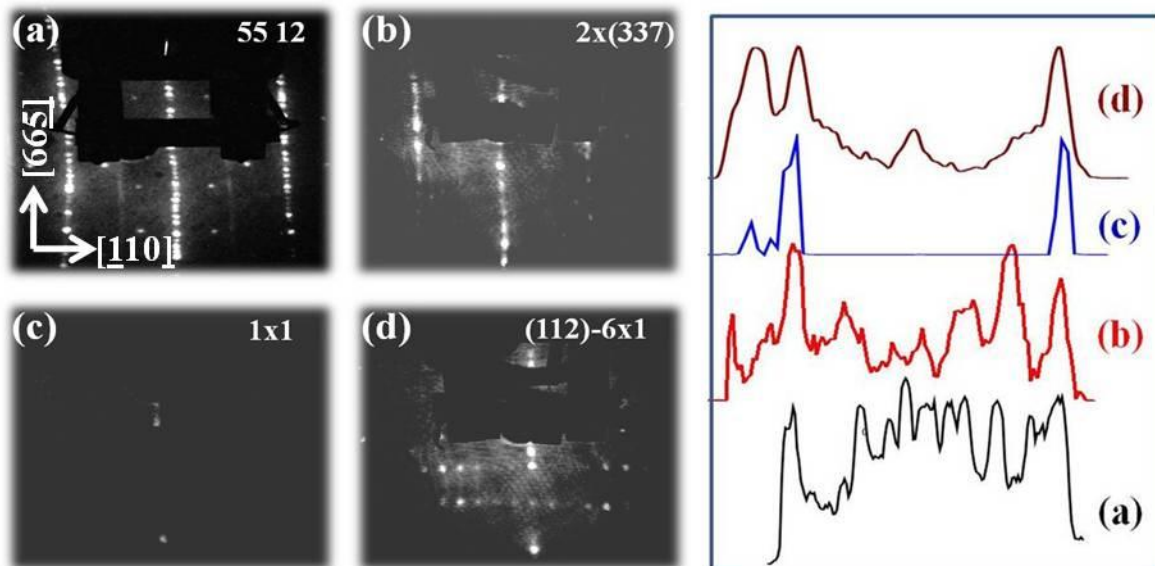
Fig. 4.9: *LEED patterns observed during adsorption/desorption studies of Al/Si(5 5 12)-2x1 system. The right panel shows the intensity lines scans of respective LEED pattern shown in the left panel along [66$\underline{5}$] direction.*

Beyond 6min of adsorption the uptake curve show an increase in its slope compared to the previous segment of the (<6min) of the uptake curve shown in Fig. 4.8. Following the well know procedure for uptake coverage calibration, this break in the slope of the uptake curve correspond to the completion of 1ML, of Al on the surface. Above 1ML of adsorption the uptake curve increases linearly with coverage showing the formation of second uniform

monolayer on the surface. In this region LEED pattern shows 1x1 diffraction pattern shown in Fig. 4.9(c). At around 12min of adsorption the curve shows another break with a change in the slope thus indicating that the surface consists of two flat layers of Al on the surface corresponding to a coverage of 2ML of Al on the surface. Beyond this coverage (>2ML) the slope of the uptake curve is less than that of the previous part of the uptake curve. If the layer by layer growth continues beyond 2ML one expects an increase in the slope compared to the previous segment of the uptake curve. Thus, we observe that above 2ML there is a deviation from layer by layer growth mode. There is the formation of islands above 2ML of Al deposition which reduces the overlayer Auger signal thereby bringing down the intensity ratio from that expected for perfect layer by layer growth mode. This behaviour is similar to that observed for Si(111) where, growth follows by 2ML SK mode with the formation of islands above 2ML of flat Al layer.

4.2.3   Residual thermal desorption

Fig. 4.10 shows the results of residual thermal desorption of Al on Si(5 5 12) surface. In the desorption studies a certain coverage of Al adsorbed at RT is annealed to different temperatures for fixed interval of time and after each annealing the composition and structure residue present on the surface is analyzed by AES and LEED. In Fig. 4.10 the ratio of Auger intensities of Al LVV (68eV) and Si LVV (92eV) peaks are plotted versus annealing temperature. From the uptake curve analysis for RT deposition, it follows that in the case of desorption curve shown in Fig. 4.10 there is about ~2ML of flat Al layer on the surface just prior to the onset of desorption process and the LEED shows 1x1 pattern shown in Fig. 4.9(c) from the surface. Up to a temperature of 150°C the intensity ratio falls showing the agglomeration of Al islands in to islands. This is followed by a flat region where the intensity ratio does not show any appreciable change with increase in temperature. The ratio in this saturation region of the desorption curve corresponds to a coverage of 1.25ML of Al on the surface showing that surface morphology consist of agglomerated islands above a partially covered second Al monolayer. Further increase beyond a temperature of 300°C brings about more agglomeration of islands and desorption curve shows another plateau with Auger ratio corresponding to 0.5ML. This suggests that at an annealing temperature of 700°C surface morphology consists of agglomerated Al islands above 0.5ML of 2D Al layer on the surface. The temperature range 600-750°C is marked

by this flat saturated region showing absence of any appreciable change in the surface morphology. In the temperature range 450-750°C we observe LEED pattern shown in Fig. 4.9(d). The intensity line scan of LEED pattern along [66$\underline{5}$] direction shows a unit cell dimension of 2.3nm for this structure showing that the structure corresponds to (112)-6x1 reconstruction i.e., there is a conversion of 1x1 phase in to (112)-6x1 reconstruction at this range of annealing temperature (6-10mV). Beyond an annealing temperature of 10mV the intensity ratio falls showing the desorption of Al from the surface. In the temperature range 750-900°C we observe a different LEED pattern. The intensity line scan taken along the [66$\underline{5}$] direction shows that the structure consists of 2×337 facets as seen in Fig. 4.9(b) which has been reported for Au and other metals on Si (5 5 12) surface, to be made up of quasi 1D metal nanochain structures. The interchain separation of these facets determined by measuring the separation between the LEED spots along the [66$\underline{5}$] direction is 3.2 nm. The absence of the weak streak along the ($\underline{1}$10) direction indicates that the periodicity along this direction remains to be that of bulk structure. Here as seen in the adsorption case at RT where 2x(337) facet was observe for about 0.3ML of Al adsorption, during desorption studies prior to the desorption of Al from the surface, the (112)-6x1 reconstruction converts in to 2x(337) facet. Beyond a temperature of ~1000°C Al desorbs completely from the surface showing clean Si(5 5 12)-2x1 pattern shown in Fig. 4.9(a).

When we compare the desorption behaviour of RT adsorbed same coverage of Al (~2ML) on Si(111) surface to that of Si(5 5 12) surface to that of Si(5 5 12) surface the main difference that we find is the occurrence of the two plateaus seen at around temperatures of 300°C and 700°C. These plateaus are the signature of the (5 5 12) surface which is endowed with facets which provide strong bonding sites for the adsorbed metal atoms. Also it can be seen that temperature range in desorption takes place is much broader for Si(5 5 12) surface compared to Si(111) surface, which is a common feature of group III metal adsorption on Si(5 5 12) surface which again is a manifestation of the trenched morphology of this high index surface providing stable adsorption sites for the metal atoms.
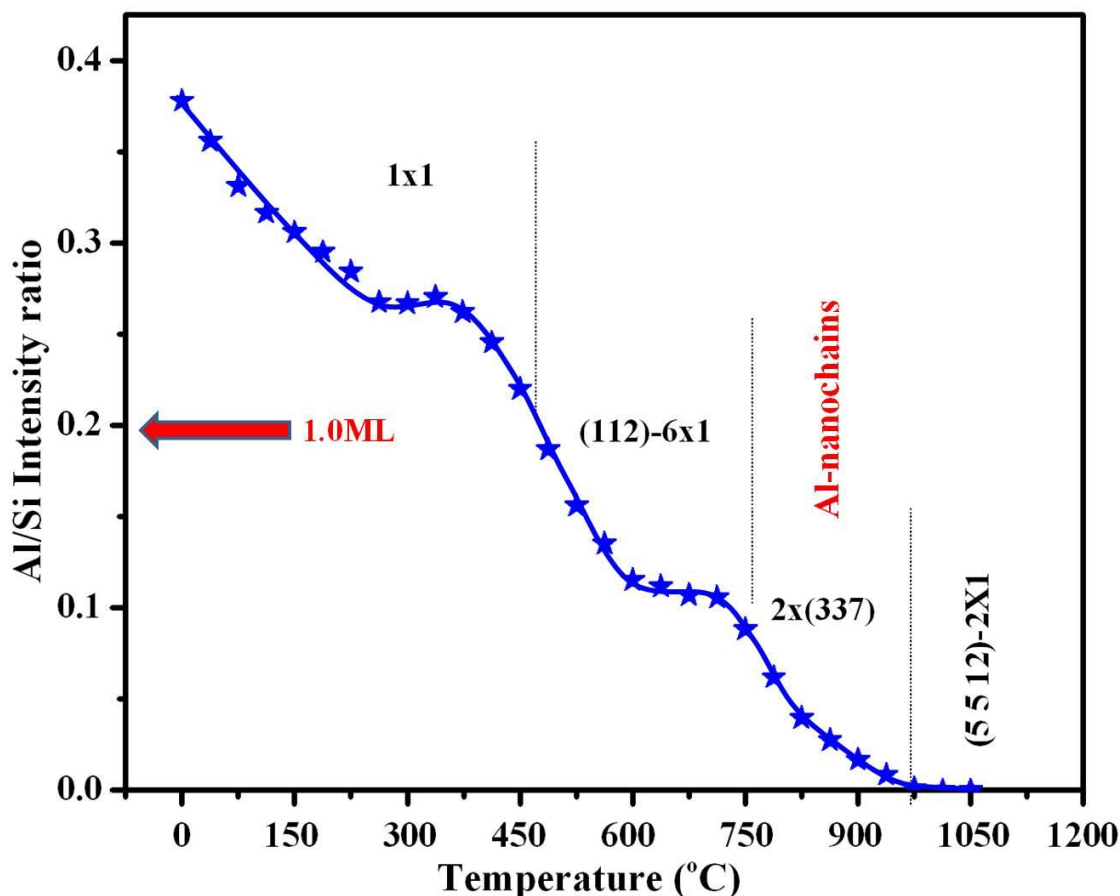
Fig. 4.10: *Residual thermal desorption curve for RT adsorbed Al on Si(5 5 12)-2x1 surface. Ratio of Auger signals of Al LVV (68eV) and Si LVV (92eV) signals are plotted are versus annealing temperature.*

4.2.4   High temperature adsorption

Fig. 4.11 shows the uptake curves corresponding to adsorption at higher substrate temperatures. The graph shows the ratio of Auger intensities of Al LVV (68eV) to Si LVV (92eV) peak plotted versus deposition time. The adsorption uptake for room temperature adsorption is also shown in the figure for comparison. Fig. 4.11(b) shows the uptake curve for adsorption at a temperature of 300°C. The uptake shows a linear rise in the intensity ratio up to a ratio of about 1.75ML and above which the curve shows saturation of the intensity ratio. This flat region of the curve shows the formation of islands on the surface. Thus compared to RT adsorption because of the increased diffusion at higher temperature, agglomeration takes place at
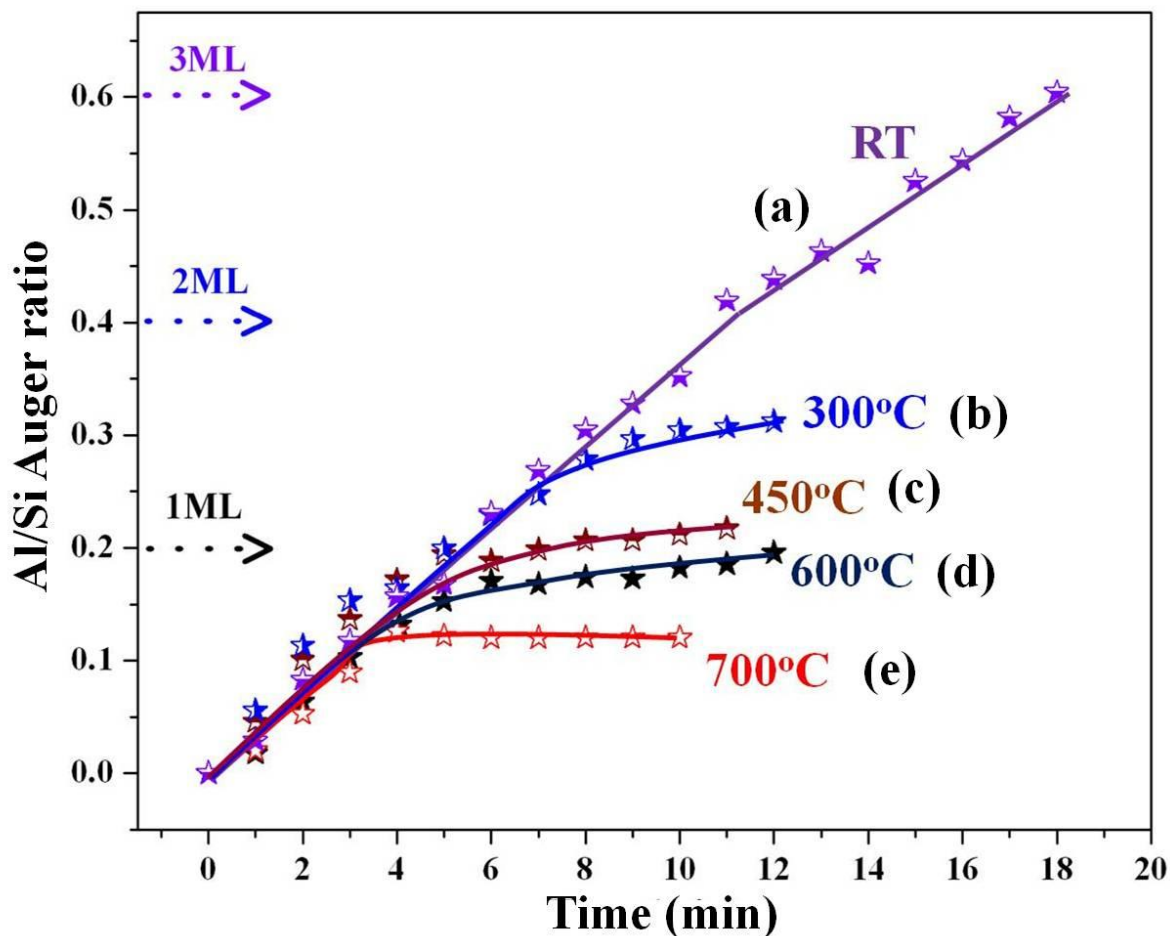
Fig. 4.11: *Uptake curve for adsorption at higher substrate temperatures for Al/Si(5 5 12)-2x1 system. Ratio of Auger signals of Al LVV (68eV) and Si LVV (92eV) signals are plotted are versus deposition time.*

a much lower temperature resulting in the formation of islands before the completion of 2 flat layer of Al on the surface. At about 450°C of substrate temperature shown in Fig. 4.11(c) the uptake curve shows saturation around an intensity ratio of 0.2 which corresponds to a coverage of 1ML of Al on the surface. Thus, at this temperature formation of island takes place above 1ML of Al flat layer on the surface which corresponds to 1ML SK growth mode. For a higher temperature of 600°C the uptake curve (Fig. 4.11(d)) shows the island formation takes even before the completion of first monolayer of flat Al on the surface. For the case of adsorption at 700°C, the uptake curve (Fig. 4.11(e)) saturates at about 0.5ML of Al. At this temperature desorption of Al from the surface is evident from the desorption curve discussed previously.

Hence this flat region of the uptake curve results from lesser sticking coefficient of the Al on the surface. We infer that overall, the growth mode at higher substrate temperatures follows SK mode with onset of the formation of islands at lesser and lesser coverage with increase of substrate adsorption temperature.

4.3   Adsorption/desorption of Ga on Si(111)-7x7 surface

4.3.1   Introduction

Si surfaces are shown to host several interesting reconstructions having novel structural and electronic properties.[18-20] Group III metal adsorption on Si also forms a prototypical system for studying Schottky barrier formation and to form p- and n-type delta doped structures.[21] These reconstructions can be altered or new novel reconstruction can result when metal atoms are adsorbed on the surface. Another interest is in the heteroepitaxy of GaN/Si system for GaN integration in to Si industry.[22,23] Recent literature shows an increased interest in the Ga/Si(111)-7x7 system as it was shown that the system exhibits interesting ordered nanostructures like formation of ordered assembly of magic clusters. In literature Ga was shown to follow SK growth mode on Si(111) surface and several superstructural phases were observed.[24-31] It has been previously shown that the structural evolution of these interfaces is strongly kinetic dependent. We perform careful adsorption studies of Ga on Si(111) surface to understand the growth mode and also subject the adsorbed adlayer for residual thermal desorption to elucidate the role of kinetics in the formation different superstructural phases. In this section we present a systematic study of adsorption/desorption of Ga on Si(111) surface to understand overlayer evolution and to construct a complete 2D phase diagram for the Ga/Si(111)-7x7 by carrying out studies *in-situ* in UHV using the conventional Auger Electron Spectroscopy (AES) and Low Energy Electron Diffraction (LEED).

4.3.2   Room temperature adsorption

Fig. 4.12 shows the adsorption uptake at RT for Ga/S(111) system. Uptake curve is a plot of ratio of Auger intensities of Ga (MNN, 55 eV) to Si (LVV, 92 eV) plotted versus deposition time in min. Fig. 4.12 shows that as the Ga is adsorbed on the surface the intensity ratio rises linearly with increase in the coverage showing the formation of uniform layers of Ga on the surface. At around 10 min of adsorption we observe a change in the slope of the uptake

curve which marks the completion of a monolayer of Ga on the surface as per the accepted analysis of Auger uptake curve. Beyond 10mins of adsorption, the slope of the uptake curve is smaller than the first segment of the uptake curve showing the formation of second layer on the surface due to attenuation of the first layer signal by second layer adatoms. This linear segment which extends up to about 20min of adsorption of Ga marks the formation of uniform second layer of Ga on the surface. With further adsorption beyond 20min the
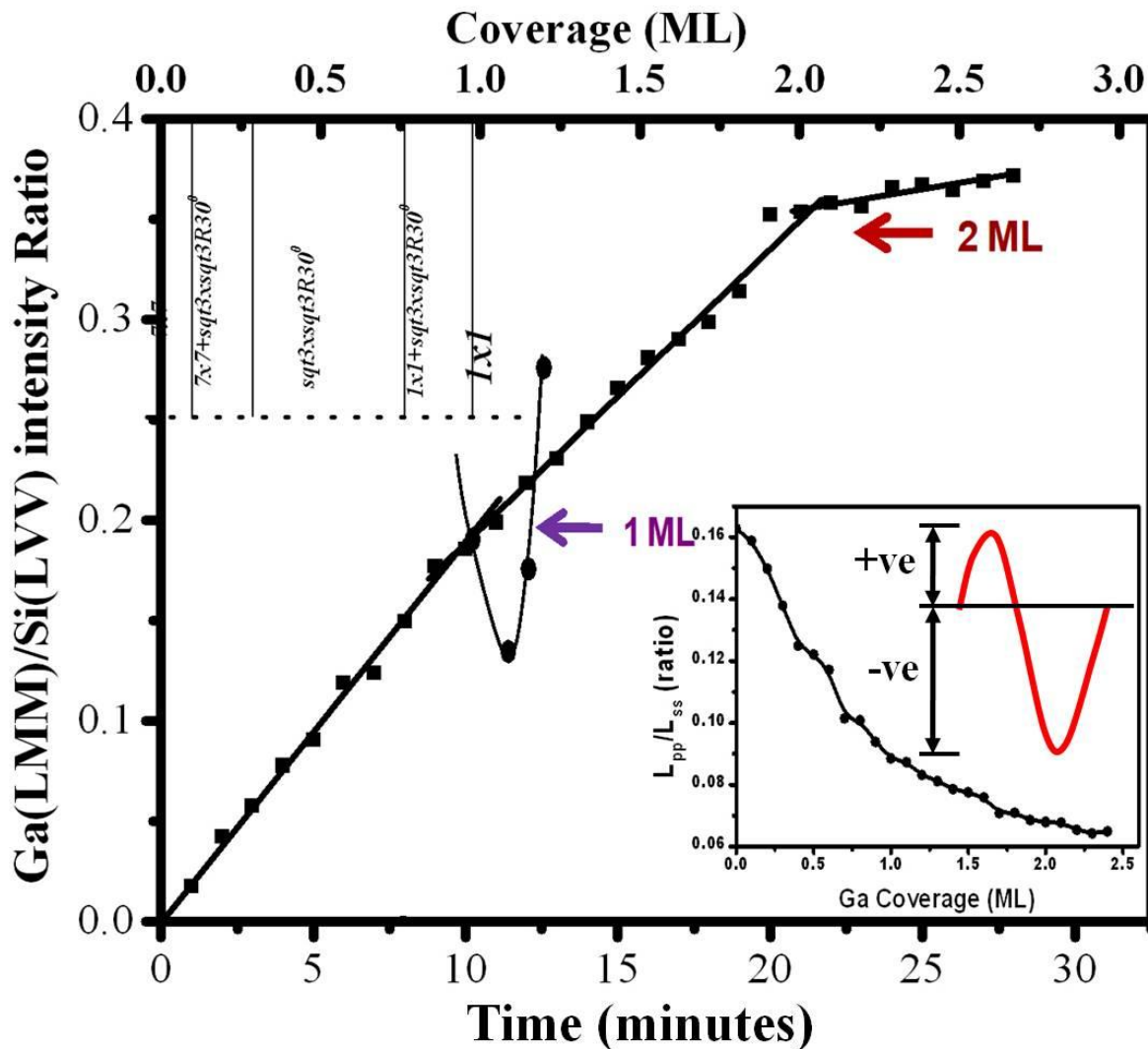
Fig. 4.12: *Room temperature uptake curve Ga/Si(111)-7x7 system. Auger intensity ratio of Ga (MNN, 55 eV) to Si (LVV, 92 eV) is plotted versus deposition time. SSQ is also shown for accurate monolayer calibration. Inset shows the plot of ratio of excursions of Si LVV (92eV) peak versus coverage.*

uptake curve shows a reduced slope compared to the previous segments of the uptake curve indicating a very slowly varying signal. This corresponds to the formation Ga islands on the surface, since island formation will result in a slowly varying Auger signal. Fig. 4.12 also shows the SSQ (sum of squares of errors) plot which is obtained by calculating the errors in slops about a point where a break point is suspected.[11] The minimum of the SSQ shows that a break in slope occurs at 1ML which gives us calibration of flux as 0.1ML/min. Thus, as seen in the literature we also observe a 2ML SK growth mode for Ga/Si(111)-7x7 system at room temperature, where we observe the formation of 3D islands above 2ML of flat Ga layer. During this Ga uptake, we
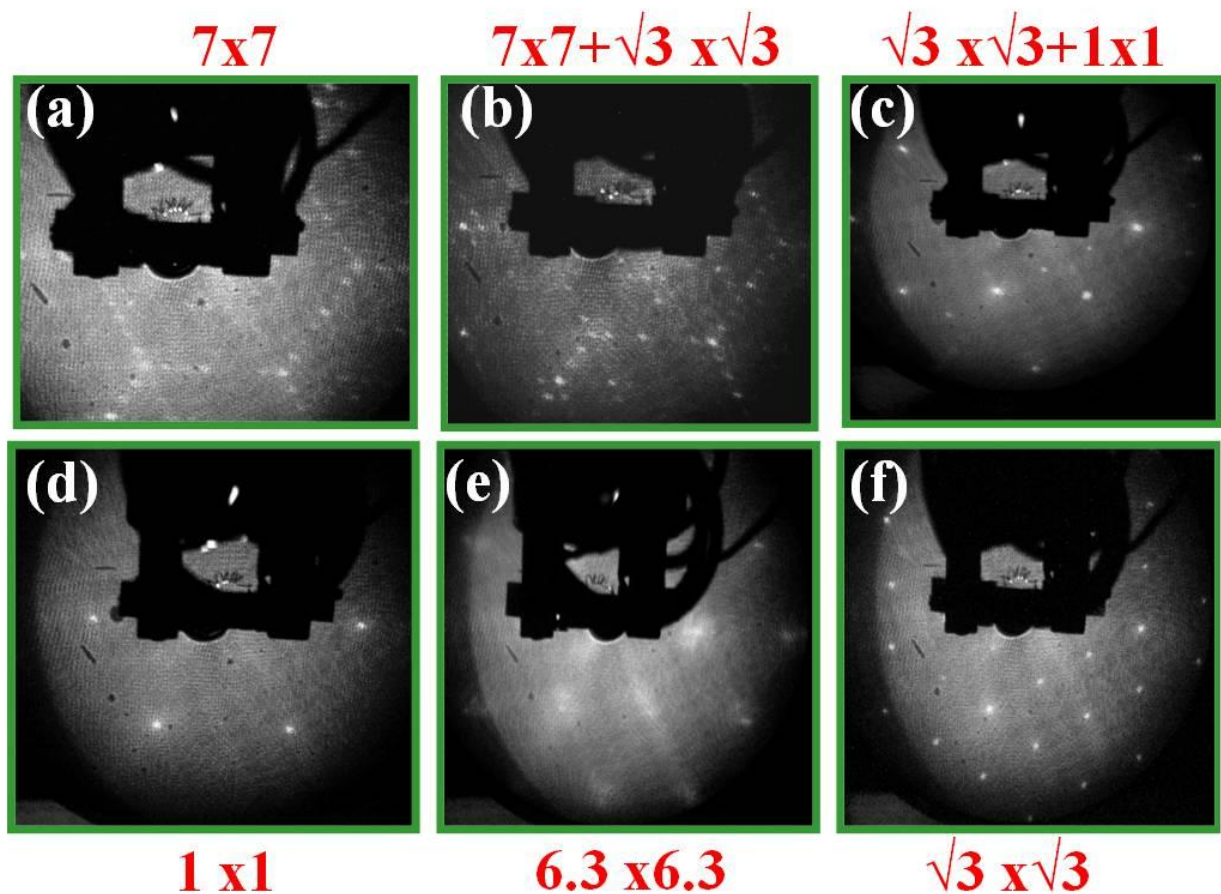
Fig. 4.13: *LEED images (63 eV beam energy) of various surface phases observed during Ga adsorption and desorption on Si(1 1 1) 7x 7 surfaces. (a), (b,) (c), (d), (e) and (f) shows the 7x7, 7x 7 + √3x√3R30°, 1x1 + √3x√3R30°, 1x1, 6.3x6.3 and √3x√3R30° LEED pattern respectively.*

also monitor the shape of the Si LVV peak. It has been previously shown that[32] the asymmetry in the Si LVV Auger peak form the surface arises from the 2p electrons which constitutes the

dangling bonds on the surface. To calculate the dangling bond density on the surface we use the upper and lower excursions in the (dN/dE) spectra which directly correspond to the p–p electron state contribution (Lpp) and the s–s and s–p state contributions (Lss), respectively. The ratio (Lpp/Lss) is proportional to the Si dangling bond density and is shown in the figure as an inset. To understand the influence of the adsorbate on the dangling bonds of the Si(111) surface we calculate the excursion ratio of the differentiated Si LVV (92eV) peak for different coverages which is shown as an inset to Fig. 4.12. It can be seen that as Ga is adsorbed on the surface, the dangling bond density monotonically decreases and around ~2ML where it saturates. This also explains why Ga on Si(111) follows 2ML SK growth mode as seen by the uptake curve.

To understand the change in the surface structure we have performed LEED measurements at different stages of adsorption of Ga on the surface. As Ga is adsorbed on the surface, the intensities of the fractional order spots weakens and at around 0.3ML we observe a mixed phase with √3x√3 reflection which persists up to a coverage range of 0.3 to 0.8ML as shown in the Fig. 4.13(b). There are no previous reports of the observation of the √3x√3 phase at RT for the case of Ga/Si(111)-7x7 system, though this has been observed in the case of Ga adsorption on Si(111)-2x1 surface. This is the first observation of this phase at RT on the Si(111) 7x7 reconstructed phase.   For coverage above 0.8ML we observe an intensification of the integral spots 1x1 spots shown in 4.13(d).   The LEED pattern of Si (7x7), modified (7x7) and Si (1x1)-Ga surface phases are shown in Fig. 4.13.

4.3.4   Residual thermal desorption

To study the thermal stability of the adsorbed adlayer we have performed residual thermal desorption studies, as described earlier. Fig. 4.14 shows a plot of intensity ratio of Auger signal of Ga MNN (55eV) to Si LVV (92eV) peak versus annealing temperature. Curve (a) in Fig. 4.14 corresponds to a Ga coverage of 2.5ML adsorbed at RT, where the surface
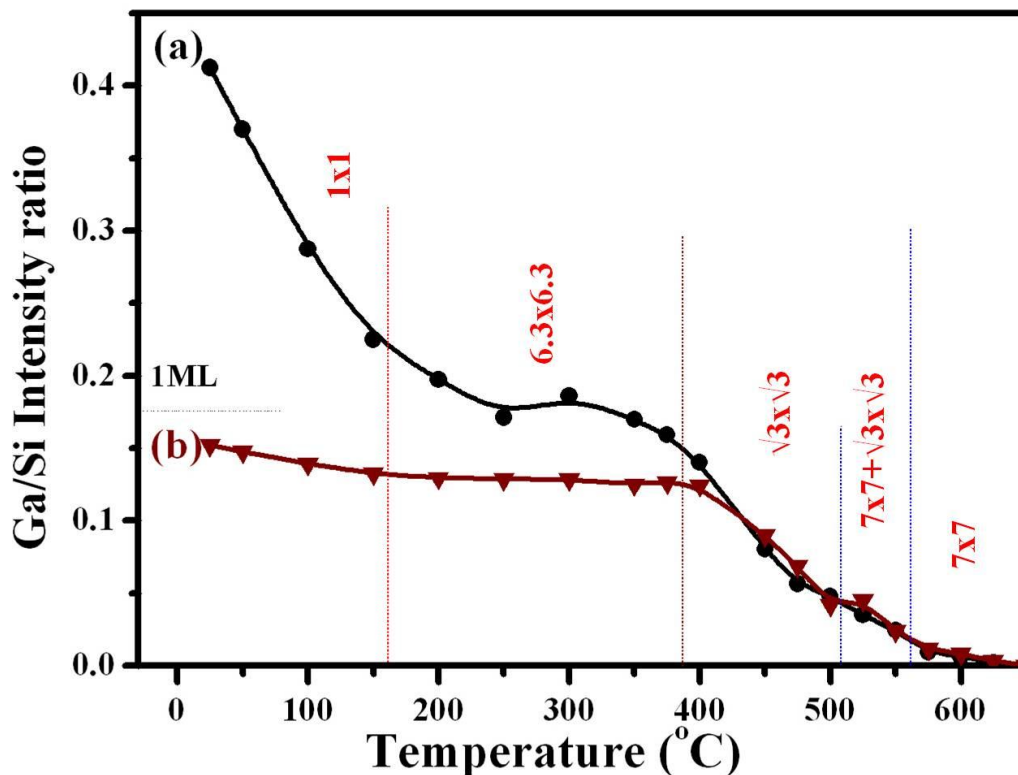
Fig. 4.14: *Ga/Si Auger intensity ratio as a function of temperature for two coverages, (a) 2.5 ML and (b) 1.2 ML.*

morphology prior to the desorption as seen in the discussion of uptake consists of 3D islands above 2ML of flat Ga layer. With increasing annealing temperature in the range up to 200°C the curve (a) shows decrease in intensity ratio and it shows saturation at around 0.17 which corresponds to a coverage of 1ML of Ga on the surface. Thus, as the temperature is increased Ga adatoms above 1ML, start agglomerating into islands as seen by the reduction in the Auger signal from the adatoms. Here 1ML forms a stable layer, which is strongly bonded to the Si(111) surface for Ga on Si(111) surface above which agglomeration takes place. We observe that with increase in temperature in the region, the (1x1) LEED loses background intensity and becomes sharper. In the temperature range of 200°C to 400°C the desorption curve shows a flat region with no appreciable change in the intensity ratio. In this region LEED shows incommensurate 6.3x6.3 reconstruction on the surface which is shown in Fig. 4.13(e). With further annealing beyond 400°C Ga adatoms desorbs from the surface resulting in reduction of intensity ratio in this region. We observe √3x√3 reconstruction which is shown in Fig. 4.13(f) in

the temperature range of 420–510$^{\text{o}}$C, where the coverage is ~ 0.6–0.3 ML. At about a temperature of 550$^{\text{o}}$C we observe reflection from 7x7 reconstruction showing a mixed √3x√3 + 7x7 surface phase shown in Fig. 4.13(b) which is observed up to a temperature of ~600$^{\text{o}}$C. Ga desorbs from the surface completely beyond 600$^{\text{o}}$C showing the clean Si(111)-7x7 pattern. Curve (b) in Fig. 4.14 shows the desorption curve for an initial Ga coverage of about 0.9ML where the surface morphology consists of 0.75ML of partially covered 2D layer of Ga. The curve remains essentially flat showing no appreciable change in the intensity ratio up to a temperature range of ~400$^{\text{o}}$C which show the stability of the adsorbed first layer. Beyond 400$^{\text{o}}$C this desorption curve matches well with that of curve (a) showing the kinetics of desorption beyond this temperature remains the same in this region.

4.3.5   High temperature adsorption

Fig. 4.15 shows the results of the adsorption studies carried out at higher substrate temperatures. The figure shows plot of Auger intensity ratio of Ga LMM (55eV) and Si LVV (92eV) peak plotted versus deposition time in minutes. High temperature uptake for Ga adsorption at a substrate temperature of 150$^{\text{o}}$C is shown curve (b) in Fig. 4.15. This uptake shows a linear rise in the intensity ratio up to a coverage of 1ML showing the formation of a uniform layer of Ga on the surface. Above 1ML the intensity ratio shows saturation leading to a flat region with no appreciable change in the intensity ratio which indicates the formation of islands on the surface. Thus, at 150$^{\text{o}}$C we observe that the growth proceeds by SK growth mode with the formation of islands above 1ML of flat Ga. Curve (c) in Fig. 4.15 corresponds to the uptake curve for adsorption performed at a substrate temperature of 350$^{\text{o}}$C. In this case the uptake curve shows a linear rise up to a coverage of about 0.8ML showing the formation of uniform 2D layer. However, the intensity ratio saturates beyond 0.8ML showing that the island formation starts before the first 2D layer is complete. Thus, at this temperature growth follows SK growth mode with formation 3D islands above 0.8ML of Ga. Curve (d), (e) and (f) in Fig. 4.15 represent Ga adsorption on Si(111)-7x7 surface at substrate temperatures 450$^{\text{o}}$C, 500$^{\text{o}}$C and 550$^{\text{o}}$C, respectively. Here all these curves show an exponential form showing the absence of any.
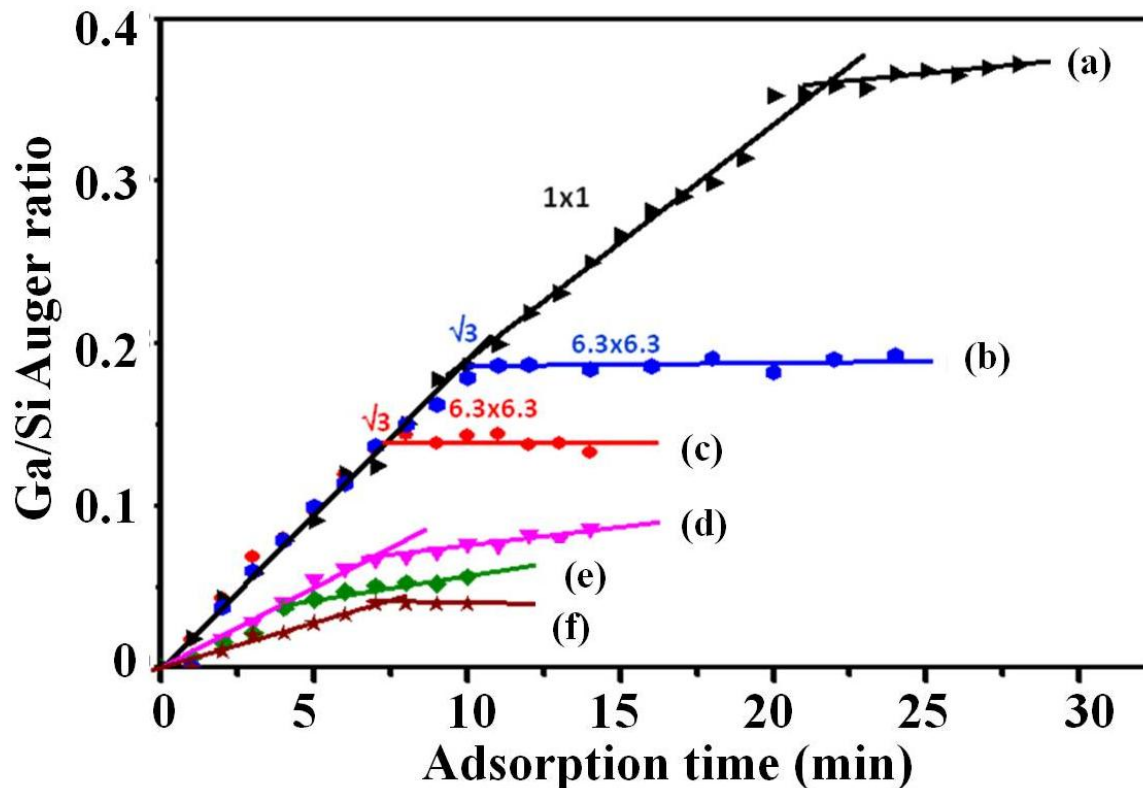
Fig. 4.15: *Uptake curves for adsorption at higher substrate temperatures for Ga/Si(111)-7x7 system. Auger intensity ratio of Ga (MNN, 55 eV) to Si (LVV, 92 eV) is plotted versus deposition time.*

sharp breaks which depicts the formation of only 3D islands on the surface with increase in the coverage of Ga on the surface. The reduction in the Auger intensities for 500°C compared to the case of adsorption at 450°C results from the formation of larger islands with more 3D character. Thus, we observe that the growth mode of Ga/Si(111) system changes from the SK mode at lower temperature (<450°C) to VW growth mode at higher deposition temperatures. These experiments show the role of kinetics in determining the evolution surface morphology.

We have carried out LEED studies at different adsorption stages to study the changes in the surface structure with adsorption of Ga on the surface. Different superstructural phases observed during the study is shown in the Fig 4.16. For the case of adsorption at 150°C, the intensity of the fractional order spots of the 7x7 (Fig. 4.16(a)) becomes weaker and at about 0.33ML of Ga we observe √3x√3-R30° phase pattern as seen in the Fig. 4.16(c). We observe this phase up to a coverage of 0.9ML beyond which we observe the incommensurate (6.3x6.3)
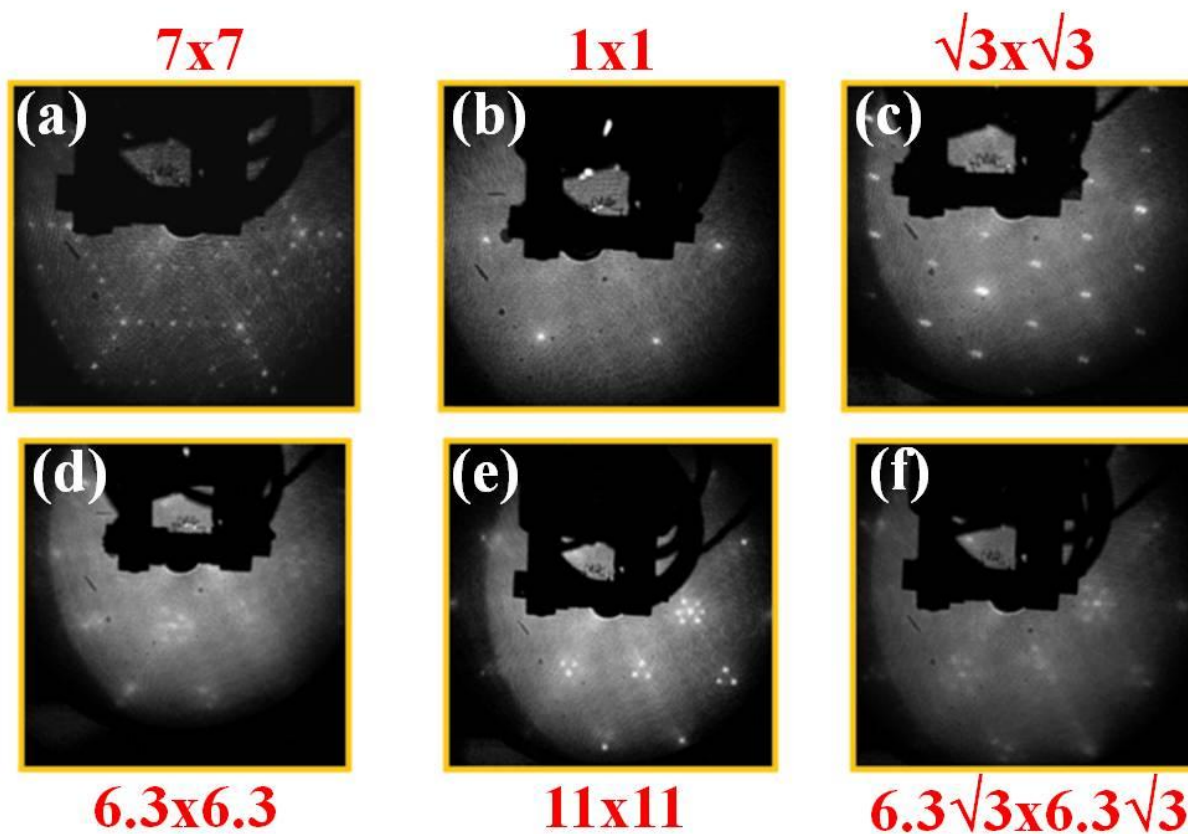
Fig. 4.16: *Different superstructural phases observed for high temperature adsorption of Ga on Si(111)-7x7 surface.*

pattern as shown in the Fig. 4.16(d), which also marks the 3D island growth on the surface and is also seen in the uptake curve as the saturation of Auger intensity ratio discussed previously. For the case of adsorption at 350^oC LEED pattern shows a similar trend as that of 150^oC showing the $\sqrt{3}x\sqrt{3}$ phase in the coverage range of 0.3 to 0.7ML. Above 0.8ML we observe 6.3x6.3 reconstruction which is also evident by the Auger uptake curve showing 3D island growth in this range for this temperature. To identify the phase we have used the intensity line scans of the LEED pattern considering the integral spots as reference. For initial Ga adsorption in the coverage from 0.2ML to 0.3 ML, the LEED pattern shows a mixed phase of $7x7+\sqrt{3}x\sqrt{3}$-R30^o in the case of adsorption at 450^oC. We observe $\sqrt{3}x\sqrt{3}$-R30^o reconstruction only within the range of 0.3ML to 0.7 ML and above up to 0.9 ML 6.3x6.3 phase has been observed, which converts into
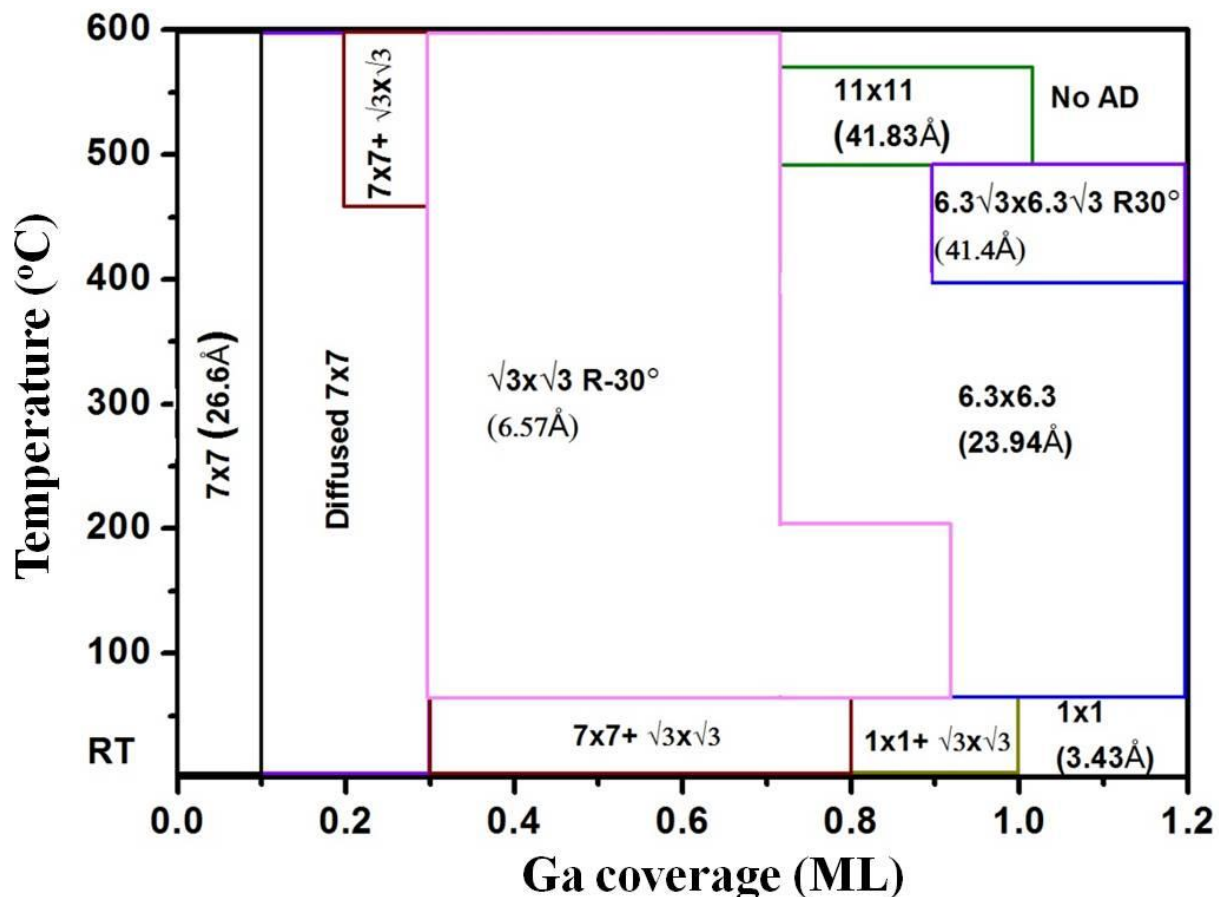
Fig. 4.17: *Phase diagram for Ga/Si(111)-7x7 system. Temperatures of occurrences of different superstructural phases are shown versus Auger intensity ratio of Ga (MNN, 55 eV) to Si (LVV, 92 eV).*

a $6.3\sqrt{3}x6.3\sqrt{3}$-R30° at the Ga coverage of 1.0ML, as shown in Fig. 4.16(f). In the case of Ga adsorption at 500°C we observe $\sqrt{3}x\sqrt{3}$-R30° for a Ga coverage range of 0.3ML to 0.6 ML, which converts to 11x11 phase at a coverage of 0.7 ML shown in Fig. 4.16(e).

We have performed several adsorption/desorption experiments to find the different kinetic path ways to obtain different superstructural phases of Ga on Si(111) surface and the results are summarized in the form a 2D phase diagram which is shown in Fig. 4.17. In the phase diagram, temperature and coverage range of occurrence of different phases are depicted. In the case of RT adsorption we observe a mixed $7x7+\sqrt{3}x\sqrt{3}$-R30° phase in the coverage range of 0.3-0.8ML which becomes $1x1+\sqrt{3}x\sqrt{3}$-R30° at a coverage of 0.8ML. Above 1ML at room temperature we observe 1x1 pattern as seen in the phase diagram. In the temperature range of

100-200°C, √3x√3 phase is observed for a coverage range of 0.3 to 0.9ML which converts in to the 6.3x6.3 for the higher coverages at the same substrate temperature. Above 200°C the 7x7 reconstruction converts into √3x√3 pattern for the coverage range of 0.3-0.7ML, which changes into the 6.3x6.3 phase upon further Ga adsorption. In the temperature range 400-450°C, we observe the 6.3√3x6.3√3-R30^o phase for the Ga coverage range of 0.9-1.2ML. We observe a mixed phase of 7x7 + √3x√3 for a Ga coverage of ~0.2ML in the temperature range 450-550°C which, with further adsorption converts to the pure √3x√3 phase. With further adsorption in the same temperature range we observe the 11x11 for a Ga coverage of 0.8ML to 1.0ML.

4.4   Conclusions

We have performed systematic adsorption/desorption studies of Al on Si(111)7x7 and Si (5 5 12)2x1surface, *in-situ* in UHV using AES and LEED as chemical and structural probes. Room temperature uptake curve for Al on Si(111)7x7 surface shows deviation from layer by layer growth above 2ML of Al on the surface. We have performed Auger uptake simulation and its comparison with experimental uptake confirms that the RT adsorption of Al on Si(111) follows Stranski-Krastanov growth mode. Residual thermal desorption studies shows the absence of cluster migration at lower temperatures and the desorption curve for different coverages studied shows agglomeration of adatoms followed by the formation of different superstructural phases on the surface. High temperature adsorption of Al on Si(111) surface shows SK growth mode with the formation of islands before the completion of 2D layer of Al. Our several adsorption/desorption studies show different superstructural phases viz. pure 7x7, √3x√3, √7x√7,c-phase, γ7x7 and α7x7 and several mixed phases 1x1+1x1, γ7x7+1x1+1x1, γ7x7+√3x√3, √3x√3+ √7x√7x , √3x√3+c-phase and 7x7+√3x√3. Analysis of LEED spot intensity line scan shows a periodicity of eight for the γ7x7 phase. Based upon several adsorption/desorption studies, we have arrived at a 2D phase diagram for the Si(111)-7x7 system which shows several kinetic path ways to obtain the different reconstructions observed. We observe that growth mode for RT adsorption of Al on Si(5 5 12) surface follows a similar trend as that that of Si(111) surface showing deviation of layer by layer growth mode above 2ML of Al on the surface. Residual thermal desorption studies on Si(5 5 12) surface shows plateaus in the desorption curve manifesting the faceted nature of the surface with observation of (112)-6x1 and 2x(337) facets on the surface. With our careful studies we are able to form self assembled

nanochains of Al during both adsorption and desorption process. At higher substrate temperatures the growth mode proceeds by SK growth mode with progressive reduction in the coverage for onset of the formation of islands with increase in substrate temperature.

Adsorption at room temperature of Ga on Si(111) follows SK growth mode and at high temperatures the growth mode changes to VW mode. With our careful experiments using low flux rate of adsorption we are able to see $\sqrt{3} \times \sqrt{3}$ reconstruction at room temperature which has not been observed previously. Residual thermal desorption studies shows agglomeration of Ga above 1ML, showing the monolayer stability. We have observed several superstructural phases like 7x7, $\sqrt{3} \times \sqrt{3}$, 6.3x6.3, $6.3\sqrt{3} \times 6.3\sqrt{3}$ and 11x11 and the mixed phase of $7x7 + \sqrt{3} \times \sqrt{3}$. Results of several careful adsorption/desorption experiments are summarized in the form of a 2D superstructural phase diagram.

References

[1] J. J. Lander and J. Morrison, Surf. Sci. **2**, 553 (1964).

[2] G. V. Hansson, R. Z. Bachrach, R. S. Bauer, and P. Chiaradia, J. Vac. Sci. Technol. **18**, 550 (1981).

[3] T. Kinoshita, S. Kono, and T. Sagawa, Phys. Rev. B **32**, 2714 (1985).

[4] G. V. Hansson, J. M. Nicholls, P. Martensson, and R. I. G. Uhrberg, Surf. Sci. **168**, 105 (1986).

[5] M. K. Kelly, G. Margaritondo, J. A. Anderson, D. J. Frankel, and G. J. Lapeyre, J. Vac. Sci. Technol. A **4**, 1396 (1986).

[6] R. J. Hamers, Phys. Rev. B **40**, 1657 (1989).

[7] K. Nishikata, K. Murakami, M. Yoshimura, and A. Kawazu, Surf. Sci. **269-270**, 995 (1992).

[8] M. Yoshimura, T. Takaoka, T. Yao, T. Sato, T. Sueyoshi, and M. Twatsuki, Mat. Res. Soc. Symp. Proc. **259**, 157 (1993).

[9] A. V. Zotov, E. A. Khramtsova, S. V. Ryzhkov, A. A. Saranin, A. B. Chub, and V. G. Lifshits, Surf. Sci. **316**, L1034 (1994).

[10] C. Argile and G. E. Rhead, Surface Science Reports **10**, 277-356 (1989).

[11] M. Stampanoni, A. Vaterlane, M. Aeschlimann, F. Meier, and D. Pescia, J. Appl. Phys. **64**, 5321 (1988).

[12] D. Briggs and M. P. Seah, Practical Surface Analysis By Auger and X-ray Photoelectron Spectroscopy, 2nd Edition, John Wiley and Songs, Ltd, Chichester, UK (1990).

[13] D Briggs and J. T. Grant, Surface Analysis By Auger and X-ray Photoelectron Spectroscopy, Comwell Press, Trowbridge, UK (2003).

[14] S. Tougaard, Copyright (c) 2000-2002 Quases-Tougaard Inc. (n.d.).

[15] S. Tanuma, C. J. Powell, and D. R. Penn, Surf. Interf. Anal. **21**, 165 (1993).

[16] Wolfgang S. M. Werner and C. J. Powell, SESSA Package (2006).

[17] G. V. Hansson, R. Z. Bachrach, R. S. Bauer, and P. Chiaradia, Phys. Rev. Lett. **46**, 1033 (1981).

[18] A. Hryciw, Y.C. Jun, and M.L. Brongersma, Nat. Mater. **9**, 3 (2010).

[19] T. Schmidt, S. Gangopadhyay, J.I. Flege, T. Clausen, A. Locatelli, S. Heun, and J. Falta, New J. Phys. **7**, 193 (2005).

[20] H.F.O. Schmidt and T.J. Watson, IBM J. Res. Dev. **43**, 351 (1999).

[21] H.J. Gossmanna and E.F. Schubert, Crit. Rev. Solid State Mater. Sci. **18**, 1 (1993).

[22] J.I. Hong, Y. Chang, Y. Ding, Z.L. Wang, and R.L. Snyder, Thin Solid Films2 **519**, 3608 (2011).

[23] A. Krost and A. Dadgar, Mater. Sci. Eng. B **93**, 77 (2002).

[24] B. Bourguignon, K.L. Carleton, and S.R. Leone, Surf. Sci. **204**, 455 (1988).

[25] M.Z. Allmang and L.C. Feldman, Surf. Sci. **191**, L749 (1987).

[26] T. Thundat, S.M. Mohapatra, B.N. Dev, W.M. Gibson, and T.P. Das, J. Vac. Sci. Technol. A **6**, 681 (1988).

[27] J.E. Rowe, G. Margaritondo, and S.B. Christman, Phys. Rev. B **15**, 2195 (1977).

[28] M. Morita, S.N. Takeda, M. Yoshikawa, A. Kuwako, Y. Kato, and H. Daimon, Appl. Surf. Sci. **254**, 7872 (2008).

[29] H.H. Chang, M.Y. Lai, J.H. Wei, C.M. Wei, and Y.L. Wang, Phys. Rev. Lett. **92**, 066103 (2004).

[30] Q. H. Wang and M. C. Hersam, Small **4**, 915 (2008).

[31] M. Otsuka and T. Ichikawa, Japan. J. Appl. Phys. **24**, 1103 (1985).

[32] D. E. Ramaker, F. L. Hutson, N. H. Jurler, and W. N. Mei, Phys. Rev. B **33**, 2547 (1986).

Chapter V

Initial stages of growth of In on Si(111)-7x7 and

Si(5 5 12)-2x1 surfaces

In this chapter we describe the results of adsorption/desorption of In on low index Si (111) and high index Si (5 5 12) surfaces using experiments carried out in UHV using AES, LEED and EELS as surface structural and chemical probes. Growth modes of In on the two surfaces is identified and compared. Based on several adsorption/desorption experiments a complete 2D phase diagram is proposed.

5.1   Adsorption/desorption of In on Si(111)-7x7

5.1.1   Introduction

Indium is known to induce a number of ordered surface phases on Si (111)-7x7 substrate surfaces in the submonolayer regime[1-4]. Several studies have focused on the atomic and electronic properties of these submonolayer phases[5-7]. Though a few reports are present on the low temperature growth of In, at and beyond one monolayer, a combined systematic adsorption/desorption study of the system in the submonolayer regime seems to be essential to reveal the kinetics of growth and other related aspects.[8-10] Hirayama et al., has reported the observation of five phases viz. 7x7, $\sqrt{3}$x$\sqrt{3}$, $\sqrt{31}$x$\sqrt{31}$, 4x1, and 1x1 in a temperature and coverage range of 300-600°C and 0-1.5ML, respectively.[11] The other available phase diagram in the literature are restricted to the very narrow temperature range and hence do not give the complete picture.[12,13]   We present consolidated results obtained by performing careful adsorption/desorption experiments in Ultra High Vacuum (UHV) probed by Auger Electron Spectroscopy (AES) and Low Energy Electron Diffraction (LEED), in the form of a 2D-phase diagram. Major changes in the observed phase diagram with those in the literature are presented. We show that In on Si (111) follows Stranski-Krastanov growth mode, which also depends on

the growth parameters. In the desorption studies we find an anomalous behavior of the three dimensional (3D) islands spreading into layers before evaporation.   We have observed the $2\sqrt{3}$x$2\sqrt{3}$-In phase during residual thermal desorption of In from the Si (111)7x7 surface. We try to shed some light on the atomic geometries of this phase by *ab initio* Density Functional Theory (DFT) calculations by considering the existing model for the well studied Si(111) $2\sqrt{3}$x$2\sqrt{3}$-Sn phase and simulate STM images for the model. On Si (5 5 12) during desorption studies we observe clustering and layering process which is compared with the behavior of In on Si (111) surface. We observe the formation of quasi 1D chains during adsorption/desorption process. A re-entrant layering process is observed which is also accompanied by re-entrant changes in surface structure of (5 5 12) surface. We discuss these issues in the light of recent literature on quantum size effect in ultrathin films and the presence of step-edge barrier in the growing clusters.

5.1.2   Room temperature adsorption

Fig. 5.1 is obtained by adsorbing In onto the substrate for fixed time intervals, and measuring the Auger intensities of Si and In. The figure shows the evolution of intensity ratio of In MNN (404) eV and Si LVV (92) eV with time (also marked as coverage), by keeping the substrate at room temperatures for different time intervals. In Fig. 5.1(a) the time interval for each adsorption is 1minute and for Fig. 5.1(b) it is 2 minutes. Both uptake curves (a) and (b) in Fig. 5.1 show an initial linear rise with a break at 5 minutes of adsorption, which corresponds to a ratio of 0.18.[14] We observe another break at a ratio 0.36. The breaks are attributed to the attenuation of the Auger signal by the next top layer.   The slope of this part of the curve is higher than that of the first layer growth. It seems that the first layer is accompanied by the formation of large Indium islands, which eventually (>1ML) form a complete layer during the subsequent layer growth, which consequently increases the In/Si ratio. After 10minutes of adsorption, though slopes of both curves (a) and (b) in Fig. 5.1 decrease, they show different adsorption characteristics due the difference in the adsorption intervals (1minutes and 2minutes respectively). The flat region of the curve for coverages >2ML, which begins at a ratio of 0.36, shows the formation of 3D In islands, which is typical of the Stranski-Krastanov (SK) growth mode. This has also been previously reported in the literature for the growth of In on Si (111)

7x7 surface. The formation of islands on 2ML can be attributed to the layer-dependent mobilities of In adatoms. The epitaxial first layer (as seen by LEED), leads to a near epitaxial second layer, which has enough defects to hinder adatom mobility and thus encouraging 3D island formation. Above 15 minutes (3ML) of adsorption the In/Si rises as shown in the figure which is due to the attenuation of the Silicon signal because of low inelastic mean free path of Si 92eV Auger electrons (5.3Å) .

Fig. 5.2 shows the changes in the Si 92 eV LVV peak profile, with adsorption of Indium on Si (111) 7x7 surface. The ratio of the positive and negative excursions of Si 92eV peak with Indium adsorption coverage is shown in the inset of Fig. 5.2. The deconvolution of the Si (LVV)
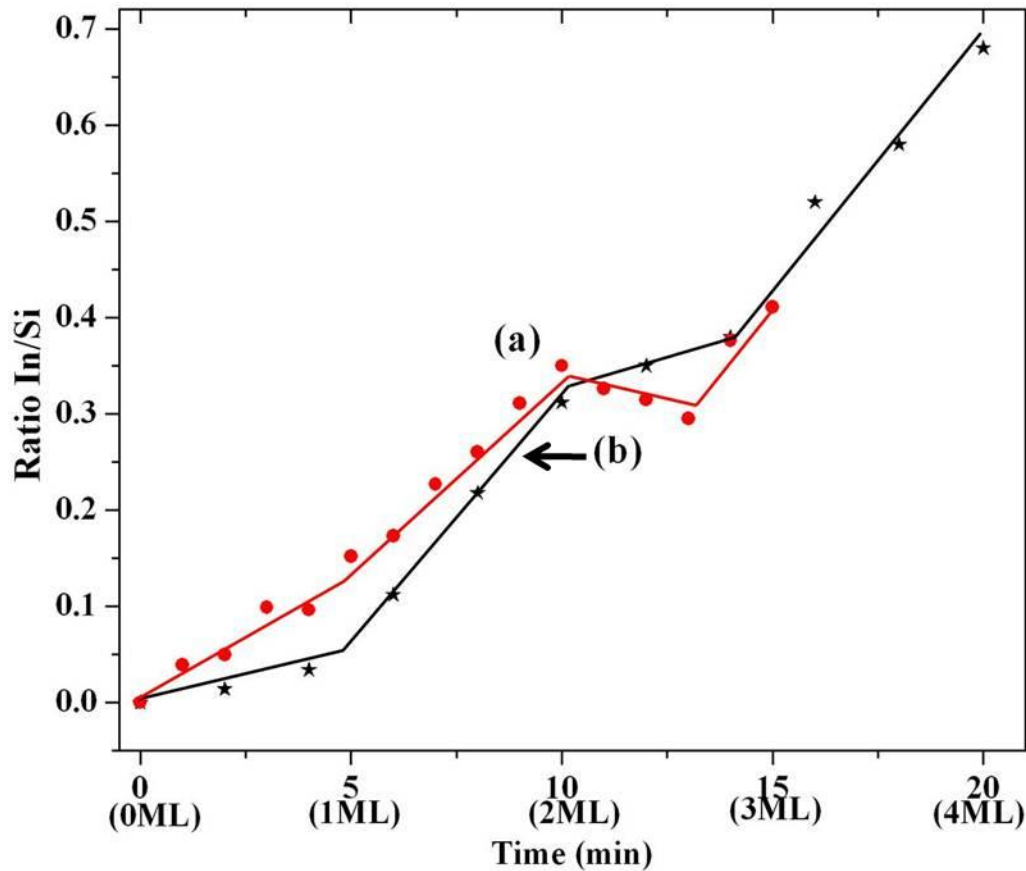
Fig. 5.1: *Auger uptake for In adsorption on Si (111)7x7 at RT showing the ratio of In MNN to Si LVV intensities as a function of time. Corresponding coverage is shown in brackets. In (a) adsorption interval is 1min and in (b) it is 2min.*

auger peak in the N(E) mode, enables the extraction of the contribution of the p-electron states to the Auger transition.[15]   The density of the dangling bonds (valence band states), which are predominantly p- in character, can thus be monitored by observing changes in the intensity of the corresponding components. This becomes easily accessible in the Auger spectra acquired in the first derivative mode, since the upper excursion of the peak corresponds directly to the p-p
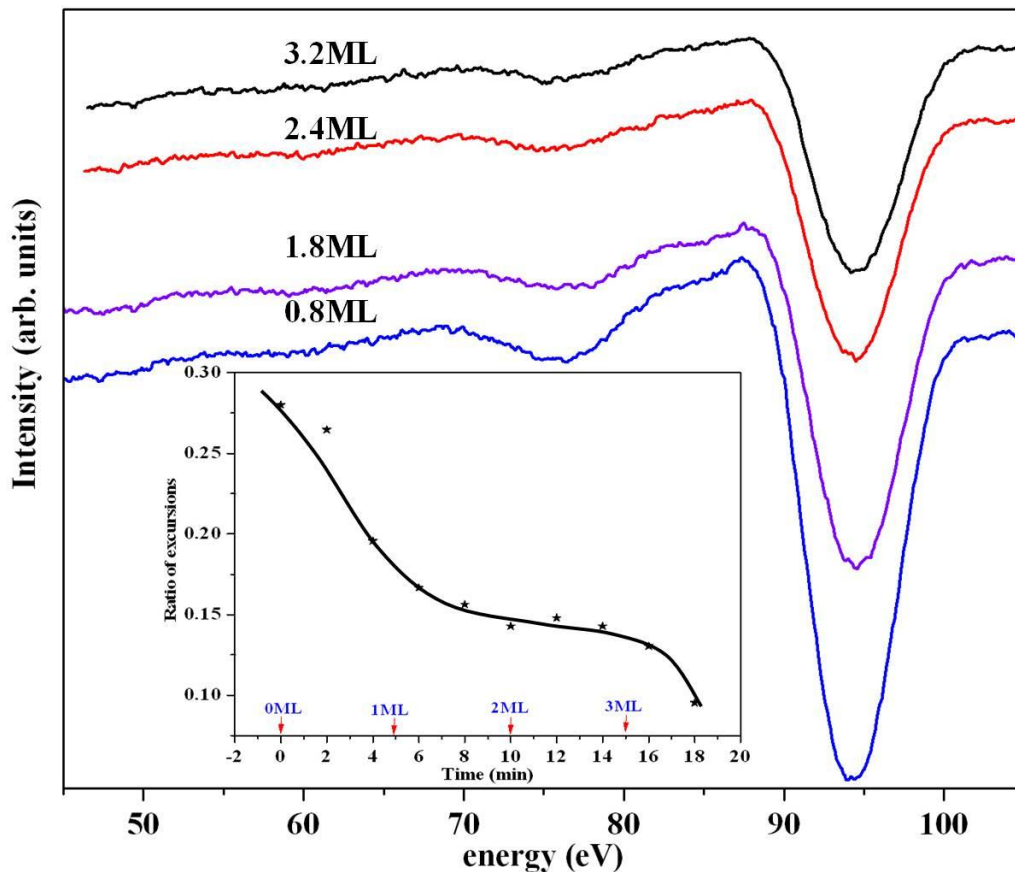
Fig. 5.2: *Figure shows changes in the Auger Si LVV peak as In is adsorbed. Ratio of +ve and -ve excursions of differentiated Si LVV Auger peak with coverage of In is shown as inset.*

electron state contribution (L_{pp}), and the lower excursion is due to the s-s and s-p states (L_{ss}). Thus, in Fig. 5.2 the plot of the ratio of the positive to the negative excursion (L_{pp}/L_{ss}) of the Si (LVV) 92 eV peak as a function of the In deposition, manifests the change in the valence band due to the changing dangling bond density. The ratio falls up to 10 minutes of adsorption showing the saturation of dangling bond on the silicon surface which coincides with completion of 2ML of indium on the silicon surface. The curve is almost flat after this point, showing the

saturation of dangling bonds at 2ML of indium. We observe a dip in the curve after this point, which is due to the attenuation of the Si signal by In overlayer.

5.1.3   Residual thermal desorption

The AES intensity of In (404eV) to Si (92eV) peaks by varying the annealing temperature is shown in Fig. 5.3. Fig. 5.3(a) is the desorption curve for RT adsorbed 3.5ML of In on Si (111)-7x7 surface. Initially the ratio falls to 0.4 up to 285° C and remains almost same up to 435° C. In the temperature range of RT to 285°C, the initial fall in the Auger ratio is due to the agglomeration of the third layer In atoms, thus yielding a ratio of 0.4 in the temp range of 285°C to 435°C. Here the flat portions of the curve shows that surface morphology remains essentially the same in this region. Above 435° C, we see an anomalous behavior of the AES ratio increase, with temperature. This increase in ratio by 0.2 is due to the onset of the conversion of 3D islands into layers and finally the fall in the ratio corresponds to the layer by layer desorption of In from the surface. Thus, In atoms do not desorb from the surface due to stronger cohesive forces, but spread as layers before desorption.

Fig. 5.3(b) shows desorption of 2.3ML of RT deposited In. Here the AES ratio and the surface morphology remains almost the same up to 435°C since there is hardly any island formation above 2ML. Above this temperature the In-Si ratio rises by about 0.1 because of the layering of the islands and finally indium desorbs from the surface. Comparing the above two desorption curves we infer that the final rise in the AES ratio before desorption is higher for 3.2ML case than 2.3ML since the amount of the adatoms that are agglomerated in the SK mode, and during the initial temperature regime (0-285°C) is different in the two cases. So higher the coverage, the final rise will be higher because of the layer formation.

Desorption curve Fig. 5.3(c) of RT deposited 1.2ML indium consists of a flat region followed by fall in the intensity ratio with rise in temperature. Here the surface morphology initially on the surface consisted of ordered one monolayers plus 2D growth on top of it. As there are no 3D islands present in this case, the final rise in the AES ratio due to the conversion of 3D islands to layers cannot happen here. Our observations clearly bring out the picture of Stranski-Krastanov growth mode for adsorption of Indium on Si (111) surface. Close inspection of (a) and (b) in Fig. 5.3, shows that there is a threshold temperature for the conversion of In islands to layers. This may be due to the barrier at the step edges on the 3D island, which

prevents the atoms from diffusing down the step edges and thereby suppressing layer formation. However, at higher temperatures the adatoms may attain the necessary energy to overcome the step-edge barriers, to convert from the island to layer configuration.
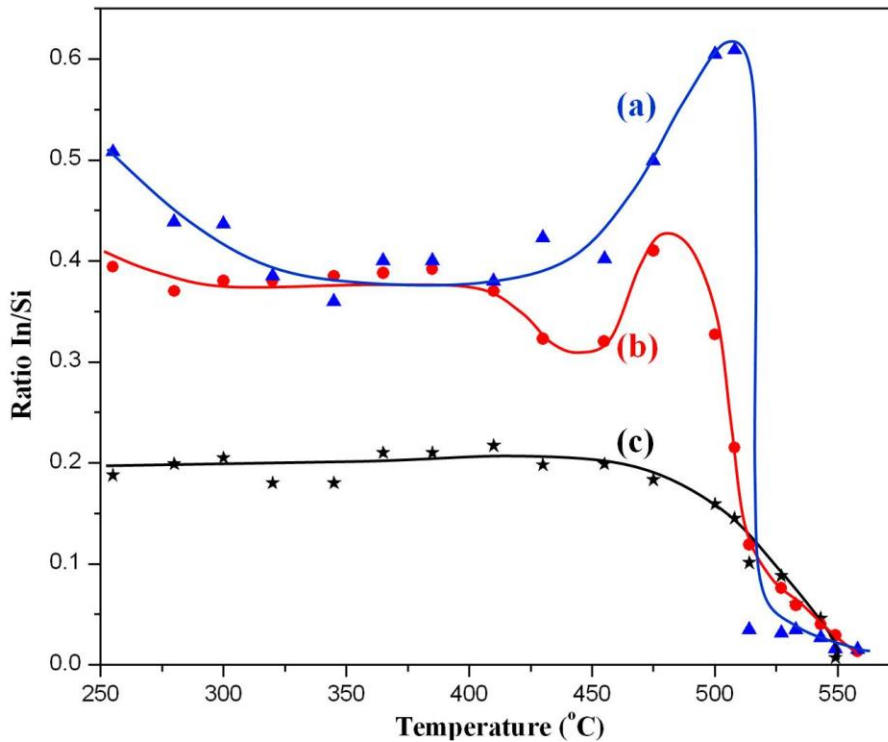
Fig. 5.3: *Residual thermal desorption curves for In on Si (111)-7x7 for different initial coverages, (a) 3.5ML, (b) 2.3ML and (c)1.2ML. Graph shows the ratio of In MNN to Si LVV Auger intensity ratio versus annealing temperature.*

5.1.4   Phase diagram

In Fig. 5.4 we present the consolidated phase diagram of the careful and systematic adsorption and residual thermal desorption (annealing) studies of the adsorbed In adatoms on the Si (111) surface at different substrate temperatures for various adsorbed coverages.   This 2D phase diagram of the Si (111)-In system depicts the evolution of the different superstructural phases induced by In on the Si(111) surface as function of temperature where the ratio of Auger intensities of In MNN (404eV) and the Si LVV (92eV) peaks gives the calibrated coverage and the LEED studies manifest the ensuing surface atomic arrangement (symmetry) in reciprocal space.

Different 2D-phases observed during the study are Si(111)7x7-In, Si(111)√3x√3R30°-In, Si(111)4x1 3D-In, Si(111)2√3x2√3R30°-In and Si(111)√7x√3-In whose observed LEED pattern are shown in Fig. 5.5. For brevity, we shall call the above phases as 7x7, √3, 4x1, 2√3 and√7x√3 respectively, in the following discussions. Fig. 5.5(a) represents the characteristic LEED image of the Si (111)7x7 reconstruction, which is explained by the well established DAS model described in chapter 2.[16] The fractional order spots become weaker with In adsorption and disappear at around 2ML, resulting in the Si (111)1x1 pattern shown in Fig. 5.5(e). The transition from 7x7 to other reconstructions is accompanied though the 1x1 pattern which is clear from the phase diagram in Fig. 5.4. Consider the well-studied √3 (shown in Fig. 5.5(b)) phase
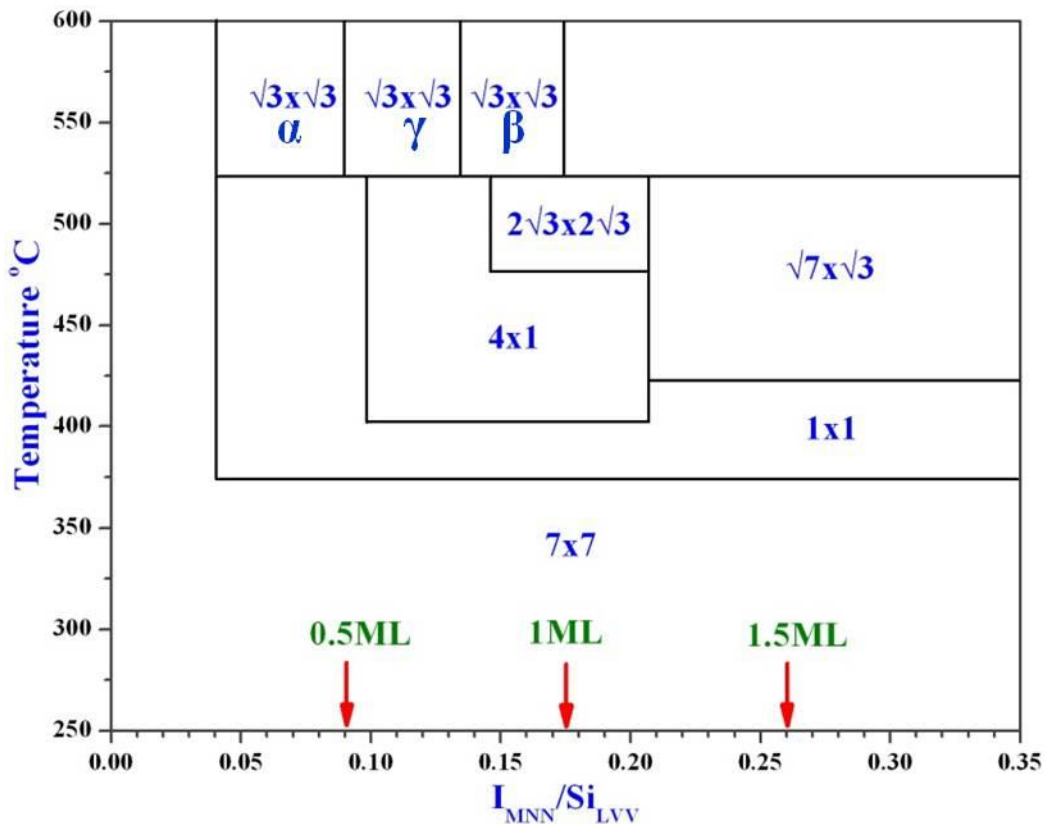
Fig. 5.4: *Si (111)–In 2D phase diagram, which show different superstructural phases as a function of substrate temperature and ratio of Auger intensities of In MNN (404 eV) to Si LVV (92 eV) peak. Calibrated coverage in monolayer is also shown with arrow marks.*

induced by In on Si(111) surface.[17] This phase has a relatively simple geometry of having In atoms residing at the T_4 hollow sites shown in Fig. 5.5(g), where each In atom (valence 3^+) bonding with three Si atoms on the unreconstructed 1x1 Si(111) surface resulting in a coverage

of 1/3ML, as first reported by Lander and Morrison.[1] The phase designated as α-Si (111)-√3-In (in short α-√3), is widely observed in the literature in the In coverage range of 0.2 to 0.4ML. However, in our phase diagram in Fig. 5.4 we see that the √3 phase extends from the coverage range of about 0.2ML to 1ML of In on the surface. Lander and Morrison had also observed a β-Si (111)-√3-In (in short β-√3) phase at room temperature with the continual deposition of In on to the α-√3 phase at a coverage of around 1ML.[1] This β-√3 phase can be the same as the √3 phase observed by us around 1ML, though adsorption temperature in the two studies are different. This phase is modeled to have a triplet In geometry above the T_4 sites. The fact that we also see the √3-In phase between the α-√3 (0.33ML) and β-√3 (1ML) suggests the presence of an intermediate atomic arrangement yielding the same √3 symmetry. We recall the early works on Si (111)-√3-Ag structure, where there were competing models for 0.33, 0.66 and 1ML, prompts us to designate this intermediate phase as √3-γ at around 0.6ML.[18] The observation of √3-Ag structures at 0.33, 0.66 and 1ML was explained by proposing that the coverage of the phase is preparation history dependent.[19,20] Thus, the dependence of the surface phases on growth kinetics calls for more controlled experiments and understanding. The Si (111)√31x√31R9°-In phase at 0.6ML, has been reported by RHEED, STM studies and not by LEED observations.[12,21] In our LEED study the phase is not observed, which can be attributed to the differences in the probing depths by the two techniques or differences in sample preparation.

In recent years there has been a great interest regarding the 4x1-In phase, which comprises of self assembled 1D atomic chains on the silicon surfaces. Structural model proposed by Bunk et al.[23] for 4x1 reconstruction is shown in Fig. 5.5(h) which shows 1D chains of the In as well as the reconstruction of underlying Si layer. In our phase diagram the phase is observed in the coverage range of 0.5ML to 1.2ML and the LEED observed is shown in Fig 5.5(c). A √7x√3 phase is observed above 1.2ML coverage and above 400°C, which is shown in Fig 5.5(f). The combined STM-LEED study of J. Kraft et al. has resolved the confusion between the 1x1R30° and √7x√3 phases by identifying the weak spots in the LEED pattern and their STM results revealed two coexisting unit cells of √7x√3 phases with different atomic geometries, appearing as 1x1R30°.[24] Though in our LEED pattern, the fractional order spots are not very well resolved, the coverage and temperature regime, and the sequence of appearance in the phase diagram suggest that the LEED pattern corresponds to the √7x√3 phase.
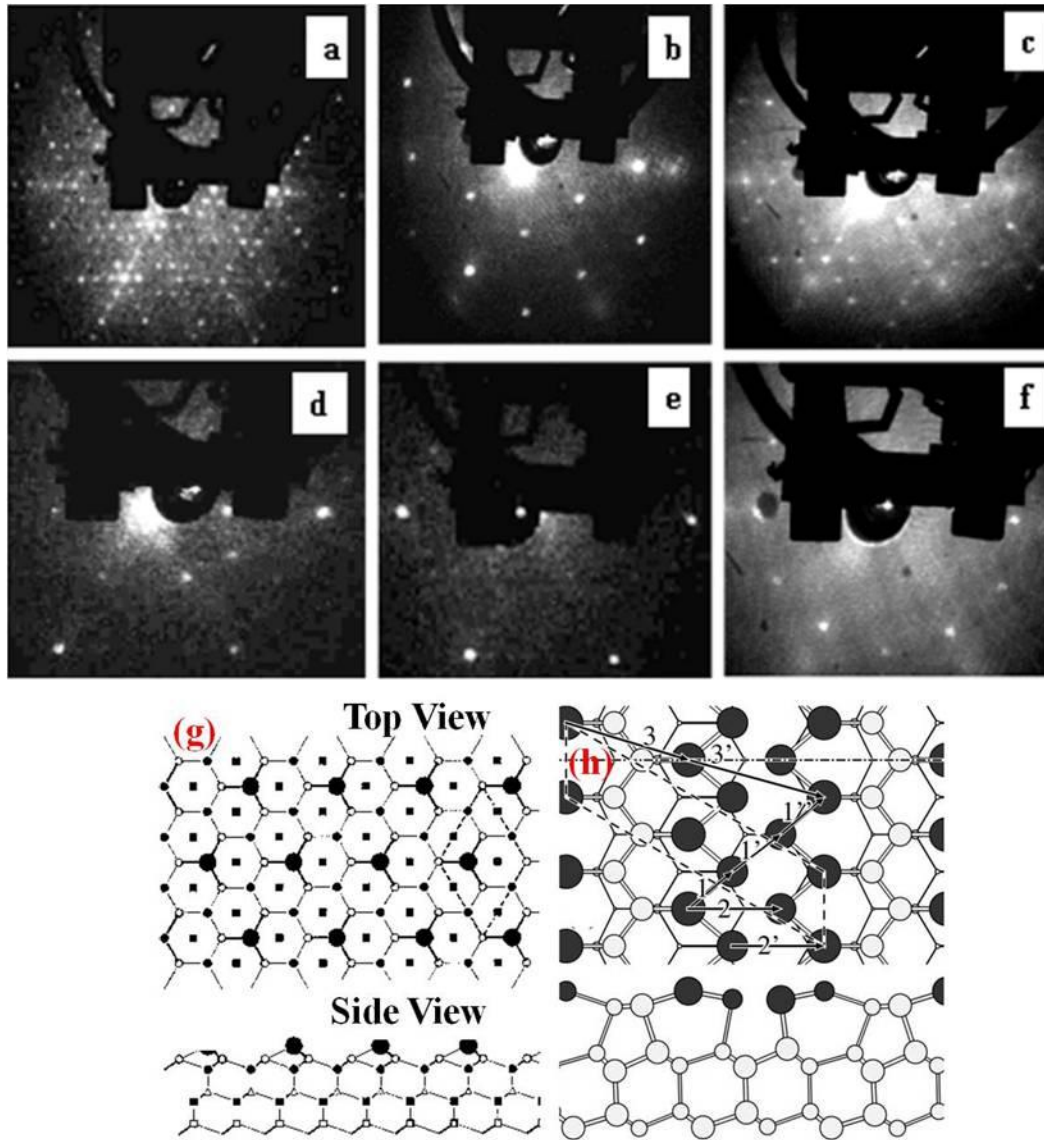
Fig. 5.5: *Different two dimensional phases observed for the In/Si(111) system during adsorption and desorption processes. (a) Si(111)7x7-In, (b) Si(111)√3x√3R30^o-In, (c) Si(111)4x1 3D-In, (d) Si(111)2√3x2√3R30^o-In (e) Si(111)1x1R30^o-In (f) Si(111)√7x√3-In (g) structural model for √3x√3 surface[22] and (h) 4x1 surface.[23]*

5.1.5   *ab initio* DFT modeling of Si (111)-2√3x2√3R30^o-In surface

We report here the rarely observed Si(111)2√3x2√3R30^o-In phase as shown in Fig. 5.5(d), which was first reported to be an intermediate state between the α and β-√3 phases at room temperature in the coverage range of 0.5 to 1ML.[1]   It has been attributed to different

structural models with different coverages considering triplets of In atom at different sites on the bulk truncated Si (111) surface, and later Aiyama et al. reported the phase as resulting from cooling of the √3-In phase. Since, then any results or discussion of this phase have not appeared in the literature.[12]   As shown in the phase diagram in Fig. 5.4, we observe the phase during annealing studies at around 1ML at ~ 450°C. However, it has to be noted that this phase is only observed during residual thermal desorption experiments, whereas our attempts to observe it during adsorption were not successful. When one carefully observes the desorption curve of In on the Si (111) surface from literature it is clear that the final In desorption from the surface takes place in a narrow temperature range.[25] Since we observe 2√3 phase in this region where one cannot measure the coverage precisely, it could be the reason for non-reproducibility of the phase in the literature.

We study here the atomic geometry of the 2√3 phase using *ab inito* density functional theory and simulate STM images. To calculate the bulk lattice constant of silicon, total energy calculations have been performed, considering silicon unit cell as face centered cubic with two atom basis. Total energy per unit cell is calculated as a function of lattice constant and cubic spline fitting is performed on the data. Lattice constant is found to be 5.47Å, which is within 0.8% of the experimental results and agrees well with other calculations using pseudopotentials and GGA.[26]
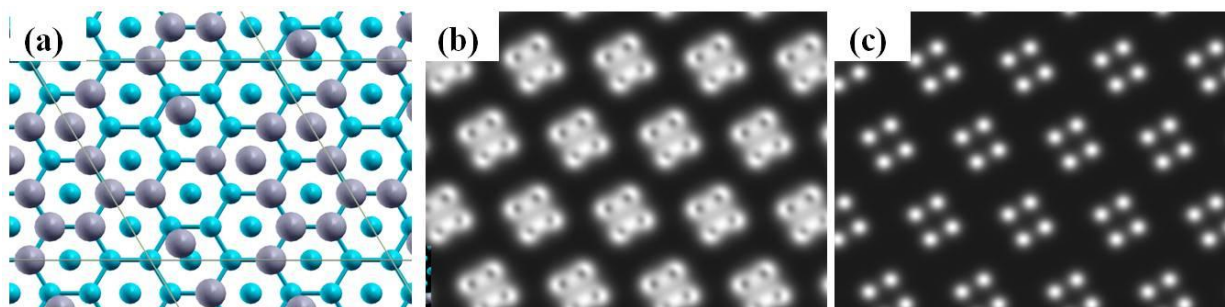
Fig. 5.6: *Results of ab initio DFT based STM image simulation of Si (111)2√3x2√3R30°-In phase. (a) Model, (b) Filled state STM image calculated for +1.5V and (c) Empty state STM image calculated for –1.5V.*

The coverage range, temperature and symmetry of the 2√3-In phase observed here is expected to be very proximal to the Si (111)2√3x2√3R30°-Sn (2√3-Sn in short) phase. Si (111)2√3x2√3R30°-Sn phase, which has received a lot of attention in recent years, serves as a template for studying quantum size effects in the ultra thin Sn film.[27] This was observed by Erupt

and Morrison by Low Energy Electron Diffraction studies in the approximate coverage of 1ML at about 450^oC.[28] The structural model proposed by C. Tornevik et al. has been supported by other experimental results.[29,30] The different adsorption sites on the bulk truncated Si(111) surface considered in this model are T_1 (on-top), H_3, T_4 and on top site.[22] The Sn model used for In is shown in Fig. 5.6(a), which consists of fourteen In atoms in two subsequent layers. Eight In atoms in the first layer are placed at on-top sites with the two other In atoms at the bridge sites; thus ten In atoms satisfy all the dangling bonds of the twelve silicon atoms present in the $2\sqrt{3}$ unit cell. Out of the four remaining In atoms, two lie at the T_4 sites and the other two at the H_3 sites, as shown in Fig. 5.6(a). The structure is allowed to relax to achieve the minimum energy configuration for the $2\sqrt{3}$-In.

	Filled state STM image: distance (Å)				Filled state STM image: distance (Å)			
	T_4-T_4	H_3-H_3	T_4-H_3	$\Delta(T_4H_3)$	T_4-T_4	H_3-H_3	T_4-H_3	$\Delta(T_4H_3)$
For Sn	3.7±0.2	4.2±0.2	5.3±0.2	0.9±0.3	4.6±0.2	4.2±0.2	5.3±0.2	0.5±0.2
For In Present calculation	3.59	3.59	4.29	0.00	3.59	3.59	4.29	0.00

Table 5.1: *Table of interatomic separations of top four atoms from DFT calculations for Si (111)$2\sqrt{3}x2\sqrt{3}R30^o$-In phase and from the experimental observation for Si(111)$2\sqrt{3}x2\sqrt{3}R30^o$-Sn*[29].

The simulated STM image for sample biases of +1.5V and -1.5V, which corresponds to filled and empty state images respectively, is shown in Fig. 5.6(b) and Fig. 5.6(c). Both images show four bright protrusion. In the empty state image the bright protrusions are well separated in intensity, whereas in the filled state image, the intensities overlap. These protrusions corresponds to the four In atoms which are at the top of the surface, of which two lie at T_4 and the other two lie at the H_3 sites. In the filled state image we also observe dark region at the center of each bright protrusion, which corresponds to the bright protrusions in the empty state image. The details of the relaxation calculation is summarized in Table 5.1 which shows the separation between the top lying atoms, from the $2\sqrt{3}$-In DFT calculations and that reported for

the $2\sqrt{3}$-Sn phase.[29] In the case of $2\sqrt{3}$-Sn phase the Sn atoms lying in T_4 and H_3 showed height differences, which for the filled state image ~0.9Å and for the empty state image ~0.5Å respectively and suggest an electronic and geometric origin of height differences. But the simulated STM images in the present study shows equally bright protrusions in both filled and empty state image as indicated by the value of zero for Δ (T_4H_3) in Table 5.1. The reason for the intensity difference is the adsorption site energies, whereas our calculation for the case of In adlayer suggests that even different adsorption sites may result in the equal height of adsorption and equal intensity. This may be attributed to the weak bonding between the silicon and the second layer of In atoms where the In atoms tend to adopt its bulk lattice parameters. Other measured parameters like H_3-H_3 distance and T_4 -T_4 distances show considerable differences between the two cases as shown in Table 5.1.

5.2   Adsorption/desorption of In on Si (5 5 12)2x1 surface

5.2.1 Introduction

Si (5 5 12) 2x1 surface is a very interesting surface with its inherent trenched morphology. These faceted grooves provide researchers an opportunity to grow 1D nanostructures with unprecedented assembly control. These systems display novel structural and electronic properties and also enable the understanding of low dimensional physics of metallic overlayers. This indeed was proved by several researchers[31,32], immediately after it was first discovered by Baski et al.[33] The (5 5 12) surface lies about 30.5° below the (001) plane as shown in Fig. 5.7, which is a cross-sectional schematic view of the bulk silicon cut perpendicular to the [66$\underline{5}$] direction.[33,34] The (5 5 12) unit cell is composed of two units of (337) and one unit of (225) facets, and a 2x1 reconstruction of the bulk truncated structure minimizes the energy by reducing the number of dangling bonds from 48 to 23.[34] Detailed structural analysis has shown that the 2x1 reconstruction consists of a (337) unit with a dimer-adatom row, another (337) unit with a trimer row and a (225) unit with a dimer-adatom and trimer row. As shown in the figure the surface can also be decomposed into different combinations of (225), (337), (112), (113) and (7 7 17). It is also reported that under appropriate kinetic conditions, metal adsorption can lead to the conversion of the (5 5 12) surface into different facets.[35]
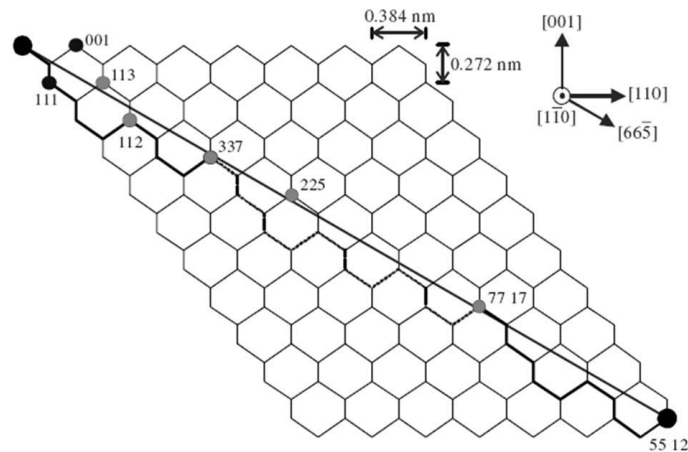
Fig. 5.7: *A cross-sectional view of the bulk Si cut perpendicular to the [66$\underline{5}$] direction showing the Si (5 5 12) surface which lies about 30.5^{o}C from the horizontal (001) plane. The solid circles mark unit cells of number of bulk-terminated orientations. Also shown are the different facets (113), (225), (337), (112) and (7 7 17).*

5.2.3   Room temperature adsorption

Fig. 5.8(a) and 5.8(d) shows the LEED pattern of the clean Si (111)-7x7 and Si (5 5 12)2x1 surface reconstructions respectively. Also shown in Fig. 5.8 are the line scans of the different LEED patterns of Si (5 5 12) surface along the [66$\underline{5}$] direction. The 7x7 reconstruction, which has 19 dangling bonds per unit cell, is well described by the famous DAS (dimer-adatom-stacking fault) model[16], with characteristic six fractional order spots between the sharp bulk spots while the high index Si (5 5 12) surface, has 16 fractional spots contributed by the (337) and (225) facets that it comprises of. Of the 23 dangling bonds of the (5 5 12) six, nine and eight originate from the dimer (337), (225) and tetramer (337) units respectively.[34] The faint streak, which goes parallel to the [6 6 $\underline{5}$] direction, marks the x2 periodicity of the reconstruction along the [$\underline{1}$10] direction.[32] From the analysis of intensity line scans along the [66$\underline{5}$] direction, the distance between two consecutive spots in reciprocal space is found to be 1.17nm^{-1} which corresponds to 5.35nm in real space.[32] The spacing along the [$\underline{1}$10] direction 8.15nm^{-1} (real space distance of 0.77nm) is double the periodicity of the unreconstructed surface along this direction.
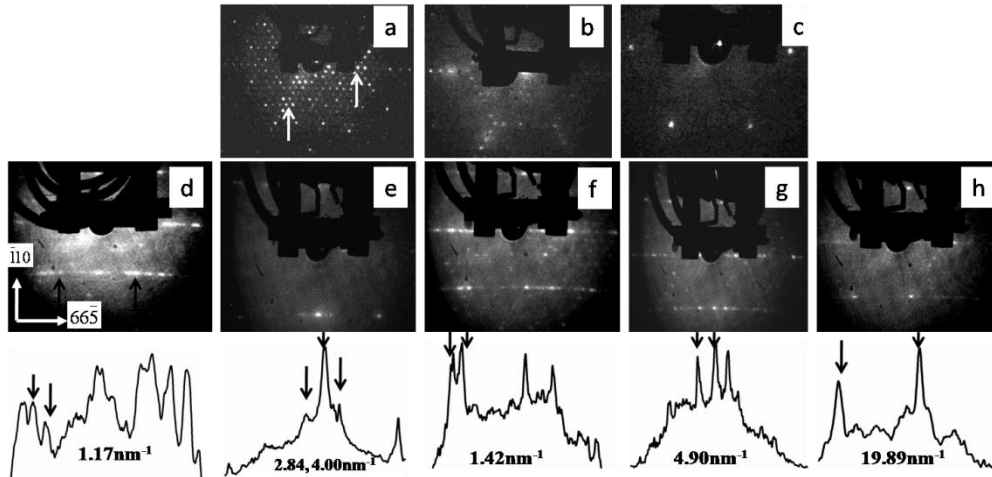
Fig. 5.8: *The LEED pattern observed during RT adsorption of In Si (111)7x7 (a to c) and Si (5 5 12) 2x1 surface (d to h). a) Clean Si (111)7x7 b) after adsorption of 1ML of In c) Si (111)1x1 surface with 2ML In adsorption d) Clean Si (5 5 12) 2x1 surface e) after adsorption of 0.2ML of In, representing the (225) and (335) facets f) after 0.5ML of In, showing the 2x(225) facet g) after 1.5ML adsorption of In, showing 2x113 facet h) after 2ML adsorption showing the bulk 1x1 spots. The line scans of the LEED pattern for the Si (5 5 12) surface taken along [66$\underline{5}$] direction are shown at the bottom panel.*

We carried out adsorption experiments to understand the growth mode of In on the two surfaces with different substrate structures. Fig. 5.9 shows the uptake curve for the adsorption of In on the Si (111)-7x7 and Si (5 5 12)-2x1 surface kept at room temperature (RT). Reports in literature show that the growth of In on the Si (111)-7x7 surface proceeds in the Stranski-Krastanov mode, with 3D islands on an uniform pseudomorphic In layer up to 2ML.[8,9] In Fig. 5.9 the ratio of Auger signals of In MNN (404eV) to the Si LVV (92eV) transitions is plotted against the deposition time. The overall trend of growth of In on the two surfaces shows a linear segment up to about ten minutes of adsorption which we attribute to the completion of 1ML and the second 10min segment is linear with a higher slope.[25] However, the uptake curve of the two surfaces (111) and (5 5 12) show differences in both the segments of the curve. To accurately determine the break point, we have used the SSQ (sum of squares of errors) method from the literature, where one calculates the errors in the slopes of the linear fit to the points around which a break is suspected.[14] The calculated SSQ is plotted as a dashed curve along with the uptake curve in Fig. 5.9, whose minima corresponds to the break point at 10 min of adsorption. On Si (111) we take this point to correspond to 1ML and thus the flux rate is determined to be 0.1ML per minute.[14]
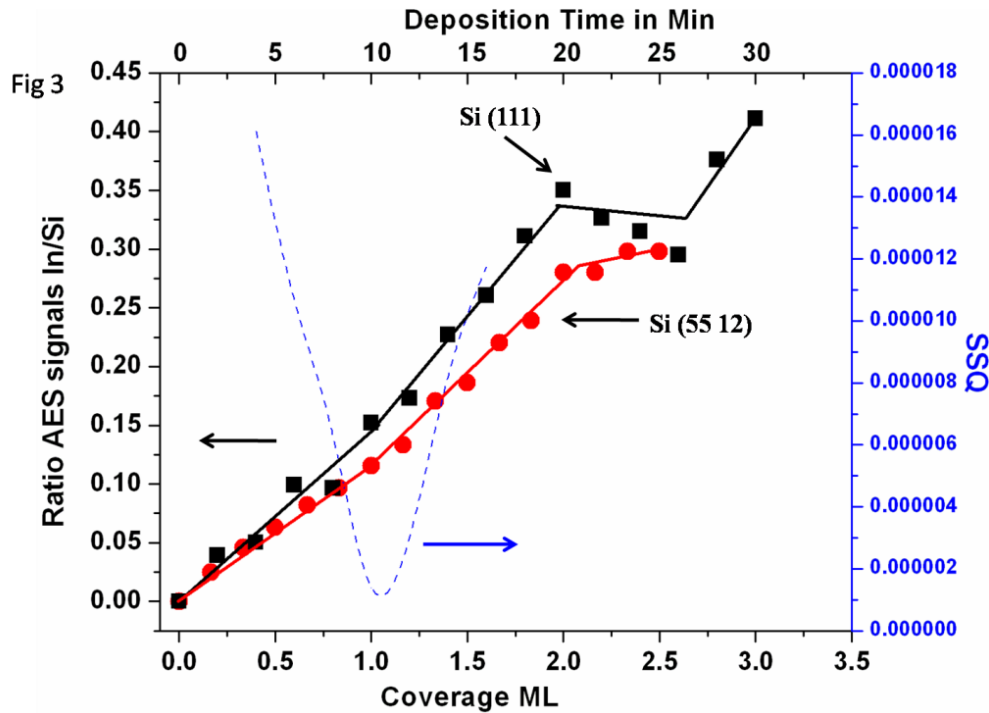
Fig. 5.9: *The Auger uptake curve for RT In adsorption. The corresponding deposition time is shown in the top x-axis. The right y-axis represents the SSQ calculated to find the break in the uptake curve, which is shown as dashed curve in the figure.*

The interpretation of LEED for room temperature adsorption becomes difficult owing to the low intensity of the fractional order spots and slight disorder in the surface phases formed. However, intensity line scans change in the LEED pattern observed. On the Si (111)-7x7 surface with 0.5ML adsorption of In, the fractional order spots becomes weak (Fig. 5.8(b)) and disappear at 2ML, resulting in a clear (1x1) pattern (Fig. 5.8(c)). On the Si (5 5 12)-2x1 surface, when 0.2ML of In is adsorbed, the weak streak along the [66$\underline{5}$] direction vanishes, showing that the x2 periodicity of the reconstruction is lifted along the [$\underline{1}$10] direction, resulting in the bulk truncated (5 5 12) surface. The lattice separation becomes 0.384nm along this direction and the line scan along the [66$\underline{5}$] direction (Fig. 5.8(e)) shows the unit cell periodicity of two facets viz. (225) and (337).[25] Thus, we infer that the two differently structured (337) units undergo structural transformation to become a single (337) unit. The fractional order spots along the [66$\underline{5}$] direction diminish in intensity with adsorption up to 0.5ML. At around 0.5ML of adsorption, the intensity line scan along the [66$\underline{5}$] direction shows the formation of a well ordered In induced 2x(225) facet as shown in Fig. 5.8(f). Previous studies on Au and Sb on Si (5 5 12) surface have shown that these facets consist of adsorbate induced quasi 1D (one dimensional) chain like

features.[32,36] Though the exact structure and electronic properties of these facets are known for other systems, there are hardly any known for In.[36] The interchain separation can be measured by calculating the separation of the spots in the LEED pattern which is found to be 1.42nm^{-1} in reciprocal space, which corresponds to a real space distance of 4.4nm. When the coverage is increased, we observe weakening of the fractional order spots.

For coverages greater than 1ML the slope of the second part of the segment of the uptake curve is higher, as shown in Fig. 5.9. This increase in the slope of the uptake curve shows the formation of second layer of In on the surface. At about a coverage of 1.5ML, we observe LEED fractional order spots which correspond to 2 x (113) facet shown in Fig. 5.8(g), which is previously reported to be consisting of 1D nanochains.[35] The analysis of the line scan along [66$\underline{5}$] gives a reciprocal lattice spacing of 4.90nm^{-1}, which is equivalent to 1.28nm. When the coverage becomes 2ML the uptake curve saturates, indicating the formation of 3D islands on the surface. This behavior is qualitatively similar for both the surfaces and the growth proceeds in a similar fashion. The intensity of fractional order spots becomes very weak at this coverage and we could only observe bulk spots in the LEED pattern on both the surfaces as shown in Fig. 5.8(c) and 5.8(h). Further deposition of Indium results in the rise of intensity of AES ratio for Si (111) surface which is attributed to the layering of the islands. But we could not observe similar behavior on the Si (5 5 12) surface, which shows only the saturation of intensity ratio. Also we observe from Fig. 5.9 some differences between the uptake curves on the two surfaces. The ratio of AES intensities for the two surfaces, Si (111) 7x7 and Si (5 5 12)-2x1, deviate less below 1ML, but is greater for higher coverages, due to the structural differences of the two surfaces. Thus, overall growth is in the Stranski-Krastanov mode with anomalous clustering and layering of In adatoms on the Si (111) surface. A schematic of the general morphology of the observed growth mode on the two surfaces is shown in Fig. 5.10(a) assuming a final coverage of 3ML on the surface. The schematic also shows the desorption of 3ML In system at different temperatures which will be described while explaining the thermal desorption results.

In the recent literature there is a lot of interest regarding the quantum size effects in metallic thin overlayer formation.[37] Researchers have observed that under favorable conditions, assisted by the kinetics of the growth, the quantum size effect energy can find a certain minima leading to certain metastable phases which have preferred island sizes.[38] In the present experiments for the observed growth morphology, we speculate that the quantum size effect may

be dominating during the growth leading to certain island sizes. As the coverage on the surface increases, the confinement effect induced stability reduces and the size of the islands becomes large and consequently agglomerate to form layers. We will refer back to these observations
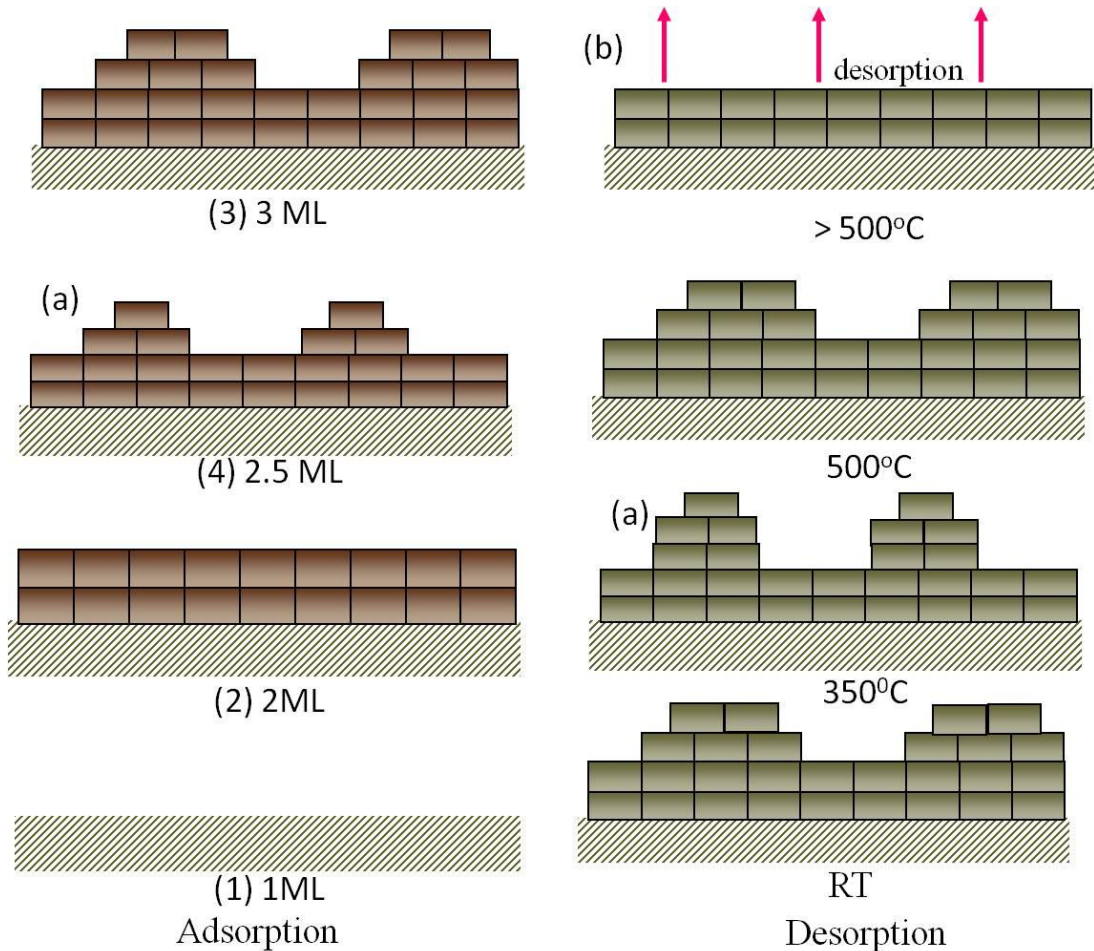
Fig. 5.10: *(a) A schematic for the adsorption sequence for 3ML In on Si (111) and Si (5 5 12) surfaces. (b) A schematic of the desorption sequence of the In from the Si (111) surface assuming an initial coverage of 3ML.*

while describing the residual thermal desorption results. As previously demonstrated (for other metals) by our group[32] and others[36], our present experiments have shown that the trenches on the Si (5 5 12) surface can be used as templates to grow 1D In nanochains. We note that the major structural change in the LEED pattern on the Si (111) surface takes place at 2ML i.e. the conversion of the 7x7 reconstruction into 1x1 and on the Si (5 5 12) surface, we observe conversion to facets at around 1ML. This will be later corroborated with the desorption process.

5.2.3 Residual thermal desorption

The thermal stability of the system is studied by residual thermal desorption experiments where the system is subjected to annealing at different temperatures for fixed times, and the consequent AES and LEED results are shown in Fig. 5.11 and Fig. 5.12 respectively. Fig. 5.11 shows the variation of the ratio of the In (404eV) MNN peak to the silicon (92eV) LVV peak with annealing temperature for both Si (111) and Si (5 5 12) surfaces. For comparison, we have presented two representative data from Si (111) and Si (5 5 12) surfaces. For Si (111) surface the initial coverage on the surface is about 3.5ML consisting of two flat layers of In with islands above. For the Si (5 5 12) surface initial coverage on the surface is 2.2ML with two flat In layers plus islands on top. This description of the initial morphology follows from the interpretation of the observed uptake curve. The overall trend of the two desorption curves are the same, but with subtle differences. To facilitate discussion, we divide the desorption curve into five different regions, marked as [1], [2]… [5] in Fig. 5.11. Both the curves show an initial fall in the intensity ratio up to a temperature of 300^oC (region [1]), 2nd region from $300-450^oC$, where the intensity remains constant, followed by a rise in the intensity ratio at a temperature of 450^oC (region [3]) and a final steep fall in the ratio with temperature (region [4] & region [5]). These observations can be explained as follows: When the adsorbed adlayer is subjected to annealing, there is an initial fall in the intensity ratio due to the agglomeration of the adatom into larger clusters, which costs energy because of the creation of new surfaces. This is compensated by the strain relaxation in the as-adsorbed overlayer, due to the 14.8% lattice mismatch between surface and overlayer[8]. The electron diffraction shows the 1x1 pattern from the overlayer as shown in Fig. 5.5(e) and 5.8(h), which becomes sharper with annealing. The Arrhenius activation energy for agglomeration is calculated to be 0.08 eV on the (111) surface and 0.11 eV on (5 5 12) surface[39].

The flat portion of the desorption curve (region [2] in Fig. 5.11) shows that the morphology on the surface remains essentially the same in this temperature range. Compared to the previous region, on the Si (5 5 12) surface we observe a few fractional order spots as shown in Fig. 5.12. From the line scan of the LEED pattern we could not identify the phase to be of any particular facet as the number of reflections is limited and very weak. The rise in the intensity ratio in region [3] in Fig. 5.11, has the same temperature of about 450^oC on the two surfaces, and
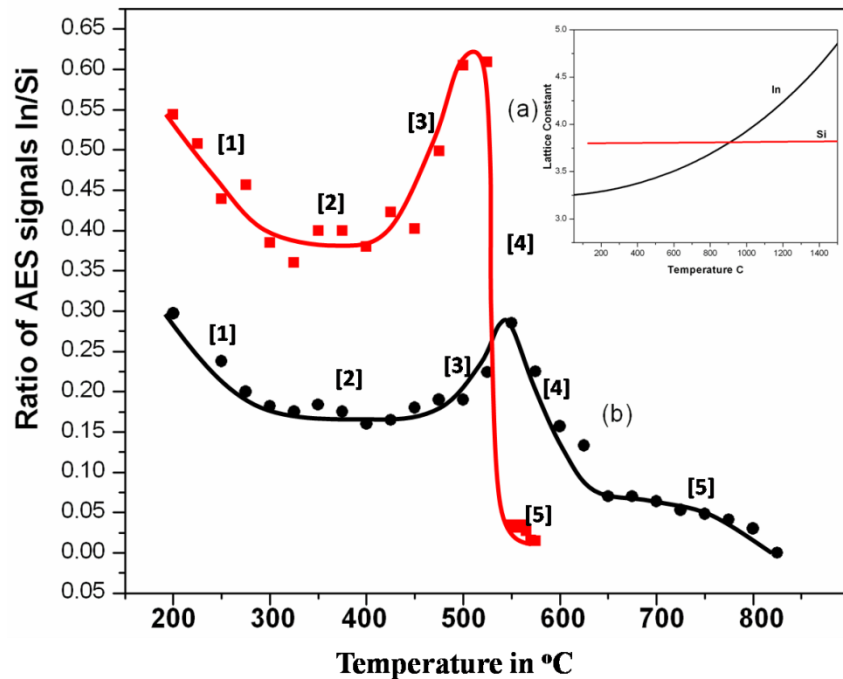
Fig. 5.11: *Desorption curves of In on Si (111) (curve a) and Si (5 5 12) (curve b). The ratio of AES signal of In MNN (404eV) to Si LVV (92eV) is plotted versus annealing temperature. The different regions on the two curves are marked in square brackets [1], [2] etc.. The inset in the figure shows the variation of the Si and In lattice parameters with temperature.*

is attributed to the In islands converting into layers and consequently increasing the AES ratio. The activation energy for this layering is calculated to be 0.28eV on (111) and 0.40eV on (5 5 12) surfaces. The similarity in temperature on the two surfaces suggests presence of an energy barrier for layering. This could be the step-edge diffusion barrier which prevents the agglomerated clusters from layering. In this region at around 500°C the line scan along the [66$\underline{5}$] direction shows (Fig. 5.8(g)) the presence of the 2x(113) facets on the surface. This is the same phase that we observed during the room temperature adsorption process at around 1.5ML. On the (111) surface we observe two superstructural phases viz. $\sqrt{7}$x $\sqrt{3}$-In (Fig. 5.5(f)) and 4x1-In (Fig. 5.5(c)). [40]

One of the important things to note here is that the stable layer above which clustering takes place is different for the two surfaces. In the case of Si (111) surface the agglomeration and layering takes place above the first flat 2ML of In, whereas for the Si (5 5 12) surface this happens on 1ML of In. Correlating with the LEED observations, the disappearance of the fractional order spots to 1x1 pattern on the 7x7 surface and the conversion of the 2x225 facet to
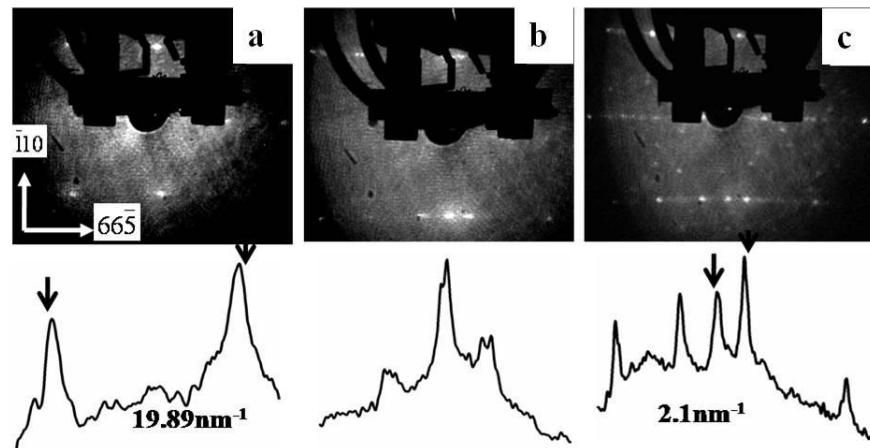
Fig. 5.12: *LEED pattern observed during residual thermal desorption experiments for Si (5 5 12) surface. a) The diffraction pattern in the region [1] in Fig. 5.11, b) The LEED pattern in region [2] in Fig. 5.11, c) The 2x(337) facet obtained at 600°C with a coverage of 0.75ML. The line scans of the LEED pattern for the Si (5 5 12) surface taken along [66$\underline{5}$] direction are shown in the bottom panel.*

2x113 facets on (5 5 12) surface takes place at the above mentioned coverages, respectively. This can be related to the saturation of dangling bonds on the surfaces. On Si (111) surface, we have previously reported that the dangling bonds are saturated around 2ML of In adsorption, as inferred from the Si LVV (92eV) peak excursion ratio.[25] From a similar procedure we have estimated that on Si (5 5 12) surface this takes place around 1ML of In adsorption, as the trenches may provide a more effective way of saturating the dangling bonds.[25]

Beyond region [3] in Fig. 5.11, on both the surfaces, the intensity ratio falls because of the onset of desorption (sublimation) of Indium adatoms from the surface. The complete desorption for In on Si (111) surface takes place around 600°C and on the Si (5 5 12) at about 850°C. The onset temperature for desorption is different on the two surfaces- 500°C for Si (111) and 550°C for Si (5 5 12) surface. This temperature is higher for the Si (5 5 12) as compared to Si (111) surface, showing stronger bonding sites on the (5 5 12) surface owing to better co-ordination on this facetted surface. Another observation is that the desorption of In adatoms on the Si (5 5 12) surface takes place over a wide temperature range of 300°C with a long tail, while on Si (111) it is around 50°C. This desorption at higher temperatures indicates the facetted nature of the (5 5 12) surface which provides stronger adsorption sites for the In adatoms. This region we have further divided into two subunits, region [4] and [5] shown in Fig 5.11. On the Si (111) surface region [4] is very narrow and the 2√3x2√3 reconstruction (Fig. 5.5(d)) is

observed in this region.[41]   At around 600°C on the Si (5 5 12) surface, the coverage is about 0.75ML and we observe an ordered LEED pattern. The intensity line scan taken along the [66$\underline{5}$] direction shows that the structure consists of 2x337 facets as seen in Fig. 5.12(c) which has been reported for Au and other metals on Si (5 5 12) surface, to be made up of quasi 1D metal nanochain structures.[35,41] The interchain separation of these facets determined by measuring the separation between the LEED spots along the [66$\underline{5}$] direction is 3.2nm. The absence of the weak streak along the ($\bar{1}$10) direction indicates that the periodicity along this direction remains to be that of bulk structure. Here we find that the activation energy is high on the (111) surface, compared to the value 0.80eV on (5 5 12) owing to the fast desorption on the (111) surface with temperature.

On the (111) surface the final surface geometry after the sharp desorption is the Si (111) √3x√3R30° (Fig. 5.5(b)) – In surface, which appears in region [5], as indicated by the LEED pattern.[42] This is planar with bulk truncated silicon structure and is a stable surface as all the dangling bonds are satisfied.[42] Since the surface is chemically passivated, the In layers lying above are bonded with a specific energy to the substrate allowing a fast desorption in a narrow temperature window. In this region on the (5 5 12) surface, at around 700°C we observe the 2x(225) from the LEED pattern, which is the same surface phase as the one observed during the RT adsorption at 0.5ML. The difference in the value of the activation energies of 4.4eV on (111) and 0.54eV on (5 5 12) surface reflects the different facets from which desorption of In atoms takes place. The dangling bond density on the (113) surface is less than that on the (337) which in turn is less than that on the (225) unit, and is manifested in the desorption sequence as well.[34] The desorption region around 600°C (region [4]) marks the formation of 2x(337) facet which, owing to the lesser number of dangling bonds, shows comparatively weaker bonding and hence allows faster desorption as compared to the final desorption from the (225) facet (region [5]). Finally above 600°C on (111) and around 850°C on (5 5 12) surfaces, we retrieve the clean 7x7 and 2x1 reconstructions, respectively. A schematic of the desorption process for the Si (111) surface is shown in Fig. 5.10(b) assuming an initial coverage on the surface to be 3ML. For the Si (5 5 12) surface the overall picture remains the same, except that the stable layer is 1ML instead of 2ML in the (111) case.

Thus, qualitatively we observe a kind of retracing of the adsorption pathway during desorption with the sequence being (225) + (337) − 2x (225) − 2x (337) − 2x (113). The facet 2x

(337) could not be observed by LEED during the room temperature adsorption, due to weak fractional order spots. This reversibility in structural transformation on Si (5 5 12) surface and the clustering and layering on Si (111) surface show that the effect is geometric without any chemical interaction at the interface.

       The clustering and layering evident in the adsorption and desorption process, is attributed to different origins. In case of the desorption process, the role of quantum size effect is minimal since the energy gain involved may be very less in comparison to other high temperature effects. If we look at the process thermodynamically, there is a huge lattice mismatch of about 14.8% and different thermal expansion coefficients.[8] Thus, adsorbed ln clusters when subjected to annealing start agglomerating on top of a wetting layer, in a narrow temperature range. In the inset Fig. 5.11 we have plotted the bulk lattice parameters of silicon and indium as a function of temperature.[43] We find that with application of temperature there is a gradual reduction in the lattice mismatch which promotes layering of the In islands, due to reduced strain. Since the onset of the temperature for layering on both the surfaces is about 450°C, it is independent of the substrate surface geometry. Thus, the layering results from the relaxation of strain as well as the In atoms overcoming the step-edge diffusion barrier on islands.

5.3 Conclusions

       We have studied the behavior of In adatoms on Si (111)-7x7 and Si (5 5 12)-2x1 surfaces. On both surfaces the room temperature adsorption show Stranski-Krastanov growth mode with island formation starting above 2ML. The analysis of the excursion curves for Si (111) surface shows that the dangling bond saturation takes place at 2ML adsorption of Indium. We have summarized our results of adsorption and residual thermal desorption of Si (111)7x7-In system in the form of a 2D phase diagram, which depicts the evolution of the different interfacial phases as a function of temperature and coverage. The phase diagram presented here shows significant differences compared to that reported in the past. One of the main observations is the occurrence of three √3-In phases, which spans the coverage range from 0.2 to 1ML. These, we have assigned as √3-α, √3-β and √3-γ phases with 0.33, 1.0 and 0.66ML coverages respectively. Another phase observed during annealing is the 2√3 phase, and to shed some light on this structural phase, we have considered the proximal 2√3-Sn model. We have performed density functional theory based STM image simulation for the model, which will facilitate direct

comparison with future experiments. For the $2\sqrt{3}$-In phase we find subtle differences with the model proposed for $2\sqrt{3}$-Sn phase, after performing energy minimization calculations. A comparative study of clustering and layering effects on both Si (111) and Si (5 5 12) surface is presented. On Si (111) surface above 2ML we observe layering of 3D clusters which may be due to the quantum size effects operating at these low dimensional islands. We observe the differences in the stable layer above which agglomeration takes place for the two surfaces. The onset temperature of desorption and the temperature regime in which In completely desorbs from the surface is attributed to effective dangling bond saturation and strain relaxation, and the presence of a step-edge diffusion barrier. A comparison of the thermal expansion coefficient of In and Si at higher temperature shows that there is a reduction in the lattice mismatch between the adsorbate and substrate leading to lowering of strain which helps in the layering of In clusters. We have monitored the surface symmetry during adsorption and desorption, which shows different superstructural phases on Si (111). On the Si (5 5 12) surface we observe the formation of quasi 1D nanochain structures on the 2x225, 2x113 and 2x337 facets.

References

[1] J. Morrison, J. Appl. Phys. **36**, 1706 (1965).

[2] Yoichiro Yagi, Akio Yoshimori, Kiminori Kakitani, and Hiroko Kaji, Surface Science **601**, 1642-1645 (2007).

[3] Sang-il Park, Phys. Rev. B **36**, (1987).

[4] J. Ahn, J. Byun, J. Kim, and H. Yeom, Physical Review B **75**, 2-5 (2007).

[5] J. Wang, Huasheng Wu, Ricky So, Y. Liu, M. Xie, and S. Tong, Physical Review B **72**, 1-5 (2005).

[6] U. Ramsperger, Appl. Phys. Lett. **22**, 4169 (2002).

[7] S. Mizuno, Y. Mizuno, and H. Tochihara, Physical Review B **67**, 1-8 (2003).

[8] M. S. Finney, C. Norris, and P. B. Howes, Surf. Sci. **277**, 330 (1992).

[9] H. Ofner, S. L. Surnev, Y. Shapira, and F. P. Netzer, Phys. Rev. B **48**, 10940 (1993).

[10] Manhui Sun, Chuan Hu, R.G. Zhao, and Hang Ji, Thin Solid Films **489**, 111 (2005).

[11] H. Hirayama, S. Baba, and A. Kinbara, Appl. Surf. Sci. **33/34**, 193 (1988).

[12] T. Aiyama and S. Ino, Surf. Sci. **82**, L585 (1979).

[13] J. Kraft, M. G. Ramsey, and F. P. Netzer, Phys. Rev. B **55**, 5384 (1996).

[14] C. Argile and G. E. Rhead, Surface Science Reports **10**, 277-356 (1989).

[15] D. E. Ramaker, F. L. Hutson, N. H. Jurler, and W. N. Mei, Phys. Rev. B **33**, 2547 (1986).

[16] K. Takayanagi, Y. Tanishiro, S Takahashi, and M. Takahashi, Surf. Sci. **164**, 367 (1985).

[17] S. Mizuno and Y. O. Mizuno, Phys. Rev. B **67**, 195410 (2003).

[18] M. Katayama, R. S. Williams, M. Kato, E. Nomura, and M. Anno, Phys. Rev. Lett. **66**, 2762 (1991).

[19] S. M. Shivaprasad, S. Bera, and Y. Aparna, Bull. Mater. Sci. **21**, 111 (1998).

[20] S. Kono, Surf. Rev. Lett. **1**, 359 (1994).

[21] A. A. Saranin, A. V. Zotov, A. N. Tovpik, M. A. Cherevik, E. N. Chukurov, V. G. Lifshits, M. Katayama, and K. Oura, Surf. Sci. **340**, 36 (2000).

[22] J. P. LaFemina, Surf. Sci. Rep. **16**, 133 (1992).

[23] O. Bunk, G. Falkenberg, J. H. Zeysing, L. Lottermoser, R. L. Johnson, M. Nielsen, F. Berg-Rasmussen, J. Baker, and R. Feidenhans'l, Phys. Rev. B **59**, 12228 (1999).

[24] J. Kraft, S. S. Surnev, and F. P. Netzer, Surf. Sci. **36**, 340 (1995).

[25] K. Jithesh, M. Kumar, and S. M. Shivaprasad, J. Nanosci. Nanotechnol. **9**, 5417 (2009).

[26] S. Ozkaya, M. Cakmak, and B. Alkan, Surf. Sci. **602**, 1376 (2008).

[27] L. L. Wang, X. C. Ma, S. H. Ji, Y. S. Fu, Q. T. Shen, J. F. Jia, K. F. Kelly, and Q. K. Xue, Phys. Rev. B **77**, 205410 (2008).

[28] P. J. Estrup and J. Morrison, Surf. Sci. **2**, 464 (1964).

[29] C. Tornevik, M. Hammer, N. G. Nilsson, and S. A. Flodstrom, Phys. Rev. B **44**, 13144 (1991).

[30] L. Ottaviano, G. Profeta, L. Petaccia, and C. B. Nacci, Surf. Sci. **554**, 109 (2004).

[31] Jin-Feng Jia, Xi Liu, Jun-Zhong Wang, Jian-Long Li, X. S. Wang, Qi-Kun Xue, Zhi Qiang Li, Zhenyu Zhang, and S. B. Zhang, Phys. Rev. B **66**, 165412 (2002).

[32] M. Kumar, V. K. Paliwal, A. G. Joshi, and S. M. Shivaprasad, Surf. Sci. **596**, 206 (2005).

[33] A. A. Baski, S. C. Erwin, and L. J. Whitman, Science **269**, 1556 (1995).

[34] J. R. Hahn and J. M. Seo, with Yong-Zhu, Surf. Sci. **601**, 1831 (2007).

[35] A. A. Baski, K. M. Saoud, and K. K. Jones, Appl. Surf. Sci. **182**, 216 (2001).

[36] S. S. Lee, N. D. Kim, C. G. Hwang, H. J. Song, and J. W. Chung, Phys. Rev. B **66**, 115317 (2002).

[37] M. C. Tringides, M. Jatochowski, and E. Bauer, Phys. Today **51**, (2007).

[38] D. K. Goswami, K. Battacharjee, B. Satpati, S. Roy, P. V. Satyam, and B. N. Dev, Surf. Sci. **601**, 603 (2007).

[39] V. K. Paliwal, A. G. Vedeshwar, and S. M. Shivaprasad, Phys. Rev. B **66**, 1-5 (2002).

[40] K. Jithesh, U. V. Waghmare, and S. M. Shivaprasad, Appl. Surf. Sci. **256**, 348 (2009).

[41] M. Kumar, V. K. Paliwal., A. G. Vedeshwar, and S. M. Shivaprasad, Surf. Sci. **600**, 2745 (2006).

[42] D. Tzeli, I. D. Petsalakis, and G. Theodorakopoulos, J. Phys. Chem. C **113**, 13924 (2009).

[43] S.Weitroub, Proc. Phys. Soc. (London) **B66**, (1953).

Chapter VI

Growth and characterization of InN thin films on Al$_2$O$_3$

In this chapter we present a study of the growth and properties of InN and address several issues related to this. Band gap, of InN in literature shows a spectrum of values which have been ascribed to different reasons. We carefully design several experiments for the growth of InN using MBE and analyze the results using several complementary characterization tools to zero in on the actual band gap value of InN and address the reasons for the varied values in literature. A study of carrier concentration dependence of effective mass of InN is also presented. Surface electron accumulation in InN is studied using XPS valence band measurements.

6.1   Introduction

Outstanding electronic properties of InN, like smallest effective mass, largest mobility, highest peak and saturation velocities and smallest band gap, among nitride semiconductors make it an attractive and promising material for photonic and electronic devices.[1] Among other group III nitrides it is the least studied due to difficulties in producing good quality InN films, resulting from its low dissociation temperature, the high equilibrium vapor pressure of nitrogen and also unavailability of suitable lattice matched substrates.[2] One of the most important electronic properties of InN, which is much debated by researchers, is its band gap. With the synthesis of high mobility, low carrier concentration, polycrystalline, RF sputtered films by Tansley and Foley in 1986,[3] the band gap of wurtzite InN was accepted to be 1.89eV, but more recent results showed much lower values.[4] Initial reports indicated a value of 1.1eV,[5] progressively reducing to lower values of 0.90 eV,[6] 0.80-0.7eV,[7-9] and 0.65-0.6eV[10,11] have been proposed. Observation of higher band gap has been attributed to several reasons such as strong Moss Burstein shift, quantum size effects, oxygen inclusion and stoichiometry changes,[12-15] while for the low band gap the reasons include defects, non-stoichiometry, film non-uniformity and Mie-resonances.[12,16] However, the full range of

reported experimental observation is not fully understood and thus, the issue needs to be addressed by a spectrum of complementary characterization performed on samples prepared under controlled growth parameters.

6.2.   High band gap value

We revisit the plausible reasons for the high band gap of InN grown on bare c-plane sapphire using a PA-MBE system equipped with accurate flux and temperature measurement.
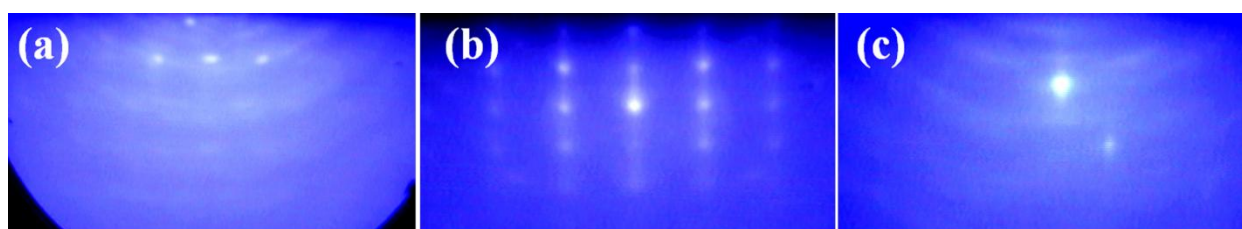
Fig. 6.1: *RHEED pattern after growth for InN samples grown at temperature a) 400°C, b) 450°C and c) 500°C*

MBE has the distinct advantage over other methods like MOCVD since the substrate temperature can be independently chosen irrespective of the nitrogen source. One of the important reasons for the observed band gap of InN, which has not been considered seriously, is the influence of deviation from stoichiometry. Thus, along with other plausible reasons we perform systematic XPS analysis to probe the influence of stoichiometry on the band gap of InN. We show here that crystallinity and orientation of InN films result from the carefully chosen kinetic growth conditions and deterministically influence the observed band gap value.

InN epilayers were grown on (0001) sapphire substrate by plasma assisted MBE operating at a base pressure of $< 3x10^{-11}$Torr and houses several characterization techniques as described earlier. Metallic indium was supplied at a flux rate of $4.4x10^{13}cm^{-2}s^{-1}$ by a standard effusion cell at a temperature of 800°C in all the experiments determined by the Accuflux Atomic Absorption Spectrometer. The plasma source operated at 375W was used for supplying activated nitrogen with a flow rate of 4.5 sccm, yielding a growth rate of about 0.15μmh^{-1}, determined by an *in-situ* QCTM and later confirmed *ex-situ* with a surface profile analyzer and cross-section SEM.   Chemically pre-cleaned sapphire substrates were and out-gassed at 500°C for one hour in the preparation chamber and further out-gassing is performed at 800°C in the growth chamber for 30min so that the streaky RHEED diffraction pattern characteristic of clean sapphire (0001) surface is obtained. We have chosen three substrate

temperatures, 400°C, 450°C and 500°C for the growth of InN, monitored by a K-type thermocouple and an optical pyrometer. The samples were characterized *ex-situ* by PL, FESEM, powder XRD and X-ray Photoelectron Spectroscopy (XPS) using Al K$_\alpha$ radiation (1486.6eV).
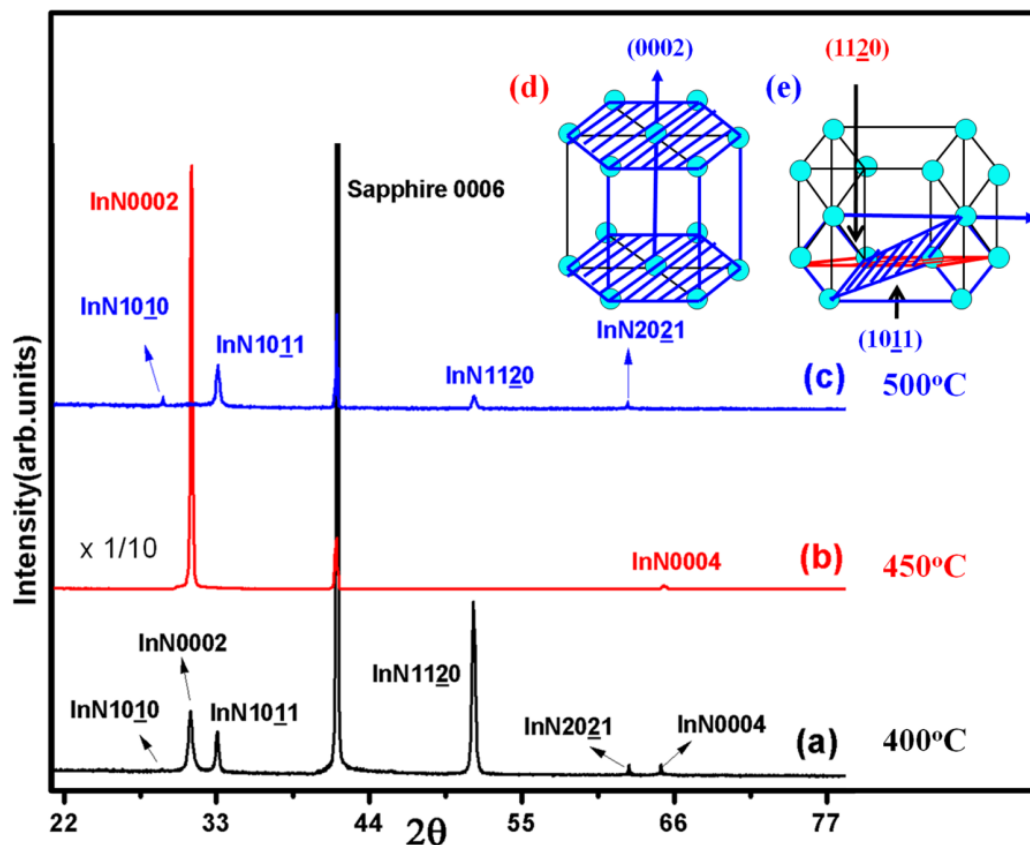
Fig. 6.2: *Results of XRD measurements on InN samples grown at temperature a) 400°C, b) 450°C and c) 500°C. Inset show schematics for wurtzite InN unit cells in different orientations.*

It has been reported that on bare sapphire substrate, without nitridation or use of buffer layer for growth, one obtains InN of high band gap value[17]. For the present study we have grown InN film at three temperatures viz. 400°C, 450°C and 500°C using MBE on bare c-plane sapphire without any nitridation or having any buffer layers.

We have used *in-situ* RHEED to determine the surface crystallinity of the grown samples. Fig. 6.1 shows the respective RHEED pattern for samples grown at 400°C, 450°C and 500°C. The RHEED pattern in Fig. 6.1(a) shows spots superimposed on a faint ring pattern which shows that the film surface grown at 400°C is predominantly polycrystalline in nature. From the RHEED pattern shown in Fig. 6.1(b) for the 450°C, we observe a dominant

spotty pattern with weak streaks, which is an indication of the transmission through a rough single crystalline film. The absence of any circular streaks as seen in Fig. 6.1(a) indicates the absence of polycrystallinity in this sample. The RHEED pattern for the 500°C sample shown in Fig. 6.1(c) is similar to that observed for the 400°C sample, where spots superimposed on faint ring like pattern are observed, which indicates polycrystalline nature of the sample surface. Thus, our RHEED study shows that among the different temperatures studied, the surface region of the sample grown at 450°C is single crystalline, while others show polycrystallinity. This can be due to a surface effect or different orientation of growth of single crystalline features.
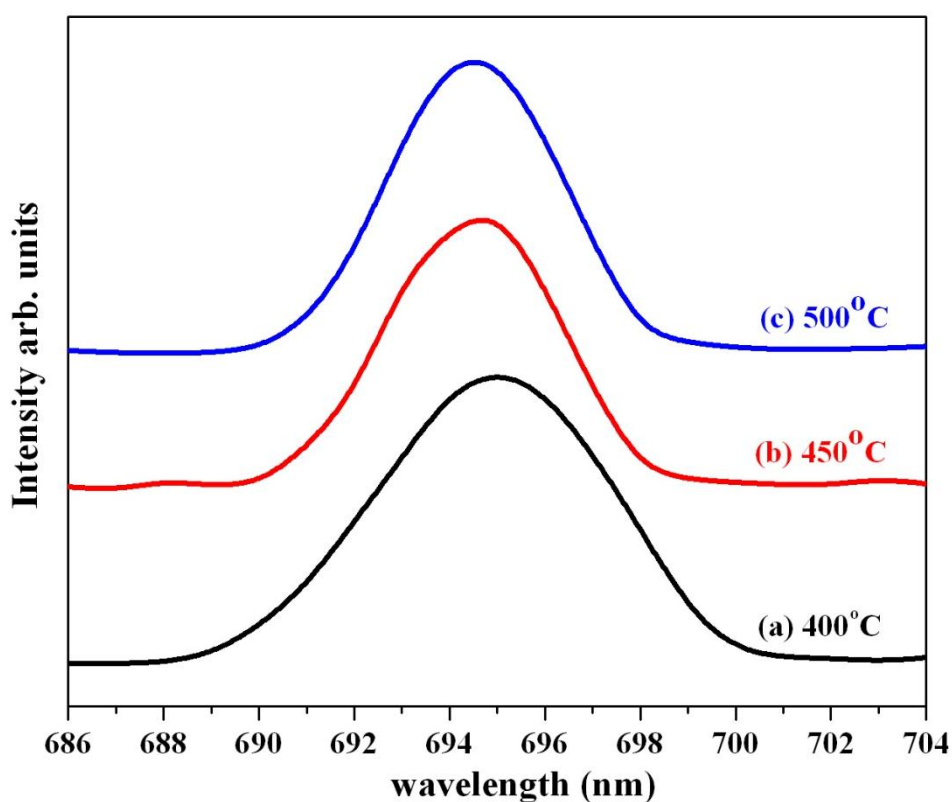
Fig. 6.3: *Photoluminescence measurements on InN samples grown at temperatures a) 400°C, b) 450°C and c) 500°C.*

Thus, X-ray diffraction measurements are performed and the θ-2θ pattern are shown in Fig 6.2(a), Fig. 6.2(b) and Fig. 6.2(c) for InN films grown at 400°C, 450°C and 500°C, respectively. As in RHEED, X-ray diffraction also shows that the sample grown at 450°C is single crystalline in nature. In the case of this InN film two diffraction peaks (0002) and (0004) are observed, in addition to the (0006) reflection from the sapphire substrate, at diffraction angles (2θ), 31.2^o, 65.27^o, and 41.66^o respectively. Absence of other reflections

confirms that at 450°C single crystalline wurtzite InN (α-phase) grains are parallel to the c-axis of the sapphire substrate.

At the slightly lower growth temperature of 400°C, besides the on-axis peaks (0002), (0004) and the sapphire (0006), we observe peaks at 33.09°, 51.6° and 62.66°, which correspond to the off-axis crystal planes of wurtzite InN (10$\underline{1}$1), InN (11$\underline{2}$0) and InN (20$\underline{2}$1) respectively, as shown in Fig. 6.2(a). At the higher temperature of 500°C, Fig. 6.2(c), we observe that on-axis reflections are completely absent in this sample. The sample shows peaks of InN (10$\underline{1}$1), InN (11$\underline{2}$0) and InN (20$\underline{2}$1) apart from the sapphire (0006) peak. FWHM of 648 arc-sec of InN (0002) peak for InN film grown at 450°C is much less than that of 1330 arc-sec of InN(0002) grown at 400°C which reiterates the high crystalline quality of the α-InN film formed at 450°C. We observe that the reflections observed on samples grown at 450°C are completely absent in 500°C sample and vice-versa, whereas the 400°C grown sample has all the reflections. A schematic of the corresponding planes for the main reflections in the two cases is shown in Fig. 6.2(d) and Fig. 6.2(e). The figure clearly indicates that while InN grows with its c-axis parallel to the c-axis of Al₂O₃ at 450°C, at 500°C InN grows with its c-axis parallel to the a-b plane of substrate, while at 400°C both orientations coexist. Thus, 500°C grown sample is not polycrystalline as indicated by RHEED but shows a different orientation of the wurtzite InN growth with respect to the substrate. The combination of RHEED and XRD studies thus show that 450°C is the optimum temperature for InN growth, with c-orientation parallel to that of the bare sapphire substrate. Our study clearly demonstrates that the crystalline orientation of the sample is strongly dependent on subtle changes in the substrate temperature.

To address issues related to the varied band gap values reported in the literature, we probe the band edge emission using Photoluminescence measurements.[17] Most of the band gap data available in the literature for InN have been obtained using absorption measurements.[17] Hamberg and Granqvist have shown that band gap broadening results in an under-estimation of the measured band gap values for samples with carrier concentration above $10^{19} cm^{-3}$.[18] Strong change in refractive index near the band gap edge limits the use of absorption squared plots to estimate band gap values. The first observation of PL in the case of InN film came only in 2002, which may be due to the poor quality of the materials synthesized earlier.[19] We have observed photoluminescence with a strong band edge emission on our samples ascertaining the good quality of the films grown.

Photoluminescence spectra measured at room temperature on our samples are shown in Fig. 6.3. Fig. 6.3(a), (b) and (c) show PL spectra from InN samples grown at 400°C, 450°C and 500°C respectively. All the samples show emission at nearly 1.78eV, similar to the high band gap value reported by Tansley and Foley,[3] and the FWHM of the three samples grown at 400°C, 450°C and 500°C are respectively 16meV, 13meV and 11meV. Recent MBE studies have attributed the observed high band gap value to the polycrystallinity of the sample.[14] However, since all the samples studied here show similar high band edge values and are of single α-phase, it can be inferred that by our combined *in-situ* RHEED and XRD studies, the orientation of growth of α-InN does not have any influence on the observed high band gap.
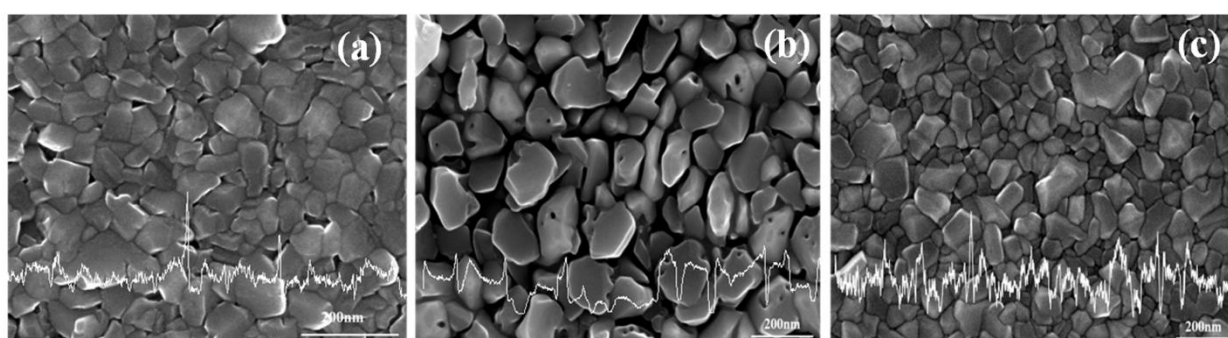
Fig. 6.4: *FESEM images for InN samples grown at temperatures a) 400°C, b) 450°C and c) 500°C. Also shown are the average roughness line scans.*

Since the observed high band gap for InN has sometimes been assigned to quantum size effects[14] determined by the grain sizes, we have mapped the surface morphology of the grown films by FESEM which is shown in Fig. 6.4(a), (b) and (c) for samples grown at 400°C, 450°C and 500°C, respectively. Line scans showing roughness of the FESEM images are also shown on the micrographs. From Fig. 6.4(a), for growth at 400°C, it is clear that surface morphology of this sample consists of large grains forming a quasi-continuous film which could be due to merging oxynitride at grain boundaries. At 450°C, the FESEM image shown in Fig. 6.4(b) consists of large and well separated grains. Fig. 6.4(c) shows the FESEM image of the InN film grown at substrate temperature of 500°C where it is apparent that the film consists of a large numbers of grains of various sizes, but are smaller in size compared to the other two temperatures. Thus, the three samples grown at different temperatures with different grain sizes show the same band edge emission suggesting same InN phases. We see that the observed average grain size is about ~ 100nm which is quite large for any quantum size effects to have any appreciable influence on the band gap value.

Also, the line scans show that different samples vary in surface smoothness and hence film uniformity along with crystallite sizes also do not seem to influence the band gap of InN.
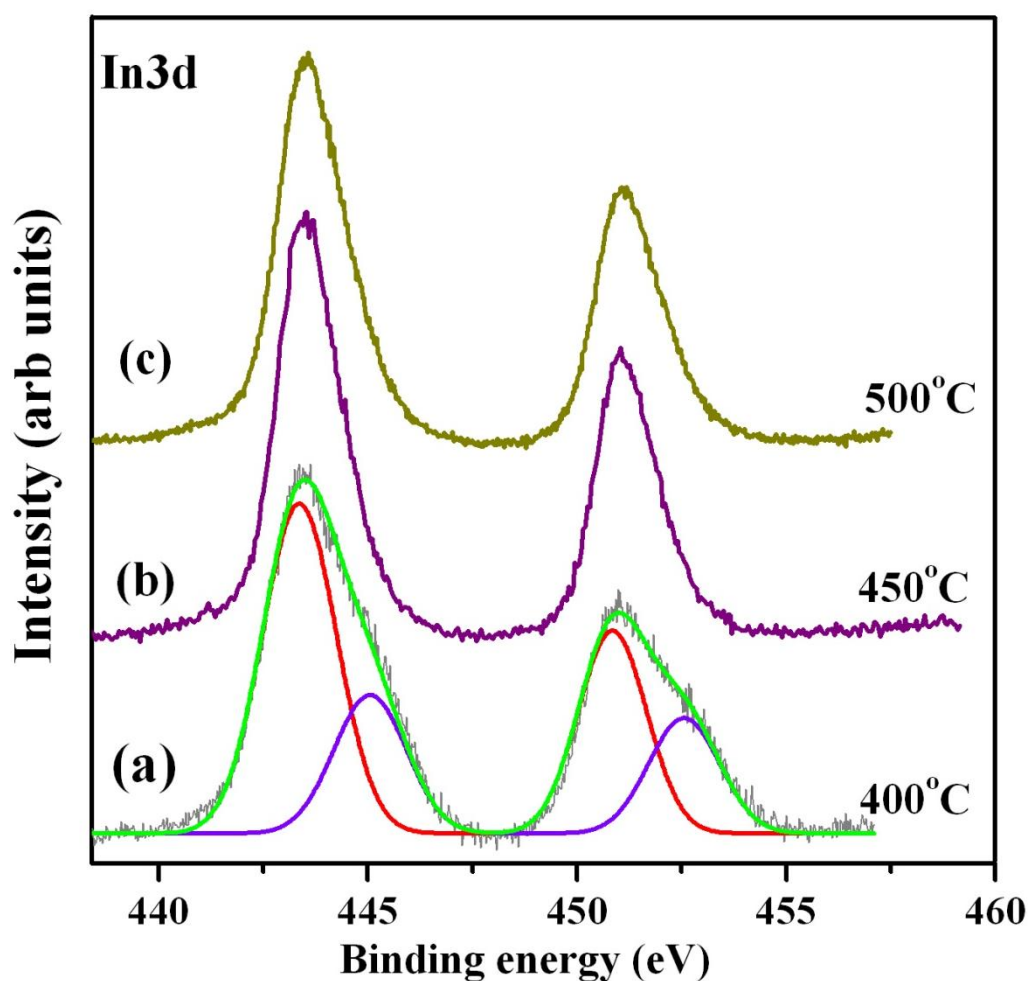
Fig. 6.5: *In 3d core level XPS spectra for InN samples grown at temperatures a) 400°C, b) 450°C and c) 500°C.*

Formation of oxynitride/oxide at grain boundaries has also been suggested to be a factor that enhances band gap.[15] To address this, XPS results of our samples are shown in Fig. 6.5. The figure consists of normalized In *3d* core level peak from InN samples grown at 400°C, 450°C and 500°C, deconvoluted into (shown only for 400°C sample) components arising from different contributions of In bonding with In, N, O, hydroxide, etc..[20] From the figure it is clear that InN film grown at 400°C has broader In $3d_{5/2}$ peak as compared to those grown at higher temperatures. This In $3d_{5/2}$ peak is de-convoluted into Gaussian components from InN contribution and that from indium oxide or indium oxynitride related contributions
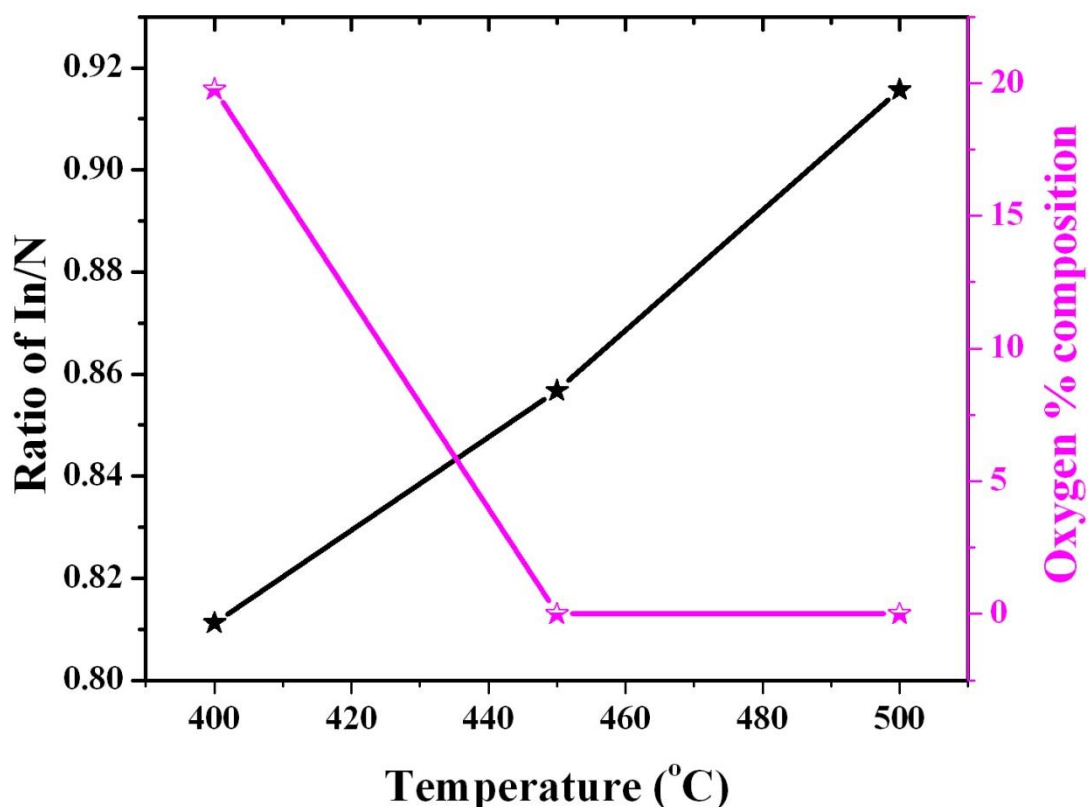
Fig. 6.6: *Ratio of In to N and percentage composition of oxygen versus growth temperature.*

at 443.5eV and 444.7eV binding energies, respectively.[20] Since at 400°C growth temperature the formation of indium oxide can be neglected,[21] the extra component can be attributed to the presence of oxynitride in this film. We do not see any oxynitride related peak in XRD pattern, suggesting that it is amorphous and could be at the grain boundaries, as reported earlier,[15] and be the reason for seeing fused grains in the FESEM images.

Oxygen in the InN films has been attributed in the past to the exposure of samples to atmosphere, where they adsorb at grain boundaries and form oxynitrides[4] or by the diffusion of oxygen from the sapphire substrate to the InN layers.[22] We have ensured by Mass Spectrometry that there is no oxygen ($< 10^{-15}$ torr partial pressure) in the MBE growth chamber. Fig. 6.6 shows the relative percentage composition of oxygen (on alternate y-axis) by measuring the core level XPS peaks plotted versus growth temperature.[23] Fig. 6.6 indicates that sample grown at 400°C has 20% oxygen and at higher temperatures the percentage of oxygen is zero. Absence of oxygen in samples grown at 450°C and 500°C with well-separated granularity also suggests that the source of oxygen may not be originating from the ambient. Presence of oxygen in the sample grown at 400°C may be through diffusion from the substrate, while is absent for higher temperatures, for which reasons are

not clearly understood. In Fig. 6.6, we have plotted the ratio of In to N computed from the XPS survey scan, which clearly shows that all the as grown samples are N rich. Since MBE is a non-equilibrium growth technique involving kinetic influences, such a nitrogen rich stoichiometry is possible and hence can be considered to be the source of background doping. Fig .6.6 shows that, with increase in temperature, the ratio of In/N increases but the band edge emission remains at 1.78eV irrespective of the variation in the stoichiometry, again reiterating the presence of a single InN wurtzite phase.
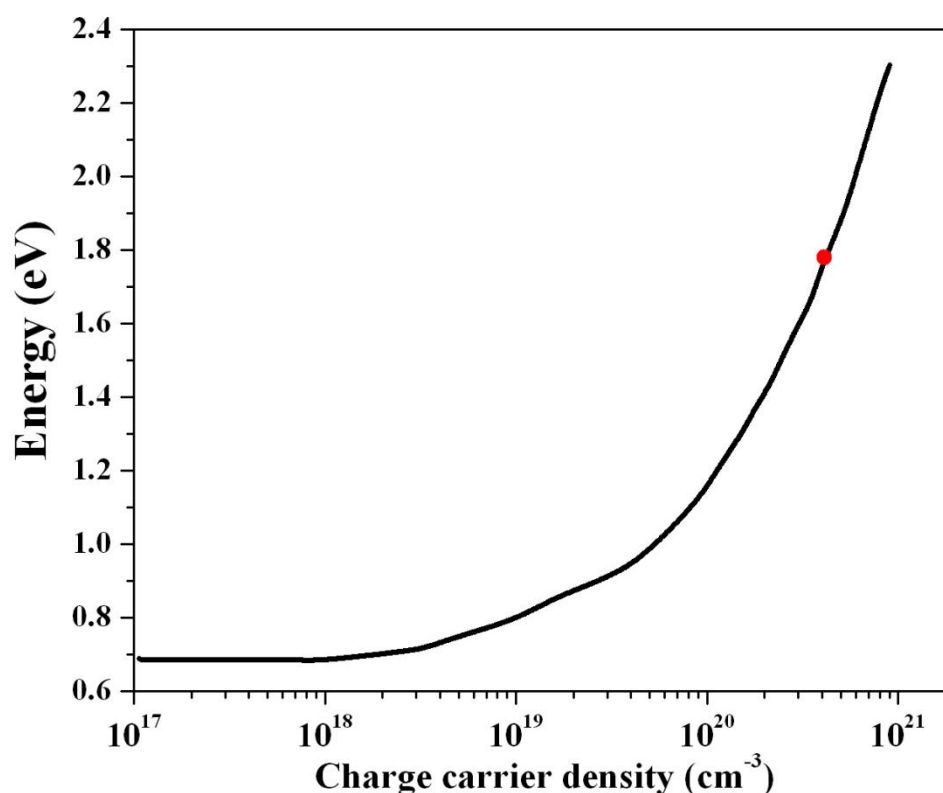
Fig. 6.7: *Observed band gap values plotted versus carrier concentration. The curve shows the theoretical carve[24] and the dot shows experimental value.*

        A number of reports have attributed the observed high band gap of InN to Moss-Burstein shift[8,13] which occurs when carrier concentration exceeds the conduction band density of states forming the Fermi level in the conduction band. As a result, electrons fill the bottom of the conduction band and the band gap measured is increased.   Hall measurements of our InN films yield the carrier concentration of unintentional n-doping to be ~ 4×10^{20} cm⁻³. The theoretical prediction by Wu *et al.*[16] (shown in Fig. 6.7) for the above mentioned carrier concentration should give a band gap of ~ 1.78eV, which matches quite well with 1.78eV. Thus, our studies suggest that among the different factors suggested in the literature Moss-Burstein effect can explain the observed band gap in our degenerately n-

doped InN films. Though at such a high background doping level one may expect alloying effects, we do not observe any core-level shifts and thus such effect can be discounted.[4]

6.3   Low band gap value

Study of group III nitrides is an interesting area of research since they form continuous alloys that span the infrared to ultraviolet region and have immense potential in optoelectronic applications such as full spectrum solar cells, white light emitting diodes, etc.[25-27] Among them, InN is attractive as it has the smallest effective mass and largest predicted mobility of 14,000cm^2/V-sec.[28] However, InN has remained a puzzling material and a common consensus has not been arrived at regarding the reported crystallinity dependent material parameters such as effective mass and band gap owing to its low dissociation temperature.[29] The complexity and ambiguity has led to a wide spectrum of reported band gap values from 0.6 to 2.2eV, using different experimental techniques.[4,29] The higher band gap value observed has been largely argued to be resulting due to the presence of indium oxide, hydroxide, or oxynitride and related complexes.[30] Shubina et al. have attributed, the low band edge PL emission of 0.7-0.8eV, to Mie resonances due to the presence of In metallic clusters segregated at the grain boundaries which lead to the modification of the dielectric constant of the material.[31] In their XRD pattern the peak at 33° (2θ) has been attributed to the presence of metallic In clusters. However, K.M. Yu *et al.* have assigned the XRD feature at 33° to the presence of polycrystalline wurtzite InN d(10$\underline{1}$1) crystallites, as they could not observe other metallic In interplanar distances either by XRD or SAED.[32]

Literature shows unintentional dopant density values up to ~ 2x10^{21}cm^{-3} in InN from various sources[4] which has been attributed to the presence of oxygen, hydrogen, excess nitrogen and to nitrogen vacancies, but a conclusive agreement has not yet been arrived at.[4] Also, the influence of InN crystallinity on the background doping level is yet to be addressed. Beginning with Trainor and Rose in 1974, there have been several attempts to correlate the band gap variation with carrier concentration.[33]   The generally accepted Moss-Burstein shift[34,35] occurs when the carrier concentration becomes larger than the conduction band edge density of states and the measured absorption edge shows higher values than the actual band gap of the material. Tansley and Foley used an empirical fit to suggest that high band gap InN materials show a weak dependence on carrier concentration.[17]   Later Davydov *et al.* have shown that Moss-Burstein shift calculated using a parabolic conduction band with an

effective mass of $0.1m_o$ fits well the band gap variation.[6] However, in a later study the same calculation is found to severely over estimate the observed band gap values.[36] Another successful attempt to elucidate the band gap variation of MBE grown samples was carried out by *Wu et al.*, who used both parabolic and non-parabolic conduction band to evaluate the shift, though it was found that the former method with an effective mass of $0.07m_o$, over estimates the shift.[37,38] For narrow band gap semiconductors, since the conduction band edge gets modified because of the interaction between valence and conduction bands, a non parabolic conduction band calculated using **k.p** band structure evaluation method was employed. They calculated the conduction band dispersion by solving Kane's two band **k.p** model,[39] as follows:

$$E_c(k) = E_G + \frac{\hbar^2 k^2}{2m_0} + \frac{1}{2}\left(\sqrt{E_G^2 + 4E_P \frac{\hbar^2 k^2}{2m_0}} - E_G \right) \qquad (6.1)$$

where, E_G is the direct band gap energy, and E_p is an energy parameter related to the momentum matrix element, $\frac{2}{m_0} |< S\,|\,P_x\,|\,X\,>|^2$. Based on experimental results they have assumed a band gap value of 0.7eV and the value of E$_P$ (=10eV) was deduced by the fit of experimentally obtained effective mass variation with carrier concentration.[37] Though the predicted curve explains well the MBE results, we find that data obtained from samples grown using other experimental techniques (discussed later) fall well below the curve. For the high carrier concentration material with low band gap, this has led to the argument that low band gap value is the result of defect level emission.[4] Different theoretical predictions for the Moss-Burstein shift available in the literature have been mainly derived based upon limited observations or have considered only samples grown solely using MBE. But a consideration of several data by all techniques in the literature is essential to evaluate the goodness of fit and to assign the band gap variation to the Moss-Burstein shift. It is also to be noted that effective mass, a key factor in the device performance and a potential parameter in deriving the Moss-Burstein shift, is also endowed with a range of reported theoretical values from $0.06m_0$ to $0.59m_0$[40] and experimental values from $0.04m_0$ to $0.24m_0$.[29] Since the Kane matrix element is independent of compounds, the variation of effective mass with band gap is linear, and this for InN with low band gap requires low effective mass.[41] However, the occurrence of the high band gap in InN (1.9eV) with an effective mass of $0.11m_0$ falling on the linear curve has led to an ambiguous situation.[41]

Literature also shows attempts to relate the band gap variation with stoichiometry, quantum size effects, polycrystallinity, film non-uniformity and also to alloying related to the unintentional dopant and the host material.[4]   Recent experimental results, largely not exclusively based on MBE, support a lower band gap value. Since the full spectrum of reported band gap values is not completely understood, assigning a band gap to InN is still elusive. The main reason complicates the comparison of results is the lack of systematic studies on samples grown under same growth conditions and on modified sapphire substrates and characterized by several complementary tools.

In the early part of this chapter, we have addressed the causes for the high band gap of InN on sapphire by studying the dependence of its properties on growth temperature.[42] Our systematic investigation suggested that presence of oxygen, stoichiometry, polycrystallinity and quantum size effect do not bear upon the high band gap observed for InN. Complementing this, the present work is an attempt towards being able to assign a proper band gap value of InN, by carefully designing an experiment to grow InN simultaneously on four differently modified c-plane sapphire substrates under the same growth conditions. We have chosen Molecular Beam Epitaxy for InN growth since growth temperature can be independent of the N_2 source and in an oxygen free UHV environment. With this approach, we evaluate several proposed reasons in the literature for the band gap variations of InN and correlate the variation in the carrier concentration and band gap with the crystallinity of the material and with respect to the Moss-Burstein shift.

InN is grown using Radio Frequency Plasma Assisted Molecular Beam Epitaxy with base pressure of 5×10^{-11} torr and oxygen partial pressure $< 10^{-14}$ torr measured by Residual Gas Analyzer (RGA).   The growth is performed simultaneously on four Al_2O_3 (0001) substrates, each modified differently based on several reports on methods to improve the quality of InN films.[43-45] All the substrates are mounted together in the growth chamber using a specially designed substrate holder. Different samples grown are designated as sample-A: InN/Sapphire (0001), sample-B: InN/LT-InN/Sapphire (0001), sample-C: InN/nitrided Sapphire (0001) and sample-D: InN/GaN (2μm)/Sapphire (0001). The main InN layer for all samples is grown at $425^{o}C$ for two hours and the thickness measured using Surface Profile Analyzer and cross sectional SEM is 0.3μm. Indium flux rate is calibrated using *in-situ* Atomic Absorption Spectroscopy (Accuflux SVTA), Reflection High Energy Electron Diffraction (RHEED) and Quartz Crystal Thickness Monitor (QCTM), and is found to be

$4.4 \times 10^{13} cm^{-2} s^{-1}$. N_2 flux rate for all the InN growth is 4.5sccm with a Radio Frequency (RF) plasma forward power of 375W. Sample A has 0.3μ InN grown on bare Al_2O_3 (0001). For sample B the low temperature InN (LT-InN) layer of 30nm was grown at 300°C. Nitridation of the sapphire substrate is done for sample C at 550°C by exposing it to nitrogen plasma (N_2*) for 1 hour. GaN epi-layer wafer of 2μm grown by Hydride Vapor Phase Epitaxy (HVPE) is used in sample D. Surface crystallinity measurements have been performed using *in-situ* RHEED and for crystallinity studies powder X-ray Diffraction has been carried out using Bruker D8 diffractometer with Cu Kα X-rays and the High Resolution XRD measurements have been carried out in a four crystal Bruker D8 Discover diffractometer. Surface morphology has been studied using Field Emission Scanning Electron Microscopy (FESEM) and Atomic Force Microscopy (AFM). For stoichiometry and composition measurements, X-ray Photoelectron Spectroscopy (XPS) has been performed with Mg-K_α (1253.6eV) X-ray source with a relative composition detection resolution of 0.05%. Band gap values are obtained from reflectivity measurements in conjunction with transmission measurements using Perkin-Elmer Lamda 900 UV/Vis/IR spectrometer. To determine carrier concentration, Hall measurements have been carried out using Vander-Pauw method, in a magnetic field of 0.58T at Room Temperature (RT).
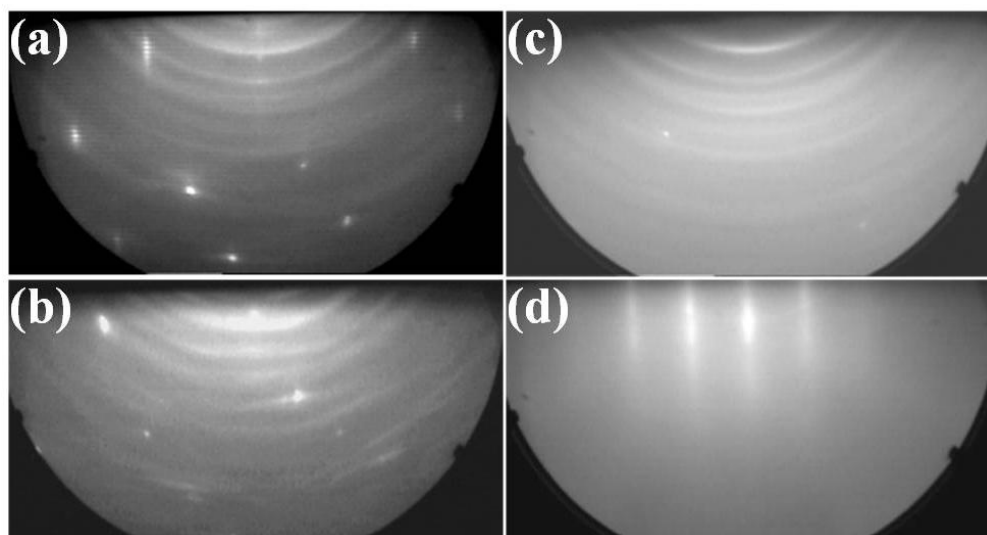
Fig. 6.8: *(a), (b), (c) and (d), show in-situ RHEED pattern taken e//<11$\underline{2}$0> for samples A, B, C and D respectively.*

In Fig. 6.9 and 6.8, (a), (b), (c) and (d) show the FESEM images and corresponding RHEED pattern, for samples A, B, C and D respectively. The figure shows (Fig. 6.9) that samples A, B and C have a granular morphology and the corresponding RHEED (Fig. 6.8) is

a spotty plus ring pattern characteristic of polycrystalline surfaces. The rms roughness of these surfaces measured by AFM is 3-5nm, as listed in Table 6.1. Fig. 6.9(d) shows a microscopically smooth InN film when grown on GaN epilayer, and the inset corresponding to this shows streaky RHEED pattern with an AFM rms roughness of ~ 1nm as shown in Table 6.1.
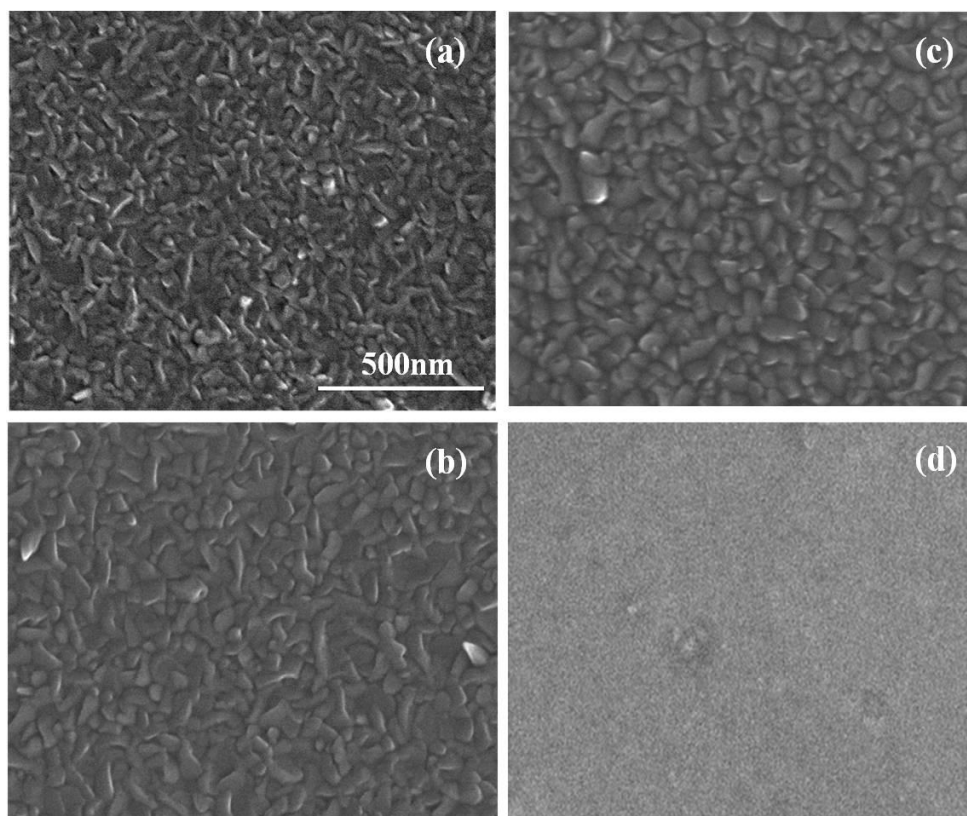
Fig. 6.9: *(a), (b), (c) and (d), show FESEM images for samples A, B, C and D respectively.*

Band edge absorption of the four InN samples grown has been found from reflectivity measurements[46] and are shown in Fig. 6.10, where sample A has a band edge at 2.12eV, sample B at 2.17eV, sample C at 1.92eV and sample D at 0.63eV. It is interesting to note that irrespective of the fact that the samples are prepared under the same growth conditions, they possess different band gaps enabling us to address the contentious issue of the role of surface modifications and presence of impurities such as oxygen. Fig. 6.11 shows the XPS core-level spectra of In 3d peak measured for samples A through D. For comparison the spectrum of an intentionally oxidized InN sample surface is also shown as Fig. 6.11(e) which has a wider FWHM due to the presence of an additional oxide peak at 445eV along with the main InN peak at 443.5eV. The fact that Fig. 6.11(a) to 6.11(d) have only InN related core level peaks show clearly the absence of oxygen in all the four samples.[47-49] The ratio of In/N

calculated from XPS survey scan has an accuracy of 0.05% and is listed in Table 6.1, which shows that all the four InN films have stoichiometric composition, and hence we can infer that in our samples In is only bonded to N, rather than with oxygen.[23]

Sample	Resistivity-ρ (Ω-cm)	Carrier density-n (cm^{-3})	Hall mobility-μ (cm^{2}V^{-1}s^{-1})	XPS – In/N %composition ratio	AFM – rms roughness (nm)	XRD 0002 peak FWHM (arc-sec)
A	2.1x10^{-4}	6.0x10^{20}	47	1.01	3.5	1391
B	1.9x10^{-4}	5.0x10^{20}	63	1.04	5.7	1260
C	2.0x10^{-4}	4.0x10^{20}	77	1.01	3.2	1726
D	3.1x10^{-3}	3.1x10^{19}	60	1.01	1.1	780

Table 6.1: *Different experimentally measured parameters: resistivity, carrier density, hall mobility, XPS % composition ratio, AFM roughness, FWHM of XRD 0002 peaks for samples A, B, C and D respectively.*

Since MBE growth in UHV results in only InN formation, but shows both high (~2eV) and low band gaps (~0.6eV), on differently modified substrates, discounts the role of oxygen in influencing the band gap. However, since the morphologies of these stoichiometric InN films, as shown in Fig. 6.9, are different, we probe the structural properties carefully.

In Fig. 6.12, (a), (b), (c) and (d) are the θ-2θ XRD scans for samples A, B, C and D respectively, with peaks at 31.28^{o} and 65.31^{o} corresponding to the (0002) and (0004) *hkil* planes characteristic of c-oriented wurtzite InN. Epilayer and substrate related peaks viz., GaN (0002), GaN (0004) and Al$_2$O$_3$ (0006) appear at 34.50^{o}, 72.75^{o} and 41.68^{o}, respectively. In the case of samples A, B and C in addition to the on-axis planes InN(0002), InN(0004) we
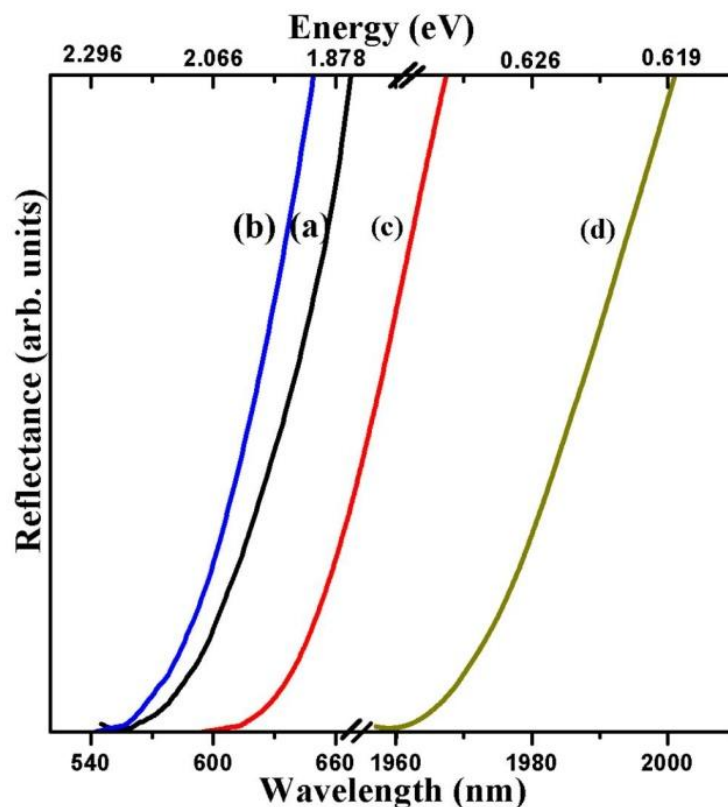
Fig. 6.10: *(a), (b), (c) and (d) show Reflectance spectra at RT for samples A, B, C and D respectively.*

observe less intense extra peaks at 33.18^o, 56.92^o, and 73.15^o which we attribute to off axis c-wurtzite planes InN(10$\underline{1}$1), InN(10$\underline{1}$3) and InN(10$\underline{1}$4), respectively. This suggests that samples A, B, and C along with predominant c-oriented crystallites also have a few crystals with other orientations, resulting in a weak polycrystalline component of the film which was also clearly observed by RHEED. We find sample D, which shows a band edge of about 0.63eV, has no peak around 33^o in the XRD pattern, while samples A, B, and C show a peak at 33.18^o which, we assign to the orientation (10$\underline{1}$1) of wurtzite InN. As discussed earlier Shubina et al.,[31] had attributed this peak to metallic In causing low band gap in their films. But our data shows that samples having this XRD feature at around 33.18^o show high band gap (~2eV), whereas sample D which has a low band edge value (~0.7eV) does not have this peak. Though peaks, In (101) at 32.96^o and InN (10$\underline{1}$1) 33.18^o are difficult to resolve. Since there are no other metallic In related reflections and that we don't observe low band gap
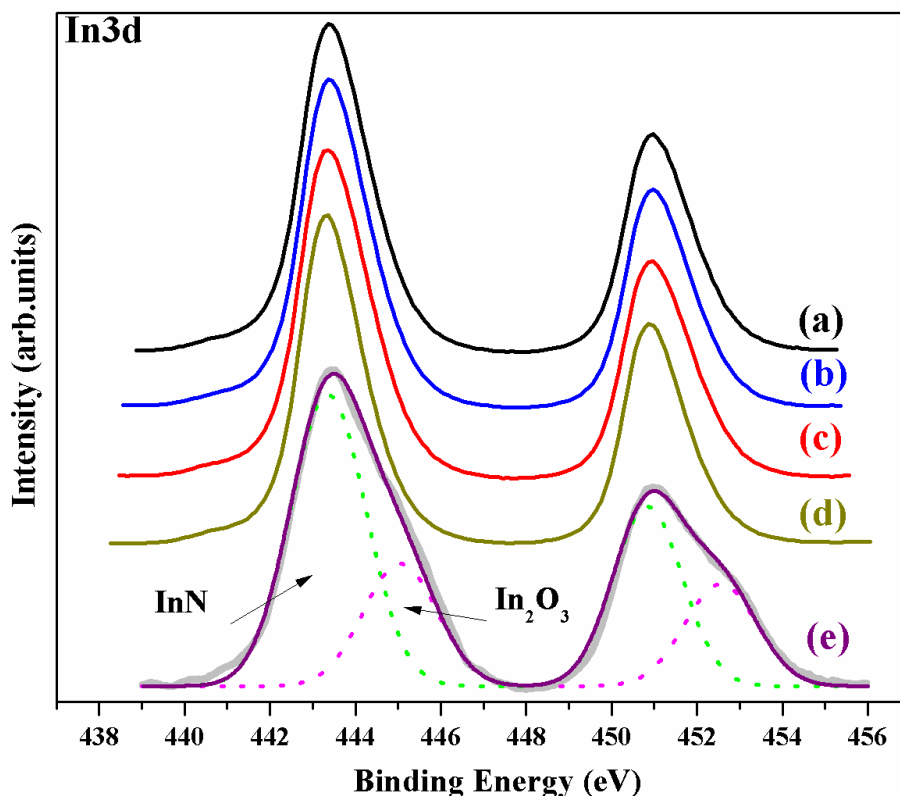
Fig. 6.11: *(a) through (d) XPS core-level spectra of In 3d peak for sample A through B. (e) shows an example of a sample containing oxynitride related contribution, for comparison.*

value on these samples, we unambiguously ascribe the feature to InN wurtzite crystallites having (10$\underline{1}$1) growth orientations.[32] As a further evidence to show the absence of (10$\underline{1}$1) orientation or metallic In related contribution in sample D, as an inset to Fig. 6.12, HRXRD 2θ-ω scan is shown. It can be seen that only wurtzite InN (0002) peak is present. Also, since XPS core-level peaks in Fig. 6.11 and the stoichiometry in Table 6.1 show clearly that In is bonded only to N to form stoichiometric InN films.[31,50] Thus, the study clearly excludes the role of any metallic In or any oxynitride in determining the band gap of InN film. The defect density in the film is manifested in the width of the (0002) XRD peak, and the measured FWHM of the (0002) peak of all the four samples are listed in Table 6.1. The values clearly show a wider FWHM (1200 to 1700 arcsec) in the orientationally polycrystalline A, B and C samples, while sample D has a value of 730 arcsec. Thus, we reiterate that simultaneously grown InN film on differently surface modified substrates can show low and high band gap can only be due to orientational disorder in the InN wurtzite crystallites.

      To study the dependence of band gap variation with carrier concentration, we have performed Hall measurements on the four samples. Results of our measurements (star

symbols) along with various experimental measurements reported in the literature are consolidated in Fig. 6.13 (Ref. 5, 6, 12). Sample A, B, C and D respectively show carrier concentrations of $6.0 \times 10^{20} cm^{-3}$, $5.0 \times 10^{20} cm^{-3}$, $4.0 \times 10^{20} cm^{-3}$ and $3.1 \times 10^{19} cm^{-3}$. It can be seen that there is an order of magnitude reduction in the carrier density in the low band gap sample D compared to larger band gap samples. Since we have clearly ruled out presence of
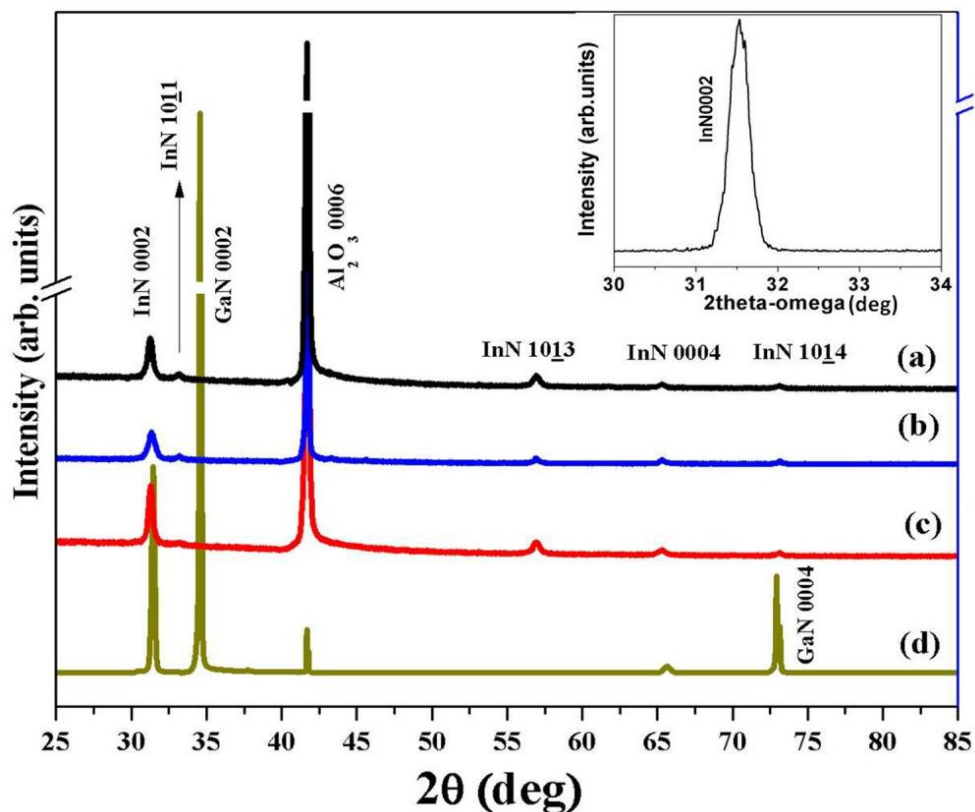
Fig. 6.12: *(a), (b), (c) and (d) show XRD pattern for samples A, B, C and D respectively. Inset shows high resolution XRD scan.*

impurities as unintentional dopants and the fact that the films are stoichiometric (Table 6.1) possibility of excess nitrogen can be ruled out, and thus the high carrier concentration can be due to nitrogen vacancies, as has been attributed to other III nitrides as well.[15] For InN growth on bare sapphire substrate the lattice mismatch in the two epitaxial directions viz. $[11\underline{2}0]_{InN}\|[11\underline{2}0]_{sapphire}$ and $[10\underline{1}0]_{InN}\|[11\underline{2}0]_{sapphire}$ are -25.4% and +29.2% which is much closer to each other in absolute magnitude compared to other III nitrides on bare sapphire which, for example, for GaN are respectively equal to -33.0% and +16.0%.[51] Owing to this close lattice match in the two orientations in c-plane, InN tends to grow with both epitaxial relationships resulting in grains with both epitaxial orientations in the c-plane.[43] This, azimuthally mis-oriented, but directionally c-oriented grains will lead to mismatched

boundaries in the film, inhibiting the formation of smooth films and cause defects at the interfaces. Our results, based on the specially designed experiment, suggest that the background dopant causing high carrier concentration is due to the interfacial lattice mismatch, leading to interfacial defect states in the conduction band of InN. This is also corroborated by the crystalline quality of samples shown in Fig. 6.9 and Fig. 6.12 where sample D shows high quality single crystalline smooth film. The weak polycrystalline nature of samples A, B and C with their rough surfaces also suggest increased defects owing to orientational grain boundaries and to poor lattice match with sapphire in orientation of growth other than in c-axis. In these samples we have observed reflections corresponding to other orientations of growth viz. InN (10$\underline{1}$1), InN (10$\underline{1}$3) and InN (10$\underline{1}$4) which will lead to poorer lattice match than c-oriented growth forming interfacial defects. As described earlier a narrower FWHM of sample D, shown in Table 6.1, also indicates fewer defects in this film. Thus, we ascribe the variation in the carrier density in our samples to the variation in the crystallite orientation.

Observing the considerable scatter in the reported band gap values from various sources, shown in Fig. 6.13, we have carried out a non-linear curve fit of the experimental data to the Levenberg-Marquardt algorithm which is based on chi-square minimization.[52,53] We observe from Fig. 6.13 that there are reported high band gap values with low carrier concentration from the earlier work by Tansley and Foley[17] using RF-sputtering, but, have not been reproduced in the literature since. There is a possibility of continuous alloying or mixture of indium oxide and indium nitride, which as per effective medium theory can result in an in-between band gap value. It has been shown that indium oxide shows a very weak dependence of band gap with carrier concentration[54] as seen in Fig. 6.13 for the fit by Tansley and Foley. This prompts us to exclude these experimental values from the following analysis. M. Alevi *et al.*[55] have used an empirical exponential fit to their data of the band gap variation with carrier concentration for their HPCVD grown InN/GaN/Sapphire samples, and show that the fundamental band gap of InN is about 1.20eV. Since the trend of the data points presented in Fig. 6.13 shows clearly that the Moss-Burstein curve for InN follows an exponential form, we have fit an exponential function to the available data points. Chi-square minimization for this empirical exponential function shows a good agreement with the data and yields a band gap value of 0.7eV, which is higher than the recent reported
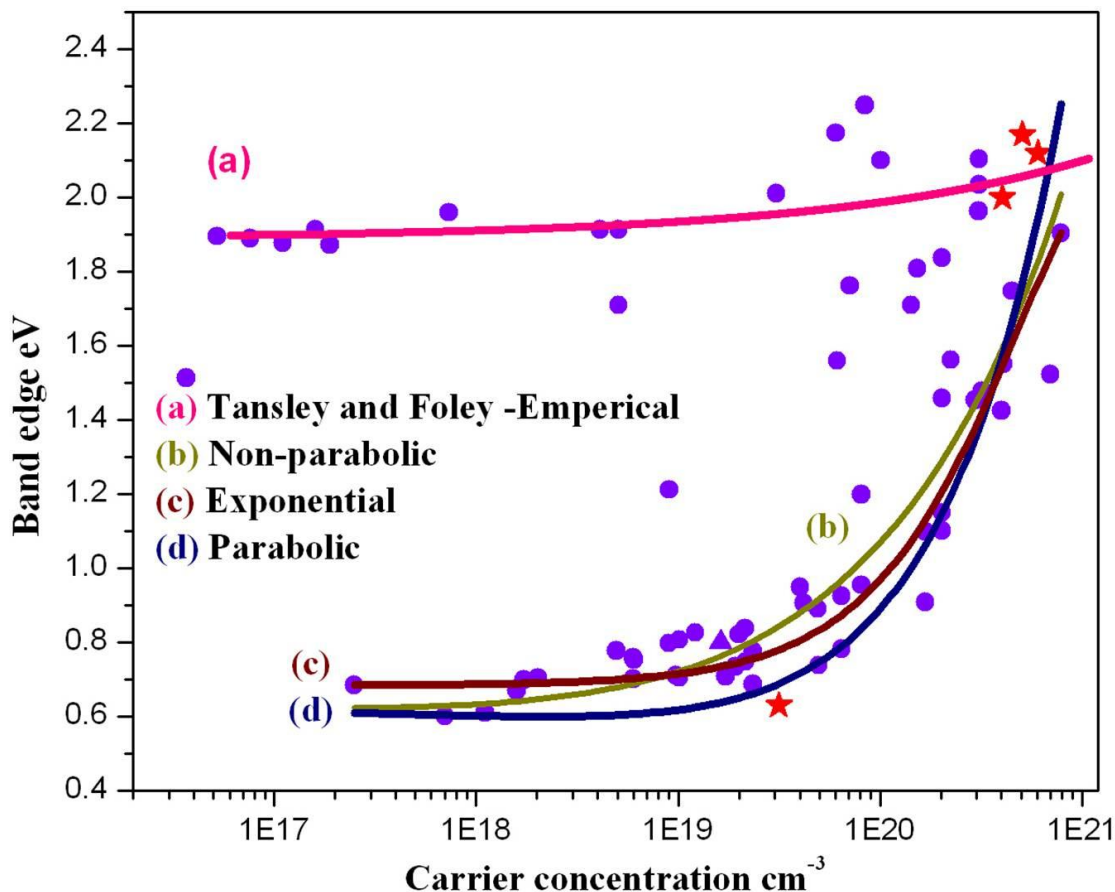
Fig. 6.13: *Different reported experimental band gaps for InN from literature (Ref. 5, 6, 12) and present experiments, along with Moss-Burstein shift calculations: (a) Tansely Foley empirical data, (b) assuming parabolic conduction band (c) empirical exponential function and (d) assuming non parabolic conduction band. Data markers having star symbols are from the present experiments.*

value.[29] As discussed in the introduction, a parabolic conduction band has been used in many reports to derive the Moss-Burstein shift. We have performed a non-linear fit to the data, assuming parabolic conduction band with effective mass (m^*) as the fitting parameter. The hole effective mass in the valence band is assumed to be that of free electron and the band gap value is fixed to the recently accepted value of 0.64eV. Effective mass obtained from this fit is about ~$0.15m_0$ which is higher than most of the reported values.[29] Also it can be seen that the best fit obtained after chi-square minimization for parabolic conduction band assumption shown in Fig. 6.13, underestimates the shift especially in case of band gap data for low carrier concentration material, suggesting the need for a non-parabolic conduction band for InN. As described earlier, a carrier concentration dependent effective mass resulting from non-parabolic conduction band has been much argued for InN[16] which is based on the experimental observation that effective mass varies with carrier concentration. We have

observed that, depending on the crystallinity of the samples, the carrier concentration changes and hence effective mass can vary for the samples. We have performed a non-linear curve fit to the data shown in Fig. 6.13, assuming a non-parabolic conduction band with energy parameter E_p as the fitting parameter. Using the conduction band dispersion given by equation (6.1), a non-linear curve fit yields a band gap value of ~0.64eV and E_p of 9.5eV, which is close to the value deduced for E_p in Ref.[37]. We find that calculation with non-parabolic conduction band yields a better fit to most of the experimental data. It has to be noted that for both the parabolic and non-parabolic calculations, we have taken into account the conduction band renormalization effects due to electron-electron interaction and electron-ionized impurity interaction, considering the dielectric constant to be 6.7,[40] without which it deviates from literature values leading to a poor fit. Observation of low band gap values well below the calculated curve for InN having high carrier concentration has led to the argument that the low band gap infrared emission results from the defect states of a high band gap InN material.[4] The equi-distribution of data points above and below the fitted curve shown in Fig. 6.13 suggests that the large scatter in the values can be attributed to measurement errors in measuring the band gap due to band broadening and strong change of refractive index near the band edge.[4] Thus, the results suggest that orientational polycrystallinity which changes the observed effective mass owing to band non-parabolicity can be directly related to the carrier concentration for InN.

6.4   Effective mass – Reflectivity measurements

In the previous section we have discussed the absorption edge dependence on carrier concentration, for InN films, owing to Moss-Burstein shift which could be well explained by considering non-parabolic conduction band resulting from its narrow band gap. Effective mass is given by the following equation[56,57],

$$m*(k) = \frac{\hbar^2 k}{dE_c(k)/d\,k} \tag{6.2}$$

For a parabolic conduction band we have,

$$E_c = \frac{\hbar^2 k}{2m_e} \tag{6.3}$$

where m$_e$ represents the effective mass of electrons in the conduction band. Now using eq.(6.2), it follows that for a parabolic conduction band,

m*(k) = m$_e$ = constant

Thus, for a parabolic conduction band effective mass is a constant. For a non-parabolic conduction band described by eq.(6.1),

$$m*(k) = f(k)$$

or $\quad m*(k) = f(n) \Leftarrow k = (3\pi^2 n)^{1/3}$

where n is the electron concentration. It follows that for non-parabolic conduction band effective mass is wave vector dependent i.e. it is a function of free electron carrier concentration. To observe such effects in our samples we have measured effective mass as a function of carrier concentration using reflectivity and Hall measurements.

The effective mass appears in the following equation[56,57],

$$\omega_p^2 = \frac{Ne^2}{m^* \varepsilon \varepsilon_\infty} \tag{6.4}$$

where ε_∞ is the optical dielectric constant ε_o is the vacuum permittivity, N is free electron carrier concentration and is the charge on an electron. In eq.(6.4) we neglect the tensor characteristics of the electron effective mass.

Reflectivity of semi-infinite medium can be written as[58,59],

$$R = \frac{(n-1)^2 + k^2}{(n+1)^2 + k^2} \tag{6.5}$$

Here n is the real part of the refractive index and k is the extinction coefficient. The relation between n and k is given by the complex dielectric function,

$$\varepsilon(\omega) = (n - k)^2 \tag{6.6}$$

Also if other contribution besides the free-electron carrier concentration can be neglected, this can be approximated by[60],

$$\varepsilon(\omega) = \varepsilon_\infty \left(1 - \frac{\omega^2}{\omega(\omega + i\gamma)}\right) \tag{6.7}$$

where γ is the electron damping constant. It can be seen that using eq.(6.6) and (6.7) we can write,

$$n = n(\omega, \gamma, \omega_p)$$
$$k = k(\omega, \gamma, \omega_p)$$
(6.8)

From eq.(6.5) and (6.8) it follows that,

$$R = R(\omega, \gamma, \omega_p)$$
(6.9)

Thus, it follows that by fitting eq.(6.9) to the experimental data one can extract the value of plasma frequency. If we use more complicated dielectric function containing the phonon contribution it does not change the value of ω_p significantly. For determination of N from Hall measurements we use the standard equation[56],

$$N = \frac{r}{eR}$$
(6.10)

Here r is the scattering factor and R is the Hall constant. The sample that we consider for the present analysis consists of degenerately doped samples, for which r is essentially equal to 1. It follows that by knowing the plasma frequency and carrier concentration effective mass can be calculated.

Fig. 6.14 shows the reflectivity spectra for a sample having carrier concentration of $4.3 \times 10^{20} \text{cm}^{-3}$. In the reflectivity spectra reflectance is plotted for frequency of incident infrared radiation. Plasma reflection edge correspond to a region in the reflectance spectra where the material changes from fully reflecting to fully absorbing state dropping the reflectivity to almost zero value. In Fig. 6.14 also shown is the fitted curve using eq. (6.9). The best fit yields a value for plasma frequency 5414cm^{-1} and damping constant 1580cm^{-1}. Table 6.2 shows the results of reflectivity analysis performed on InN samples having different carrier concentration.
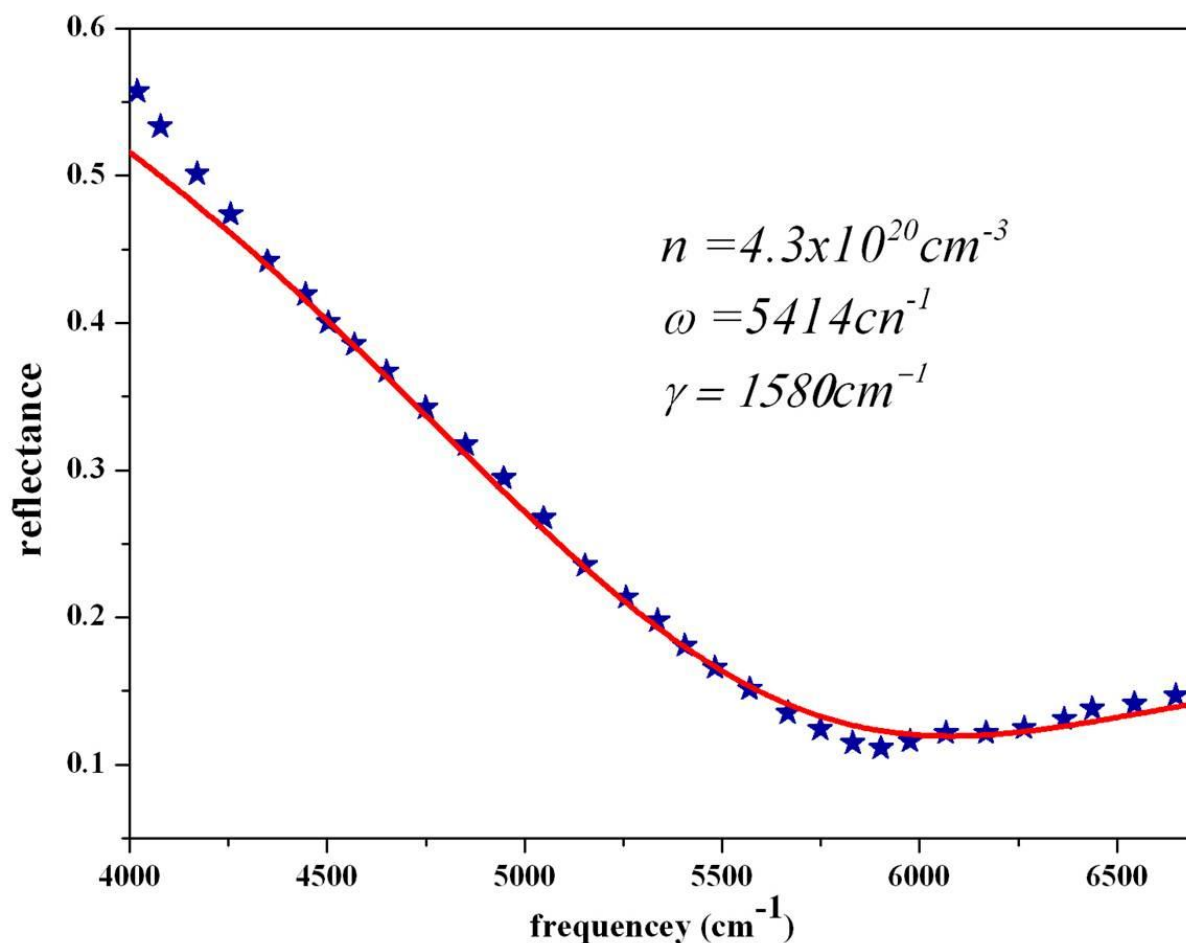
Fig. 6.14: *Experimental (stars) and calculated reflectance (red curve) spectra of InN sample having carrier concentration 4.3x10²⁰cm⁻³.*

n (cm⁻³)	ω_p (cm⁻¹)	γ (cm⁻¹)
6.0x10¹⁹	2000	500
4.3x10²⁰	5414	1580
7.0x10²⁰	5720	1600
1.3x10²¹	7092	1611

Table 6.2: *Plasma frequency and damping constants obtained after fitting experimental reflectance spectra for different samples.*

Using plasma reflection edge and carrier concentration measured, we have calculated effective mass for different samples using eq. (6.4). In this calculation, isotropically averaged values of optical constant $\varepsilon_\infty = 6.7$[40] from literature is used. Fig. 6.15 shows the results of effective mass calculation performed on samples having different carrier concentration. In Fig. 6.15
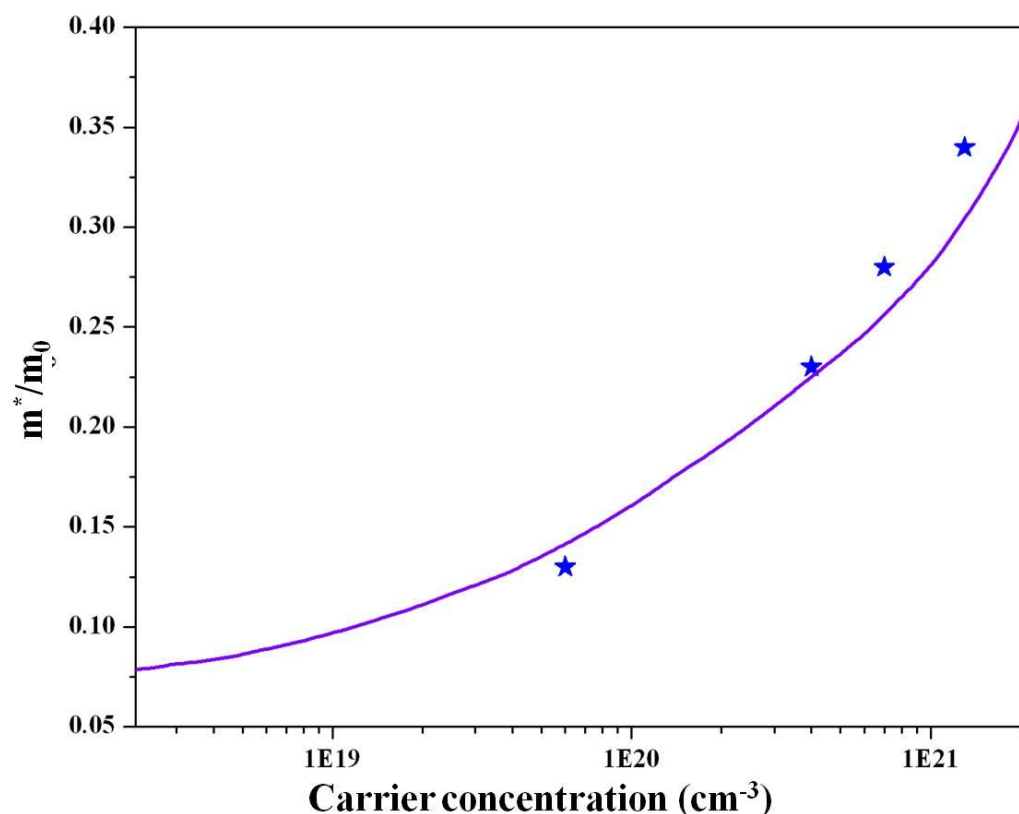
Fig. 6.15: *Experimental (stars) and calculated (purple curve) effective mass for samples having different carrier concentrations.*

calculated effective mass is plotted versus free electron carrier concentration measured using Hall effect. Also plotted in Fig. 6.15 are the theoretically calculated values using eq. (6.1) and eq. (6.2) taking a value of the energy parameter $E_p \sim 10 eV$, obtained by fitting the absorption edges data with carrier concentration. Figure shows that there is a good agreement between the experimentally observed values and that calculated theoretically assuming a non-parabolic conduction band for InN. This shows that effective mass of InN is indeed carrier concentration dependent. Thus, it is necessary to consider the non-parabolicity of the conduction band in order to elucidate the fundamental properties of InN.

6.5   Surface electron accumulation – XPS valence band measurements

Different predicted properties of InN have attracted much attention for application in high efficiency solar cells and high speed-electronic devices. One of the key problems in the realization of InN based device application has been proposed to be related to the unusual phenomena of strong electron accumulation on as-grown InN surfaces.[61] This surface electron accumulation layer causes problems in p-doping in InN as it will cause an n-type surface inversion layer which will prevent direct electrical contact to the bulk InN.[62] The
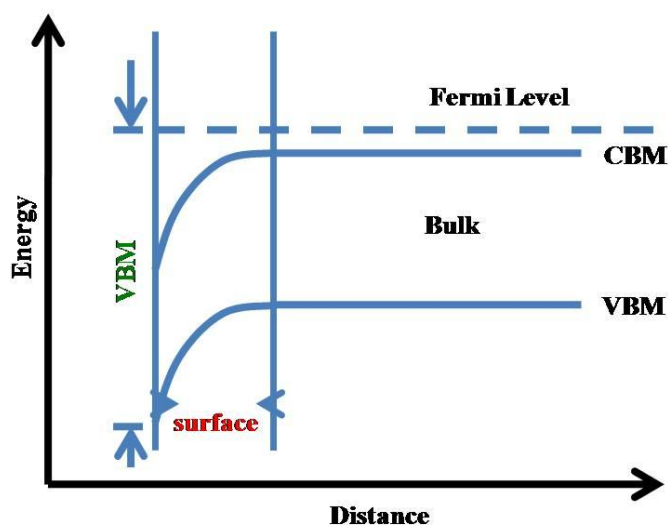
Fig. 6.16: *A schematic of band diagram near the surface of InN films.*

observation of sheet carrier concentration as a function of thickness of InN films showed non-vanishing sheet density, in the limit of thickness, tends to zero which gave an indirect evidence of surface electron accumulation in InN.[63]   Later studies using HREELS charge density depth profile have showed the presence of an increased charge density on InN surface.[61]   The surface electron accumulation layer will be manifested as band bending near the surface as shown in the Fig. 6.16 and the extend of band bending can be measured using XPS valence band measurements by calculating Valence Band Maximum (VBM) shown in Fig. 6.16.[64]

XPS measurements have been carried out using non-monochromatic Mg K_α X-rays having energy $hv = 1256.6eV$. Fig. 6.17 shows the valence band spectra of two InN samples having different carrier concentrations. VBM have been calculated from valence band spectra by extrapolating the leading edges of the spectra.[65] We have performed valence band measurements on samples having different carrier concentration. Fig. 6.18 summarizes the results of the measurements for samples having different carrier concentrations. In the Fig. 6.18 VBM measured from XPS spectra is plotted versus carrier concentration measured using Hall effect.
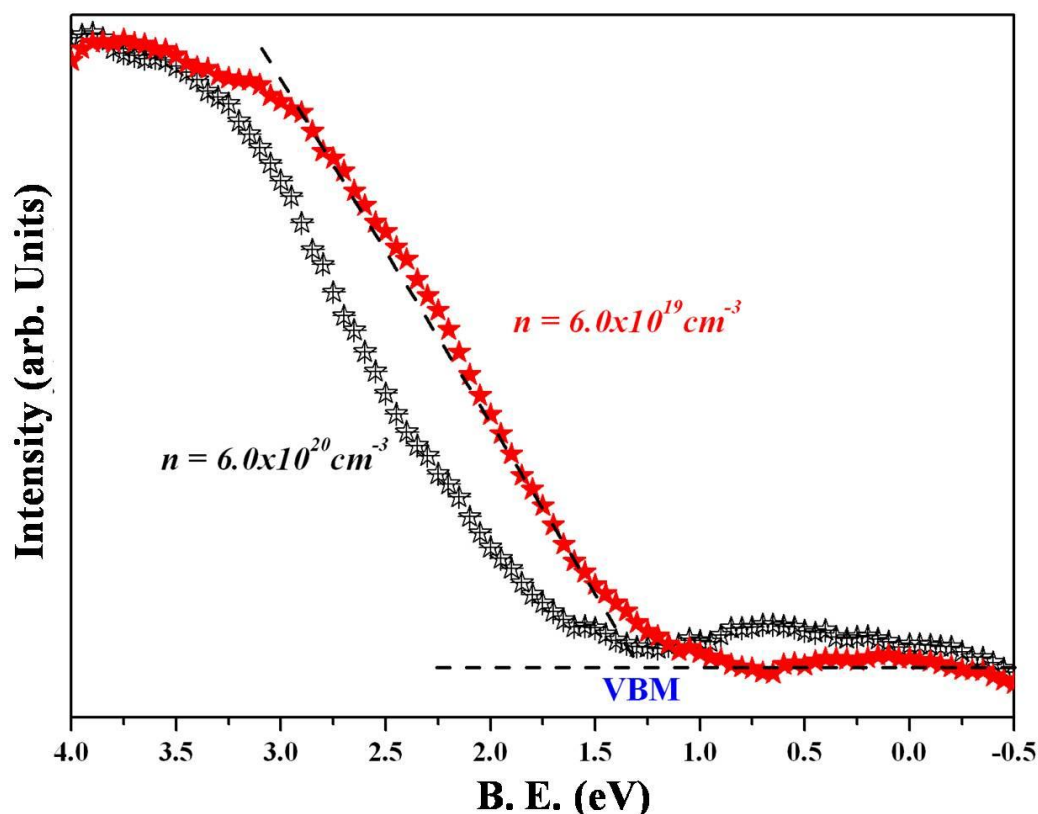
Fig. 6.17: *XPS valence band spectra for InN samples having two different carrier concentrations.*

As suggested in the literature we indeed observe a surface electron accumulation layer for low carrier concentration samples as shown in the Fig. 6.18. For higher carrier concentration VBM shows saturation. These effects can be explained as follows.[66] For a given bulk Fermi level the surface Fermi level position is determined by the consideration of charge neutrality. If the Fermi level is located below the branch point, some donor surface states will be unoccupied and hence positively charged. This surface charge must be balanced by a space charge due to downward band bending leading to an increase in the near surface electron density. For low carrier concentrations, surface band bending is large resulting in large surface electron accumulation. But as the bulk Fermi level increases (as carrier concentration increases), the reduction in band bending means that the space charge is no longer sufficient to balance the surface state charge, causing the Fermi level to move closer to the branch point near the surface in order that fewer donor states are un-occupied reducing the surface state charge. As the carrier concentration increases the bulk Fermi level approaches the branch point and the surface Fermi level must also therefore approach the branch point causing the band bending tend to zero. This can be clearly seen in the Fig. 6.18 as the carrier

concentration in the sample increases the VBM saturates showing the absence of any band bending.
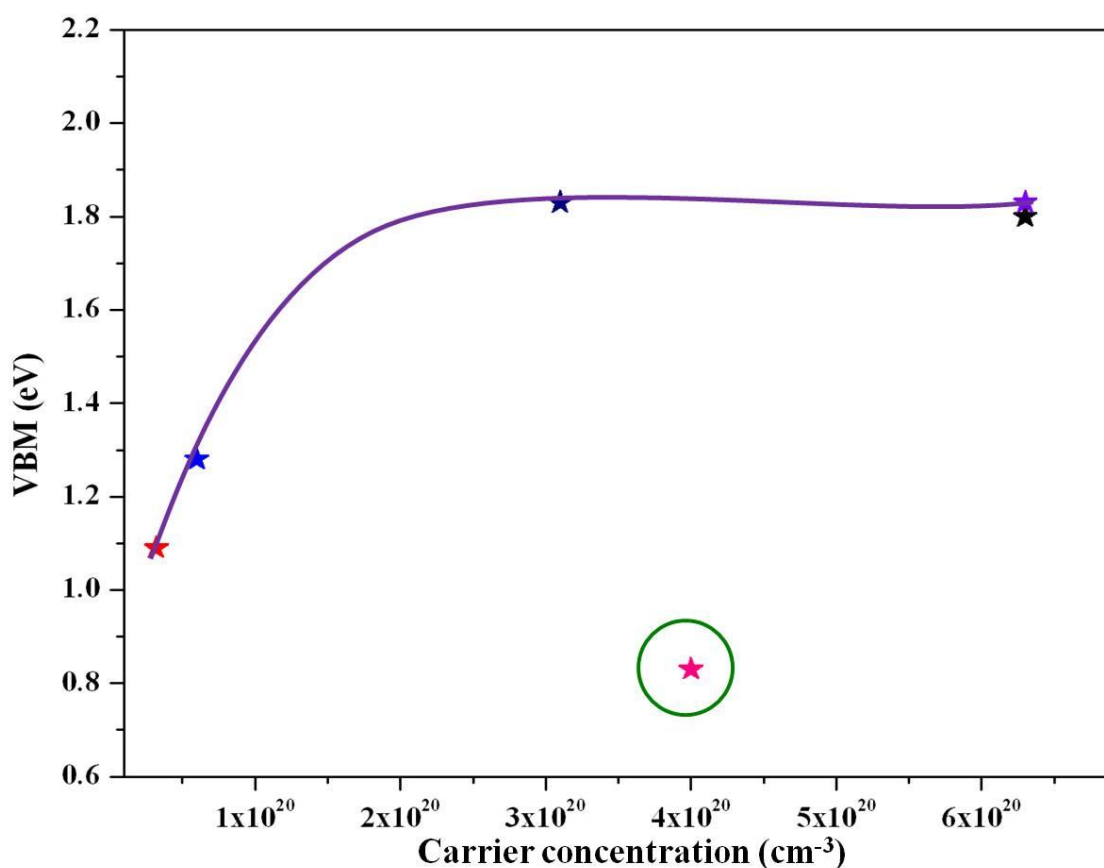
Fig. 6.18: *Measured XPS VBM vs. carrier concentrations.*

All the samples used for the measurements shown in Fig. 6.18 show wurtzite c-oriented (0001) films. It has been theoretically shown in the literature that for wurtzite surfaces the surface charge accumulation is unavoidable because of the donor surface states. Recent calculation predicts the absence of surface electron accumulation in non-polar surfaces. Fig. 6.18 also show a data point which deviates from the general trend shown in Fig. 6.18 lies much below other data points. Fig. 6.19 shows the XRD measurements on this sample. We observe peaks at 33.09^o, 51.6^o and 62.66^o, which correspond to the off-axis crystal planes of wurtzite InN (10$\underline{1}$1), InN (11$\underline{2}$0) and InN (20$\underline{2}$1) respectively besides the sapphire (0006) reflection. It can be seen that sample does not contain any c-oriented peak and the sample show a few other orientations, (10$\underline{1}$1) the most being prominent. Thus, there is an absence of surface electron accumulation in these orientations of InN. Recent calculation predicts the absence of surface electron accumulation on non polar surfaces.[67-69]

Our experimental measurement is in accordance with these predictions. However, more experiments are necessary to confirm these observations.
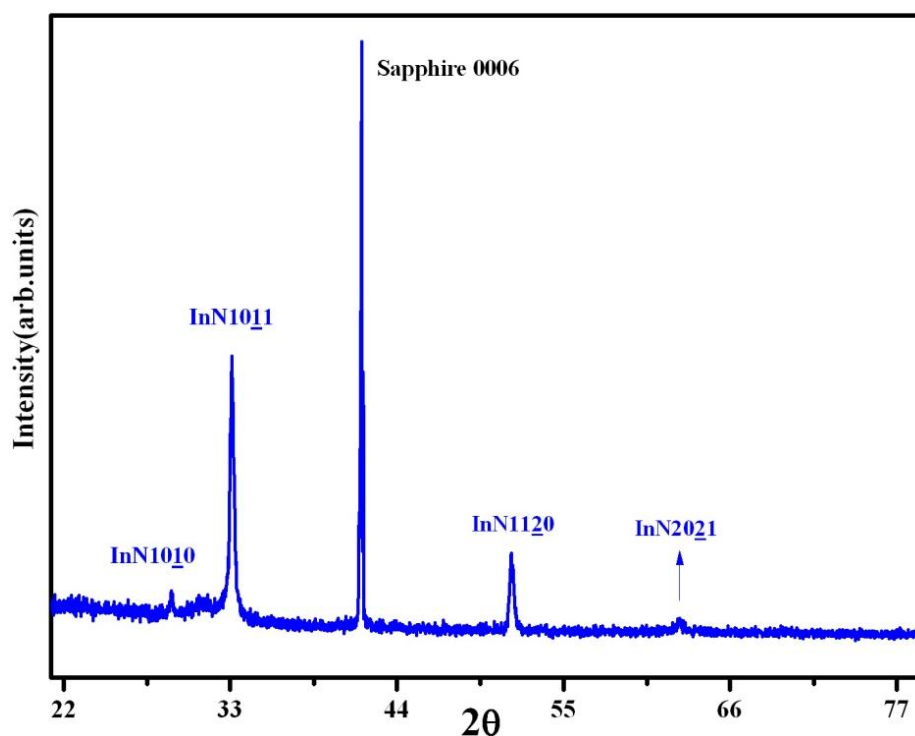
Fig. 6.19: *XRD pattern for sample (encircled data in Fig. 6.18) which do not have (0002) orientation.*

6.6   Conclusions

To address the factors that have been attributed in the literature to the high band gap observed for InN grown on bare sapphire, we have grown InN films by MBE and probed by complementary techniques. All the samples grown at 400°C, 450°C and 500°C are crystalline (wurtzite) α-InN and show a band edge emission at 1.78eV, irrespective of the growth temperature. Our results indicate that factors like quantum size effect, non-uniformity and presence of oxynitrides can be discounted as plausible reasons that result in the high band gap value. We demonstrate that single crystalline wurtzite InN can be grown on bare sapphire and its c-axis orientation depends strongly on substrate temperature. The optimum temperature for the growth of single crystalline c-oriented InN film on sapphire substrate is identified to be 450°C. At 500°C the c-axis of InN is parallel to the substrate a-b plane but at 450°C we observe it to be parallel to the substrate c-axis. At a still lower temperature of 400°C, single phase InN consisting of both orientations of growth is observed. We infer that crystal orientation and In/N stoichiometry do not influence the band gap of InN. In these

nitrogen rich InN films we conclude that strong Moss-Burstein effect can explain the observed high band gap. To address the low band gap problem we have grown InN simultaneously in an appropriately designed experiment on four differently surface modified sapphire (0001) substrates, which eliminates the effects due to variations in the growth conditions and characterized by several complementary probes. The surface sensitive and bulk probes have enabled us to rule out the possibility of Mie-resonances as reason for the low band gap feature of InN and Indium oxynitride or oxide as causes for high band gaps as perceived in the literature. We also discount the presence of impurities as unintentional dopants in the InN film and the measured carrier concentration is shown to correlate with interfacial lattice mismatch induced bulk defects. We unambiguously demonstrate here that the high bad gap ($\approx$ 2eV) is induced by azimuthally mis-orientation of wurtzite InN crystallites, while a singularly c-oriented InN film formed on GaN epilayer, show a low band gap ($\approx$ 0.7eV). A comprehensive analysis of band gap values reported for InN in literature grown using different growth techniques, and in the present work, show an empirical exponential dependence of the band gap, values on carrier concentration. Moss-Burstein shift calculated, assuming parabolic conduction band yields a high effective mass value which is not reasonable, prompting the need of considering a non-parabolic conduction band for InN to explain its properties. A Moss-Burstein shift based on non-parabolic conduction band is found to explain well the observed band gap variation in literature, and the present work, and yields the fundamental band gap value of InN to be 0.64eV. We have performed reflectivity and Hall measurements on different InN samples and calculated the effective mass by measuring the plasma frequency using Drude model for dielectric function. Experimentally measured effective mass is found to agree well with the theoretically calculated assuming a non-parabolic conduction band for InN. Thus, our analysis clearly suggests the necessity to consider non-parabolicity of conduction band of InN in order to elucidate its fundamental properties. On other hand as non-parabolicity originates from conduction band valence band interaction owing to the narrow band gap, our observations also supports a narrow band gap for InN. We have carried out XPS valence band measurements to calculate the valence band maxima for samples having different carrier concentrations so as to look into the issue regarding surface electron accumulation layer in InN. Our data shows surface electron accumulation for (0001) surface of InN and absence on (10$\underline{1}$1) surface.

References

[1] N. Ma, X. Q. Wang, F. J. Xu, N. Tang, B. Shen, Y. Ishitani, and A. Yoshikawa, Appl. Phys. Lett. **97**, 222114 (2010).

[2] R. Cusco´, N. Dome`nech-Amador, L. Artu´s, T. Gotschke, K. Jeganathan, T. Stoica, and R. Calarco, Appl. Phys. Lett. **97**, 221906 (2010).

[3] T. L. Tansley and C. P. Foley, Electron. Lett. **20**, 1066 (1984).

[4] K. S. A. Butcher and T. L.Tansley, Superlattices Microstruct. **38**, 1 (2005).

[5] T. Inushima, V. V. Mamutin, V. A. Vekshin, S. V. Ivanov, T. Sakon, M. Motokawa, and S. Ohoya, J. Cryst. Growth **227**, 481 (2001).

[6] V. Yu Davydov, A. A. Klochikhin, R. P. Seisyan, V. V. Emtsev, S. Ivanov V., F. Bechstedt, J. Furthmuller, H. Harima, A. V. Mudryi, J. Aderhold, O. Semchinova, and J. Graul, Phys. Status. Solidi B **229**, R1 (2002).

[7] Y. Nanishi, Y. Saito, and T. Yamaguchi, Japan. J. Appl. Phys. **42**, 2549 (2003).

[8] J. Segura-Ruiz, A. Molina-Sa´nchez, N. Garro, A. Garcı´a-Cristo´bal, A. Cantarero, F. Iikawa, C. Denker, J. Malindretos, and A. Rizzi, Phys. Rev. B **82**, 125319 (2010).

[9] J. Wu, W. Walukiewicz, K. M. Yu, J. W. Ager III, E. E. Haller, H. Lu, W. Schaff, Y. Saito, and Y. Nanishi, Appl. Phys. Lett. **80**, 3967 (2002).

[10] M. Higashiwaki and T. Matsui, J. Cryst. Growth **269**, 162 (2004).

[11] J. Kamimura, K. Kishino, and A. Kikuchi, Appl. Phys. Lett. **97**, 141913 (2010).

[12] T.-T. Kang, A. Hashimoto, and A. Yamamoto, Appl. Phys. Lett. **92**, 111902 (2008).

[13] C.-K. Chao, H.-S. Chang, T.-M. Hsu, C.-N. Hsiao, C.-C. Kei, S.-Y. Kuo, and J.-I. Chyi, Nanotechnology **17**, 3930 (2006).

[14] V. Yu. Davydov, A. A. Klochikhin, V. V. Emtsev, D. A. Kurdyukov, S. Ivanov V., V. V. Vekshin, F. Bechstedt, J. Furthmuller, J. Aderhold, J. Gral, A. V. Mudryi, H. Harima, A. Hashimoto, A. Yamamoto, and E. E. Haller, Phys. Status. Solidi B **234**, 787 (2002).

[15] A. Terentjevs, A. Catellani, and G. Cicero, Appl. Phys. Lett. **96**, 171901 (2010).

[16] J. Wu, W. Walukiewicz, S. X. Li, R. Armitage, J. C. Ho, E. R. Weber, E. E. Haller, H. Lu, W. J. Schaff, A. Barchz, and R. Jakiela, Appl. Phys. Lett. **84**, 2805 (2004).

[17] L. T. Tansley and C. P. Foley, J. Appl. Phys. **59**, 3241 (1986).

[18] I. Hamberg and C. G. Granqvist, J. Appl. Phys. **60**, R123 (1986).

[19] T. Yodo, H. Yona, H. Ando, D. Nosei, and Y. Harada, Appl. Phys. Lett. **80**, 968 (2002).

[20] A. L. Yang, H. P. Song, H. Y. Wei, X. L. Liu, J. Wang, P. X. Q. Lv, and and Z.G. Wang Jin, S. Y. Yang, Q. S. Zhu, Appl. Phys. Lett. **94**, 163301 (2009).

[21] T. Yodo, Y. Kitayama, K. Miyaki, H. Yona, Y. Harada, K. E. Prince, and K. S. A. Butcher, J. Cryst. Growth **269**, 145 (2004).

[22] D. Alexandrov, K. S. A. Butcher, and M. Wintrebert-Fouquet, J. Vac. Sci. Technol. A **22**, 954 (2004).

[23]Handbook Of X-Ray Photoelectron Spectroscopy, Perkin Elmer Corporation, Waltham (1979).

[24] J. Wu, W. Walukiewicz, W. Shan, K. M. Yu, J. W. Ager III, E. E. Haller, H. Lu, and W. J. Schaff, Phys. Rev. B **66**, 201403 (2002).

[25] J. Grandal, J. Pereiro, A. Bengoechea-Encabo, S. Fernández-Garrido, M. A. Sánchez-García, E. Muñoz, E. Calleja, E. Luna, and A. Trampert, Appl. Phys. Lett. **98**, 061901 (2011).

[26] H. -W. Lin, Y.-J. Lu, H. -Y. Chen, H.-M. Lee, and S. Gwo, Appl. Phys. Lett. **97**, 073101 (2010).

[27] S. Nakamura and M. Riordan, Scientific American **300**, 70 (2009).

[28] V. M. Polyakov and F. Schwierz, Appl. Phys. Lett. **88**, 032101 (2006).

[29] J. Wu, J. Appl. Phys. **106**, 011101 (2009).

[30] B. Monemar, P. P. Paskov, and A. Kasic, Superlattices Microstruct. **38**, 38 (2005).

[31] T. V. Shubina, S. V. Ivanov, V. N. Jmerik, D. D. Solnyshkov, V. A. Vekshin, P. S. Kop'ev, A. Vasson, J. Leymarie, A. Kavokin, H. Amano, K. Shimono, A. Kasic, and B. Monemar, Phys. Rev. Lett. **92**, 117407-1 (2004).

[32] K. M. Yu, Z. Lilental-Weber, W. Walukiezicz, W. Shan, J. W. Ager III, S. X. Li, R. E. Jones, E. E. Haller, H. Lu, and W. J. Schaff, Appl. Phys. Lett. **86**, 071910 (2005).

[33] . W. Trainor and K. Rose, J. Electron. Mater. **3**, 821 (1974).

[34] E. Burstein, Phys. Rev. B **67**, 775 (1954).

[35] T. S. Moss, Proc. Phys. Soc. **67**, 775 (1954).

[36] K. Sugita, H. Takatsuka, A. Hashimoto, and A. Yamamoto, Phys. Status. Solidi B **240**, 421 (2003).

[37] J. Wu, W. Walukiezicz, W. Shan, K. M. Yu, J. W. Ager III, E. E. Haller, H. Lu, and W. J. Schaff, Phys. Rev. B **66**, 201403 (2002).

[38] J. Wu, W. Walukiezicz, W. Shan, K. M. Yu, J. W. Ager III, E. E. Haller, H. Lu, and W. J. Schaff, Appl. Phys. Lett. **84**, 2805 (2004).

[39] E. O. Kane, J. Phys. Chem. Solids **1**, 249 (1957).

[40] A. Kasic and M. Schubert, Phys. Rev. B **65**, 115206 (2002).

[41] B. R. Nag, Phys. Status. Solidi B **237**, R1 (2003).

[42] S.M.Shivaprasad, J. Appl. Phys. **109**, 093513 (2011).

[43] T. Yamguchi, D. Muto, T. Araki, N. Maeda, and Y. Nanishi, Phys. Status. Solidi C **109**, 093513 (2008).

[44] Y. Yao, T. Sekiguchi, Y. Sakuma, N. Ohashi, Y. Adachi, H. Okuno, and M. Takeguchi, Cryst. Growth Des. **8**, 11073 (2008).

[45] G. Koblmuller, C. S. Gallininat, S. Bernardis, J. S. Speck, G. D. Chern, E. D. Readinger, H. Shcen, and M. Wraback, (n.d.).

[46] V.Singh, Opt. Mater. **12**, 1998 (2006).

[47] T. Nagata, G. Koblmuller, O. Bierwagen, C. S. Gallinat, and J. S. Speck, Appl. Phys. Lett. **95**, 132104 (2009).

[48] P. D. C. King, T. D. Veal, H. Lu, S. A. Hatfield, W. J. Schaff, and C. F. McConville, Surf. Sci. **602**, 871 (2008).

[49] P. D. C. King, T. D. Veal, C. E. Kendrick, L. R. Bailey, S. M. Durbin, and C. F. McConville, Phys. Rev. B **78**, 033308 (2008).

[50] K. Scott, A. Butcher, M. Wintrebert-Fouquet, P. P.-T.Chen, K. E. Prince, H. Timmers, S. K. Shresthta, T. V. Shubina, S. V. Ivanov, R. Wuhrer, M. R. Phillips, and B. Monemar, Phys. Status. Solidi C **2**, 2263 (2005).

[51] Y. Nanishi, Y. Saito, and T. Yamaguchi, Japan. J. Appl. Phys. **42**, 2549 (2003).

[52] K. Levenberg, The Quarterly Of Applied Mathematics **2**, 164 (1944).

[53] D. Marquardt, SIAM Journal Of Applied Mathematics **11(2)**, 431 (1963).

[54] A. Ghani Bhuiyan, K. Sugita, K. Kasashima, A. Hashimoto, A. Yamamoto, and V. Yu. Davydov, Appl. Phys. Lett. **83**, 4788 (2003).

[55] M. Alevi, R. Atalay, G. Durkaya, A. Weesekara, A. G. U. Perera, N. Dietz, R. Kirste, and A. Hoffman, J. Vac. Sci. Technol. A **26(4)**, 1023 (2008).

[56] N. W. Ashcroft and N. D. Mermin, Solid State Physics, Saunders (1976).

[57] Charles Kittel, Introduction To Solid State Physics, 7th Ed., Wiley (1996).

[58] O.S. Heavens, Thin Film Physics. Ed. Methuen, London (1970).

[59] M. Born and E. Wolf, Principles Of Optics, Pergamon Press (1968).

[60] P. Perlin, E. Litwin-Staszewska, B. Suchanek, W. Knap, J. Camassel, T. Suski, R. Piotrzkowski, I. Grzegory, S. Porowski, E. Kaminska, and J. C. Chervin, Appl. Phys. Lett. **68**, 1114 (1996).

[61] I. Mahboob, T. D. Veal, and C. F. McConville, Phys. Rev. Lett. **92**, 036804-1 (2004).

[62] R. E. Jones, K. M. Yu, S. X. Li, W. Walukiewicz, J. W. Ager, E. E. Haller, H. Lu, and W. J. Schaff, Phys. Rev. Lett. **96**, 125505 (2006).

[63] H. Lu, W. J. Schaff, L. f. Eastman, and C. E. Strutz, Appl. Phys. Lett. **82**, 1736 (2003).

[64] T.D. Veal, I. Mahboob, L. F. J. Piper, C.F. McConville, H. Lu, and W. J. Schaff, J. Vac. Sci. Technol. B **22(4)**, 2175 (2004).

[65] C.-T. Kuo, S.-C. Lin, K.-K. Chang, H.-W. Shiu, L.-Y. Chang, C.-H. Chen, S.-J. Tang, and S. Gwo, Appl. Phys. Lett. **98**, 052101 (2011).

[66] P. King, T. Veal, P. Jefferson, S. Hatfield, L. Piper, C. McConville, F. Fuchs, J. Furthmüller, F. Bechstedt, Hai Lu, and W. Schaff, Physical Review B **77**, 1-6 (2008).

[67] D. Segev and C. G. Vand de Walle, Europhys. Lett. **76**, 305 (2006).

[68] C. G. Vand de Walle and D. Segev, J. Appl. Phys. **101**, 081704 (2007).

[69] C. -L. Wu, H. -M. Lee, C. -T. Kuo, C. -H. Chen, and S. Gwo, Phys. Rev. Lett. **101**, 106803 (2008).

Chapter VII

Lattice Matching Epitaxy for GaN and InN growth on Ga and In induced superstructures of Si

In this chapter we propose a novel method to grow good quality GaN and InN on reconstructed Si surfaces. We use different 2D phase diagrams of metal induced submonolayer superstructural phases on Si surfaces discussed chapter in IV and V as guidance to obtain surface phases and grow InN and GaN on these phases using MBE. We study the grown films using several complementary characterization tools to understand the influence of these modified interfaces on the over grown films. We explain the observed results using what we call as 'lattice matching epitaxy' of these reconstructed unit cells with the unit cell of the nitride overlayer.

7.1   Growth of GaN on Ga induced reconstructions of Si(111)-7x7

7.1.1   Introduction

As it is difficult to synthesis GaN nitride from its molten state using single crystal growth method, they are usually grown on foreign substrates.[1]   Among the different substrates used, SiC and sapphire are most common.[2] A dislocation density of low 10^8cm^{-2} has been achieved for best samples grown by optimizing the growth processes for GaN growth.[3]   However, in order to increase the performances of high power devices like lasers, material with better crystalline quality is needed. A dislocation density of $<10^7 \text{cm}^{-2}$ has been achieved by using Epitaxial Lateral Over Growth of GaN on sapphire.[4] Another important substrate for GaN growth is Si,[5,6] which has many advantages compared to SiC and sapphire like high crystal quality, low cost, good electrical & thermal conductivity, availability of large-area size as a substrate, etc., There are some fundamental problems for the growth of GaN on Si to be circumvented such as cracking in the epitaxial layer because of strain due to large mismatch in the lattice parameters (~17%) and thermal expansion coefficients (~54%). These high mismatches results in a high density of threading dislocations of the order of

(10^9–10^{10} cm^{-2}) in the GaN film on silicon substrates, which significantly affects the performance of the GaN based devices. Several types of growth methods like use of various buffer layers, different conditions of growth and annealing processes have been tried by researchers to obtain crack free high quality GaN on Si substrates. Device applications are hindered by the fact that cracks appear randomly on the grown GaN films. There are approaches reported in literature to reduce dislocation density in the GaN films. Techniques including conventional growth by MBE or MOCVD using various buffer layers like GaN, AlN, SiC, Si_3N_4, HfN etc., combination of MBE and MOCVD, growth on patterned substrate, selective area epitaxy, conventional ELOG, mask less ELOG, pendo-epitaxy, wafer bonding and film lift-off, use of surfactant like Bi, Ni etc., have already been used in order to find successful processes for the growth and/or the realization of GaN-based devices on silicon substrates.[4,7-11] Recent literature shows a great interest in using surface modifications of the substrate as an alternate method for buffer layer because of process compatibility and flexibility. For example methods like formation of superstructural phase of Ga by adsorbing submonolayer quantities of Ga and nitridation of substrates results in modified substrate forming suitable initial template for nucleation of GaN and results in the formation of less defected GaN.

We have previously obtained 2D phase diagram for Ga/Si(111)-7x7 system by doing several adsorption/desorption experiments in UHV using AES and LEED. Here we use these reconstructions as a template to grow GaN and study the effect of these modified interfaces on the overgrown GaN film.

7.1.2   Results and discussions

Though sapphire has been the mainstay substrate[2] to form III-nitride hetroepitaxial structures, it is essential to form them on silicon[5,6] to make it a commercially viable technology for large scale applications such as High Brightness Light Emitting Diodes (HB-LEDs) or Full Spectrum Solar Photovoltaics, which can have significant contributions towards energy security.

Motivated by the concept of Domain Matching epitaxy[12], in this work we demonstrate a novel approach to mitigate the silicon/GaN mismatch by using integral lattice matching. We form Ga induced stable superstructural phases on Si(111) surface and subsequently use these
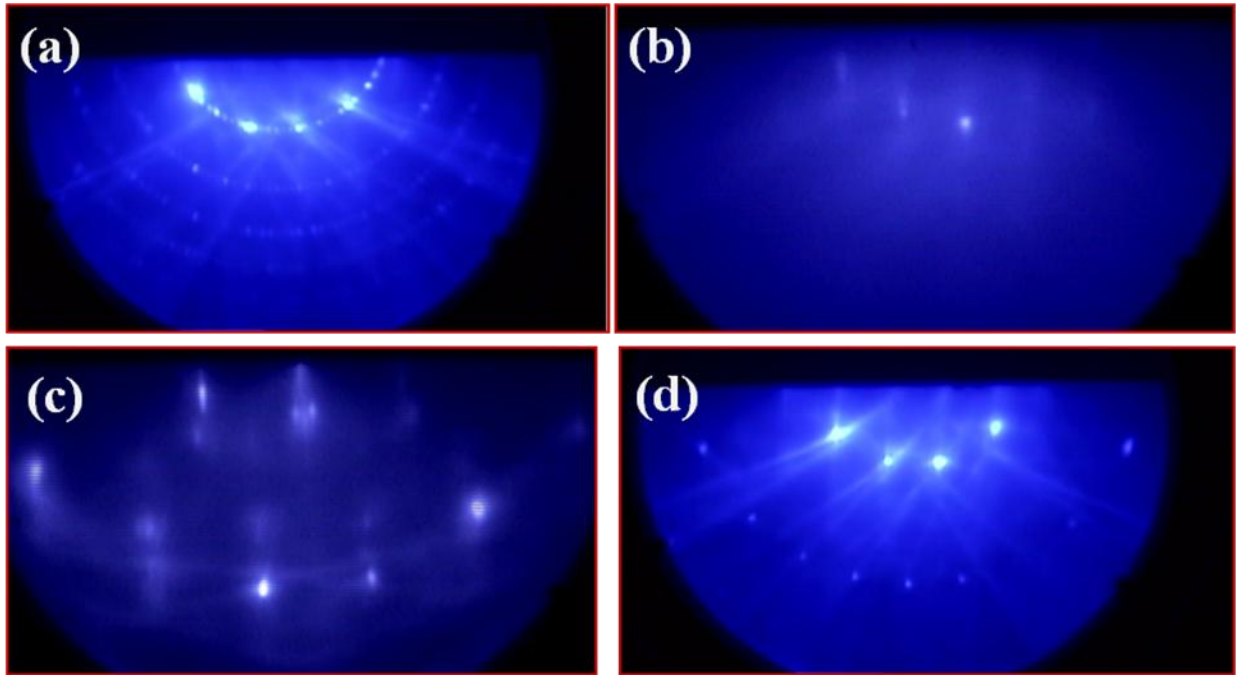
Fig. 7.1: *RHEED pattern of different superstructural phases of Si used to grow GaN (a) clean Si(111)-7x7, (b) Si(111)1x1-Ga, (c) Si(111)6.3x6.3-Ga, and (d) Si(111) √3x√3-R30ᵒ-Ga*

unit cells as templates for GaN epitaxy. In the past we have reported 2D-phase diagrams of several metal/Si surfaces, demonstrating possibility of forming several stable surface phases by kinetic control.[13,14] Using three stable Ga/Si(111) surface phases, with different integral-lattice-matching schemes, we demonstrate that the Si(111)- $\sqrt{3}$x$\sqrt{3}$-R30ᵒ-Ga phase results in high quality GaN epitaxial layers, as evidenced by XRD, PL, RHEED, FESEM and XPS. We feel this approach can open up a new route in modifying Si surfaces and rendering them suitable for III-nitride epitaxy.[15]

In the first experimental phase, Ga is deposited onto a clean Si(111)-7x7 surface at a flux rate of 0.1ML/min, in the ultra high vacuum chamber equipped with Auger Electron Spectroscopy (AES) and Low Energy Electron Diffraction (LEED). As discussed in chapter 4 the first two Ga layers grow in the Frank-van-der Merwe (layer-by-layer) mode and show a (1x1) LEED pattern, on top of which 3D islands are formed in the Stranski-Krastanov (layer + islands) morphology.[9,16] We choose two Ga coverages (1.1 and 2.2 ML) on Si(111) surface and anneal them to different temperatures, while monitoring the resulting phases by *in-situ* LEED and AES (1ML ~ 6.8×10^{14} atoms/cm^2, the bulk truncated Si(111) density). The residual thermal desorption curves for these two systems has been shown and discussed in chapter 4, which is a study of the thermal stability using Auger Ga(LMM)/Si(LVV) intensity
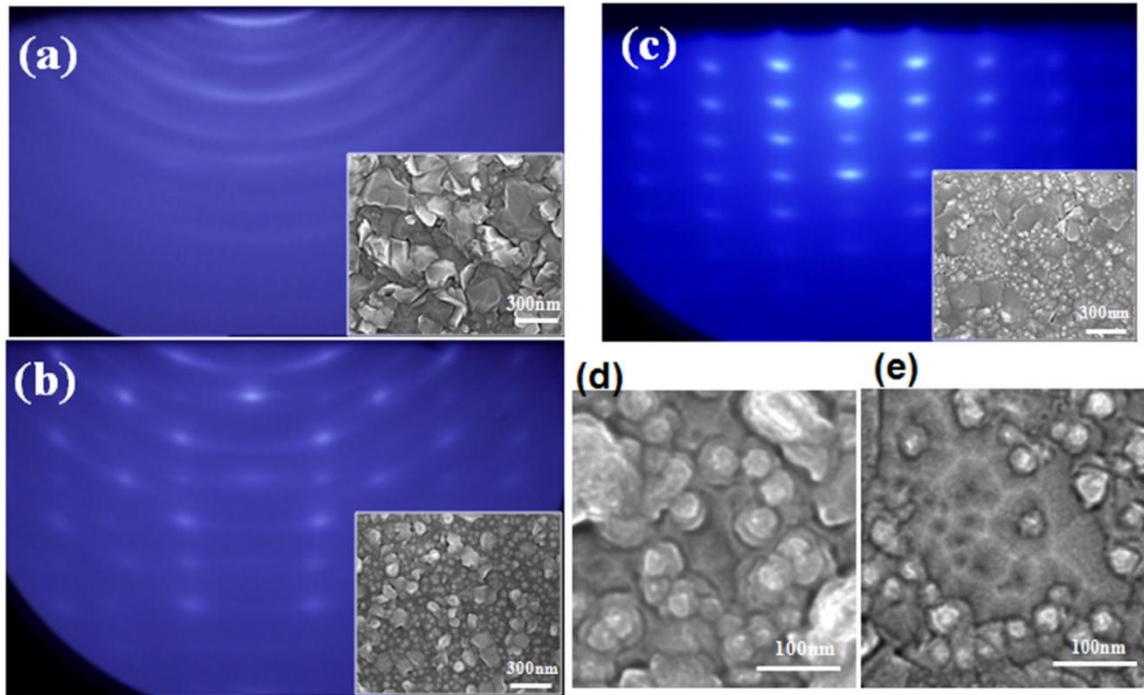
Fig. 7.2: *RHEED pattern of GaN films grown on (a) 1x1, (b) 6.3x6.3, and (c) √3x√3-R30°
reconstructed surfaces. The inset in each pattern shows the corresponding FESEM
micrograph. (d) and (e) show the magnified FESEM images for GaN grown on 6.36.3 and
√3x√3-R30° reconstructed surface, respectively.*

ratio, and the structural phases observed by RHEED is shown in Fig. 7.1. At room
temperature, the surfaces have an Auger intensity ratio of 0.20 and 0.37 respectively, and a
(1x1) RHEED pattern, which shows that the (7x7) reconstruction of the RHEED is lifted by
Ga adsorption. As temperature reaches 200°C, the 2nd layer Ga adatoms agglomerate into 3D
islands on a stable monolayer at a ratio of 0.17, with a (6.3x6.3) reconstruction which is
stable up to 450°C. The monolayer slowly desorbs in the $400-600^{o}$C temperature range, with
a $\sqrt{3}x\sqrt{3}R30^{o}$ structural phase. This phase subsequently leads to the clean Si(7x7) phase at
630°C as Ga completely desorbs from Si(111). As shown in Fig. 7.1, in this thermal
desorption process we are able to identify three stable reconstructed surface phases of the
Ga/Si interface, namely (1x1), (6.3x6.3) and $(\sqrt{3}x\sqrt{3})$ $R30^{o}$ phases. By measuring the RHEED
spot distances by line scans, the respective unit cell dimensions are determined to be 3.8Å,
23.4Å, and 6.57Å, respectively. Since the *a, b* dimensions of the GaN unit cell are 3.19Å, the
(1x1) phase appears to have the least misfit (19%) for epitaxy, among the three surface
phases studied.

        After identifying the optimal conditions for obtaining the surface phases by
AES/LEED, the second phase of experiments is performed in a Plasma Assisted Molecular

Beam Epitaxy (PA-MBE) system with *in-situ* RHEED. Now in the MBE chamber, by three independent growth experiments we obtain the (1x1), (6.3x6.3) and the ($\sqrt{3}$x$\sqrt{3}$) Ga induced phases (by Ga deposition followed by annealing), as observed by RHEED. On each of these three templates, we grew 1.5µm thick GaN by effusing Ga from a Knudsen cell at 1000°C and a N$_2$* plasma at 350W with a flow rate of 4.5sccm, while keeping the substrate at 400°C. However, for the (1x1) phase, a brief 5min N$_2$* plasma nitridation at 150°C was used to stabilize the phase, before depositing GaN at 400°C. We characterize these GaN films by RHEED, XRD, PL, XPS and FESEM to evaluate the quality of the overlayers. Fig. 7.2 shows the RHEED pattern with the corresponding FESEM images as insets, while Fig. 7.3 shows the XRD pattern with the PL spectra as inset, for the GaN films grown on the three surface phase templates. In the figures (7.2 & 7.3) (a), (b) and (c) corresponds to the GaN growth on (1x1), (6.3x6.3) and ($\sqrt{3}$x$\sqrt{3}$)-R30^{o} reconstructed surface, respectively. The Fig. 7.2 (d) and (e) represent the higher magnification scan of FESEM images of GaN grown on (6.3x6.3) and ($\sqrt{3}$x$\sqrt{3}$)- R30^{o} reconstruction surface, respectively.

The RHEED pattern for GaN grown on the (1x1) reconstructed surface phase shows concentric rings, suggesting an amorphous-like and textured film[17] as evident from the FESEM morphology which shows a granular morphology, with a surface roughness of 3.4nm. The XRD shows (Fig. 7.3(a)) a low intensity peak corresponding to (0002) planes[18] with a FWHM of 540 arc-sec. RHEED and XRD results suggest low crystallinity regions smaller than the coherence length of RHEED (10-20nm). The corresponding PL shows a broad band edge at 360 nm, which corresponds to 3.44eV with FWHM of 0.32eV (Fig. 7.3 inset a). Also by XPS we measure the surface N:Ga composition ratio to be 0.94 using appropriate values of the atomic sensitivity factors.[19] Thus, for the growth on Si(111)-1x1 phase the GaN formed is amorphous and non-stoichiometric. In Fig. 7.2(b); for GaN grown on (6.3x6.3) surface phase, the RHEED now shows clear poly-crystallinity with amorphous rings laced with slightly elongated spots (Fig. 7.2(b)), while FESEM (inset) shows a well connected morphology of small features embedded in large GaN islands and the surface roughness is measured to be 3nm using AFM.[20] XRD of this film shows the GaN(0002) with FWHM of 460 arc sec (Fig. 7.3(b)) and the intensity is four times that of the (1x1) case, while the PL band edge emission is located at 362 nm (3.43eV) with FWHM of 0.30eV *i.e.* narrower than in the (1x1) case. The XRD pattern clearly shows that GaN grows in the
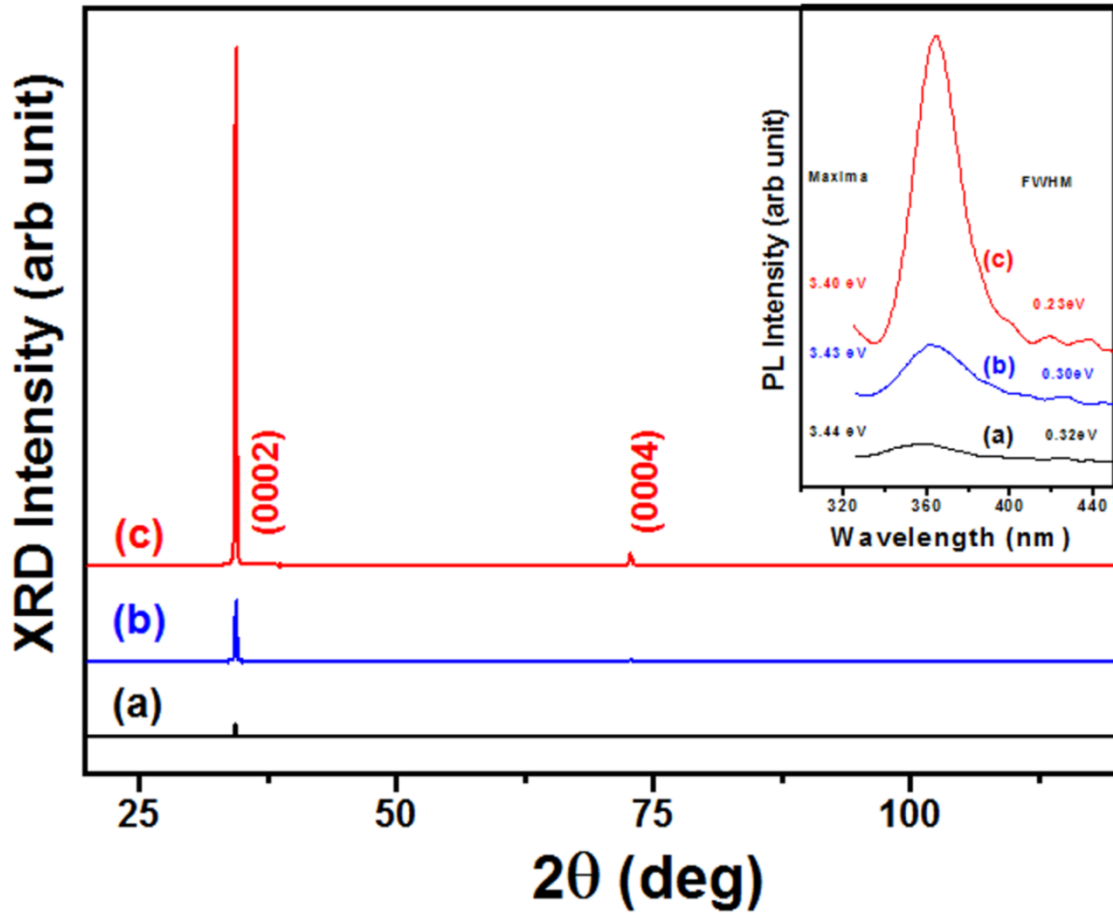
Fig. 7.3: *The XRD spectra; inset shows the PL spectra for GaN films grown on (a) 1x1, (b) 6.3x6.3, and (c) $\sqrt{3}x\sqrt{3}$-R30° reconstructed surfaces.*

wurtzite phase with the c-axis perpendicular to the substrate. XPS measurements show N/Ga surface composition ratio of 0.96 indicating that GaN formed is still slightly nitrogen deficient. Figures 7.2(c) & 7.3(c) show characterization results for 1.5µm GaN on ($\sqrt{3}x\sqrt{3}$) reconstructed Ga induced Si(111) surface. The RHEED pattern in this case is a well ordered spotty pattern, manifesting the formation of a single crystal wurtzite GaN. The XRD shows a high crystallinity with preferred orientation of [0001] direction. The (0002) peak has 360 arc-sec FWHM and a very high intensity (24 times the (1x1) case and the 6 times the (6.3x6.3) case). We also observe a high intensity PL band emission edge at 3.40eV[21] with an FWHM of 0.23eV and near surface stoichiometry by XPS with the N:Ga ratio of 0.99. Fig. 7.2 (d) and (e) show high magnification FESEM images of GaN surfaces of the films grown on (6.3x6.3) and the ($\sqrt{3}x\sqrt{3}$)-R30° templates. It can be clearly seen that the film is single crystalline with several faceted dislocations. As compared to the literature[22], the density and size of these dislocation are low and comparable to those observed for AlN buffer layers on

Si. We also see these dislocations pits being filled by small islands of GaN leading to the bimodal island size distribution with a low surface roughness of 1.8nm.
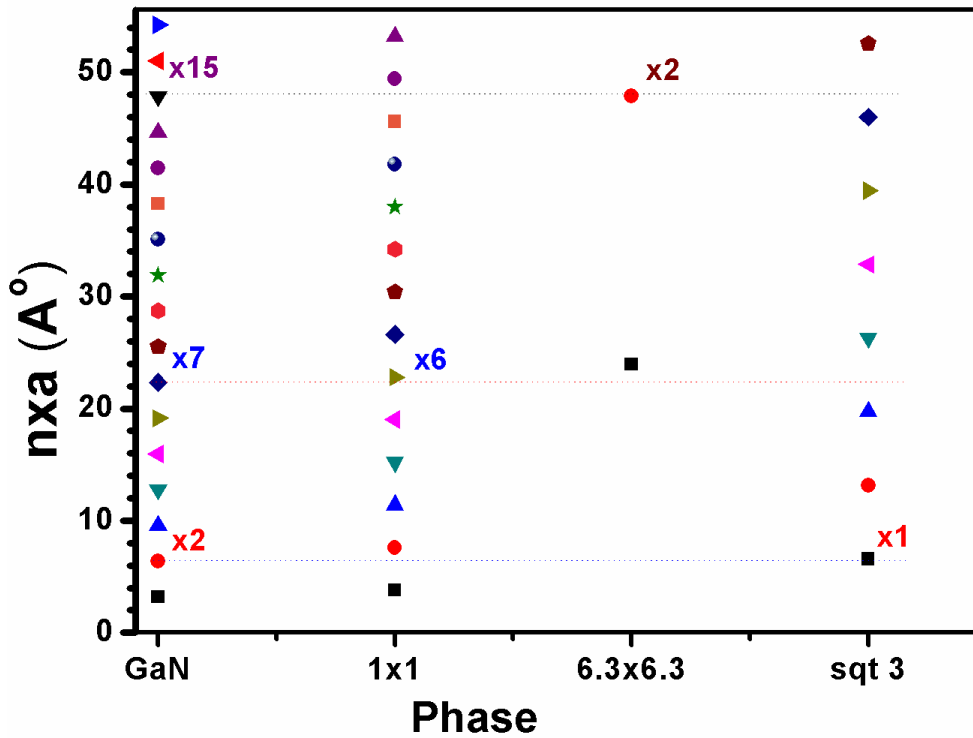
Fig. 7.4: *Lattice parameter matching of GaN with 1x1, 6.3x6.3 and √3x√3 R30º phases*

All these results clearly reveal that the GaN grown on the (√3x√3) reconstructed surface is of superior quality, which can be attributed to the following: The relation between lattice parameters of Ga induced superstructural (1x1), (6.3x6.3) and (√3x√3) with GaN lattice is; $a_{(1x1)} = 1.19$ a_{GaN}, $a_{(6.3x6.3)} = 7.5a_{GaN}$ and $a_{(\sqrt{3}x\sqrt{3})} = 2.04a_{GaN}$ and thus manifest the integral lattice matching epitaxy of GaN as 6/5, 15/2 and 2/1, respectively as shown in Fig. 7.4. The misfit is maximum in case of (1x1), because six GaN unit cell match with five unit cells of (1x1), resulting in a 17% lattice mismatch. This strain can be relaxed by the formation of an amorphous-like GaN overlayer. In the case of (6.3x6.3) in a large domain, fifteen unit cells of GaN match with two unit cells of (6.3x6.3), with a lattice mismatch of 7% per unit cell, resulting in the polycrystalline GaN. The (√3x√3) R30º has nearly double the lattice parameter of GaN and thus the lattice matching happens at every alternate unit cell of GaN, yielding a high quality epitaxial GaN films. Thus, (√3x√3)-R30º surface phase offers the best template for the epitaxial growth of GaN, as compared to the other two reconstructions studied. The FWHM of the (0002) peak in XRD (360 arc-sec) is comparable to the best reported for GaN on Si surfaces with AlN buffer layers.

7.2   Growth of InN on In induced reconstructions of Si(111)-7x7

7.2.1   Introduction

As discussed earlier, among the III-nitrides, forming high quality InN films that have great optoelectronic potential remains enigmatic due to its low dissociation energy which restricts growth temperature that is necessary for epitaxy.[23]   Several surface modifications such as nitridation of substrate and use of different buffer layers prior to growth and Epitaxial Lateral Over Growth (ELOG) are employed in search of recipes to form stable and high performance GaN 2D-films, but not much is explored for InN growth. Though, sapphire has been the most desirable substrate, there is a growing interest of growth of InN on Si, motivated by the need to integrate with the well established silicon technology.[24,25]

Nitridation of sapphire substrates leading to a thin AlN layer or growth of AlN buffer layer prior to the main layer growth was shown to eliminate the azimuthal mis-orientation of InN grains on bare sapphire substrates leading to better quality films.[23]   GaN as buffer has shown to be promising owing to its low epitaxial mismatch with InN.[26-28]   Use of alternating low and high temperature InN layers was shown to improve the crystalline quality of the material, but has been relatively less successful.[29] Though literature shows the use of the above methods in the case of InN growth on Si substrates as well, due to limited studies in literature the understanding of mechanism and progress in making high quality films are lacking.[30-32]

7.2.2   Results and discussions

The present study is a demonstration of In induced stable interfacial superstructural phases on Si (111), as templates for growth. This work assumes importance since this is an overwhelming necessity to obtain epitaxial growth at reduced substrate temperature, due to low dissociation temperature of InN. Plasma Assisted Molecular Beam Epitaxy is the preferred technique to study InN growth, since the growth temperature chosen can be independent of the N source.   We study InN growth using Plasma Assisted Molecular Beam Epitaxy (PA-MBE) by controlled and careful experiments. The experiments involve firstly, the formation of the In metal induced superstructural phases in the submonolayer regime, followed by growth of epitaxial InN films. The films formed are characterized by employing several complementary characterization tools to identify the superstructural interfacial phase

formed and also to evaluate the quality of the InN film. We then correlate the 2D unit cells of the superstructure and InN overlayer in terms of Lattice Matching Epitaxy (LME).

Several research groups, including ours have previously shown the formation of several In induced submonolayer superstructural phases on Si surfaces, viz. Si (111)-1x1-In,
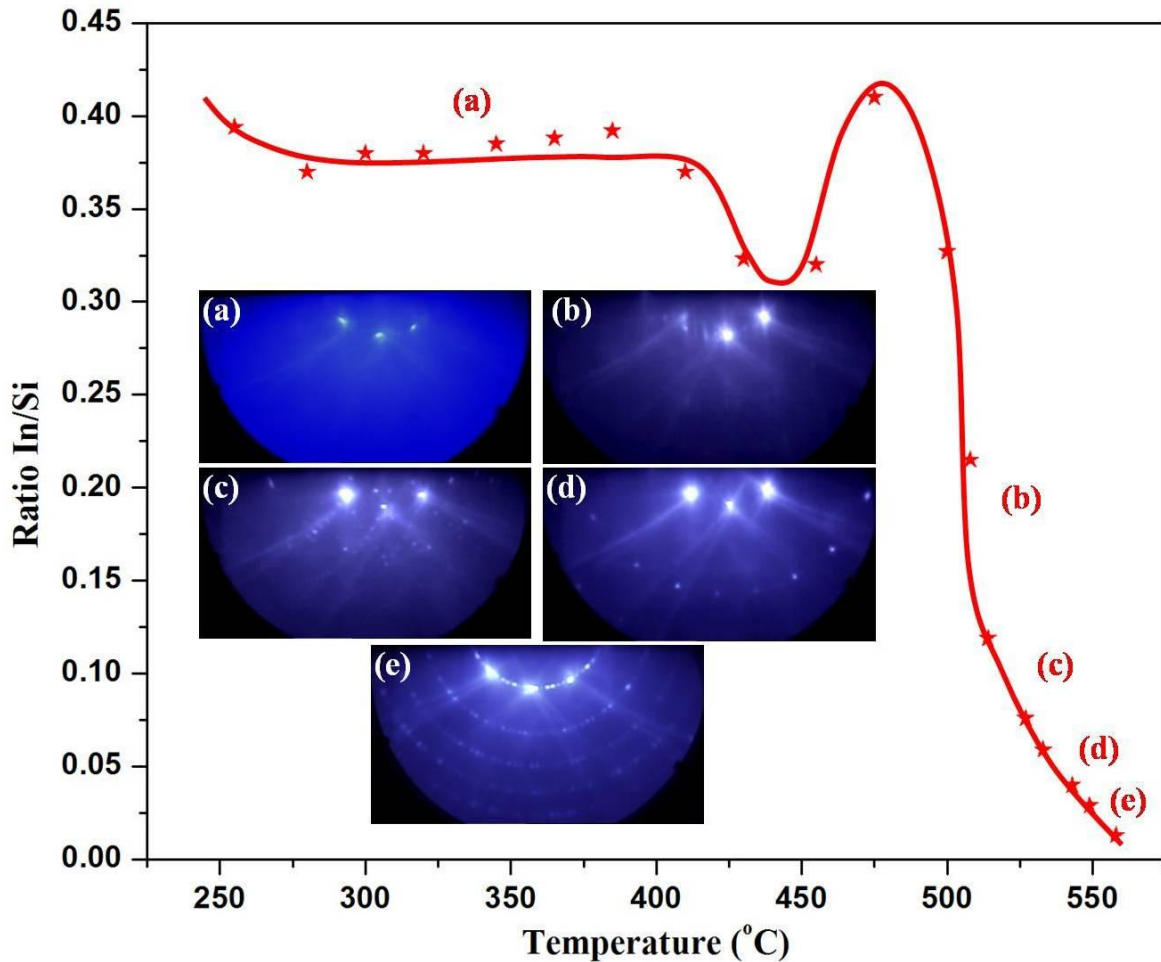
Fig. 7.5: *Residual thermal desorption curve of ~2ML of In on Si(111)-7x7 surface. Graph shows the ratio of Auger intensities of In MNN (404eV) to Si LVV (92eV) peak versus annealing temperature. RHEED patterns of different superstructural phases of Si a) Si(111)1x1-In, b) Si(111)4x1-In, c) Si(111)√31x√31-In, d) Si(111)√3x√3-In and e) Si(111)7x7 are shown in inset.*

Si (111)-√31x√31R±19°-In, Si (111)-√3x√3R30°-In, Si (111)-4x1-In on the Si (111)-7x7 surface. Based upon several experiments in UHV and using *in-situ* Low Energy Electron Diffraction (LEED) and Auger Electron Spectroscopy (AES) measurements, we have previously reported 2D phase diagram that show several kinetic pathways for the formation of these surface structural phases. An InN growth temperature is chosen as low as 300°C, since all the observed phases are stable at this temperature. Nitrogen flux is set to be 4.5sccm

and In flux used is $4.4 \times 10^{13} \text{cm}^{-2}\text{s}^{-1}$, which results in the InN growth rate of 0.3μm per hour as determined by surface profile analyzer and cross section FESEM. FESEM is also used to study the surface morphology, and the film crystallinity is determined by XRD measurements. Optical emission from the sample is carried out using room temperature Photoluminescence (PL) both in the visible and IR regions and charge carrier concentration is estimated by Hall Effect measurements using Vander Pauw method. Stoichiometry measurements are done by X-ray Photoelectron Spectroscopy using MgK$_\alpha$ source. InN samples grown on phases, 7x7, √31x√31, √3x√3, 4x1 and 1x1 are denoted as sample A, B, C, D and E respectively in the following discussions. The kinetic desorption pathway is represented by the desorption curve which plots the In/Si Auger ratio versus annealing temperature shown in Fig. 7.5. The Auger ratio of In MNN (404eV) peak to Si LVV (92eV) peak is plotted versus annealing temperature. The residual thermal desorption process involves deposition of certain monolayer of In on the surface, annealing the substrate to fixed interval of time and monitoring the residual In on the surface with structural and chemical probes. Fig. 7.5 shows the progressive appearance of different phases viz., (a) 1x1, (b) 4x1, (c) √31x√31, (d) √3x√3 and (e) 7x7 as In desorbs from the surface. The different superstructural phases are identified by the respective RHEED pattern and are also shown in Fig. 7.5. Now InN of 0.3μm is deposited on different phases of Si(111)-In system. Surface morphology of the grown InN films obtained by FESEM is shown in Fig. 7.6(a), (b), (c) and 2(d) for samples A, B, C, D and E, and their respective RHEED pattern as insets. Fig. 7.6 (a), (b), (c) show large InN crystallites of random shapes and their corresponding RHEED pattern depict broken ring pattern, that is characteristic of a polycrystalline surface. Fig. 7.6(d) shows the FESEM image for InN grown on 4x1 phase which has closely packed hexagonal crystallites with average grain size of ≈100nm having pyramidal tops. The inset of Fig. 7.6 (d) shows corresponding broken ring RHEED pattern where the elongated spots (arcs) have a high spot to background intensity contrast, suggesting a random arrangement of
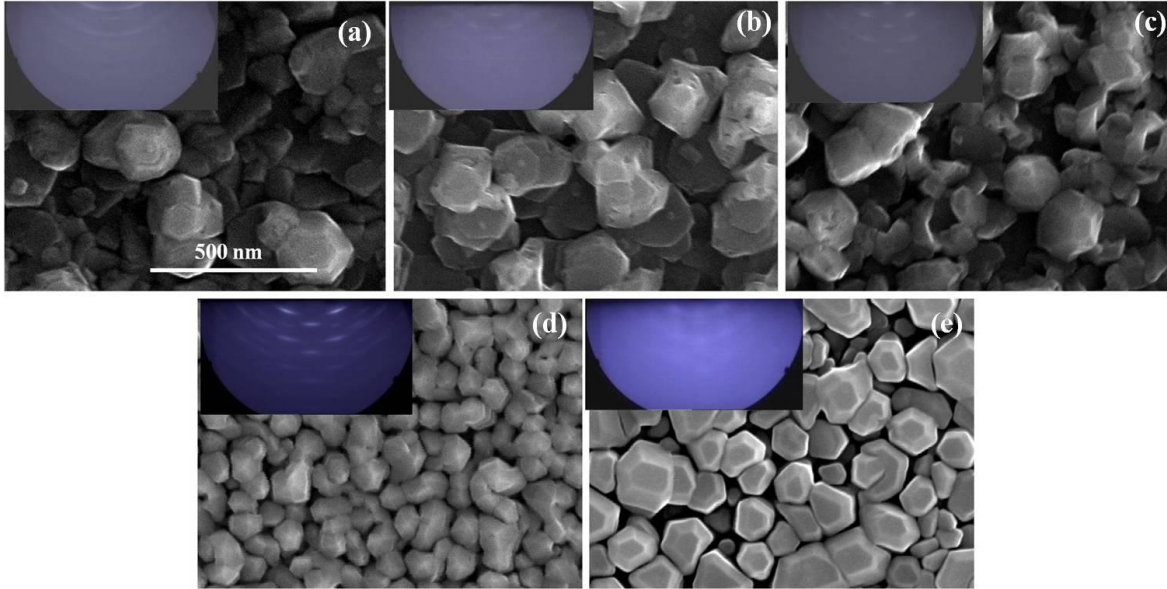
Fig. 7.6: *FESEM image after growth of InN films grown on a) Si(111)7x7, b) Si(111)√31x√31-In, c) Si(111)√3x√3-In, d) Si(111)4x1-In and e) Si(111)1x1-In. Inset shows the respective RHEED pattern of the films.*

crystallites. The InN grown on 1x1 surface shows a morphology in Fig. 7.6(e) which consists of larger hexagonal grains with flat tops. Inset to Fig. 7.6(e) show RHEED pattern, which is markedly different from that of other films grown, showing a spotty plus streaky pattern superimposed on a faint ring background. This manifests better ordered InN crystallites formed preferentially on the 1x1 phase as compared to films grown on other superstructures. The Root Mean Square (RMS) surface roughness of the different samples grown is measured by AFM, over a 5x5μm^2 area. Samples A, B and C show RMS roughness of $\approx$ 35nm whereas samples D and E show a value of $\approx$15nm indicating that films formed on 1x1 and 4x1 surfaces, have smoother surface morphology.

Fig. 7.7(a)-(e) depict the θ-2θ XRD scans for samples A, B, C, D, and E, respectively, showing that wurtzite InN films are formed. Fig. 7.7(a) and 4(b) show the XRD pattern for InN grown on clean Si 7x7 and In induced Si(111)-√31x√31 phase, which clearly shows crystalline InN (0002) and InN (0004) peaks at 31.33^o and 65.37^o respectively. The Fig. 7.7(a) and Fig. 7.7(b) also show a weak presence of InN (10$\underline{1}$1) and InN (10$\underline{1}$3) orientations assigned to peaks at angles 33.16^o and 57.04^o. Fig. 7.7(c), (d) and (e) are the XRD pattern for InN grown on the √3x√3 and 4x1 superstructural phases, which have only crystalline peaks related to InN (0002) and InN (0004). A resolved scan of the (0002) wurtzite InN reflections on different samples (after subtracting the contribution from the K$_{α2}$ X-ray component) are
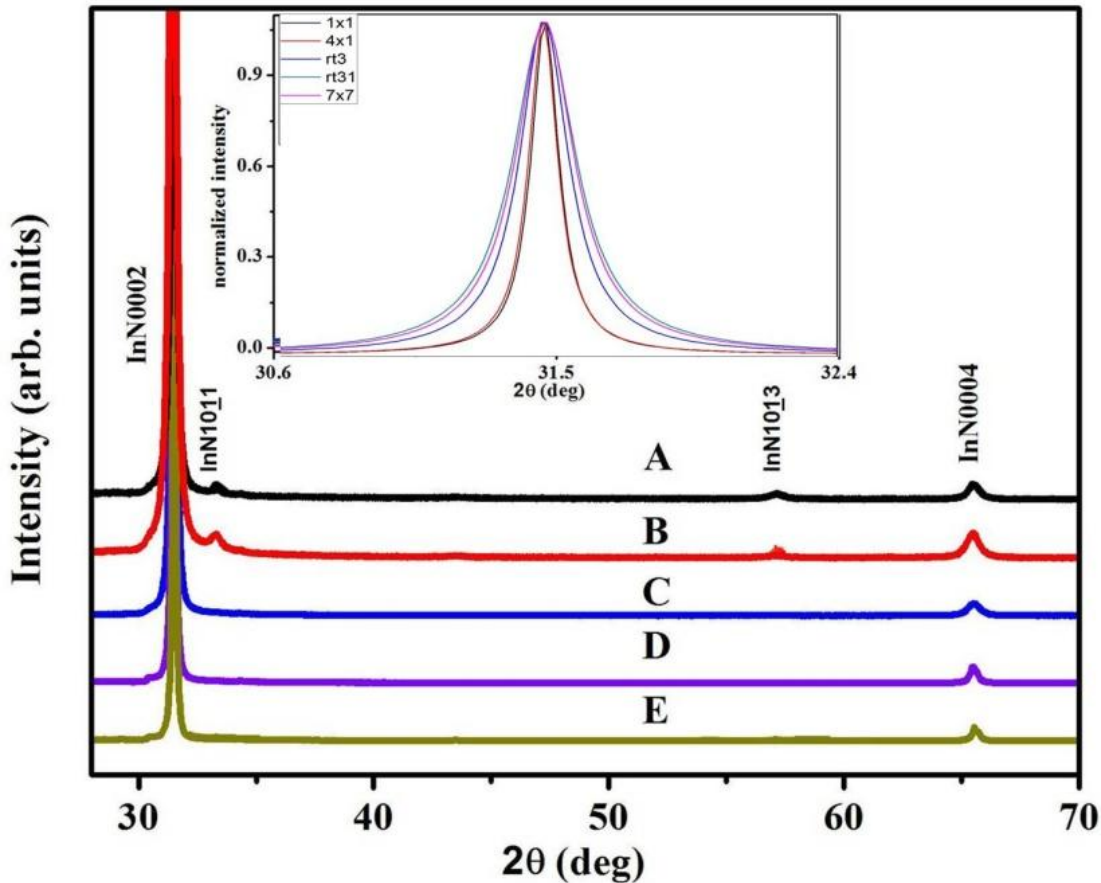
Fig. 7.7: *XRD patterns of InN films grown on a) Si(111)7x7, b) Si(111)√31x√31-In, c) Si(111)√3x√3-In, d) Si(111)4x1-In and e) Si(111)1x1-In. Inset shows FWHM of (0002) reflection of wurtzite InN for different samples.*

shown as inset in Fig. 7.7 for all samples, A through E. FWHM of (0002) reflection for samples A, B and C show a value of ≈ 1000arcsec, whereas samples D and E have a significant lower value of 645arcsec. Thus, XRD results also show better crystalline quality for samples D and E as compared to other InN films formed.

Observation of PL in InN has been rare, especially in high carrier concentration samples, due to the poor material quality of the films. The first observation of PL in InN was only possible in 2002 which revised the band gap of InN to be ≈0.7eV rather than the prior accepted value of 1.89eV. We have observed PL on all five samples which spans from the visible to infrared regions, testifying the material quality of the films and are shown in Fig. 7.8. The observed PL peak positions for samples A, B, C, D and E are 2.07, 2.98, 2.08, 1.38 and 0.74eV, with FWHM of 470meV, 630meV, 470meV ,40meV, 40meV, respectively. Thus, consistent with RHEED, FESEM, AFM and XRD measurements our PL results also

show that InN grown on 4x1 and 1x1 show low band gap and a narrow FWHM, clearly indicating better crystallinity.

To account for the variation in the PL peak position observed, we have measured charge carrier concentration on all the samples A, B, C, D and E by 0.58T Hall
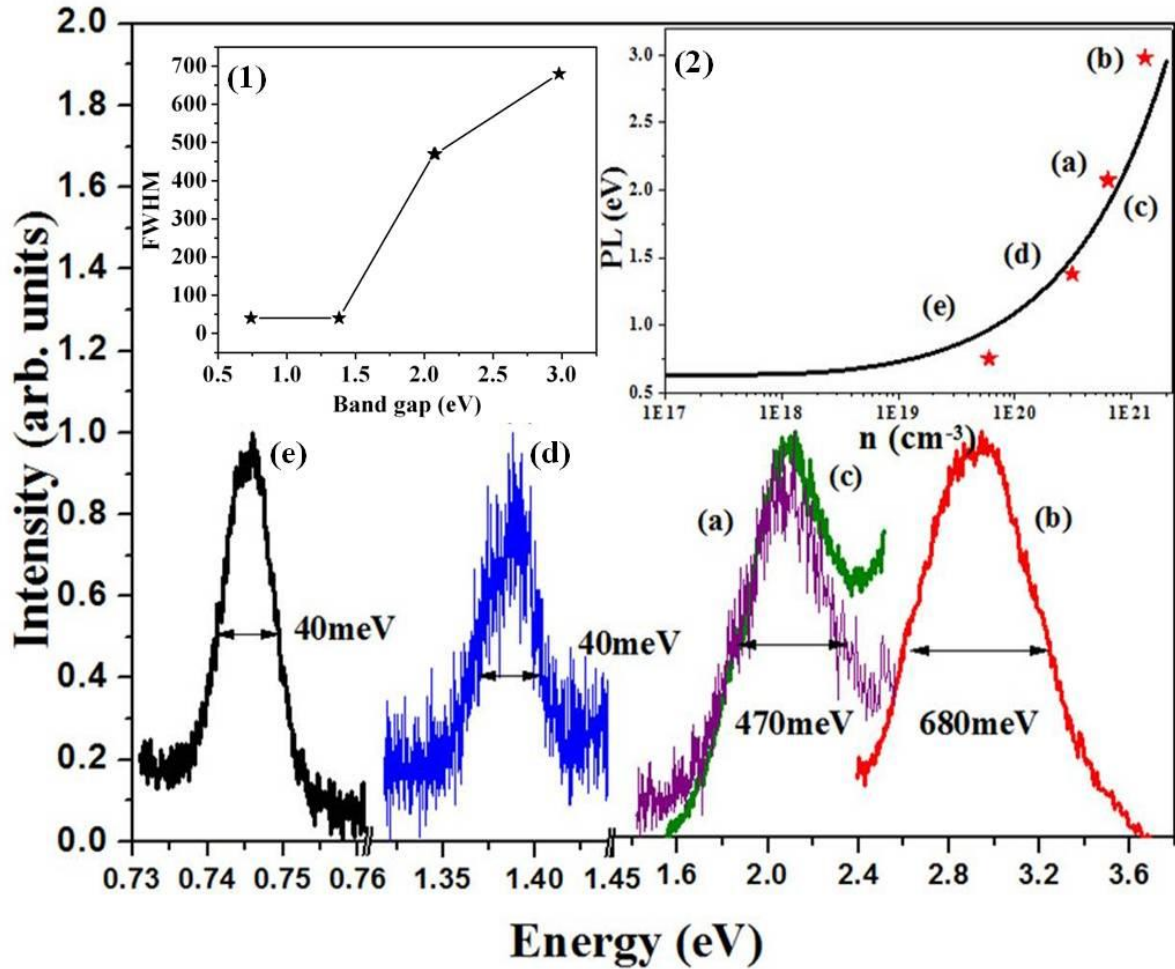
Fig. 7.8: *Photoluminescence of InN films grown on a) Si(111)7x7, b) Si(111)√31x√31-In, c) Si(111)√3x√3-In, d) Si(111)4x1-In and e) Si(111)1x1-In. Inset (1) shows plot of FWHM of PL peak versus band gap and inset (2) shows the experimental band edge plotted versus carrier concentration along with theoretical Moss-Burstein.*

measurements, as 6.3×10^{20} cm^{-3}, 1.3×10^{21} cm^{-3}, 6.3×10^{20} cm^{-3}, 3.1×10^{20} cm^{-3}, and 6.0×10^{19} cm^{-3} respectively. We can see that there is an order reduction in the carrier concentration for InN grown on the 1x1 surface. Inset (2) to Fig. 7.8 shows a plot of the band gap versus carrier concentration based on the Moss Burstein shift. The band gap values obtained by PL in the present experiments, show very good agreement with the Moss-Burstein shift predictions, and thus the variation in the observed PL peak positions from 0.74 to 2.98eV can be

attributed to Moss Burstein shift of the Fermi level to a value much above the conduction band minima. It has been suggested that the interaction of the valence band and conduction band results in variation in the effective mass of charge carriers resulting in a non-parabolic conduction band for InN owing to its narrow band gap.[33] As shown in the inset of Fig. 7.8 our experimental data points fall on the theoretical Moss-Burstein prediction based on non-parabolic conduction band.   As the stoichiometry determination from XPS shows that all samples are stoichiometric with In to N ratio of 1.0 ± 0.05, other factors that influence band gap values, such as In inclusion (Mie-resonances), oxynitride and oxides, can be excluded[34]. Inset (1) in Fig. 7.8 shows a plot of FWHM of the PL peak versus carrier band gap observed which shows a reduction in the PL peak width for lower carrier concentration showing improvement in the quality of the film.

To understand why the 4x1 and 1x1 superstructures result in better epitaxial InN films, we invoke Lattice Matching Epitaxy for different interfaces used, by calculating the 2D unit cell parameters for the different superstructural phases and evaluate the epitaxial matching relation to the InN lattice parameter. The in plane lattice constant of InN and that of bulk truncated (unreconstructed) Si (111) surface are respectively equal to 3.57Å (a*) and 3.80Å (a). Thus, for a given reconstruction, for example for 7x7 phase, since the unit cell is expanded to seven times that of bulk lattice constant, the lattice parameter is given $7 \times a = 26.60$Å. As $7a^* \approx 7a$, we can infer that 7th unit cell of InN matches epitaxially with the fist unit cell of 7x7 reconstruction and we denote this epitaxial relationship as 7/1. Following on the similar line we calculate the epitaxial relationship for other phases. It can be found that closest lattice matching for different phases 7x7, √31x√31, and √3x√3 are 7/1, 6/1 and 2/1 respectively. For 4x1 surface there are two kinds of lattice matching viz. along 'X4' direction its 4/1 and along 'X1' its 1/1 with 76% mismatch along 'X4' and 6% along 'X1' directions respectively. InN has least mis-match with 1x1 surface along both directions where the first unit cell of InN matches with the first unit cell of 1x1 phase with a lattice mismatch of about 6%. Hence Lattice Matching Epitaxy criterion shows that phases 7x7, √31x√31, and √3x√3 have higher mismatch with InN, whereas 4x1 and 1x1 phases form a low mismatched template,   resulting in superior InN films on these later templates. We have already shown that in the case of GaN on Ga induced phases of Si (111), Si (111) √3x√3R30°-Ga reconstruction yields a better template with reduced mismatch enabling the growth of less defected high quality GaN film formed at a much lower temperature than usually employed.

7.3   Conclusions

Several promising applications proposed for InN because of its various fundamental attributes are hindered by the difficulty in synthesizing good quality films due its low dissociation temperature. Motivated by this necessity to reduce the growth temperature and to integrate the nitrides in to well established Si industry we have developed a novel method of using reconstructed unit cell of Si(111)-7x7 surface as a lattice matched template for III-nitride growth. We have obtained the several In induced reconstructions of Si(111)-7x7 such as Si(111)-√31x√31-In, Si(111)-√3x√3-In, Si(111)-4x1-In and Si(111)-1x1-In by carrying out desorption studies using RHEED. InN is grown on all these reconstructions and the quality of the film is analyzed using several complementary characterization tools. We observe a superior quality film for InN grown on 4x1 and 1x1 surfaces. On 1x1 surface carrier concentration measurements using Hall effect shows one order difference in the unintentional dopant density. We invoke LME of the unit cells of these superstructural phases with the unit cell of InN to explain the observed results which shows a better lattice matching with 1x1 unit cell. Observed variation in the carrier concentration on different InN samples is explained using Moss-Burstein shift. Our results also justify the necessity of considering non-parabolic conduction band to explain the property of InN. Thus using novel LME we are able to grow good quality InN at much low temperature than usually employed. These results also indicate the criticality of the interface in deciding the material quality of the films. We have also verified LME for the growth of GaN. In this case we have used the Ga induced superstructural phases of Si(111)-7x7 surface. Our results show a superior quality film in the case of GaN grown on √3x√3 surface which again is explained using LME. Our results show that we are able grow a very good quality GaN at a very low temperature than usually used. Thus, the new approach of Lattice Matching Epitaxy appears to be a very useful method to form epitaxial group III-nitride film with low dislocation density and high quality structural and optical properties. However, more work is essential to optimize growth conditions. A plethora of superstructural phases are possible with the adsorption of metals on various Si surfaces, and the fact that the pre-metal coverage is in submonolayer, it will not interfere with the performance of the device even if other metals are used for obtaining the suitable and stable phase desired.

References

[1] L. Liu and J. H. Edgar, Mater. Sci. Eng. R. **37**, 61 (2002).

[2] A. R. Woll, R. L. Headrick, S. Kycia, and J. D. Brock, Phys. Rev. Lett. **83**, 4349 (1999).

[3] S. A. Kukushkin, A. V. Osipov, V. N. Bessolov, B. K. Medvedev, V. Nevolin K., and K. A. Tcarik, Rev. Adv. Mater. Sci. **17**, 1 (2008).

[4] J. T. Ku, T. H. Yang, J. R. Chang, Y. Y. Wong, W. C. Chou, C. Y. Chang, and C. Y. Chen, Japan. J. Appl. Phys. **49**, 04DH06 (2010).

[5] A. Krost and A. Dadgar, Mater. Sci. Eng. B **93**, 77 (2002).

[6] K. P. Beh, F. K. Yam, C. W. Chin, S. S. Tneh, and Z. Hassan, J. Alloys Compd. **506**, 343 (2010).

[7] J. Neugebauer, Phys. Status. Solidi C **0**, 1651 (2003).

[8] P. Kumar, S. Bhattacharya, B. R. Mehta, and S. M. Shivaprasad, J. Nanosci. Nanotechnol. **9**, 5659 (2009).

[9] P. Kumar, M. Kumar, B. R. Mehta, and S. M. Shivaprasad, Appl. Surf. Sci. **256**, 480 (2009).

[10] M. J. Kappers, M. A. Moram, D. V. Sridhara Rao, C. McAleese, and C. Humphreys J., J. Cryst. Growth **312**, 363 (2010).

[11] N. H. Zhang, X. L. Wang, Y. P. Zeng, H. L. Xiao, J. X. Wang, H. X. Liu, and J. M. Li, J. Phys. D: Appl. Phys. **38**, 1888 (2005).

[12] J. Narayan and B. C. Larson, J. Appl. Phys. **93**, 278 (2003).

[13] V. K. Paliwal, A. G. Vedeshwar, and S. M. Shivaprasad, Phys. Rev. B **66**, 245404 (2002).

[14] M. Kumar, V. Govind, K. Paliwal, A. G. Vedeshwar, and S. Shivaprasad M., Surf. Sci. **2745**, 600 (2006).

[15] K. H. Lee, J. Y. Lee, J. You, D. Uklee, and T. Kein, J. Mater. Res. **24**, 3032 (2009).

[16] P. Kumar, M. Kumar, and S. M. Shivaprasad, Appl. Phys. Lett. **97**, 122105 (2010).

[17] J. Ohta, H. Fujioka, H. Takahashi, M. Sumiya, and M. Oshima, J. Cryst. Growth **233**, 779 (2001).

[18] L. S. Chuah, Z. Hassan, S. S. Ng, and H. A. Hassan, J. Nondestruct. Eval. **28**, 125 (2009).

[19] C. D. Wagner, W. M. Riggs, L. E. Davis, J. F. Moulder, and G. E. Muilenberg, Handbook Of X-Ray Photoelectron Spectroscopy, PerkinElmer Corp., Eden Prairie, MN, (1979).

[20] A. P. Chiu, N. C. Chen, P. H. Chang, and C. F. Shih, Phys. Status. Solidi C **3**, 2014 (2006).

[21] E. Calleja, M. A. S. Garcıa, F. J. Sanchez, F. Calle, F. B. Naranjo, E. Munoz, U. Jahn, and K. Ploog, Phys. Rev. B **62**, 16826 (2000).

[22] K. A. Bertness, A. Roshko, N. A. Sanford, J. M. Barker, and A. V. Davydov, J. Cryst. Growth **287**, 522 (2006).

[23] T. Araki, Y. Saito, T. Yamaguchi, M. Kurouchi, Y. Nanishi, and H. Naoi, J. Vac. Sci. Technol. B **22(4)**, 2139 (2004).

[24] Z. -Y. Li, S. -M. Lan, W. -Y. Uen, Y. -R. Chen, M.-C. Chen, Y. -H. Huang, C. -T. Ku, S. -M. Liao, T. -N. Yang, S. -C. Wang, and G. -C. Chi, J. Vac. Sci. Technol. A **26(4)**, 587 (2008).

[25] T. Yodo, H. Yona, H. Ando, and D. Nosei, Appl. Phys. Lett. **80**, 968 (2001).

[26] C. S. Gallinat, G. Koblmuller, J. S. Brown, S. Bernardis, J. S. Speck, G. D. Chern, E. D. Readinger, H. Shen, and M. Wraback, Appl. Phys. Lett. **89**, 032109-1 (2006).

[27] C. S. Gallinat, G. Koblmüller, J. S. Brown, and J. S. Speck, Journal Of Applied Physics **102**, 064907 (2007).

[28] E. Dimakis, E. Iliopoulos, K. Tsagaraki, Th. Kehagias, Ph. Komninou, and A. Georgakilas, J. Appl. Phys. **97**, 113520 (2005).

[29] Y. Nanishi, Y. Saito, and T. Yamaguchi, Japan. J. Appl. Phys. **42**, 2549 (2003).

[30] Y. -H. Wang and W. -L. Chen, Physica E **41**, 848 (2009).

[31] C. C. Huang, R. W. Chuang, S. J. Chang, J. C. Lin, Y. C. Cheng, and W. J. Lin, J. Electron. Mater. **37**, 1054 (2008).

[32] K. R. Wang, L. W. Tu, S. J. Lin, Y. L. Chen, Z. W. Jiang, M. Chen, C. L. Hsiao, K. H. Cheng, J. W. Yeh, and S. K. Chen, Phys. Status. Solidi B **243**, 1461 (2006).

[33] J. Wu, W. Walukiezicz, W. Shan, K. M. Yu, J. W. Ager III, E. E. Haller, H. Lu, and W. J. Schaff, Phys. Rev. B **66**, 201403 (2002).

[34] K. S. A. Butcher and T. L.Tansley, Superlattices Microstruct. **38**, 1 (2005).

Chapter VIII

Summary, conclusions and future outlook

8.1   Background

The promising applications of InN are not yet been able to be exploited due to the ambiguous values of the material parameters experimentally obtained, a problem which originates from its low dissociation temperature. Literature shows a spectrum of values for different fundamental properties of this material. One of the aims of the thesis is to design experiments to evaluate the various suggested reasons in the literature on the measured band gap of InN grown on $Al_2O_3(0001)$ substrate. InN is also proposed to exhibit phenomenon like surface electron accumulation which has not yet been comprehensively studied. On the other hand, incorporating III nitrides into the well established Si industry is another major challenge. In the literature attempts in this direction is quite nominal in the case of InN. Si surfaces are endowed with fascinating reconstructions induced by metal adsorption which offers the possibility of using them as templates for foreign adsorbates. Thus, we have carefully studied the formation of different superstructural phases of group III metals on Si surfaces so as to find a lattice matched template for the growth of good quality InN and GaN. The summary of the work carried out and the results obtained are given below.

8.2   Summary and conclusions

The reconstructions of the Si surface are rich in structural and electronic properties. Metal adsorption on Si surfaces offers the possibility of formation of several ordered nanostructures on the surface. On the other hand, high index Si surface can be kinetically manipulated with metal adsorption to form ordered nanochains of metal adatoms. Use of these reconstructions as lattice matched growth template for group III-nitride growth has not yet been explored. In search of a suitable interface for the formation of III nitrides on Si surfaces we have performed careful adsorption/desorption studies of Al, Ga and In on Si surfaces. Studies have been performed *in situ* in UHV (base pressure $<5 \times 10^{-11}$ torr) using surface sensitive tools viz., AES and LEED.

8.2.1   Metal induced superstructural phases on Si surfaces

As reported earlier we observe a Stranski-Krastanov growth mode for Ga/Si(111)-7x7 system for room temperature adsorption which transforms to the island growth mode at higher temperatures. One of the important results of our studies is the room temperature observation of the √3x√3 phase, which has not been previously reported in literature. Residual thermal desorption studies of the room temperature adsorbed Ga shows the agglomeration of Ga adatoms above 1ML of Ga layer showing monolayer stability. LEED studies show several super structural phases viz. √3x√3, √3x√3+7x7, 1x1 and incommensurate phase viz. 6.3x6.3, 6.3√3x6.3√3 and 11x11. Based on the results of several adsorption/desorption studies we have constructed a 2D phase diagram for the system which shows the coverage and temperature ranges of occurrence of various superstructural phases for the Ga/Si(111)-7x7 system.

Literature shows ambiguity concerning the growth mode of Al/Si(111)-7x7 system. Our experimental study along with the theoretical simulation of room temperature Al uptake show the deviation of the growth mode from layer by layer growth above 2ML. We observe the formation of islands on the surface above 2ML and the simulation shows that the island density and the area covered by islands increase with coverage of Al above 2ML. At higher substrate temperatures we observe pure Stranski-Krastanov growth mode showing the formation of islands at the lower coverages with increase in substrate temperature of adsorption. We have performed a careful residual thermal desorption study of room temperature adsorbed adlayer of having different initial coverages. For coverage much higher than 2ML we do not observe agglomeration at low annealing temperatures, indicating the absence cluster migration. Overall trend of the desorption curve shows monotonic reduction of Auger signal suggesting agglomeration of Al adatoms on the surface. Irrespective of the initial coverage on the surface the different desorption curves are observed to follow the same desorption path for the temperature range were the desorption of Al is appreciable from the surface (>600°C). This region is also marked by several superstructural phase of Al on th surface. LEED observation during all stages of adsorption and desorption processes showed different superstructural phases viz. α7x7, γ7x7, √7x√7, c-phase and √3x√3. We have observed a periodicity of 8 for the γ7x7 phase. The c-phase has been only observed for the case of adsorption of Al on Si(111)-2x1 phase and we have observed this for the first time on Si(111)-7x7 surface. The region between the transitions of one phase to the other is marked

by the observation of several mixed phases viz. 1x1+1x1, γ7x7+1x1+1x1, γ7x7+√3x√3, √3x√3+ √7x√7x , √3x√3+c-phase and 7x7+√3x√3. Results of several adsorption/desorption experiments performed for Al/Si(111)-7x7 system have been summarized in the form of a phase diagram for the various superstructural phases observed for the system. There have been no previous reports of adsorption/desorption studies of Al on Si(5 5 12)-2x1 surface. Our studies show that Al/Si(5 5 12)-2x1 interface shows that the growth mode at room temperature deviates from the layer by layer mode above 2ML, due to the formation of islands on the surface. This is similar to the behavior of Al on Si(111)-7x7 surface. We have observed the formation of 2x(337) facets which consist of self assembled nanochains of Al on the surface. Residual thermal desorption studies show stable plateaus in the desorption curve which is the characteristics of the facetted (5 5 12) surface providing stable adsorption sites for adatoms. During the desorption process we observe (112)-6x1 reconstruction as well the nanochain 2x(337) phase. Higher temperature adsorption shows SK growth mode with formation of islands occurring at lower coverages with increase in substrate temperature.

Adsorption/desorption studies carried out for In on the Si surfaces show anomalous behavior. Up to 2ML adsorption of In on Si(111)-7x7 surface, the formation of layer by layer growth mode is seen. Above 2ML we observe formation of islands on the surface which disintegrate into layers at high coverages. Thus, there is anomalous clustering of adatoms on the surface. We have looked into these observations in the light of literature on quantum size effects in the growing over layer, which confines the adatoms into islands. As the islands grow in size, such effects become negligible and the islands decay into layers. Residual thermal desorption for In/Si(111)-7x7 system shows coverage dependent behavior. For coverages <2ML the desorption curve shows monotonous behavior with no appreciable change on the surface. For coverage >2ML we observe clustering and layering of adatoms on the surface. The anomalous layering during desorption process has been attributed to the strain relaxation in In islands as well as the In adatom overcoming the step-edge barrier at higher substrate temperatures. LEED studies during the adsorption/desorption studies show several superstructural phases viz. √3x√3, √7x√3, 4x1 and 2√3x2√3. We did not observe the √31x√31 phase in LEED but have observed it using RHEED in our MBE system. The 2√3 phase has been reported once previously and there are no reports concerning its structure. We have studied the structure of the phase by geometry relaxation calculation using *ab-initio* Density Functional Theory and simulated STM images for the phase. The results of adsorption/desorption studies have been summarized in the form of a phase diagram for

In/Si(111)-7x7 system. One of the main differences we observe from the literature is the occurrence of the √3x√3 reconstruction throughout the entire coverage range of 0.3-1ML., in our combined adsorption/desorption experiments carried for this system. There have been no previous reports of the initial stage studies of In on Si(5 5 12)-2x1 surface. The results obtained for the In/Si(111)-7x7 have been compared with the behavior of In on Si(5 12)-2x1 surface. The clustering and layering observed in the case of In/Si(111) system is manifested in the case of (5 5 12) surface also during adsorption at room temperature. The overall trend of the residual thermal desorption behavior, though is same on the two surfaces shows subtle differences. We observe differences in the stable layer upon which clustering takes place, onset temperature of desorption of In from the surface and the final tail of the desorption curve. In the case of (5 5 12) surface the final desorption region shows a broader tail which is a sign of the facetted nature of the surface and the desorption tail has two segments having two different slopes manifesting the different dangling bond density on this surface in the two region. LEED shows different facets in the two regions. We have observed nano chains of In on the Si(5 5 12) surface which are manifested as 2x(337) and 2x(225) facets in LEED. On Si(5 5 12) surface the desorption curve not only shows a morphological reversal during desorption in terms of clustering and layering but we also observe an interesting structural retrace on the surface.

8.2.2   Issues regarding the band gap value of InN

Literature showed a spectrum of values of the InN band gap in the range of 0.6-2eV and several reasons to account and discount the different observations. To look at the reasons for the observed high band gap of InN, we have carried out an experiment to grow three InN samples at different growth temperatures on bare sapphire (0001) substrate at the same N and In fluxes using MBE and the InN samples formed have been characterized using several complementary characterization tools. We observe a band gap value of ≈1.8eV for all the samples studied. Our results clearly exclude stoichiometry and quantum size effects as reasons for the observed high band gap for InN. The XRD measurements on all samples show a strong dependence of InN orientation on the growth temperature. One of the contentious reasons given in literature, for the observed high band gap, is the formation of indium oxide or indium oxynitride which have higher band gap values. Our XPS measurements though showed presence of the oxide phase in one of the samples but its band gap value observed from photoluminescence was similar to that of all the other samples,

ruling out oxide as playing any role on the observed band gap. Hall effect measurement on all the samples measured by the Van der Pauw method showed a degenerate level of unintentional doping with a carrier concentration $\sim 10^{20} cm^{-3}$. We observe that all the experimental data agreed well with the theoretical prediction of Moss-Burstein shift which need a non-parabolic behavior, for the variation of the observed band edge with carrier concentration. Thus, on the basis of analysis by several complementary characterization tools we confirm that the high band gap is due to the high unintentional doping in InN in accordance with the predictions of Moss-Burstein shift.

We designed another experiment to grow InN simultaneously on four differently modified sapphire substrates, using MBE, to look into the low band gap side of the reported band gap spectrum of InN. The different growth schemes are InN/Al_2O_3, InN/N*/Al_2O_3, InN/LT-InN/ Al_2O_3 and InN/GaN/ Al_2O_3. After the surfaces had been differently modified, the final growth was done simultaneously under the same growth conditions, followed by characterized by several complementary characterization tools. In the same experiments, the growth parameters remained the same but three of the four samples yielded a band gap value of $\approx$2eV and one sample showed a value of 0.6eV (grown on GaN epilayer). This shows the criticality of the role of the substrate condition in determining the InN film properties. One of the arguments previously attributed for the low band gap observed for InN was Mie-resonances, resulting from distributed metallic In clusters in InN which shifts the absorption edge to the infrared region of the electromagnetic spectrum. Our XRD and XPS measurements clearly rule out the presence of metallic indium in InN samples which showed the low band gap value, discounting the possibility of Mie-resonance as the reason for the observed low band gap for InN. Also in the same experiment, since the substrate temperature, N and In flux and coverage are same, we are able to observe high and low band gap for InN, showing no role of the growth kinetics on the band gap. The base pressure of our MBE chamber is $<5 \times 10^{-11}$ torr and the oxygen partial pressure is beyond the detection limit of residual gas analyzer attached to the chamber ($<10^{-12}$ torr). This also rules out oxygen having any role in the observed high band gap in these experiments. However, we have carried out XPS measurements to verify the presence of oxide in all the samples that can also come from the oxide substrate (Al_2O_3). This approach also showed negative results, discounting once again oxygen as a reason for the high band gap observed. Carrier concentration measurements using Hall effect in the Van der Pauw configuration also an order of magnitude less than that of the sample grown on GaN epilayer. We studied the

variation in the observed band edge with carrier concentration in the present experiments and reviewed the data existing in literature. A non-linear curve fit for the experimental data points using theoretically calculated Moss-Burstein relation with parabolic conduction band approximation for InN yielded unacceptable value for the effective mass of InN. We also performed a fit of the various experimental data values assuming a non-parabolic conduction band which gave an effective mass of $\approx 0.07m_0$ at the bottom of the conduction band which is acceptable as per literature. Thus, based on a comprehensive analysis we observe a band gap value of InN ≈ 0.6eV and the different reported variation of band gap value in the literature can be well explained invoking Moss-Burstein shift.

Our studies suggest a narrow band gap for InN with a non parabolic conduction band. For a parabolic conduction band effective mass of elections is constant and which become carrier concentration dependent in the case of non parabolic conduction band. To study these issues we have performed reflectivity measurements assuming Drude model for dielectric constant, along with carrier concentration measurements using Hall effect and calculated the effective mass as a function of carrier concentration. The measured effective mass versus carrier concentration for different samples agreed well with the theoretical calculation of effective mass assuming non parabolic conduction band for InN. This confirms that effective mass is dependent on the carrier concentration for InN and hence a non parabolic conduction band for InN. Literature showed the presence of a surface accumulation layer for InN (0001) manifested as an increase in the carrier concentration near the surface of the film, which results in surface band bending. To study such effect in our samples we have performed XPS valence band measurements on different samples having different carrier concentrations. Our results clearly show the presence of surface accumulation layer for InN (0001) surface.

8.2.3   Lattice Matched Epitaxy

We have used the phase diagram of the metal adsorption on Si(111)-7x7 surfaces as a guidance to obtain different reconstructed surfaces of Si in MBE system using RHEED so as to find a suitable interface to grow InN and GaN. We perform careful thermal desorption of about 2ML of In on the Si(111)-7x7 surface to obtain different superstructural phases viz., $\sqrt{3}x\sqrt{3}$, $\sqrt{7}x\sqrt{3}$, 4x1,$\sqrt{31}x\sqrt{31}$ and 1x1 in the MBE system. Five different growths of InN are performed at the same growth conditions on structurally modified substrates and we have studied the quality of the nitride film using several complementary characterization tools. InN grown on 4x1 and 1x1 surfaces show superior quality compared to the films grown on

other superstructural interfaces, in terms of XRD intensity and band-edge photoluminescence intensity. We explain the results using the lattice matching epitaxy of the unit cells of these reconstructions with that of InN. The observed PL peak edges on these samples again confirm the Moss-Burstein shift in InN and propose a non-parabolic conduction band for InN. Our results show lattice matching epitaxy as a novel method to grow InN at much lower temperatures than usually employed. We have also performed experiments to understand effect of LME for GaN. In this case we have used Ga induced phases of Si(111) surface as the growth template. We have grown GaN on 7x7, √3x√3 and 6.3x6.3 phases. Our results, show that GaN grown on √3x√3 shows superior film quality compared to other films which can be explained by invoking LME of these different interfaces with GaN. Our results indicate that we are able to grow good quality GaN at much lesser temperature than usually employed. Thus, we have shown LME as a novel method to grow good quality InN and GaN at very low temperature compared to that usually used, and thus can be of general significance for group III-nitride technology.

8.3   Future outlook

InN is a a promising material with several potential fundamental properties. We have carried out several experiments to lift the ambiguity concerning its basic material parameters like band gap. We believe that our results will help in the direction of obtaining definitive basic attributes for this material. Though we have obtained good quality InN in our experiments there is still enough room for further improvement and more experiments are necessary to find the optimal parameter sets and schemes to obtain the best quality material that meet device standards. Theoretical calculations based on the results of the present experimental results are necessary for further development. Another important concern is the surface electron accumulation layer in InN which may hinder device application of polar surfaces. More experiments are necessary in these directions to find ways to overcome such barriers and good understanding of this phenomenon will be of great help. Our results on metal adsorption studies on Si(111) and Si(5 5 12) surfaces show several metal induced reconstructions. Structural understanding of most of the phases is still in its infant stage, and thus combined *ab initio* calculations and LEED/STM experiments are necessary to have a thorough understanding of their structures so that their properties could be exploited. The novel method of 'lattice matching epitaxy' proposed here to grow high quality GaN and InN on Si surfaces at lower temperatures can be a general technique to form epitaxial films with

reduced strain effects arising due to lattice mismatches. Though we have grown good quality material on reconstructed Si surfaces, improvements can be made by optimizing different growth parameters as well a combination of LME and other growth schemes is also a promising possibility.   Use of the facetted Si(5 5 12) surface and its metal induced reconstructions can also serve as good template to grow III-nitrides as they may promote nucleation in the facets, followed by lateral over layer growth, with reduced defect densities.